

SEPTEMBER 2023

AJNR

VOLUME 44 • PP 999-1107

# AJNR

## AMERICAN JOURNAL OF NEURORADIOLOGY

Official Journal ASNR • ASFNR • ASHNR • ASPNR • ASSR

SEPTEMBER 2023 | VOLUME 44 | NUMBER 9 | WWW.AJNR.ORG

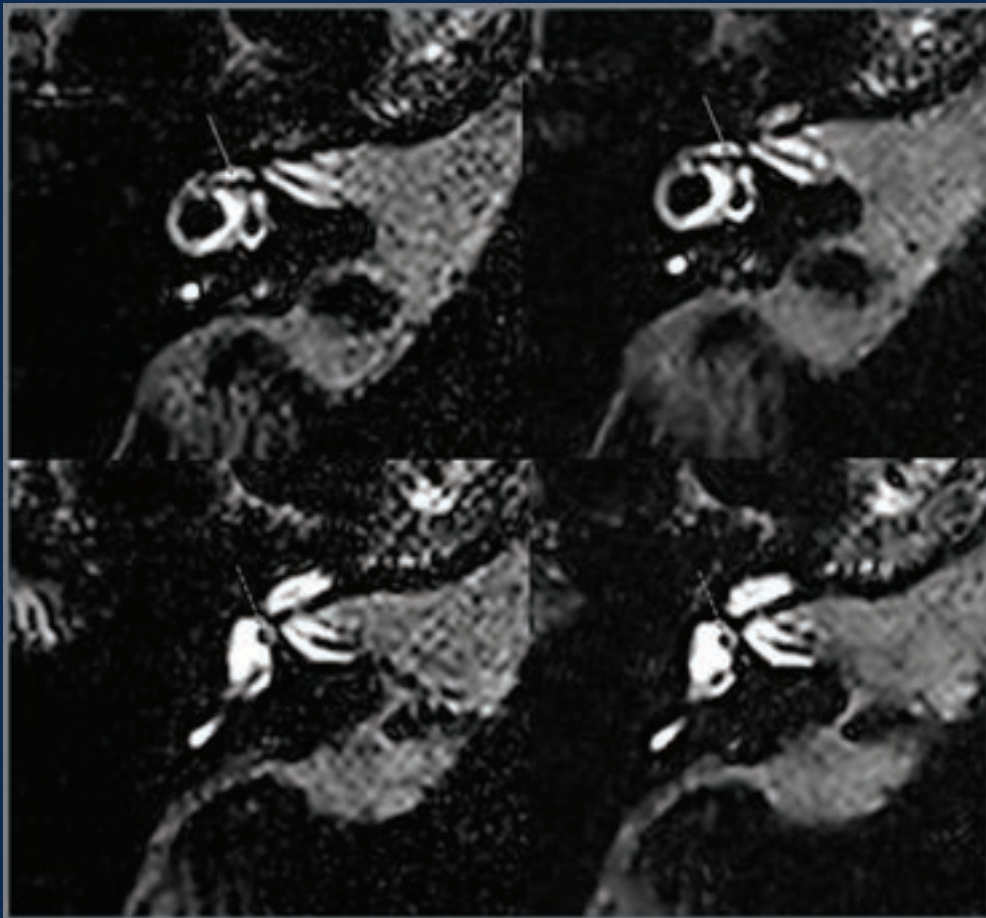
THE JOURNAL OF DIAGNOSTIC AND INTERVENTIONAL NEURORADIOLOGY

Advantage of accelerated 3D FLAIR sequence for hydrocs MR imaging

Diversity trends in neuroradiology trainees

Spaceflight analog effects on cerebral physiology

MR imaging temporal evolution of kernicterus



# FRED™ X™

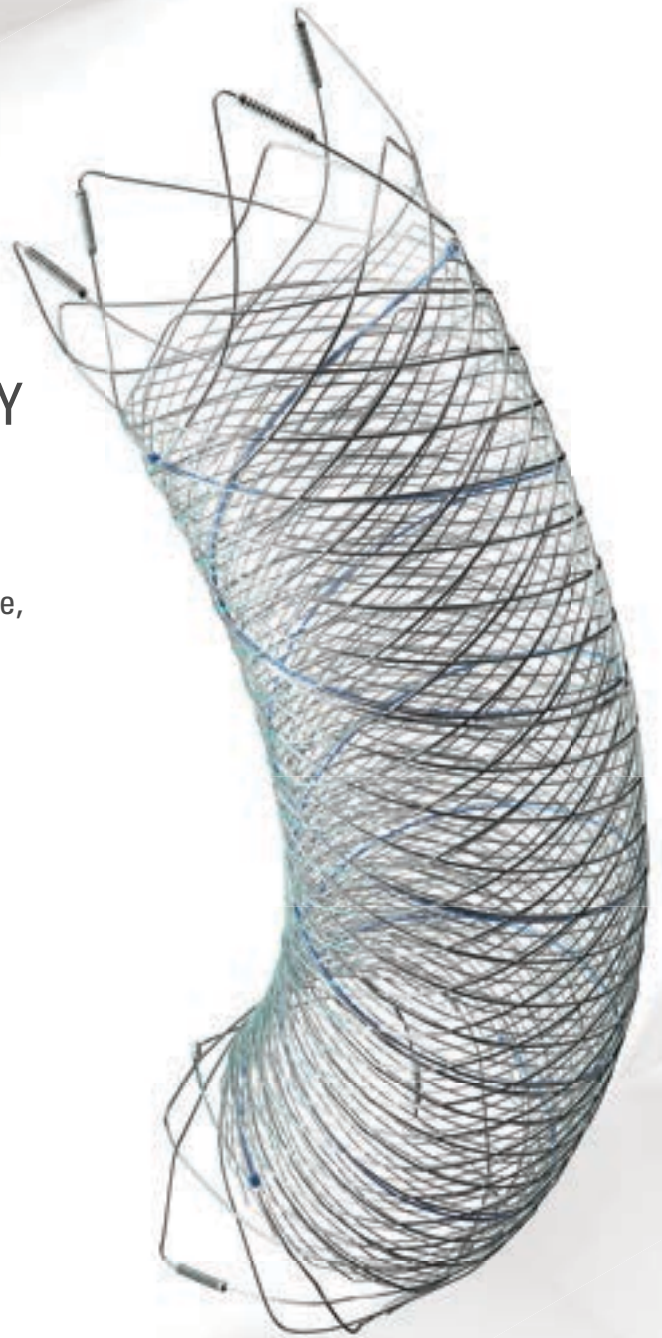
## Flow Diverter Stent

## THE NEXT ADVANCEMENT IN FLOW DIVERSION TECHNOLOGY

The FRED™ X Flow Diverter features the same precise placement and immediate opening of the FRED™ Device, now with X Technology. X Technology is a covalently bonded, nanoscale surface treatment, designed to:

- **REDUCE MATERIAL THROMBOGENICITY<sup>1</sup>**
- **MAINTAIN NATURAL VESSEL HEALING RESPONSE<sup>2,3,4</sup>**
- **IMPROVE DEVICE DELIVERABILITY AND RESHEATHING<sup>1</sup>**

The only FDA PMA approved portfolio with a 0.021" delivery system for smaller device sizes, and no distal lead wire.



For more information, contact your local MicroVention sales representative or visit our website. [www.microvention.com](http://www.microvention.com)

 **MicroVention™**  
**TERUMO**

<sup>\*</sup> Data is derived from in vivo and ex vitro testing and may not be representative of clinical performance.

<sup>1</sup> Data on file

<sup>2</sup> Tanaka M et al. Design of biocompatible and biodegradable polymers based on intermediate water concept. *Polymer Journal*. 2015;47:114-121.

<sup>3</sup> Tanaka M et al. Blood compatible aspects of poly(2-methoxyethylacrylate) (PMEA) – relationship between protein adsorption and platelet adhesion on PMEAs surface. *Biomaterials*. 2000;21:1471-1481.

<sup>4</sup> Schiel L et al. X Coating™: A new biopassive polymer coating. *Canadian Perfusion Canadienne*. June 2001;11(2):9.

**Indications for Use:** The FRED X System is indicated for use in the internal carotid artery from the petrous segment to the terminus for the endovascular treatment of adult patients (22 years of age or older) with wide-necked (neck width 4 mm or dome-to-neck ratio < 2) saccular or fusiform intracranial aneurysms arising from a parent vessel with a diameter 2.0 mm and 5.0 mm.

**Rx Only:** Federal (United States) law restricts this device to sale by or on the order of a physician. For Healthcare professionals intended use only.

MICROVENTION, FRED and HEADWAY are registered trademarks of MicroVention, Inc. in the United States and other jurisdictions. Stylized X is a trademark of MicroVention, Inc. © 2022 MicroVention, Inc. MM1222 US 03/22

# WEB™ 17

Aneurysm Embolization System

# LOWER PROFILE



## NEW SIZES



## MORE ACCESS OPTIONS



#### INDICATIONS FOR USE:

The WEB Aneurysm Embolization System is intended for the endovascular embolization of ruptured and unruptured intracranial aneurysms and other neurovascular abnormalities such as arteriovenous fistulae (AVF). The WEB Aneurysm Embolization System is also intended for vascular occlusion of blood vessels within the neurovascular system to permanently obstruct blood flow to an aneurysm or other vascular malformation.

#### POTENTIAL COMPLICATIONS:

Potential complications include but are not limited to the following: hematoma at the site of entry, aneurysm rupture, emboli, vessel perforation, parent artery occlusion, hemorrhage, ischemia, vasospasm, clot formation, device migration or misplacement, premature or difficult device detachment, non-detachment, incomplete aneurysm filling, revascularization, post-embolization syndrome, and neurological deficits including stroke and death. For complete indications, potential complications, warnings, precautions, and instructions, see instructions for use (IFU provided with the device).

VIA 21, 27, 33 - The VIA Microcatheter is intended for the introduction of interventional devices (such as the WEB device/stents/flow diverters) and infusion of diagnostic agents (such as contrast media) into the neuro, peripheral, and coronary vasculature.

VIA 17,17 Preshaped - The VIA Microcatheter is intended for the introduction of interventional devices (such as the WEB device/stents/flow diverters) and infusion of diagnostic agents (such as contrast media) into the neuro, peripheral, and coronary vasculature.

The VIA Microcatheter is contraindicated for use with liquid embolic materials, such as n-butyl 2-cyanoacrylate or ethylene vinyl alcohol & DMSO (dimethyl sulfoxide).

The device should only be used by physicians who have undergone training in all aspects of the WEB Aneurysm Embolization System procedure as prescribed by the manufacturer.

RX Only: Federal law restricts this device to sale by or on the order of a physician.

For healthcare professional intended use only.



MicroVention Worldwide  
Innovation Center PH +1.714.247.8000

35 Enterprise  
Aliso Viejo, CA 92656 USA  
MicroVention UK Limited PH +44 (0) 191 258 6777  
MicroVention Europe, S.A.R.L. PH +33 (1) 39 21 77 46  
MicroVention Deutschland GmbH PH +49 211 210 798-0  
Website microvention.com



WEB™ and VIA™ are registered trademarks  
of Sequent Medical, Inc. in the United States.

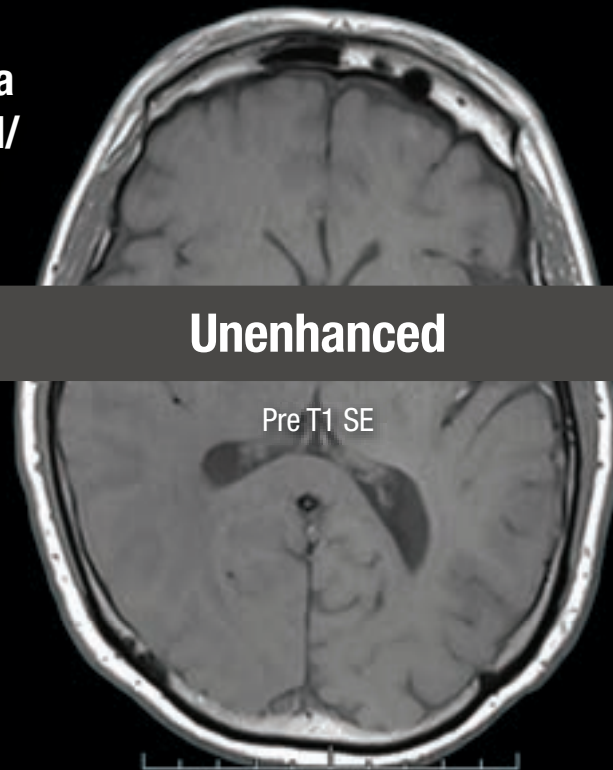
©2021 MicroVention, Inc. MM1184 WW 11/2021

# THIS IS HALF Gd\*

**\*Effective contrast enhancement at half the gadolinium dose (0.05 mmol/kg) vs a macrocyclic GBCA at a dose of 0.1 mmol/kg in approved indications in the U.S.<sup>1-6†</sup>**

  
**Vueway<sup>®</sup>**  
[gadopiclenol] injection  
485.1 mg/mL

**NO COMPROMISE IN MRI FROM BRACCO,  
YOUR TRUSTED PARTNER**



<sup>†</sup>Phase III CNS Study Design (Study GDX-44-010): Intra-individual, crossover comparison of 0.05 mmol/kg VUEWAY (gadopiclenol) injection vs. 0.1 mmol/kg Gadavist<sup>®</sup> in MRI of the CNS. Patients with known or suspected CNS lesions. Three primary visualization endpoints (lesion border delineation, lesion internal morphology, degree of contrast enhancement). The CNS study included 256 patients with known or highly suspected CNS lesion(s) with a mean age of 57 years (range: 18-84 years), and 53% female patients.

Please see Brief Summary of Prescribing Information including Boxed Warning on adjacent page.

## VUEWAY<sup>®</sup> (gadopiclenol) solution for injection

### Indications

VUEWAY injection is indicated in adults and children aged 2 years and older for use with magnetic resonance imaging (MRI) to detect and visualize lesions with abnormal vascularity in:

- the central nervous system (brain, spine and surrounding tissues),
- the body (head and neck, thorax, abdomen, pelvis, and musculoskeletal system).

### IMPORTANT SAFETY INFORMATION

#### WARNING: NEPHROGENIC SYSTEMIC FIBROSIS (NSF)

**Gadolinium-based contrast agents (GBCAs) increase the risk for NSF among patients with impaired elimination of the drugs. Avoid use of GBCAs in these patients unless the diagnostic information is essential and not available with non-contrasted MRI or other modalities. NSF may result in fatal or debilitating fibrosis affecting the skin, muscle and internal organs.**

- **The risk for NSF appears highest among patients with:**
  - **Chronic, severe kidney disease (GFR < 30 mL/min/1.73 m<sup>2</sup>), or**
  - **Acute kidney injury.**

- **Screen patients for acute kidney injury and other conditions that may reduce renal function. For patients at risk for chronically reduced renal function (e.g. age > 60 years, hypertension, diabetes), estimate the glomerular filtration rate (GFR) through laboratory testing.**
- **For patients at highest risk for NSF, do not exceed the recommended VUEWAY dose and allow a sufficient period of time for elimination of the drug from the body prior to any re-administration.**

### Contraindications

VUEWAY injection is contraindicated in patients with history of hypersensitivity reactions to VUEWAY.

### Warnings

Risk of **nephrogenic systemic fibrosis** is increased in patients using GBCA agents that have impaired elimination of the drugs, with the highest risk in patients with chronic, severe kidney disease as well as patients with acute kidney injury. Avoid use of GBCAs among these patients unless the diagnostic information is essential and not available with non-contrast MRI or other modalities.

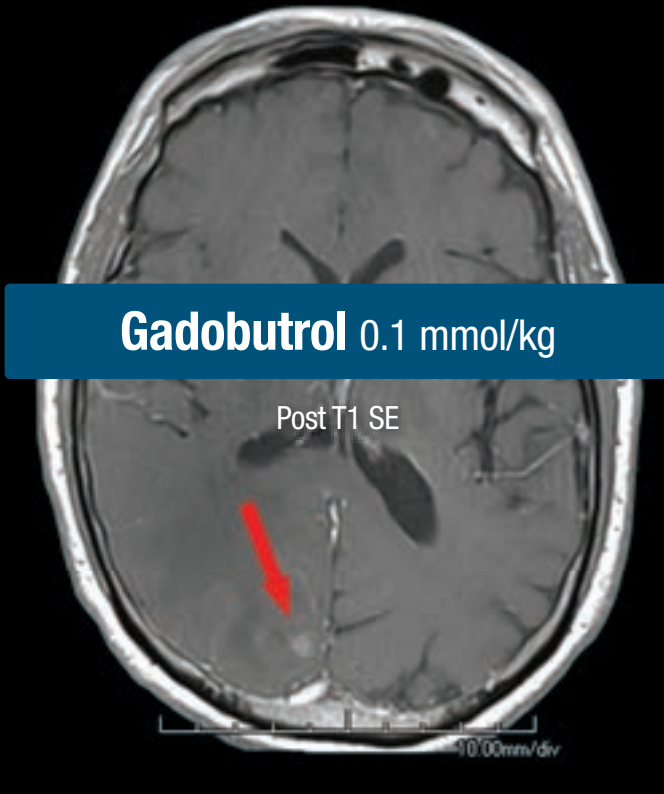
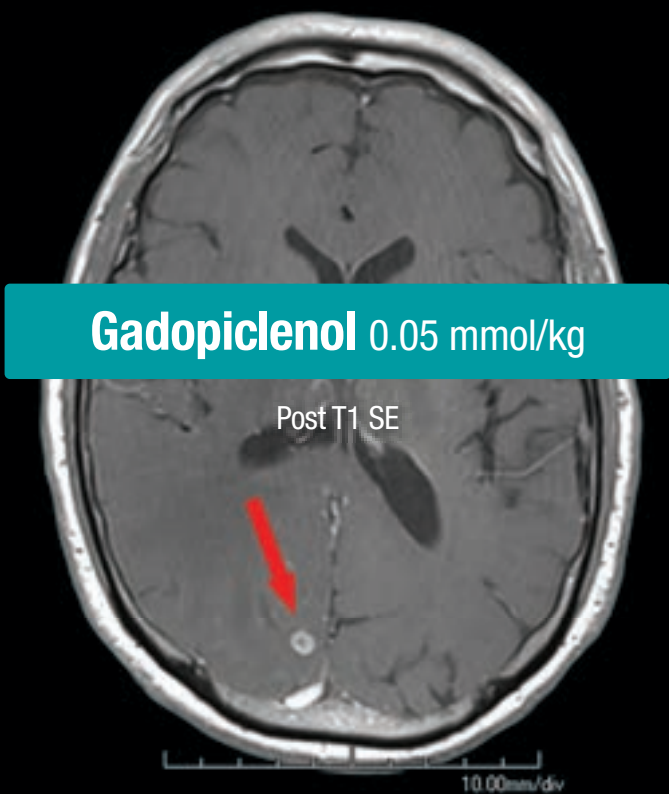
**Hypersensitivity reactions**, including serious hypersensitivity reactions, could occur during use or shortly following VUEWAY administration. Assess all patients for any history of a reaction to contrast media, bronchial asthma and/or allergic disorders, administer VUEWAY only in



LIFE FROM INSIDE

65-year-old man – 3.0 T Siemens  
Brain metastasis from lung adenocarcinoma<sup>7</sup>

SE = Spin Echo. These are representative images from reference studies; individual results may vary.



situations where trained personnel and therapies are promptly available for the treatment of hypersensitivity reactions, and observe patients for signs and symptoms of hypersensitivity reactions after administration.

**Gadolinium retention** can be for months or years in several organs after administration. The highest concentrations (nanomoles per gram of tissue) have been identified in the bone, followed by other organs (brain, skin, kidney, liver and spleen). Minimize repetitive GBCA imaging studies, particularly closely spaced studies, when possible.

**Acute kidney injury** requiring dialysis has occurred with the use of GBCAs in patients with chronically reduced renal function. The risk of acute kidney injury may increase with increasing dose of the contrast agent.

Ensure catheter and venous patency before injecting as **extravasation** may occur, and cause tissue irritation.

VUEWAY may **impair the visualization of lesions** seen on non-contrast MRI. Therefore, caution should be exercised when VUEWAY MRI scans are interpreted without a companion non-contrast MRI scan.

The most common adverse reactions (incidence  $\geq$  0.5%) are injection site pain (0.7%), and headache (0.7%).

**You are encouraged to report negative side effects of prescription drugs to the FDA. Visit [www.fda.gov/medwatch](http://www.fda.gov/medwatch) or call 1-800-FDA-1088.**

**Please see BRIEF SUMMARY of Prescribing Information for VUEWAY, including BOXED WARNING on Nephrogenic Systemic Fibrosis.**

Manufactured for Bracco Diagnostics Inc. by Liebel-Flarsheim Company LLC - Raleigh, NC, USA 27616.

VUEWAY is a trademark of Bracco Imaging S.p.A.

All other trademarks and registered trademarks are the property of their respective owners.

**References:** **1.** VUEWAY<sup>®</sup> (gadopiclenol) solution for injection, 485.1 mg/mL Full Prescribing Information and Patient Medication Guide. Monroe Twp., NJ: Bracco Diagnostics Inc.; September 2022. **2.** Robic C, Port M, Rousseaux O, et al. Physicochemical and pharmacokinetic profiles of gadopiclenol: a new macrocyclic gadolinium chelate with high T1 relaxivity. *Invest Radiol.* 2019 Aug;54:475-484. **3.** GADAVIST<sup>®</sup> (gadobutrol) Injection. Full Prescribing Information. Bayer HealthCare Pharmaceuticals Inc. Whippany, NJ; April 2022. **4.** DOTAREM<sup>®</sup> (gadoterate meglumine) Injection. Full Prescribing Information. Guerbet LLC. Princeton, NJ; April 2022. **5.** CLARISCAN<sup>™</sup> (gadoterate meglumine) injection for intravenous use. Full Prescribing Information. GE Healthcare. Chicago, IL; February 2020. **6.** ProHance<sup>®</sup> (Gadoteridol) Injection, 279.3 mg/mL Full Prescribing Information and Patient Medication Guide. Monroe Twp., NJ: Bracco Diagnostics Inc.; June 2022. **7.** Loevner LA, Kolumban B, Hutóczki G, et al. Efficacy and safety of gadopiclenol for contrast-enhanced MRI of the central nervous system: the PICTURE randomized clinical trial. *Invest Radiol.* 2023 May;58(5):307-313.

Bracco Diagnostics Inc.  
259 Prospect Plains Road, Building H  
Monroe Township, NJ 08831 USA  
Phone: 609-514-2200  
Toll-Free: 1-877-272-2269 (U.S. only)  
Fax: 609-514-2446

© 2023 Bracco Diagnostics Inc.  
All Rights Reserved. US-VW-2300022 08/23



VISIT  
[VUEWAY.COM](http://VUEWAY.COM)  
FOR MORE  
INFORMATION

**Vueway™**  
(gadopichlenol) injection, for intravenous use  
**BRIEF SUMMARY: Please see package insert of full prescribing information.**

**WARNING: NEPHROGENIC SYSTEMIC FIBROSIS (NSF)**  
Gadolinium-based contrast agents (GBCAs) increase the risk for NSF among patients with impaired elimination of the drugs. Avoid use of GBCAs in these patients unless the diagnostic information is essential and not available with non-contrast MRI or other modalities. NSF may result in fatal or debilitating fibrosis affecting the skin, muscle and internal organs.

- The risk for NSF appears highest among patients with:
  - Chronic, severe kidney disease (GFR <30 mL/min/1.73 m<sup>2</sup>), or
  - Acute kidney injury.
- Screen patients for acute kidney injury and other conditions that may reduce renal function. For patients at risk for chronically reduced renal function (e.g. age >60 years, hypertension, diabetes), estimate the glomerular filtration rate (GFR) through laboratory testing.
- For patients at highest risk for NSF, do not exceed the recommended Vueway dose and allow a sufficient period of time for elimination of the drug from the body prior to any re-administration [see Warnings and Precautions (5.1) in the full Prescribing Information].

**INDICATIONS AND USAGE**

Vueway™ (gadopichlenol) is a gadolinium-based contrast agent indicated in adult and pediatric patients aged 2 years and older for use with magnetic resonance imaging (MRI) to detect and visualize lesions with abnormal vascularity in:

- the central nervous system (brain, spine, and associated tissues),
- the body (head and neck, thorax, abdomen, pelvis, and musculoskeletal system).

**CONTRAINDICATIONS**

Vueway is contraindicated in patients with history of hypersensitivity reactions to gadopichlenol.

**WARNINGS AND PRECAUTIONS**

**Nephrogenic Systemic Fibrosis** Gadolinium-based contrast agents (GBCAs) increase the risk for nephrogenic systemic fibrosis (NSF) among patients with impaired elimination of the drugs. Avoid use of GBCAs among these patients unless the diagnostic information is essential and not available with non-contrast MRI or other modalities. The GBCA-associated NSF risk appears highest for patients with chronic, severe kidney disease (GFR <30 mL/min/1.73 m<sup>2</sup>) as well as patients with acute kidney injury. The risk appears lower for patients with chronic, moderate kidney disease (GFR 30-59 mL/min/1.73 m<sup>2</sup>) and little, if any, for patients with chronic, mild kidney disease (GFR 60-89 mL/min/1.73 m<sup>2</sup>). NSF may result in fatal or debilitating fibrosis affecting the skin, muscle, and internal organs. Report any diagnosis of NSF following Vueway administration to Bracco Diagnostics Inc. (1-800-257-5181) or FDA (1-800-FDA-1088 or [www.fda.gov/medwatch](http://www.fda.gov/medwatch)).

Screen patients for acute kidney injury and other conditions that may reduce renal function. Features of acute kidney injury consist of rapid (over hours to days) and usually reversible decrease in kidney function, commonly in the setting of surgery, severe infection, injury or drug-induced kidney toxicity. Serum creatinine levels and estimated GFR may not reliably assess renal function in the setting of acute kidney injury. For patients at risk for chronically reduced renal function (e.g., age >60 years, diabetes mellitus or chronic hypertension), estimate the GFR through laboratory testing.

Among the factors that may increase the risk for NSF are repeated or higher than recommended doses of a GBCA and the degree of renal impairment at the time of exposure. Record the specific GBCA and the dose administered to a patient. For patients at highest risk for NSF, do not exceed the recommended Vueway dose and allow a sufficient period of time for elimination of the drug prior to re-administration. For patients receiving hemodialysis, physicians may consider the prompt initiation of hemodialysis following the administration of a GBCA in order to enhance the contrast agent's elimination [see Use in Specific Populations (8.6) and Clinical Pharmacology (12.3) in the full Prescribing Information]. The usefulness of hemodialysis in the prevention of NSF is unknown.

**Hypersensitivity Reactions** With GBCAs, serious hypersensitivity reactions have occurred. In most cases, initial symptoms occurred within minutes of GBCA administration and resolved with prompt emergency treatment.

- Before Vueway administration, assess all patients for any history of a reaction to contrast media, bronchial asthma and/or allergic disorders. These patients may have an increased risk for a hypersensitivity reaction to Vueway.
- Vueway is contraindicated in patients with history of hypersensitivity reactions to Vueway [see Contraindications (4) in the full Prescribing Information].
- Administer Vueway only in situations where trained personnel and therapies are promptly available for the treatment of hypersensitivity reactions, including personnel trained in resuscitation.
- During and following Vueway administration, observe patients for signs and symptoms of hypersensitivity reactions.

**Gadolinium Retention** Gadolinium is retained for months or years in several organs. The highest concentrations (nanomoles per gram of tissue) have been identified in the bone, followed by other organs (e.g. brain, skin, kidney, liver, and spleen). The duration of retention also varies by tissue and is longest in bone. Linear GBCAs cause more retention than macrocyclic GBCAs. At equivalent doses, gadolinium retention varies among the linear agents with gadodiamide causing greater retention than other linear agents such as gadoxetate disodium, and gadobenate dimeglumine. Retention is lowest and similar

among the macrocyclic GBCAs such as gadoterate meglumine, gadobutrol, gadoteridol, and gadopichlenol.

Consequences of gadolinium retention in the brain have not been established. Pathologic and clinical consequences of GBCA administration and retention in skin and other organs have been established in patients with impaired renal function [see Warnings and Precautions (5.1) in the full Prescribing Information]. There are rare reports of pathologic skin changes in patients with normal renal function. Adverse events involving multiple organ systems have been reported in patients with normal renal function without an established causal link to gadolinium.

While clinical consequences of gadolinium retention have not been established in patients with normal renal function, certain patients might be at higher risk. These include patients requiring multiple lifetime doses, pregnant and pediatric patients, and patients with inflammatory conditions. Consider the retention characteristics of the agent when choosing a GBCA for these patients. Minimize repetitive GBCA imaging studies, particularly closely spaced studies, when possible.

**Acute Kidney Injury** in patients with chronically reduced renal function, acute kidney injury requiring dialysis has occurred with the use of GBCAs. The risk of acute kidney injury may increase with increasing dose of the contrast agent. Do not exceed the recommended dose.

**Extravasation and Injection Site Reactions** Injection site reactions such as injection site pain have been reported in the clinical studies with Vueway [see Adverse Reactions (6.1) in the full Prescribing Information]. Extravasation during Vueway administration may result in tissue irritation [see Nonclinical Toxicology (13.2) in the full Prescribing Information]. Ensure catheter and venous patency before the injection of Vueway.

**Interference with Visualization of Lesions Visible with Non-Contrast MRI** As with any GBCA, Vueway may impair the visualization of lesions seen on non-contrast MRI. Therefore, caution should be exercised when Vueway MRI scans are interpreted without a companion non-contrast MRI scan.

**ADVERSE REACTIONS**

The following serious adverse reactions are discussed elsewhere in labeling:

- Nephrogenic Systemic Fibrosis [see Warnings and Precautions (5.1) in the full Prescribing Information]
- Hypersensitivity Reactions [see Contraindications (4) and Warnings and Precautions (5.2) in the full Prescribing Information]

**Clinical Trials Experience** Because clinical trials are conducted under widely varying conditions, adverse reaction rates observed in the clinical trials of a drug cannot be directly compared to rates in the clinical trials of another drug and may not reflect the rates observed in clinical practice.

The safety of Vueway was evaluated in 1,047 patients who received Vueway at doses ranging from 0.025 mmol/kg (one half the recommended dose) to 0.3 mmol/kg (six times the recommended dose). A total of 708 patients received the recommended dose of 0.05 mmol/kg. Among patients who received the recommended dose, the average age was 51 years (range 2 years to 88 years) and 56% were female. The ethnic distribution was 79% White, 10% Asian, 7% American Indian or Alaska native, 2% Black, and 2% patients of other or unspecified ethnic groups.

Overall, approximately 4.7% of subjects receiving the labeled dose reported one or more adverse reactions.

Table 1 lists adverse reactions that occurred in >0.2% of patients who received 0.05 mmol/kg Vueway.

TABLE 1. ADVERSE REACTIONS REPORTED IN >0.2% OF PATIENTS RECEIVING VUEWAY IN CLINICAL TRIALS	
Adverse Reaction	Vueway 0.05 mmol/kg (n=708) (%)
Injection site pain	0.7
Headache	0.7
Nausea	0.4
Injection site warmth	0.4
Injection site coldness	0.3
Dizziness	0.3
Local swelling	0.3

Adverse reactions that occurred with a frequency < 0.2% in patients who received 0.05 mmol/kg Vueway included: maculopapular rash, vomiting, worsened renal impairment, feeling hot, pyrexia, oral paresthesia, dysgeusia, diarrhea, pruritus, allergic dermatitis, erythema, injection site paresthesia, Cystatin C increase, and blood creatinine increase.

**Adverse Reactions in Pediatric Patients**

One study with a single dose of Vueway (0.05 mmol/kg) was conducted in 80 pediatric patients aged 2 years to 17 years, including 60 patients who underwent a central nervous system (CNS) MRI and 20 patients who underwent a body MRI. One adverse reaction (maculopapular rash of moderate severity) in one patient (1.3%) was reported in the CNS cohort.

**USE IN SPECIFIC POPULATIONS**

**Pregnancy Risk Summary** There are no available data on Vueway use in pregnant women to evaluate for a drug-associated risk of major birth defects, miscarriage or other adverse maternal or fetal outcomes. GBCAs cross the human placenta and result in fetal exposure and gadolinium retention. The available human data on GBCA exposure during pregnancy and adverse fetal outcomes are limited and inconclusive (see Data). In animal reproduction studies, there were no adverse developmental effects observed in rats or rabbits with intravenous administration of Vueway during organogenesis (see Data). Because of the potential risks of gadolinium to the fetus, use Vueway only if imaging is essential during pregnancy and cannot be delayed. The estimated background risk of major birth defects and miscarriage for the indicated population(s) are unknown. All pregnancies have a background risk of birth defect, loss, or other adverse outcomes. In the U.S. general population, the estimated background risk of major birth defects and miscarriage in clinically recognized pregnancies is 2% to 4% and 15% to 20% respectively. Data Human Data Contrast enhancement is visualized in the placenta and fetal tissues after maternal GBCA administration. Cohort studies and case reports on exposure to GBCAs during pregnancy have not reported a clear association between GBCAs and adverse effects in the exposed neonates. However, a retrospective cohort study comparing pregnant women who had a GBCA MRI to pregnant women who did not have an MRI reported a higher occurrence of stillbirths and neonatal deaths in the group receiving GBCA MRI. Limitations of this study include a lack of comparison with non-contrast MRI and lack of information about the maternal indication for MRI. Overall, these data preclude

a reliable evaluation of the potential risk of adverse fetal outcomes with the use of GBCAs in pregnancy.

**Animal Data** Gadolinium Retention: GBCAs administered to pregnant non-human primates (0.1 mmol/kg on gestational days 85 and 135) result in measurable gadolinium concentration in the offspring in bone, brain, skin, liver, kidney, and spleen for at least 7 months. GBCAs administered to pregnant mice (2 mmol/kg daily on gestational days 16 through 19) result in measurable gadolinium concentrations in the pups in bone, brain, kidney, liver, blood, muscle, and spleen at one-month postnatal age.

**Reproductive Toxicology:** Animal reproduction studies conducted with gadopichlenol showed some signs of maternal toxicity in rats at 10 mmol/kg and rabbits at 5 mmol/kg (corresponding to 52 times and 57 times the recommended human dose, respectively). This maternal toxicity was characterized in both species by swelling, decreased activity, and lower gestation weight gain and food consumption.

No effect on embryo-fetal development was observed in rats at 10 mmol/kg (corresponding to 52 times the recommended human dose). In rabbits, a lower mean fetal body weight was observed at 5 mmol/kg (corresponding to 57 times the recommended human dose) and this was attributed as a consequence of the lower gestation weight gain.

**Lactation Risk Summary** There are no data on the presence of gadopichlenol in human milk, the effects on the breastfed infant, or the effects on milk production. However, published lactation data on other GBCAs indicate that 0.01% to 0.04% of the maternal gadolinium dose is excreted in breast milk. Additionally, there is limited GBCA gastrointestinal absorption in the breast-fed infant. Gadopichlenol is present in rat milk. When a drug is present in animal milk, it is likely that the drug will be present in human milk (see Data). The developmental and health benefits of breastfeeding should be considered along with the mother's clinical need for Vueway and any potential adverse effects on the breastfed infant from Vueway or from the underlying maternal condition. Data In lactating rats receiving single intravenous injection of [<sup>152</sup>Gd]-gadopichlenol, 0.3% and 0.2% of the total administered radioactivity was transferred to the pups via maternal milk at 6 hours and 24 hours after administration, respectively. Furthermore, in nursing rat pups, oral absorption of gadopichlenol was 3.6%.

**Pediatric Use** The safety and effectiveness of Vueway for use with MRI to detect and visualize lesions with abnormal vascularity in the CNS (brain, spine, and associated tissues), and the body (head and neck, thorax, abdomen, pelvis, and musculoskeletal system) have been established in pediatric patients aged 2 years and older.

Use of Vueway in this age group is supported by evidence from adequate and well-controlled studies in adults with additional pharmacokinetic and safety data from an open-label, uncontrolled, multicenter, single dose study of Vueway (0.05 mmol/kg) in 80 pediatric patients aged 2 to 17 years. The 80 patients consisted of 60 patients who underwent a CNS MRI and 20 patients who underwent a body MRI [see Adverse Reactions (6.1) and Clinical Pharmacology (12.3) in the full Prescribing Information].

The safety and effectiveness of Vueway have not been established in pediatric patients younger than 2 years of age.

**Geriatric Use** Of the total number of Vueway-treated patients in clinical studies, 270 (26%) patients were 65 years of age and over, while 62 (6%) patients were 75 years of age and over. No overall differences in safety or efficacy were observed between these subjects and younger subjects.

This drug is known to be substantially excreted by the kidney, and the risk of adverse reactions to this drug may be greater in patients with impaired renal function. Because elderly patients are more likely to have decreased renal function, it may be useful to monitor renal function.

**Renal Impairment** in patients with renal impairment, the exposure of gadopichlenol is increased compared to patients with normal renal function. This may increase the risk of adverse reactions such as nephrogenic systemic fibrosis (NSF). Avoid use of GBCAs among these patients unless the diagnostic information is essential and not available with non-contrast MRI or other modalities. No dose adjustment of Vueway is recommended for patients with renal impairment. Vueway can be removed from the body by hemodialysis [see Warnings and Precautions (5.1, 5.3, 5.4) and Clinical Pharmacology (12.3) in the full Prescribing Information].

**OVERDOSAGE**

Among subjects who received a single 0.3 mmol/kg intravenous dose of gadopichlenol (6 times the recommended dose of Vueway), headache and nausea were the most frequently reported adverse reactions. Gadopichlenol can be removed from the body by hemodialysis [see Clinical Pharmacology (12.3) in the full Prescribing Information].

**PATIENT COUNSELING INFORMATION** Advise the patient to read the FDA-approved patient labeling (Medication Guide).

**Nephrogenic Systemic Fibrosis** Inform the patient that Vueway may increase the risk for NSF among patients with impaired elimination of the drugs and that NSF may result in fatal or debilitating fibrosis affecting the skin, muscle and internal organs.

Instruct the patients to contact their physician if they develop signs or symptoms of NSF following Vueway administration, such as burning, itching, swelling, scaling, hardening and tightening of the skin; red or dark patches on the skin; stiffness in joints with trouble moving, bending or straightening the arms, hands, legs or feet; pain in the hip bones or ribs; or muscle weakness [see Warnings and Precautions (5.1) in the full Prescribing Information].

**Gadolinium Retention** Advise patients that gadolinium is retained for months or years in brain, bone, skin, and other organs following Vueway administration even in patients with normal renal function. The clinical consequences of retention are unknown. Retention depends on multiple factors and is greater following administration of linear GBCAs than following administration of macrocyclic GBCAs [see Warnings and Precautions (5.3) in the full Prescribing Information].

**Injection Site Reactions** Inform the patient that Vueway may cause reactions along the venous injection site, such as mild and transient burning or pain or feeling of warmth or coldness at the injection site [see Warnings and Precautions (5.5) in the full Prescribing Information].

**Pregnancy** Advise pregnant women of the potential risk of fetal exposure to Vueway [see Use in Specific Populations (8.1) in the full Prescribing Information].

**Rx only**

US Patent No. 10,973,934  
Manufactured for Bracco Diagnostics Inc. by Liebel-Flarsheim Company LLC - Raleigh, NC, USA 27616.  
Toll Free: 1-877-272-2269 (U.S. only)  
Revised November 2022

# AJNR

## AMERICAN JOURNAL OF NEURORADIOLOGY

SEPTEMBER 2023  
VOLUME 44  
NUMBER 9  
WWW.AJNR.ORG

Publication Preview at [www.ajnr.org](http://www.ajnr.org) features articles released in advance of print. Visit [www.ajnrblog.org](http://www.ajnrblog.org) to comment on AJNR content and chat with colleagues and AJNR's News Digest at <http://ajnrdigest.org> to read the stories behind the latest research in neuroimaging.

### RADIOLOGY-PATHOLOGY CORRELATION

-  999 **Benign Enhancing Foramen Magnum Lesions** *I.T. Mark, et al.*

ADULT BRAIN

### REVIEW ARTICLE

-   1002 **Unpacking the CNS Manifestations of Epstein-Barr Virus: An Imaging Perspective** *N. Soni, et al.*

ADULT BRAIN

### ACADEMIC PERSPECTIVES

- 1009 **Trends of Diversity in Neuroradiology Trainees in United States 2015–2022** *P. Prajapati, et al.*

### GENERAL CONTENTS

-   1012 **Generative Adversarial Network–Enhanced Ultra-Low-Dose [<sup>18</sup>F]-PI-2620  $\tau$  PET/MRI in Aging and Neurodegenerative Populations** *K.T. Chen, et al.*
- ADULT BRAIN
-   1020 **Deep Learning Segmentation of the Nucleus Basalis of Meynert on 3T MRI** *D.J. Doss, et al.*
- ADULT BRAIN
-    1026 **Longitudinal Changes in Cerebral Perfusion, Perivascular Space Volume, and Ventricular Volume in a Healthy Cohort Undergoing a Spaceflight Analog** *J.B. Tidwell, et al.*
- ADULT BRAIN
-  1032 **Long-Term Follow-up of Multinodular and Vacuolating Neuronal Tumors and Implications for Surveillance Imaging** *S. Dogra, et al.*
- ADULT BRAIN
- 1039 **Prospective Comparison of T1-SPACE and MPRAGE for the Identification of Intrinsic T1 Hyperintensity in Patients with Intracranial Melanoma Metastases** *A. Lasocki, et al.*
- ADULT BRAIN
-   1045 **CT Perfusion Does Not Modify the Effect of Reperfusion in Patients with Acute Ischemic Stroke Undergoing Endovascular Treatment in the ESCAPE-NA1 Trial** *N.B. Rex, et al.*
- INTERVENTIONAL
-  1050 **Intra-Arterial Thrombolysis is Associated with Delayed Reperfusion of Remaining Vessel Occlusions following Incomplete Thrombectomy** *A. Mujanovic, et al.*
- INTERVENTIONAL
-  1057 **Contrast Injection from an Intermediate Catheter Placed in an Intradural Artery is Associated with Contrast-Induced Encephalopathy following Neurointervention** *M. Fuga, et al.*
- INTERVENTIONAL

AJNR (Am J Neuroradiol) ISSN 0195–6108 is a journal published monthly, owned and published by the American Society of Neuroradiology (ASNR), 820 Jorie Boulevard, Oak Brook, IL 60523. Annual dues for the ASNR include approximately 19% for a journal subscription. The journal is printed by Intellicor Communications, 330 Eden Road, Lancaster, PA 17601; Periodicals postage paid at Oak Brook, IL and additional mailing offices. Printed in the U.S.A. POSTMASTER: Please send address changes to American Journal of Neuroradiology, P.O. Box 3000, Denville, NJ 07834, U.S.A. Subscription rates: nonmember \$452 (\$530 foreign) print and online, \$320 online only; institutions \$520 (\$594 foreign) print and basic online, \$1029 (\$1103 foreign) print and extended online, \$380 online only (basic), \$825 online only (extended); single copies are \$35 each (\$40 foreign). Indexed by PubMed/MEDLINE, BIOSIS Previews, Current Contents (Clinical Medicine and Life Sciences), EMBASE, Google Scholar, HighWire Press, Q-Sensei, RefSeek, Science Citation Index, SCI Expanded, ReadCube, and Semantic Scholar. Copyright © American Society of Neuroradiology.

- |   |      |   |                        |
|---|------|---|------------------------|
|   | 1064 | <b>Iterative Denoising Accelerated 3D FLAIR Sequence for Hydrops MR Imaging at 3T</b> <i>R. Quint, et al.</i>   | <b>HEAD &amp; NECK</b> |
|   | 1070 | <b>Early Diagnosis of Tuberous Sclerosis Complex: Prenatal Diagnosis</b><br><i>M. Bekiesinska-Figatowska, et al.</i>  | <b>PEDIATRICS</b>      |
|  | 1077 | <b>Brain Maturation Patterns on Normalized FLAIR MR Imaging in Children and Adolescents</b> <i>K. Chan, et al.</i>  | <b>PEDIATRICS</b>      |
|  | 1084 | <b>DTI of Opioid-Exposed Fetuses Using ComBat Harmonization: A Bi-Institutional Study</b> <i>J.A. Dudley, et al.</i>  | <b>PEDIATRICS</b>      |
|  | 1090 | <b>Acute and Chronic Kernicterus: MR Imaging Evolution of Globus Pallidus Signal Change during Childhood</b> <i>J. Gburek-Augustat, et al.</i>              | <b>PEDIATRICS</b>      |
|  | 1096 | <b>Validity of the Bern Score as a Surrogate Marker of Clinical Severity in Patients with Spontaneous Intracranial Hypotension</b> <i>J.L. Houk, et al.</i> | <b>SPINE</b>           |
|   | 1101 | <b>Contribution of the MP2RAGE 7T Sequence in MS Lesions of the Cervical Spinal Cord</b> <i>B. Testud, et al.</i>   | <b>SPINE</b>           |

### ONLINE FEATURES

#### LETTER

- E41 **Regarding “Automated Segmentation of Intracranial Thrombus on NCCT and CTA in Patients with Acute Ischemic Stroke Using a Coarse-to-Fine Deep Learning Model”** *M. Tortora, et al.*

### BOOK REVIEWS *R.M. Quencer, Section Editor*

Please visit [www.ajnrblog.org](http://www.ajnrblog.org) to read and comment on Book Reviews.



Quint et al showed that an accelerated 3D FLAIR sequence combined with an iterative denoising algorithm enables significant reduction in scan time without compromising image quality and diagnostic performance.



Indicates Editor's Choices selection



Indicates Fellows' Journal Club selection



Indicates open access to non-subscribers at [www.ajnr.org](http://www.ajnr.org)



Indicates article with supplemental online data



Indicates article with supplemental online video



Evidence-Based Medicine Level 1



Evidence-Based Medicine Level 2

# AJNR *go green*

***AJNR* urges American Society of Neuroradiology members to reduce their environmental footprint by voluntarily suspending their print subscription.**

The savings in paper, printing, transportation, and postage directly fund new electronic enhancements and expanded content.

The digital edition of *AJNR* presents the print version in its entirety, along with extra features including:

- Publication Preview
- Case Collection
- Podcasts
- The *AJNR* News Digest
- The *AJNR* Blog

It also reaches subscribers much faster than print. An electronic table of contents will be sent directly to your mailbox to notify you as soon as it publishes.

Readers can search, reference, and bookmark current and archived content 24 hours a day on [www.ajnr.org](http://www.ajnr.org).

ASNR members who wish to opt out of print can do so by using the *AJNR* Go Green link on the *AJNR* Website (<http://www.ajnr.org/content/subscriber-help-and-services>). Just type your name in the email form to stop print and spare our ecosystem.



# The ASNR Career Center

**The Go-To Job Site for Neuroradiology Employers and Job Seekers**

***For Job Seekers***

- Access to an expanded network of jobs via the National Healthcare Career Network
- Confidential resume posting
- Professional online profile

***For Employers***

- Employer resources to help you recruit top talent
- Multiple pricing options, including free Fellowship listings
- Resume search

**Start here: [careers.asnr.org](https://careers.asnr.org)**



# JOIN US! COMPREHENSIVE NEURORADIOLOGY COURSE

February 1-3, 2024 • Cancun, Mexico / On-Demand

ASNR's Comprehensive Neuroradiology Course offers you three days of image-rich neuroradiology review focused on:

**Adult Brain Imaging | Head and Neck Imaging | Spine Imaging  
Pediatric Neuroradiology | Advanced Imaging Techniques**

Join our award-winning faculty and engage in our interactive classroom environment, as well as during planned social and evening activities. Take advantage of a discounted, all-inclusive rate at the host hotel: the Hyatt Ziva Cancun!

*Can't attend in person? An on-demand option is also available!*

**Get all of the details and register now at [www.asnr.org/cnc24](http://www.asnr.org/cnc24).**

## Meet the Faculty

**Joshua Nickerson, MD**

Division Chief of Neuroradiology, Associate Professor, Oregon Health & Science University

**Tabassum Kennedy, MD**

Division Chief of Neuroradiology, University of Wisconsin, Madison

**Judith Gadde, DO, MBA**

Pediatric Neuroradiologist and Director of Academic Innovation, Lurie Children's Hospital of Chicago

**Mahmud Mossa-Basha, MD**

Professor of Radiology, Vice Chair of Quality & Safety, and Medical Director of MRI, University of North Carolina School of Medicine

**Wende Gibbs, MD, MA**

Director of Spine Imaging and Intervention, Barrow Neurological Institute

**Ashley Aiken, MD,**

Director of Head and Neck Imaging and Professor of Radiology and Imaging Sciences, Emory University

# Benign Enhancing Foramen Magnum Lesions

I.T. Mark, D. Black, J.C. Benson, N.G. Campeau, D.R. Johnson, S.A. Messina, C. Giannini, I. Parney, and P.P. Morris



## ABSTRACT

**SUMMARY:** Benign enhancing foramen magnum lesions have been previously described as T2-hyperintense small, enhancing lesions located posterior to the intradural vertebral artery. We present the first case with pathologic correlation. These lesions are fibrotic nodules adhering to the spinal accessory nerve. While they can enlarge with time on subsequent examinations, on the basis of the imaging characteristics and location, they do not necessitate surgical resection.

**ABBREVIATIONS:** BEFML = benign enhancing foramen magnum lesions; HSL = high-signal lesions; SAN = spinal accessory nerve

The patient was a 45-year-old woman without significant medical history who presented with a 1-year history of bilateral eye pain. The initial MR imaging performed at an outside institution showed 2 small, enhancing intradural extramedullary lesions at the foramen magnum, posterior to the intradural vertebral arteries in the subarachnoid space. The leading differential at that time was peripheral nerve sheath tumor. She presented to our institution for further evaluation of the foramen magnum lesions and underwent a lumbar puncture to evaluate malignancy, which had negative findings. Given the presenting symptoms, she underwent facial electromyography that did not demonstrate findings of denervation. She also underwent a PET/CT, which revealed no abnormal radiotracer uptake in the enhancing foramen magnum lesions or elsewhere in the body. A catheter angiogram did not show vascular enhancement associated with the lesions. She underwent further MR imaging at our institution.

## Imaging

Contrast-enhanced 3T MR imaging of the brain demonstrated 2 small, rounded avidly-enhancing intradural extramedullary lesions at the foramen magnum, posterior to the vertebral arteries, superior to their dural insertion (Fig 1). These lesions were hyperintense on T2-weighted FLAIR imaging, isointense to CSF and, therefore, undetectable on T2-weighted imaging, and did not have

restricted diffusion or susceptibility-weighted artifact. Compared with the MR imaging from 9 months prior, they were slightly increased, measuring  $8 \times 6 \times 7$  mm on the left (previously  $7 \times 5 \times 6$  mm) and  $5 \times 4 \times 5$  mm on the right (previously  $4 \times 3 \times 4$  mm). Additionally, there was a third lesion just inferior to the right lesion and not within the FOV on the prior study. This lesion had imaging characteristics similar to those of the other lesions, measuring  $7 \times 6 \times 8$  mm, and was at the level of the dural puncture of the right vertebral artery. All 3 lesions were adjacent to the spinal accessory nerve (SAN). Contrast-enhanced MR imaging of the remainder of the spine did not show any additional lesions. Given the growth during a short period, the differential diagnosis was broad and included peripheral nerve sheath tumors, metastatic disease, and inflammatory conditions such as a sarcoid. At this time, these lesions had not been previously described in the literature.<sup>1</sup>

## Operative Report

Given the differential diagnoses, the patient underwent surgical resection with a midline suboccipital craniectomy and C1 laminectomy. The lesion on the left was near the vertebral artery and its branches but was not attached to them. It was adherent to a lower cranial nerve, identified as the left SAN on intraoperative nerve monitoring. The lesion was covered with a yellow membrane over an apparent cyst with a more solid and firm component deep to that (Fig 2). Intraoperative cranial nerve monitoring indicated changes compatible with nerve irritation; therefore, a small amount of residual lesion densely adherent to the nerve was not resected. The right-sided lesions with mixed cystic and solid components were debulked because they were adherent to lower cranial nerve rootlets, suspected of being the SAN but not confirmed by electromyography. The patient had an uneventful postoperative course without findings of CSF leak or cranial nerve deficit.

Received May 21, 2023; accepted after revision June 27.

From the Departments of Radiology (I.T.M., D.B., J.C.B., N.G.C., D.R.J., S.A.M., P.P.M.), Laboratory Medicine and Pathology (C.G.), and Neurosurgery (I.P.), Mayo Clinic, Rochester, Minnesota.

Please address correspondence to Ian Mark, MD, Department of Radiology, 200 1st Street SW, Mayo Clinic, Rochester, MN 55905; e-mail: Mark.Ian@mayo.edu; @iantmark

Indicates open access to non-subscribers at www.ajnr.org

<http://dx.doi.org/10.3174/ajnr.A7955>

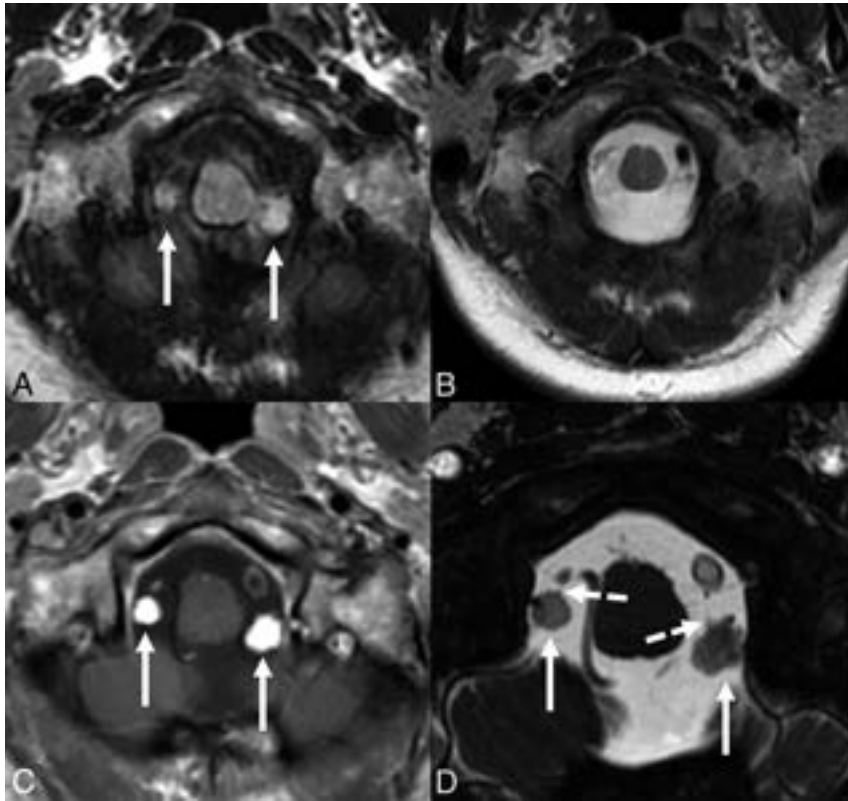


**FIG 1.** Multiple axial images show 2 intradural extramedullary lesions (*solid arrows*) at the foramen magnum posterior to the vertebral arteries, superior to their dural insertion. The lesions demonstrate hyperintense signal on T2-weighted FLAIR imaging (A), are isointense to CSF on T2-weighted imaging (B), and are avidly enhancing (C). FIESTA imaging (D) shows contact with the spinal accessory nerve (*broken arrows*).

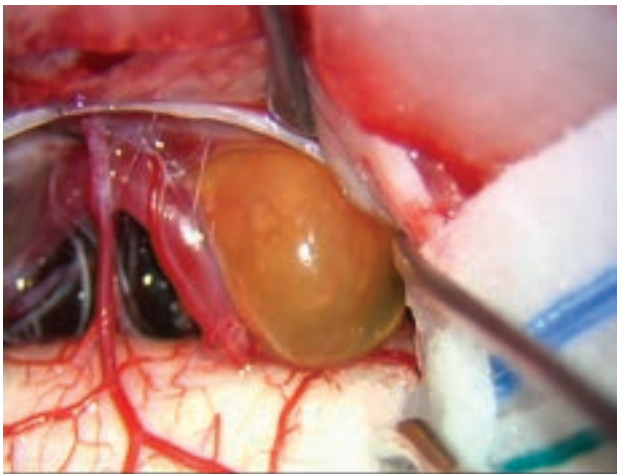


**FIG 2.** Intraoperative photograph demonstrates the lesion with a superficial yellow membrane over an apparent cyst with a more solid and firm component deep to that. The lesion was adherent to a lower cranial nerve, identified as the left SAN on intraoperative nerve monitoring.

### Pathology

Pathology received a specimen entirely composed of arachnoid tissue containing a small (11 mm), hypocellular, and densely fibrotic nodule without specific features as illustrated in Fig 3A. The nodule contained scant arachnoid cells separated by thick

collagenous fibers (Fig 3B). There were no histologic features to suggest a neoplasm or meningioma. Only focally small nests of meningothelial cap cells with focal psammoma body formation were present in the overlying arachnoid membrane (Fig 3C), a finding commonly present in the arachnoid of adults, which tends to increase with advancing age.

### DISCUSSION

This is the first pathology-proved case of benign enhancing foramen magnum lesions (BEFML). We found that these lesions are fibrotic arachnoid nodules adherent to the dorsal aspect of the SAN. It is important to demonstrate that these pathology-proved lesions are benign and do not need surgical resection.

McGuinness et al<sup>1</sup> were the first to describe BEFML by their MR imaging appearance. They noted that the enhancing lesions were hyperintense on 3D T2-weighted FLAIR, round or ovoid in morphology, and posterior to the intradural vertebral artery. The lesions were thought to represent a venous varix or a ganglia/pseudoganglia of the C1 nerve or spinal roots of

the SAN. The occult appearance on 2D T2-weighted imaging helps differentiate these lesions from the typical appearance of other lesions including meningioma, schwannoma, aneurysm, and metastasis.<sup>2</sup> A minority of meningiomas, schwannomas, and metastatic diseases can appear T2 hyperintense but not necessarily occult on T2-weighted imaging. While cystic lesions such as arachnoid, neurenteric, or synovial cysts could be occult on T2, they would not enhance.<sup>3</sup> Our patient presented and underwent surgery before the published work by McGuinness et al.

Roskopf et al<sup>4</sup> published a case report on the intraoperative appearance of BEFML without pathologic confirmation and thought that these lesions represented a venous structure. Antonucci et al<sup>5</sup> presented a single case of a patient with intracranial melanoma metastases in addition to a small enhancing left foramen magnum lesion that remained stable for 18 months, suggesting a benign process.

The largest study of these foramen magnum lesions was performed by Kogue et al,<sup>6</sup> who reviewed 3D T2-weighted FLAIR imaging of 3717 patients and found what they termed high-signal lesions (HSL) posterior to the intradural vertebral artery in 127 patients (3.4%). They noted that all lesions were in contact with the SAN. Their lesions had a mean maximum diameter of 3.8 mm, with an upper range of 11.5 mm. As was the case with our patient, they found that 8.7% of patients had foramen magnum lesions that increased in size with time. On follow-up imaging of our patient 1 year after resection, there were no signs of

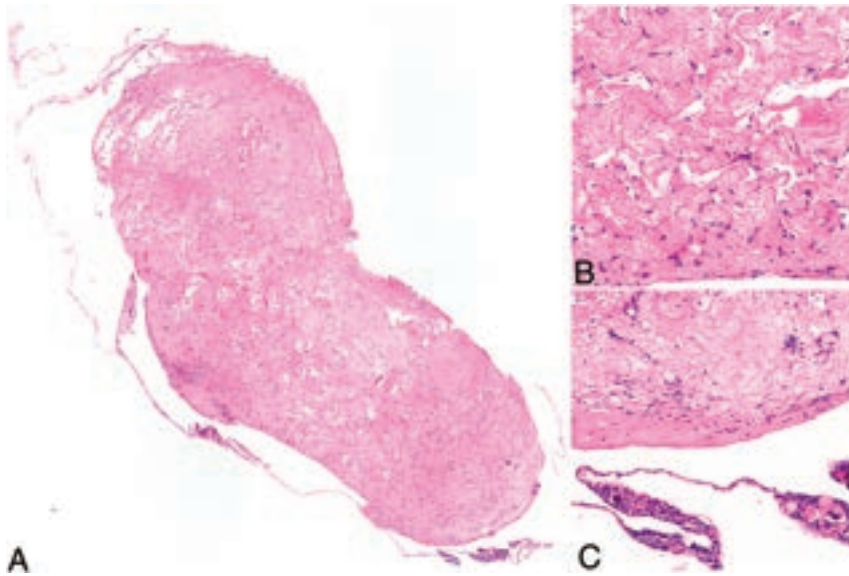


**FIG 3.** H&E sections of the resected specimen illustrate the densely fibrotic nodule (A), involving the arachnoid (B). Small nests of meningeothelial cap cells with focal psammoma body formation are present (C), adjacent to the nodule.

recurrence or progression. A subsequent study by Kogue et al<sup>7</sup> using a 3D balanced fast-field echo sequence found that all lesions contacted the SAN.

The SAN is classically known as providing motor fibers to the sternocleidomastoid and trapezius muscles. However, other studies have suggested that the SAN may transmit sensory/nociceptive signals as well.<sup>8,9</sup> Anatomically, the SAN has 2 origins: one that is derived from the upper 5 or 6 cervical spinal cord rootlets and the other arising from the brainstem. Some propose that the SAN starts with mixed motor and sensory components; however, the sensory neurons migrate to the spinal nerve. This process is often incomplete; therefore, neuron cell bodies can be found scattered throughout the nerve.<sup>10</sup>

Fahmy<sup>11</sup> suggested that ganglion cells along the SAN migrate distally with age, given the greater abundance and conspicuity of ganglion cells in a 3-month-old child compared with an adult and greater in the distal SAN relative to proximal. In a postmortem study, Tubbs et al<sup>12</sup> found that 14.8% of the specimens had focal enlargements contacting the dorsal aspect of the SAN at the foramen magnum. These enlargements were described as ectopic glial rests or heterotopias within the leptomeninges of the SAN and did not contain ganglion or neuronal cells.

Further work is needed to elucidate the true process that leads to these benign nodules associated with the SAN. Radiologists should be familiar with the typical appearance and benign nature of these lesions so that other entities do not have to be invoked in a differential diagnosis. This is the first work to show pathologic confirmation of what has been previously termed BEFML or HSL.

### Case Summary

- T2-hyperintense, enhancing, small lesions located posterior to the intradural vertebral artery at the foramen magnum have been previously described as BEFML or HSL.

- Previous work has shown that a small percentage (8.7%) of these lesions increase in size.
- These were previously presumed to be a venous varix or associated with the SAN.
- This is the first pathology-proven case compatible with a fibrotic arachnoid nodule adherent to the leptomeninges of the SAN. While they can enlarge with time, they are benign and do not require treatment.

Disclosure forms provided by the authors are available with the full text and PDF of this article at [www.ajnr.org](http://www.ajnr.org).

### REFERENCES

1. McGuinness BJ, Morrison JP, Brew SK, et al. **Benign enhancing foramen magnum lesions: clinical report of a newly recognized entity.** *AJNR Am J Neuroradiol* 2017;38:721–25 CrossRef Medline
2. Koeller KK, Shih RY. **Intradural extramedullary spinal neoplasms: radiologic-pathologic correlation.** *Radiographics* 2019;39:468–69 CrossRef Medline
3. Wang X, Song G, Chen G, et al. **Single-center clinical characteristics and treatment experience of foramen magnum neurenteric cyst: report of 6 cases and brief review of the literature.** *World Neurosurg* 2018;112:e608–16 CrossRef Medline
4. Roskopf J, Schmitz B, Beer M, et al. **Evidence for the vascular origin of benign enhancing foramen magnum lesions via intraoperative photographs: case report and review of the literature.** *Cureus* 2021;13:e2075 CrossRef Medline
5. Antonucci MU, Spampinato MV. **Imaging findings of benign enhancing foramen magnum lesions.** *AJNR Am J Neuroradiol* 2017;38:E95–96 CrossRef Medline
6. Kogue R, Maeda M, Umino M, et al. **Small high-signal lesions posterior to the intracranial vertebral artery incidentally identified by 3D FLAIR: retrospective study of 127 patients.** *Neuroradiology* 2018;60:591–97 CrossRef Medline
7. Kogue R, Maeda M, Umino M, et al. **Evaluation of a high-signal lesion posterior to the intracranial vertebral artery using 3D balanced fast-field echo imaging.** *Neuroradiology* 2019;61:1199–202 CrossRef Medline
8. Johal J, Iwanaga J, Tubbs K, et al. **The accessory nerve: a comprehensive review of its anatomy, development, variations, landmarks and clinical considerations.** *Anat Rec (Hoboken)* 2019;302:620–29 CrossRef Medline
9. Tubbs RS, Benninger B, Loukas M, et al. **Cranial roots of the accessory nerve exist in the majority of adult humans.** *Clin Anat* 2014;27:102–07 CrossRef Medline
10. Boehm KE, Kondrashov P. **Distribution of neuron cell bodies in the intraspinal portion of the spinal accessory nerve in humans.** *Anat Rec (Hoboken)* 2016;299:98–102 CrossRef Medline
11. Fahmy N. **A note on the intracranial and extracranial parts of the IXth, Xth and XIth nerves.** *J Anat* 1927;61:3298–301 Medline
12. Tubbs RS, Lancaster JR, Mortazavi MM, et al. **Do grossly identifiable ganglia lie along the spinal accessory nerve? A gross and histologic study with potential neurosurgical significance.** *World Neurosurg* 2012;77:349–51 CrossRef Medline

# Unpacking the CNS Manifestations of Epstein-Barr Virus: An Imaging Perspective

N. Soni, M. Ora, R. Singh, P. Mehta, A. Agarwal, and G. Bathla



## ABSTRACT

**SUMMARY:** Epstein-Barr virus is a ubiquitous herpesvirus that may cause both infective (encephalitis, meningitis, and so forth) and postinfection inflammatory (such as Guillain-Barré syndrome, acute disseminated encephalomyelitis) manifestations in the CNS. Diagnosis of Epstein-Barr virus–related CNS pathologies is often complicated due to a nonspecific clinical presentation and overlap with other infectious and noninfectious causes, both clinically and on imaging. The Epstein-Barr virus is also implicated in several lymphoproliferative disorders in both immunocompromised and immunocompetent hosts. MR imaging is preferred for evaluating the extent of involvement and monitoring therapy response, given its high sensitivity and specificity, though imaging findings may be nonspecific. Herein, we review the imaging spectrum of Epstein-Barr virus–associated CNS disorders.

**ABBREVIATIONS:** ADEM = acute disseminated encephalomyelitis; ATM = acute transverse myelitis; EBV = Epstein-Barr virus; EBNA = Epstein-Barr nuclear antigen; Ig = immunoglobulin; LG = lymphomatoid granulomatosis; LPD = lymphoproliferative disorder; MOG = myelin oligodendrocyte glycoprotein; PCNSL = primary CNS lymphoma; PCR = polymerase chain reaction; PTLD = posttransplant lymphoproliferative disorder; SMT = smooth-muscle tumor

The Epstein-Barr virus (EBV), also known as herpesvirus 4 human, belongs to the herpesvirus family. It is highly prevalent and affects >90% of individuals worldwide.<sup>1</sup> Primary EBV infection in childhood is usually asymptomatic. It causes infectious mononucleosis in young adults and presents with fever, lymphadenopathy, and tonsillopharyngitis.<sup>2</sup> Depending on age and immune status, CNS manifestations may occur in about 18% of patients. These include encephalitis, meningitis, cerebellitis, cranial nerve palsy, Guillain-Barré syndrome, acute disseminated encephalomyelitis (ADEM), and infectious or acute transverse myelitis (ATM).<sup>3</sup> Cheng et al<sup>4</sup> reported a cohort of 89 children with EBV-related neurologic involvement. Encephalitis and meningoencephalitis (72%) were the most common presentations, followed by Guillain-Barré syndrome (17%), ADEM

(3.4%), acute myelitis (2.2%), and posttransplant lymphoproliferative disorders (PTLDs) (1.1%). EBV also plays a vital role in several lymphoproliferative disorders (LPDs) occurring in immunocompromised and immunocompetent hosts.<sup>5-7</sup> Given the varied and nonspecific clinical manifestations, EBV antibodies and polymerase chain reaction (PCR) analysis in blood or CSF are often used for confirmation.<sup>8</sup> The high soft-tissue contrast resolution of MR imaging is an essential tool during initial work-up and follow-up.<sup>9-12</sup>

Herein, we present an illustrative review of neuroimaging manifestations of EBV-associated disorders. Understanding the clinical context and awareness of the varied imaging characteristics can facilitate management of these potentially life-threatening conditions.

## Pathogenesis

EBV is a double-stranded DNA human herpesvirus discovered in 1964. EBV is mainly transmitted through saliva; however, transmission through blood transfusions and organ transplants has been reported. EBV infects B lymphocytes, causing lytic and latent infections, and establishes life-long carrier status by residing in peripheral blood lymphocytes.<sup>13</sup> EBV can invade the CNS through a hematogenous route or retrograde along nerve fibers.<sup>14</sup> The pathogenesis of EBV-associated neurologic disease is complex, resulting from direct infection, immunologic response, and reactivation of latent infection.<sup>4</sup>

EBV infection can potentially induce demyelination, neuroinflammation, and ADEM, leading to multifocal demyelination

Received March 28, 2023; accepted after revision May 26.

From the Department of Radiology (N.S.), University of Rochester Medical Center, Rochester, New York; Department of Nuclear Medicine (M.O.), Sanjay Gandhi Postgraduate Institute of Medical Sciences, Lucknow, Uttar Pradesh, India; Department of Hematology (R.S.), University of Vermont Medical Center, Burlington, Vermont; Department of Radiology (P.M.), Mayo Clinic, Rochester, Minnesota; Department of Radiology (A.A.), Mayo Clinic, Jacksonville, Florida; and Department of Radiology (G.B.), Mayo Clinic, Rochester, Minnesota.

Neetu Soni and Manish Ora are co-first authors.

Please address correspondence to Neetu Soni, MD, DNB, FRCR, Department of Radiology, University of Rochester Medical Center, 601 Elmwood Ave, Rochester, New York, NY 14642; e-mail: drneetusoni98@gmail.com; @NeetuSo27437480

Indicates open access to non-subscribers at [www.ajnr.org](http://www.ajnr.org)

Indicates article with online supplemental data.

<http://dx.doi.org/10.3174/ajnr.A7945>

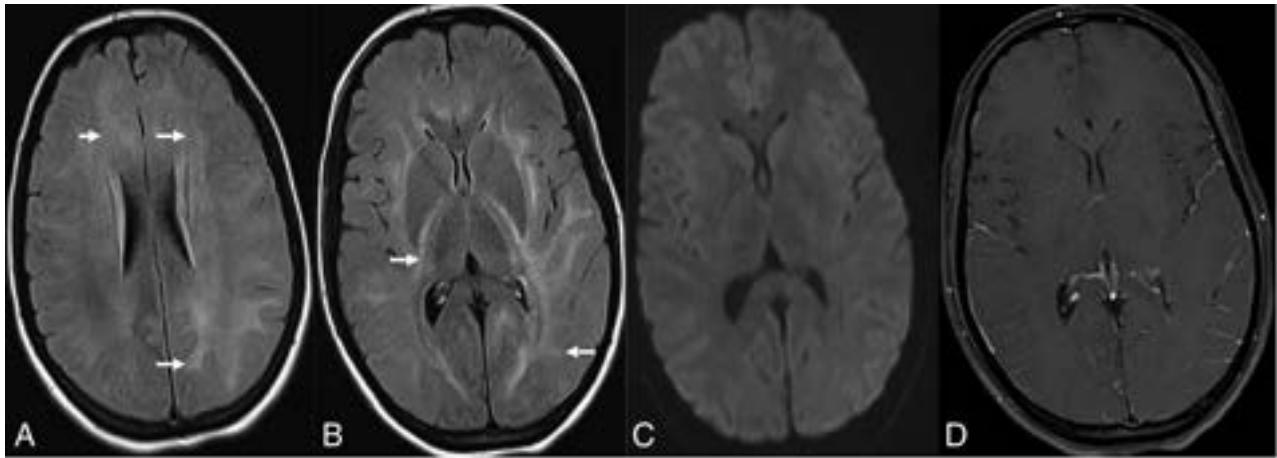


**FIG 1.** EBV meningoencephalitis in a patient with infectious mononucleosis. CSF was positive for EBV. Axial T2 FLAIR (A and B) images show multifocal areas of hyperintensity mainly within the subcortical white matter of the bilateral cerebral hemispheres (arrows) without diffusion abnormalities on axial DWI (C). Postcontrast axial T1-weighted image (D) shows diffuse leptomeningeal enhancement. The patient was fully recovered on follow-up.

in the white matter of the brain. Latent EBV infection induces Epstein-Barr nuclear antigen (EBNA) expression that cross-reacts with myelin oligodendrocyte glycoprotein (MOG), producing anti-MOG antibodies.<sup>15-17</sup> The pathogenesis remains complex and poorly understood, but in many children with ADEM, elevated serum MOG levels are observed. Yet, no correlation has been observed between anti-EBNA-1 and anti-MOG immunoglobulin titers in EBV-seropositive children.<sup>15</sup> EBV-transformed B-cells may also secrete antineuronal or anti-EBV protein antibodies that cross-react with neuronal antigens.<sup>18</sup> This likelihood is further compounded by a complex dysregulated immune response exacerbating CNS injury.<sup>14,19</sup> EBV-specific B cells may enter the brain and form a site of antigen recognition with the help of other immune cells. A recent study found that EBNA-1 mimics the glial-cell adhesion molecule, a CNS protein expressed by myelin-forming cells. Antibodies targeting EBNA-1 cross-react with the glial-cell adhesion molecule in patients with MS, potentially causing autoimmune attacks on the CNS myelin.<sup>20</sup>

EBV is an oncogenic virus associated with various epithelial, mesenchymal, and hematologic malignancies. EBV-latent membrane protein (*LMP1*) genetic deletion and high EBNA-2 expression are important for EBV-positive primary CNS lymphomas (PCNSLs).<sup>21</sup> In immunocompetent hosts, cytotoxic T-cells suppress EBV-infected lymphocytes, whereas immunosuppression leads to uncontrolled B-cell proliferation. The complex pathogenesis involves oncogenic transformation and tumor immune evasion and drives tumor cell proliferation, differentiation, invasion, metastasis, and resistance to apoptosis.<sup>17</sup> The pathogenesis of EBV-related smooth-muscle cell tumors (EBV-SMTs) remains unclear. It is suggested that EBV infects SMTs through interaction with the CD21 receptor, similar to B lymphocytes. Other potential mechanisms include overactivation of the MTOR/Akt pathway and overexpression of the MYC proto-oncogene.<sup>22</sup> The process of EBV infection and the pathogenesis of EBV-related diseases are briefly illustrated in the Online Supplemental Data.

### Diagnosis of EBV CNS Infections

Given the nonspecific clinical symptomatology, the differential considerations include infectious, noninfectious inflammatory, metabolic, autoimmune, and neoplastic etiologies.<sup>23</sup> Lesion distribution on MR imaging, duration of illness, immune status, and CSF analysis help narrow the differential considerations. Positive serum viral capsid antigen immunoglobulin (Ig) M or detection of EBV DNA through a PCR in CSF or serum or both are generally confirmatory.<sup>24</sup>

### EBV Encephalitis

EBV is a rare cause of encephalitis in children and immunocompetent adults. The most common presentations are fever (81%), headache (66%), and seizure (10%).<sup>11</sup> MR imaging is preferred for suspected encephalitis, with abnormalities found in 27.6%–80% of patients (Fig 1). Vyas et al<sup>12</sup> reported abnormal findings on brain imaging in 29/45 (64.5%) pediatric patients. Cortical/subcortical (20%), white matter (15.5%), and basal ganglia (11%) involvement were more common, followed by the thalamus (9%), brainstem (6.2%), substantia nigra (4.4%), cerebellum (4.4%), and spinal cord (3%). Diffusion restriction and susceptibility changes were seen in 24.4% and 15.5% of cases, respectively. Meningeal involvement was reported in 5%–22%.<sup>9,12</sup> Brain abscess, subdural effusion/empyema, and hemorrhage are rare.<sup>12</sup>

Most patients fully recover without sequelae, while 5%–10% of cases may be fatal.<sup>4,11,25,26</sup> For unclear reasons, patients with isolated hemispheric involvement generally have better prognoses. Similarly, about one-half of the patients with thalamic involvement have persistent deficits, while isolated brainstem involvement has a high mortality rate.<sup>9,11</sup> EBV encephalitis in immunocompromised patients may occur secondary to latent virus reactivation or a primary infection after transplantation.<sup>27,28</sup> The clinical and imaging manifestations are broadly similar, though cases with hemorrhage, ring enhancement, and masslike lesions may also be seen.<sup>27-29</sup> Correction of underlying immunosuppression is the mainstay of therapy.

### EBV Cerebellitis

EBV-associated cerebellitis is rare and may occur secondary to infection or postinfectious inflammation from antineural antibodies.<sup>30-33</sup> Frequent detection of EBV IgG and IgM antibodies in the serum and negative EBV CSF serology indicate a potential postinfectious or autoimmune phenomenon.<sup>29-31</sup> A positive CSF PCR suggests direct infiltration of the cerebellum by EBV, supported by evidence of EBV-encoded RNA expression in infiltrating inflammatory cells from cerebellar biopsies.<sup>32</sup> Children are commonly affected; the condition often occurs following infectious mononucleosis. Studies have shown no MR imaging abnormalities<sup>32</sup> to

cerebellum swelling causing obstructive hydrocephalus.<sup>34</sup> EBV-linked unilateral cerebellitis has been reported in immunocompromised adults with HIV.<sup>33</sup> EBV cerebellitis is generally self-limiting, but IV immunoglobulin may reduce the severity and duration.<sup>31</sup>

EBV-associated cranial neuropathies are rare and generally manifest as facial nerve mononeuritis, though multiple cranial nerves may rarely be affected.<sup>35</sup> Occasionally, oculomotor nerve palsy may manifest as the presenting symptom of primary EBV infection, with imaging demonstrating focal edema and enhancement at the root exit zone of the affected nerve (shooting star sign).<sup>36</sup>

### Spinal Cord Involvement

ATM is generally idiopathic or postinfectious immune-mediated demyelination, with EBV being a rare culprit.<sup>4,37,38</sup> EBV myelitis is characterized by T2 hyperintensity in the spinal cord that extends over  $\geq 2$  segments covering equal or more than two-thirds of the cord, with the thoracic cord being the most affected (Figs 2 and 3). Enhancement patterns range from none to diffuse, with leptomeningeal and nerve root enhancement reported.<sup>37,39,40</sup> EBV serologies can aid in diagnosing postinfectious EBV myelitis/ATM because MR imaging findings resemble those of other ATM etiologies. Spinal cord ischemia, MS, neuromyelitis optica, and autoimmune-related myelitis are imaging differential diagnoses for ATM. MS plaques usually affect less than one-half of the cord area and may have concomitant brain lesions. Spinal cord infarction

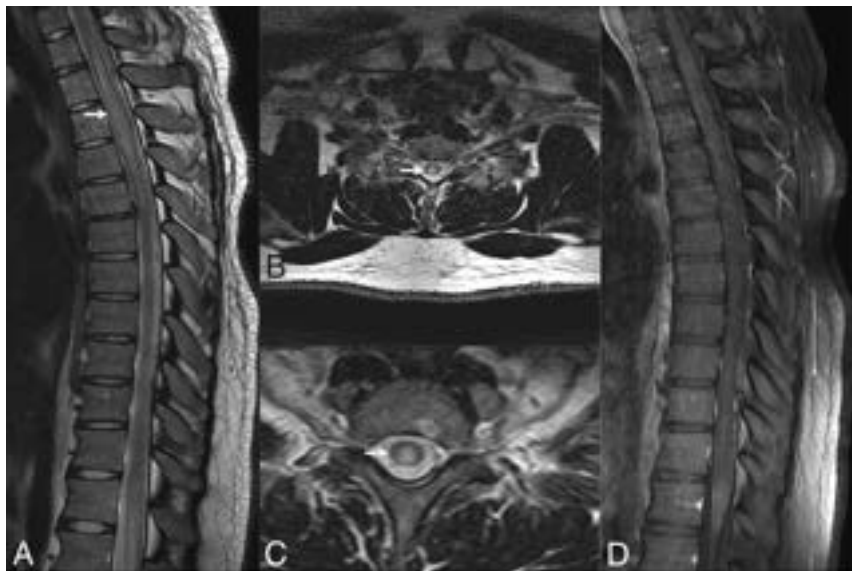


**FIG 2.** EBV-related transverse myelitis, EBV IgM-positive. T2-weighted sagittal image of the thoracic spine (A) and axial images (B and C) reveal diffuse long-segmental hyperintense signal (arrows) in the spinal cord more in the central gray matter region along with mild cervical cord swelling. No abnormal enhancement on the sagittal T1-weighted postcontrast image (D) was seen.

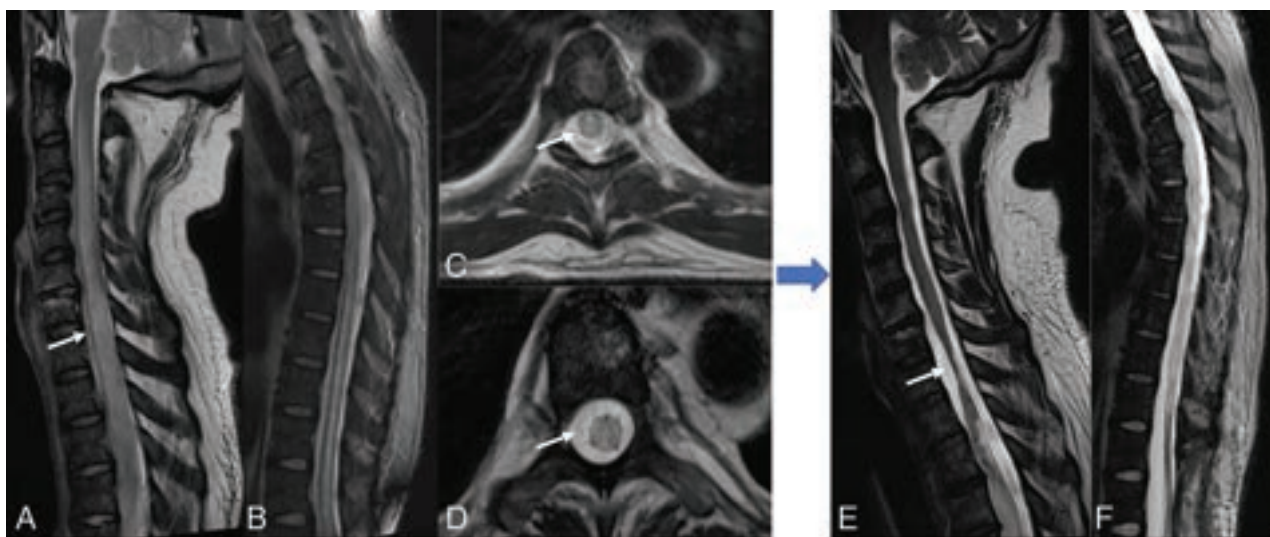


**FIG 3.** Presumed EBV myelitis, CSF EBV-positive. Conus biopsy revealed fibrin with macrophages, scant peripheral nerve myelins, and degenerating myelin, most consistent with infection. T2-weighted sagittal image of the cervical (A) and thoracic (B) spine along with axial images (C and D) reveal diffuse long-segmental T2-hyperintense signal in the spinal cord (arrows). Eight-month follow-up sagittal T2 (E and F) images show cord atrophy with persistent signal abnormality (arrow).

shows bilateral anterior horn cell T2 hyperintensity symmetrically.<sup>38</sup> Although rare in immunocompetent individuals, EBV ATM should be considered in cases of high CSF cell count atypical for idiopathic ATM.<sup>40</sup>

#### **EBV-Associated Demyelinating Disorders**

ADEM primarily affects children, with an incidence of 0.3–0.6/100,000, and may follow a viral infection or vaccination.<sup>41–43</sup> MR imaging typically shows asymmetric, multifocal white matter T2-hyperintense lesions. One-third of patients show ringlike or patchy peripheral contrast enhancement and restricted diffusion. Spinal cord involvement also occurs in about one-third of patients, manifesting as large lesions extending over multiple segments accompanied by cord edema.<sup>44</sup>

Differential considerations include MS, neuromyelitis optica, and acute hemorrhagic leukoencephalitis. Evidence of recent EBV infection, a monophasic course, and specific imaging features like periventricular sparing and the absence of Dawson fingers can help to differentiate the entity from MS.<sup>45</sup> Patients usually respond to systemic steroids, and follow-up MR imaging typically shows resolution.<sup>46</sup>

#### **Lymphoproliferative Disorders**

Age-related impaired cell-mediated immunity or iatrogenic immune suppression increases the risk of several B-cell LPDs.

These include lymphomatoid granulomatosis (LG), posttransplant and other immunodeficiency-associated LPDs, and B- and T-cell lymphomas.<sup>6,47,48</sup>

#### **Lymphomatoid Granulomatosis**

Under the World Health Organization Classification of Hematolymphoid Tumors (2022), LG is an LPD occurring exclusively in immunocompetent patients. Brain involvement is reported in up to 30% of patients with LG and is often secondary, with sporadic primary CNS involvement.<sup>49</sup> Brain lesions may be diffusely infiltrating or masslike and show nodular, perivascular, or ringlike enhancement. Subependymal extension or leptomeningeal involvement may be present (Fig 4). LG typically exhibits an angiocentric and angiodestructive infiltrate consisting of lymphocytes, histiocytes, and sporadic plasma cells, with rare neutrophils and eosinophils. Necrosis may be observed in higher-grade lesions, while well-formed granulomas are not seen. The differential diagnosis for LG includes CNS lymphoma and vasculitis.<sup>50,51</sup> Imaging findings are nonspecific and overlap with multiple tumoral and nontumoral pathologies, including glioblastoma, vasculitis, and chronic lymphocytic inflammation with pontine perivascular enhancement responsive to steroids (CLIPPERS).<sup>50–54</sup> Treatment options include observation, resection, chemoradiation, corticosteroids, interferon, immunoglobulin, and rituximab.<sup>54</sup>

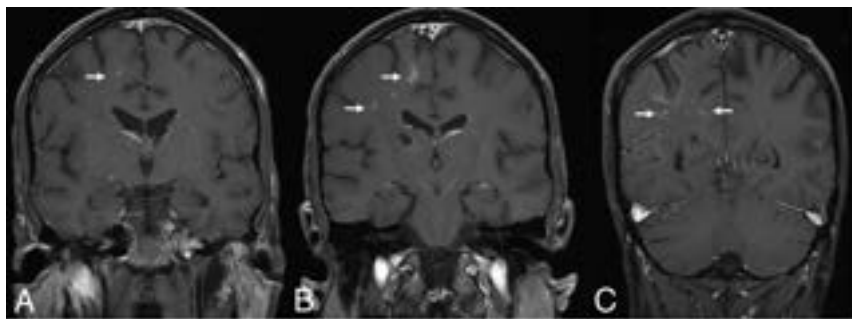


**FIG 4.** EBV lymphomatoid granulomatosis. A 40-year-old man with a history of HIV. EBV lymphomatoid granulomatosis was the finding of a prior right thalamus biopsy. Lymphohistiocytic infiltrate was the finding of a biopsy, consistent with EBV-associated lymphoproliferative disorder. Coronal T1-weighted postcontrast images show linear and punctate enhancement foci in the left parieto-occipital lobes (arrow).

#### **EBV-Positive CNS Lymphoma**

PCNSL is rare and, by definition, is confined to the brain, spinal cord, eyes, and CSF without systemic involvement. It is generally EBV-negative in immunocompetent patients and has a worse prognosis when EBV-positive.<sup>55</sup> Immunodeficiency-associated PCNSLs account for 8%–10% of cases and corresponds explicitly to EBV-positive diffuse large B-cell lymphoma.<sup>6,56,57</sup>

PCNSL in immunocompetent patients may present as solitary or multifocal lesions that restrict diffusion and enhance homogeneously, often involving

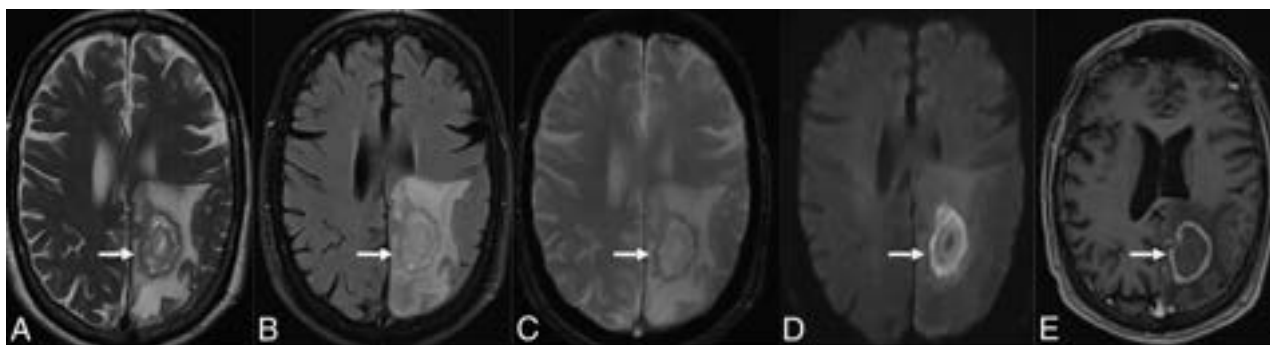


**FIG 5.** EBV-positive PCNSL in a 65-year-old male patient. T2-weighted (A) and FLAIR (B) images demonstrate the left parietal lobe necrotic T2-hyperintense lesion with a peripheral iso- to hypointense rim and surrounding white matter edema (arrows). The lesion demonstrates a hypointense rim (hemorrhage) (arrows) on the susceptibility-weighted (C) image, increased restriction on DWI (D, arrow), and a peripheral rim-enhancement pattern (arrows) on the postcontrast axial T1-weighted image (E).

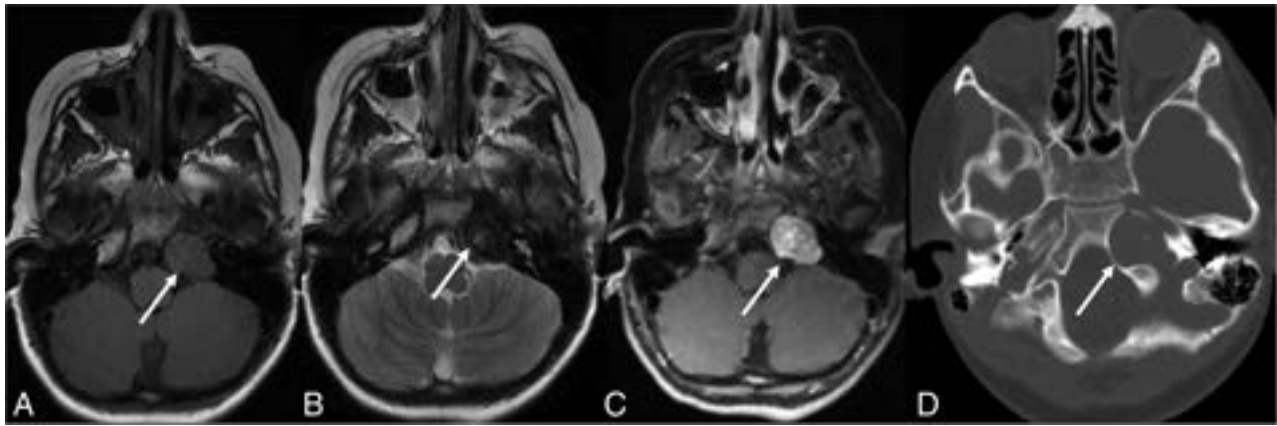


**FIG 6.** Biopsy-proved EBV-SMT. Axial FLAIR (A) and T2-weighted (B) images show a left petrous apex T2-hypointense lesion with central hyperintense foci and intense heterogeneous enhancement (arrows) on the postcontrast T1-weighted image (C) with bony remodeling (arrows) on the axial CT (D) image.

the white matter, corpus callosum, or basal ganglia (Fig 5).<sup>58</sup> Compared with glioblastoma multiforme and metastases, PCNSLs show a lower CBV, peak height on the perfusion curve, and increased diffusion restriction due to cellular density.<sup>59</sup> Stereotactic biopsy with histopathologic examination remains the criterion standard for diagnosis.<sup>60</sup> Lee et al<sup>61</sup> compared MR imaging features in 10 EBV-positive PCNSLs with 45 EBV-negative PCNSLs (neither group with HIV/AIDS). Tumor necrosis, hemorrhage, and irregular or ring enhancement were common in EBV-positive PCNSLs ( $P < .001$  each). However, ADC, maximum relative CBV, relative CBV, and Cho/NAA ratios were similar between the groups.

PCNSLs in immunosuppressed patients are usually deep, periventricular, and often multiple, with necrosis, hemorrhage, and rim enhancement.<sup>6,55</sup> Glioblastoma, metastases, and opportunistic infections are the primary differential.<sup>57,62-65</sup>

### PTLD

PTLD is a rare EBV-driven polyclonal B-cell proliferation occurring in patients posttransplantation. CNS involvement is seen in 5%–20% of PTLDs after solid organ transplantation and portends a poor prognosis. Biopsy may be essential because in some cases, there is no EBV DNA in the plasma/CSF.<sup>49</sup> Balaguer-Rosello et al identified 25 cases of EBV PTLDs in 1009 adult patients with allogeneic stem cell transplants and noted isolated CNS involvement in 36% of cases. Detection of plasma EBV DNA was significantly lower with isolated CNS PTLDs (33%) compared with extra-CNS disease (100%). MR imaging findings are nonspecific and overlap with other tumoral and nontumoral pathologies. These include solitary or multiple necrotic lesions with rim enhancement; perivascular, cranial nerve, or dural enhancement; and, rarely, choroid plexus involvement. The treatment involves reducing immunosuppression, chemoradiation, immunotherapy, and surgery.<sup>66</sup>

### EBV-Related SMTs

EBV-SMTs of the CNS are rare mesenchymal tumors that develop predominantly in immunocompromised patients, with only a few cases reported in immunocompetent patients.<sup>67-73</sup> Lee et al<sup>67</sup> were the first to link EBV with SMTs in immunocompromised patients. Symptoms depend on location, with some

patients being asymptomatic. Diagnosis often requires a biopsy. Intracranial posttransplant SMT is typically along the dural sinuses, cerebral veins, and dura mater.<sup>68</sup> Paez-Nova et al<sup>69</sup> analyzed 47 cases of intracranial EBV-SMTs, with 40% being leiomyosarcomas and 60% being leiomyomas. EBV-SMTs resemble meningiomas on imaging and should be considered in HIV-positive and posttransplant patients of any age.<sup>70</sup> Cavernous sinus involvement may occur and may present clinically as Tolosa-Hunt syndrome, but a negative response to steroids should suggest an alternate etiology, including EBV-associated neoplasia in immunosuppressed patients.<sup>68</sup> EBV-SMTs appear as dural-based extra-axial lesions with iso- to hyperdensity and substantial enhancement on CT scans. On MR imaging, lesions are often hypo- to isointense on T1-weighted images, with T2 prolongation and variable enhancement (Fig 6). Unlike PCNSL, diffusion restriction is typically absent in EBV-SMTs.<sup>71</sup> Spinal EBV-SMTs appear as intradural-extramedullary lesions and may resemble neurofibromas and schwannomas, with dumbbell-shaped tumors at the neural foramina.<sup>71,72</sup> Schwannomas stain strongly for S100 protein, while EBV-associated SMTs show minor expression. In patients with HIV, immunohistochemistry can help to differentiate EBV-SMTs from Kaposi sarcoma, schwannoma, follicular dendritic cell sarcoma, and mycobacterial pseudotumor. In a study with 61 SMTs, desmin, smooth-muscle actin, muscle-specific actin, and CD21 were positive. Negative staining included S100 (27 cases), CD34 (17 cases), epithelial membrane antigen (15 cases), and cytokeratin (5 cases).<sup>73</sup> EBV-SMTs exhibit short interlacing fascicles of atypical spindle cells with abundant eosinophilic cytoplasm.<sup>71,73</sup> The optimal treatment for EBV-SMTs is unclear and may involve excision, radiation therapy, and/or chemotherapy. Although complete resection is the most effective treatment, 40% of patients undergo partial resection due to high risk.<sup>69</sup> Recent studies have shown promise in alternative therapies such as mTOR/AKT inhibitors (sirolimus), EBV-specific immunotherapy, and demethylating agents.<sup>69,70</sup>

### CONCLUSIONS

EBV in the CNS may be associated with a spectrum of infectious, noninfectious inflammatory, and lymphoproliferative disorders.

MR imaging is preferred for evaluating and monitoring EBV-related CNS complications. Increased awareness of these uncommon but clinically relevant entities and their imaging spectrum may help with early diagnosis and therapy.

Disclosure forms provided by the authors are available with the full text and PDF of this article at [www.ajnr.org](http://www.ajnr.org).

## REFERENCES

- Dunmire SK, Verghese PS, Balfour HH Jr. **Primary Epstein-Barr virus infection.** *J Clin Virol* 2018;102:84–92 CrossRef Medline
- Smatti MK, Al-Sadeq DW, Ali NH, et al. **Epstein-Barr virus epidemiology, serology, and genetic variability of LMP-1 oncogene among healthy population: an update.** *Front Oncol* 2018;8:211 CrossRef Medline
- Weinberg A, Li S, Palmer M, et al. **Quantitative CSF PCR in Epstein-Barr virus infections of the central nervous system.** *Ann Neurol* 2002;52:543–48 CrossRef Medline
- Cheng H, Chen D, Peng X, et al. **Clinical characteristics of Epstein-Barr virus infection in the pediatric nervous system.** *BMC Infect Dis* 2020;20:886 CrossRef Medline
- Kim HJ, Ko YH, Kim JE, et al; Hematopathology Study Group of the Korean Society of Pathologists. **Epstein-Barr virus-associated lymphoproliferative disorders: review and update on 2016 WHO Classification.** *J Pathol Transl Med* 2017;51:352–58 CrossRef Medline
- Pons-Escoda A, Naval-Baudin P, Velasco R, et al. **Imaging of lymphomas involving the CNS: an update-review of the full spectrum of disease with an emphasis on the World Health Organization Classifications of CNS Tumors 2021 and Hematolymphoid Tumors 2022.** *AJNR Am J Neuroradiol* 2023;44:358–66 CrossRef Medline
- Balaguer-Rosello A, Piñana JL, Bataller L, et al. **Central nervous system involvement in Epstein-Barr virus-related post-transplant lymphoproliferative disorders after allogeneic hematopoietic stem cell transplantation.** *Transplant Cell Ther* 2021;27:261.e1–261.e7 CrossRef Medline
- Costa BK, Sato DK. **Viral encephalitis: a practical review on diagnostic approach and treatment.** *J Pediatr (Rio J)* 2020;96(Suppl 1):12–19 CrossRef Medline
- Abul-Kasim K, Palm L, Maly P, et al. **The neuroanatomic localization of Epstein-Barr virus encephalitis may be a predictive factor for its clinical outcome: a case report and review of 100 cases in 28 reports.** *J Child Neurol* 2009;24:720–26 CrossRef Medline
- Fujimoto H, Asaoka K, Imaizumi T, et al. **Epstein-Barr virus infections of the central nervous system.** *Intern Med* 2003;42:33–40 CrossRef Medline
- Doja A, Bitnun A, Ford Jones EL, et al. **Pediatric Epstein-Barr virus-associated encephalitis: 10-year review.** *J Child Neurol* 2006;21:384–91 CrossRef Medline
- Vyas S, Suthar R, Bhatia V, et al. **Brain MRI in Epstein-Barr virus meningoencephalitis in children.** *Ann Indian Acad Neurol* 2020;23:621–24 CrossRef Medline
- Thorley-Lawson DA. **EBV persistence: introducing the virus.** *Curr Top Microbiol Immunol* 2015;390:151–209 CrossRef Medline
- Rodrigo-Armenteros P, Kapetanovic-García S, Antón-Méndez L, et al. **Akinetic mutism and status epilepticus due to Epstein Barr virus encephalitis.** *Clin Neurol Neurosurg* 2019;185:105492 CrossRef Medline
- Selter RC, Brilot F, Grummel V, et al. **Antibody responses to EBV and native MOG in pediatric inflammatory demyelinating CNS diseases.** *Neurology* 2010;74:1711–15 CrossRef Medline
- Nakamura Y, Nakajima H, Tani H, et al. **Anti-MOG antibody-positive ADEM following infectious mononucleosis due to a primary EBV infection: a case report.** *BMC Neurol* 2017;17:76 CrossRef Medline
- Zhang N, Zuo Y, Jiang L, et al. **Epstein-Barr virus and neurological diseases.** *Front Mol Biosci* 2022;8:816098 CrossRef Medline
- Tsuruyama Y, Mori N, Yoshida S, et al. **Epstein-Barr virus-related encephalitis in a young woman: a case report.** *J Infect Chemother* 2020;26:741–44 CrossRef Medline
- Tao Q, Young LS, Woodman CB, et al. **Epstein-Barr virus (EBV) and its associated human cancers—genetics, epigenetics, pathobiology and novel therapeutics.** *Front Biosci* 2006;11:2672–713 CrossRef Medline
- Lanz TV, Brewer RC, Ho PP, et al. **Clonally expanded B cells in multiple sclerosis bind EBV EBNA1 and GlialCAM.** *Nature* 2022;603:321–27 CrossRef Medline
- Sugita Y, Furuta T, Ohshima K, et al. **The perivascular microenvironment in Epstein-Barr virus positive primary central nervous system lymphoma: the role of programmed cell death 1 and programmed cell death ligand 1.** *Neuropathology* 2018;38:125–34 CrossRef Medline
- Pitjadi Tirelo M, Grayson W. **Epstein-Barr virus-associated smooth muscle tumour: a case series with a significant proportion of tumours showing proclivity for cutaneous soft tissues.** *Dermatopathology (Basel)* 2019;6:133–46 CrossRef Medline
- Ellul M, Solomon T. **Acute encephalitis: diagnosis and management.** *Clin Med (Lond)* 2018;18:155–59 CrossRef Medline
- Hess RD. **Routine Epstein-Barr virus diagnostics from the laboratory perspective: still challenging after 35 years.** *J Clin Microbiol* 2004;42:3381–87 CrossRef Medline
- Shian WJ, Chi CS. **Epstein-Barr virus encephalitis and encephalomyelitis: MR findings.** *Pediatr Radiol* 1996;26:690–93 CrossRef Medline
- Hung KL, Liao HT, Tsai ML. **Epstein-Barr virus encephalitis in children.** *Acta Paediatr Taiwan* 2000;41:140–46 Medline
- Lau JS, Low ZM, Abbott I, et al. **Epstein-Barr virus encephalitis in solid organ transplantation.** *New Microbiol* 2017;40:212–17 Medline
- Babik JM, Katrak S, Miller S, et al. **Epstein-Barr virus encephalitis in a renal transplant recipient manifesting as hemorrhagic, ring-enhancing mass lesions.** *Transpl Infect Dis* 2015;17:744–50 CrossRef Medline
- Khalil M, Enzinger C, Wallner-Blazek M, et al. **Epstein-Barr virus encephalitis presenting with a tumor-like lesion in an immunosuppressed transplant recipient.** *J Neurovirol* 2008;14:574–78 CrossRef Medline
- Al-Shokri SD, Karumannil SA, Mohammed SS, et al. **Post-Epstein-Barr virus acute cerebellitis in an adult.** *Am J Case Rep* 2020;21:e918567 CrossRef Medline
- Ambrosio E, Khalighinejad F, Ionete C. **Intravenous immunoglobulins in an adult case of post-EBV cerebellitis.** *BMJ Case Rep* 2020;13:e231661 CrossRef Medline
- Hussain RS, Hussain NA. **Ataxia and encephalitis in a young adult with EBV mononucleosis: a case report.** *Case Rep Neurol Med* 2013;2013:516325 CrossRef Medline
- Liu WC, Chiu SK, Hsiang CW, et al. **Acute unilateral cerebellitis, Epstein-Barr virus, and HIV.** *Lancet Infect Dis* 2014;14:778 CrossRef Medline
- Van Lierde A, Righini A, Tremolati E. **Acute cerebellitis with tonsillar herniation and hydrocephalus in Epstein-Barr virus infection.** *Eur J Pediatr* 2004;163:689–91 CrossRef Medline
- Grassin M, Rolland A, Leboucq N, et al. **Bilateral facial nerve palsy associated with Epstein-Barr virus infection in a 3-year-old boy [in French].** *Arch Pediatr* 2017;24:564–67 CrossRef Medline
- Steiner LA, Erbay A, Pache F, et al. **Oculomotor nerve palsy as a presenting symptom of Epstein-Barr virus-associated infectious mononucleosis: case report and review of the literature.** *Case Rep Neurol* 2021;13:756–62 CrossRef Medline
- Majid A, Galetta SL, Sweeney CJ, et al. **Epstein-Barr virus myelodysplasia and encephalomyelodysplasia.** *Brain* 2002;125:159–65 CrossRef Medline
- Caldas C, Bernicker E, Nogare AD, et al. **Case report: transverse myelitis associated with Epstein-Barr virus infection.** *Am J Med Sci* 1994;307:45–48 CrossRef Medline
- Mazur-Melewska K, Breńska I, Jończyk-Potoczna K, et al. **Neurologic complications caused by Epstein-Barr virus in pediatric patients.** *J Child Neurol* 2016;31:700–08 CrossRef Medline

40. Singhi P, Sharma JP, Gautam R, et al. **Extensive longitudinal transverse myelitis associated with CSF Epstein-Barr virus infection: a case report.** *Child Neurol Open* 2021;8:2329048X211049958 CrossRef Medline
41. Ali D, Cardos B, Gorur Y, et al. **A rare case of adult acute disseminated encephalomyelitis associated with primary Epstein-Barr virus infection.** *Eur J Case Rep Intern Med* 2019;6:001094 CrossRef Medline
42. Xiong CH, Yan Y, Liao Z, et al. **Epidemiological characteristics of acute disseminated encephalomyelitis in Nanchang, China: a retrospective study.** *BMC Public Health* 2014;14:111 CrossRef Medline
43. Bathla G, Policeni B. **Acute Disseminated Encephalomyelitis.** In: *Neuroradiology: Spectrum and Evolution of Disease.* Elsevier; 2019:80–96
44. Pohl D, Alper G, Van Haren K, et al. **Acute disseminated encephalomyelitis.** *Neurology* 2016;87(Suppl 2):S38–45 CrossRef
45. Verhey LH, Branson HM, Shroff MM, et al; Canadian Pediatric Demyelinating Disease Network. **MRI parameters for prediction of multiple sclerosis diagnosis in children with acute CNS demyelination: a prospective national cohort study.** *Lancet Neurol* 2011;10:1065–73 CrossRef Medline
46. Kim S, Ahn SJ, Chu K. **Epstein-Barr virus-associated acute disseminated encephalomyelitis successfully treated with rituximab: a case report.** *Encephalitis* 2021;1:85–88 CrossRef
47. Crombie JL, LaCasce AS. **Epstein Barr virus associated B-Cell lymphomas and iatrogenic lymphoproliferative disorders.** *Front Oncol* 2019;9:109 CrossRef Medline
48. Dunleavy K, Roschewski M, Wilson WH. **Lymphomatoid granulomatosis and other Epstein-Barr virus associated lymphoproliferative processes.** *Curr Hematol Malig Rep* 2012;7:208–15 CrossRef Medline
49. Melani C, Jaffe ES, Wilson WH. **Pathobiology and treatment of lymphomatoid granulomatosis, a rare EBV-driven disorder.** *Blood* 2020;135:1344–52 CrossRef Medline
50. Xiang Y, Liu C, Xue Y, et al. **Primary central nervous system lymphomatoid granulomatosis: systemic review.** *Front Neurol* 2020;11:901 CrossRef Medline
51. Patsalides AD, Atac G, Hedge U, et al. **Lymphomatoid granulomatosis: abnormalities of the brain at MR imaging.** *Radiology* 2005;237:265–73 CrossRef Medline
52. De Graaff HJ, Wattjes MP, Rozemuller-Kwakkel AJ, et al. **Fatal B-cell lymphoma following chronic lymphocytic inflammation with pontine perivascular enhancement responsive to steroids.** *JAMA Neurol* 2013;70:915–18 CrossRef Medline
53. Dang YL, Kok HK, McKelvie PA, et al. **Chronic lymphocytic infiltration with pontine perivascular enhancement responsive to steroids (CLIPPERS) and its association with Epstein-Barr Virus (EBV)-related lymphomatoid granulomatosis: a case report.** *BMC Neurol* 2021;21:80 CrossRef Medline
54. Soleja M, Jaso JM, Chen W, et al. **Lymphomatoid granulomatosis of the central nervous system (CNS-LYG) posing a management challenge.** *Clin Case Rep* 2021;9:e04808 CrossRef Medline
55. Hajtovic S, Liu C, Diefenbach CM, et al. **Epstein-Barr virus-positive primary central nervous system lymphoma in a 40-year-old immunocompetent patient.** *Cureus* 2021;13:e12754 CrossRef Medline
56. Cree IA. **The WHO Classification of Haematolymphoid Tumours.** *Leukemia* 2022;36:1701–02 CrossRef
57. Pons-Escoda A, García-Ruiz A, Naval-Baudin P, et al. **Diffuse large B-cell Epstein-Barr virus-positive primary CNS lymphoma in non-AIDS patients: high diagnostic accuracy of DSC perfusion metrics.** *AJNR Am J Neuroradiol* 2022;43:1567–74 CrossRef Medline
58. Bathla G, Hegde A. **Lymphomatous involvement of the central nervous system.** *Clin Radiol* 2016;71:602–09 CrossRef Medline
59. Neska-Matuszewska M, Bladowska J, Saósiadek M, et al. **Differentiation of glioblastoma multiforme, metastases and primary central nervous system lymphomas using multiparametric perfusion and diffusion MR imaging of a tumor core and a peritumoral zone: searching for a practical approach.** *PLoS One* 2018;13:e0191341 CrossRef Medline
60. Talybov R, Beylerli O, Mochalov V, et al. **Multiparametric MR imaging features of primary CNS lymphomas.** *Front Surg* 2022;9:887249 CrossRef Medline
61. Lee HY, Kim HS, Park JW, et al. **Atypical imaging features of Epstein-Barr virus-positive primary central nervous system lymphomas in patients without AIDS.** *AJNR Am J Neuroradiol* 2013;34:1562–67 CrossRef Medline
62. Gandhi MK, Hoang T, Law SC, et al. **EBV-associated primary CNS lymphoma occurring after immunosuppression is a distinct immunobiological entity.** *Blood* 2021;137:1468–77 CrossRef Medline
63. Mahale P, Shiels MS, Lynch CF, et al. **Incidence and outcomes of primary central nervous system lymphoma in solid organ transplant recipients.** *Am J Transplant* 2018;18:453–61 CrossRef Medline
64. Suh CH, Kim HS, Lee SS, et al. **Atypical imaging features of primary central nervous system lymphoma that mimics glioblastoma: utility of intravoxel incoherent motion MR imaging.** *Radiology* 2014;272:504–13 CrossRef Medline
65. Sauter A, Faul C, Bitzer M, et al. **Imaging findings in immunosuppressed patients with Epstein Barr virus-related B cell malignant lymphoma.** *AJR Am J Roentgenol* 2010;194:W141–49 CrossRef Medline
66. Balaguer-Rosello A, Piñana JL, Bataller L, et al. **Central nervous system involvement in Epstein-Barr virus-related post-transplant lymphoproliferative disorders after allogeneic hematopoietic stem cell transplantation.** *Transplant Cell Ther* 2021;27:261.e1–261.e7 CrossRef Medline
67. Lee ES, Locker J, Nalesnik M, et al. **The association of Epstein-Barr virus with smooth-muscle tumors occurring after organ transplantation.** *N Engl J Med* 1995;332:19–25 CrossRef Medline
68. Raheja A, Sowder A, Palmer C, et al. **Epstein-Barr virus-associated smooth muscle tumor of the cavernous sinus: a delayed complication of allogeneic peripheral blood stem cell transplantation: case report.** *J Neurosurg* 2017;126:1479–83 CrossRef Medline
69. Paez-Nova M, Andaur K, García-Ballesteras E, et al. **Primary intracranial smooth muscle tumor associated with Epstein-Barr virus in immunosuppressed children: two cases report and review of literature.** *Childs Nerv Syst* 2021;37:3923–32 CrossRef Medline
70. Willeke VM, Anderson MP, Mahadevan A, et al. **Epstein Barr virus associated smooth muscle tumors in the central nervous system: a case report and systematic review of the literature.** *J Neurooncol* 2020;147:247–60 CrossRef Medline
71. Lohan R, Bathla G, Gupta S, et al. **Epstein-Barr virus (EBV)-related smooth muscle tumors of central nervous system—a report of two cases and review of literature.** *Clin Imaging* 2013;37:564–68 CrossRef Medline
72. Ehresman JS, Ahmed AK, Palsgrove DN, et al. **Epstein-Barr virus-associated smooth muscle tumor involving the spine of an HIV-infected patient: case report and review of the literature.** *J Clin Neurosci* 2018;52:145–50 CrossRef Medline
73. Purgina B, Rao UN, Miettinen M, et al. **AIDS-related EBV-associated smooth muscle tumors: a review of 64 published cases.** *Patholog Res Int* 2011;2011:561548 CrossRef Medline

# Trends of Diversity in Neuroradiology Trainees in United States 2015–2022

P. Prajapati, X. Wu, S. Bajaj, D. Gandhi, M. Wintermark, and A. Malhotra

## ABSTRACT

**SUMMARY:** Radiology has historically not been a very diverse field. Many steps have been taken in the past decade to increase diversity in the field and make it more inclusive. This study shows the relative trends specifically in neuroradiology trainees, and the need for reassessment and further steps to increase diversity.

**ABBREVIATION:** IMGs = International Medical Graduates

Embracing diversity and inclusion has been emphasized by the American Society of Neuroradiology (ASNR) to enhance our collective ability to improve quality and excellence.<sup>1</sup> Several steps have been taken by the ASNR to increase diversity and the representation of women and underrepresented minorities.<sup>1</sup> These are especially important given the historical lack of diversity in radiology across all practice levels.<sup>2,3</sup> The trends in diversity specific to neuroradiology are not known. We undertook this study to assess trends in diversity among neuroradiology trainees from 2014–2015 to 2021–2022.

## MATERIALS AND METHODS

All data were obtained from publicly available, nonidentifiable, summarized databases and approval from the institutional review board was not applicable.

The American Medical Association and the Association of American Medical Colleges administer the National Graduate Medical Education Census and maintain a database on training programs accredited by the Association Council for Graduate Medical Education.<sup>4</sup> The Graduate Medical Education results from 2014–2015 to 2021–2022 were accessed for demographic information for neuroradiology trainees in the United States.<sup>5</sup> The sex and racial and ethnicity breakdowns were extracted, including Black/African American, Caucasian/White, Asian,

Hispanic, and others. Data were also analyzed for US doctors of medicine, International Medical Graduates (IMGs), graduates of Canadian medical schools, and graduates in doctor of osteopathic medicine. The 2-tailed *t* test was used to calculate the statistical difference between groups, with  $P < .05$  as a cutoff for significance.

## RESULTS

In 2021–2022, there were 90 Association Council for Graduate Medical Education–accredited programs with 253 neuroradiology trainees, of which 51 (20.2%) were women. In 2014–2015, women constituted 49/166 (23%,  $P = .490$ ) neuroradiology trainees (Fig 1). The proportion of women among trainees in the past 8 years has ranged between 18% and 25%.

In 2021–2022, Blacks or African Americans constituted 8/253 (3.2%) and Hispanics were 5/253 (2.0%) of all neuroradiology trainees. The corresponding proportions in 2014–2015 were 3/215 (1.4%,  $P = .207$ ) for Blacks and 9/215 (4.2%,  $P = .162$ ) for Hispanics. The proportion of Blacks has ranged between 1.4% and 4.4%, and for Hispanics, it has ranged between 2% and 8.2% in the past 8 years (Fig 2).

Asians constituted 71/253 (28%) trainees in 2021–2022 and 73/215 (34%,  $P = .166$ ) in 2014–2015. The proportion of Asians has ranged between 25% and 34%.

Whites constituted 108/253 (42.7%) trainees in 2021–2022, down from 116/215 (54%,  $P = .015$ ) in 2014–2015. The proportion of Whites has ranged between 35.4% and 61.8%.

There were 32.7% of trainees in 2020–2021 and 23.3% ( $P < .001$ ) in 2021–2022 identified as “other/unknown for race/ethnicity,” higher compared with previous years (Fig 2).

The proportion of IMGs has increased from 44/215 (20.5%) in 2014–2015 to 75/253 (29.6%,  $P = .023$ ) in 2021–2022 and has ranged between 13.7% and 29.6% (Fig 3).

Received June 2, 2023; accepted after revision June 22.

From the Department of Radiology and Biomedical Imaging (P.P., S.B., A.M.), Yale School of Medicine, New Haven, Connecticut; Department of Radiology (X.W.), University of California at San Francisco, San Francisco, California; University of Maryland School of Medicine (D.G.), Baltimore, Maryland; and Department of Neuroradiology (M.W.), MD Anderson Cancer Center, Houston, Texas.

Please address correspondence to Ajay Malhotra, MD, MMM, Department of Radiology and Biomedical Imaging, Yale School of Medicine, Box 208042, Tompkins East 2, 333 Cedar St, New Haven, CT 06520-8042; e-mail: ajay.malhotra@yale.edu  
<http://dx.doi.org/10.3174/ajnr.A7947>

## DISCUSSION

Diversity in neuroradiology trainees is even less compared with overall radiology residents and has not shown improvement with time. While the recent proportion of women is 27%, with Blacks at 4%, and Hispanics at 6% for radiology residents nationwide,<sup>2</sup> the corresponding proportions in neuroradiology are 20% ( $P = .016$ ), 3.2% ( $P = .575$ ), and 2% ( $P = .009$ ), respectively. The proportion of Whites has decreased from 54% to 43% during the study period.

Academic radiology has seen an increase in the proportion of women in faculty ranks, especially at more senior levels and as department chairs.<sup>2</sup> Women have also seen higher representation at the leadership positions at the national level: Five of the 10 ASNR Presidents from 2010 to 2019 were women, with 3 of the 4 Presidents from 2020 to 2023 being women.<sup>3</sup> Lack of diversity at the leadership levels was previously thought to impair the ability of our field to address the underlying causes of disparities.<sup>1</sup> The ASNR Annual Program Committee has worked on creation of a program diversity checklist to encourage diverse and inclusive representation.<sup>1</sup>



FIG 1. Sex distribution in neuroradiology trainees 2015–2022.

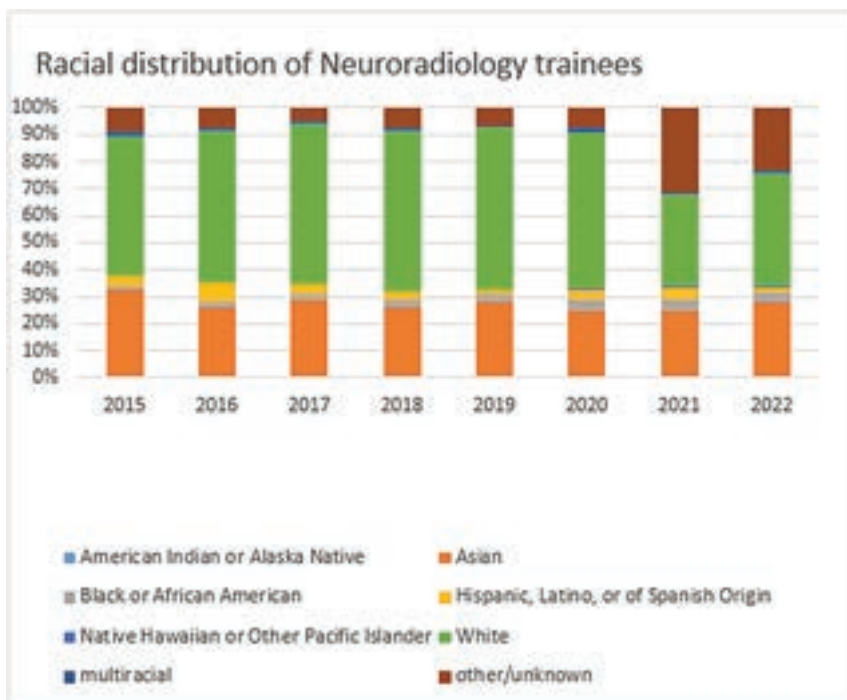


FIG 2. Racial distribution of neuroradiology trainees 2015–2022.

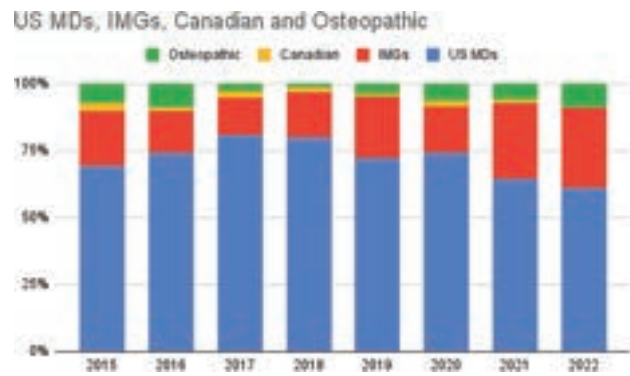


FIG 3. Proportion of US MDs, DOs, IMGs and Canadian graduates. US MD indicates United States doctor of medicine.

ASNR has also taken several steps, including webinars and podcasts, to increase awareness as well as mentorship programs within neuroradiology.

Despite the aforementioned efforts and successes, the sex and racial representation at the trainee level in neuroradiology is a reason for concern. An objective analysis of the efforts being undertaken to improve diversity as well as reasons for the problem that need further addressing may be required.

IMGs provide a broad range of diversity in our society, with members from very diverse backgrounds. The proportion of IMGs in neuroradiology is higher than the national average. In 2020, IMGs constituted 14.6% of all radiology trainees.<sup>6</sup> The proportion of IMGs in the American Board of Radiology Alternate Pathway and the proportion staying in academic neuroradiology need further study.

A limitation of this study is the increase in the number of trainees reported as other/unknown for race/ethnicity in the Association of American Medical Colleges data set.

## CONCLUSIONS

This study highlights the need for greater diversity in the field of neuroradiology and reassessment of the steps needed for this strategic imperative.

Disclosure forms provided by the authors are available with the full text and PDF of this article at [www.ajnr.org](http://www.ajnr.org).

## REFERENCES

1. Bunch PM, Loevner LA, Bhala R, et al. **The American Society of Neuroradiology: cultivating a diverse and inclusive culture to build a stronger organization.** *AJNR Am J Neuroradiol* 2021;42:2127–29 CrossRef Medline
2. Wu X, Bajaj S, Khunte M, et al. **Diversity in radiology: current status and trends over the past decade.** *Radiology* 2022;305:640–47 CrossRef Medline
3. Ahmadi M, Khurshid K, Sanelli PC, et al. **Influences for gender disparity in**

- academic neuroradiology.** *AJNR Am J Neuroradiol* 2018;39:18–23 CrossRef Medline
4. AAMC. <https://www.aamc.org/data-reports/students-residents/data/report-residents/2022/table-b3-number-active-residents-type-medical-school-gme-specialty-and-gender>. Accessed June 16, 2023
  5. Brotherton SE, Etzel SI. **Graduate medical education, 2021-2022.** *JAMA* 2022;328:1123–46 CrossRef Medline
  6. Wadhwa V, Vilanilam GK, Chhabra A, et al. **A 15-year analysis of international medical graduates matching into diagnostic radiology residency programs in the United States.** *Acad Radiol* 2022;29:137–43 CrossRef Medline

# Generative Adversarial Network–Enhanced Ultra-Low-Dose [<sup>18</sup>F]-PI-2620 $\tau$ PET/MRI in Aging and Neurodegenerative Populations

K.T. Chen, R. Tesfay, M.E.I. Koran, J. Ouyang, S. Shams, C.B. Young, G. Davidzon, T. Liang, M. Khalighi, E. Mormino, and G. Zaharchuk



## ABSTRACT

**BACKGROUND AND PURPOSE:** With the utility of hybrid  $\tau$  PET/MR imaging in the screening, diagnosis, and follow-up of individuals with neurodegenerative diseases, we investigated whether deep learning techniques can be used in enhancing ultra-low-dose [<sup>18</sup>F]-PI-2620  $\tau$  PET/MR images to produce diagnostic-quality images.

**MATERIALS AND METHODS:** Forty-four healthy aging participants and patients with neurodegenerative diseases were recruited for this study, and [<sup>18</sup>F]-PI-2620  $\tau$  PET/MR data were simultaneously acquired. A generative adversarial network was trained to enhance ultra-low-dose  $\tau$  images, which were reconstructed from a random sampling of 1/20 (approximately 5% of original count level) of the original full-dose data. MR images were also used as additional input channels. Region-based analyses as well as a reader study were conducted to assess the image quality of the enhanced images compared with their full-dose counterparts.

**RESULTS:** The enhanced ultra-low-dose  $\tau$  images showed apparent noise reduction compared with the ultra-low-dose images. The regional standard uptake value ratios showed that while, in general, there is an underestimation for both image types, especially in regions with higher uptake, when focusing on the healthy-but-amyloid-positive population (with relatively lower  $\tau$  uptake), this bias was reduced in the enhanced ultra-low-dose images. The radiotracer uptake patterns in the enhanced images were read accurately compared with their full-dose counterparts.

**CONCLUSIONS:** The clinical readings of deep learning–enhanced ultra-low-dose  $\tau$  PET images were consistent with those performed with full-dose imaging, suggesting the possibility of reducing the dose and enabling more frequent examinations for dementia monitoring.

**ABBREVIATIONS:** AC1 = Gwet's agreement coefficient 1; AD = Alzheimer's disease; CNN = convolutional neural network; GAN = generative adversarial network; SUVR = standard uptake value ratio

More than 6 million individuals are living with Alzheimer's disease (AD) in the United States. By 2060, this number is projected to increase to nearly 14 million (<https://www.cdc.gov/aging/aginginfo/alzheimers.htm>). This neurodegenerative disorder

leads to progressive, irreversible loss of memory and behavioral function.<sup>1</sup> Pathologic features of AD include accumulation of amyloid  $\beta$  into extracellular plaques and hyperphosphorylated  $\tau$  into intracellular neurofibrillary tangles, which can be identified with PET imaging.<sup>2</sup> Abnormalities of  $\tau$  mediate amyloid  $\beta$ –induced toxicity<sup>3</sup> and are a close proxy of clinical status.<sup>4</sup> Furthermore, because pathologic processes of AD begin decades before mild cognitive impairment and dementia stages, in vivo measurements of amyloid  $\beta$  plaques and tangles could enable early detection and an opportunity for intervention.<sup>5</sup> Along these lines, recent work has shown that subtle elevations in  $\tau$  PET can be detected in clinically healthy older adults and are predictive of subsequent decline.<sup>6</sup>

Advanced modalities such as simultaneous PET/MR imaging provide complementary morphologic and functional information with perfect spatiotemporal registration of the 2 imaging data sets,<sup>7</sup> all of which can facilitate the diagnosis and monitoring of dementia.<sup>8,9</sup> However, radiation exposure related to the radiotracers administered to imaging subjects presents barriers to screening, clinical follow-up, and research participation due to radiation dose

Received November 3, 2022; accepted after revision July 11, 2023.

From the Department of Biomedical Engineering (K.T.C.), National Taiwan University, Taipei, Taiwan; Departments of Radiology (K.T.C., M.E.I.K., J.O., S.S., G.D., T.L., M.K., G.Z.) and Neurology and Neurological Sciences (C.B.Y., E.M.), Stanford University, Stanford, California; and Meharry Medical College (R.T.), Nashville, Tennessee.

This work was supported by the National Institutes of Health (P41-EB015891, R01-EB025220, R56-AG071558, K99-AG068310-01A1, R01-AG048076, R21-AG058859), the Stanford Alzheimer's Disease Research Center (P30-AG06615), the Yushan Fellow Program by the Ministry of Education (NTU-112V1015-3, R.O.C.) the National Science and Technology Council grant (110-2222-E-002-015-MY3, R.O.C.), the National Health Research Institutes grant (NHRI-EX112-11205EC), and the Alzheimer's Association (AARFD-21-849349), GE Healthcare, and Life Molecular Imaging.

Please address correspondence to Kevin T. Chen, 49 Fanglan Rd, Taipei 106, Taiwan; e-mail: chenkt@ntu.edu.tw

Indicates open access to non-subscribers at [www.ajnr.org](http://www.ajnr.org)

Indicates article with online supplemental data.

<http://dx.doi.org/10.3174/ajnr.A7961>

**Table 1: Demographics and clinical indications of study population**

	Healthy Control	AD	CBS	MCI	PSP	svPPA
No.	31	5	1	4	1	2
Age (mean) (yr)	70.13 (SD, 6.43)	67.8 (SD, 13.48)	76	71.5 (SD, 10.54)	71	66, 78
Sex (female)	12	3	0	2	0	1
Amyloid status	7 P, 21 N	4 P		3 P, 1 N		

**Note:**—CBS indicates cortical basal syndrome; MCI, mild cognitive impairment; N, negative; P, positive; PSP, progressive supranuclear palsy; svPPA, semantic variant primary-progressive aphasia.

thresholds. Therefore, radiotracer dose reductions have been a target for intervention for many researchers.

Deep learning methods such as convolutional neural networks (CNNs) have been used for image identification,<sup>10</sup> generation,<sup>11,12</sup> segmentation,<sup>13</sup> and MR imaging-based attenuation correction.<sup>14,15</sup> CNNs that incorporate spatially correlated MR imaging and PET information to produce standard-quality PET images from low-dose PET acquisitions (though most such studies were conducted on [<sup>18</sup>F]-fludeoxyglucose scans) have been implemented.<sup>16–21</sup> For example, deep CNNs can reduce the radiotracer dose by at least 100-fold for [<sup>18</sup>F]-florbetaben, an in vivo biomarker of amyloid plaque buildup,<sup>22</sup> and enhancement of both simulated (undersampled in PET/MR imaging reconstruction) and true (injected with ultra-low-dose) ultra-low-dose images resulted in the production of diagnostic-quality images comparable with standard dose images.<sup>23</sup>

Here, we investigate whether similar techniques in deep learning can be used to enhance ultra-low-dose [<sup>18</sup>F]-PI-2620  $\tau$  PET/MR images to produce diagnostic-quality images. Compared with amyloid PET and plasma phosphorylated  $\tau$  biomarkers,<sup>24,25</sup>  $\tau$  PET has its strength in discriminating AD from other neurodegenerative disease<sup>26</sup> and can aid in regional cerebral  $\tau$  analysis for the identification of various tauopathies. With the uptake of a  $\tau$  tracer being more focal and having a weaker signal than amyloid PET images in general, we have found that directly applying the CNN in our previous work carries over data bias from the amyloid PET training data set.<sup>27</sup> Therefore, in this work, we implemented a generative adversarial network (GAN) structure<sup>28</sup> in addition to training the ultra-low-dose  $\tau$  enhancement CNN from scratch. In addition, in this article, we have focused on aging participants as well as those with a variety of neurodegenerative diseases. Examining asymptomatic/early dementia populations, including preclinical AD and mild cognitive impairment, is increasingly important for dementia studies, but these groups are difficult to image because the PET signal can be lower and restricted to the medial temporal lobe compared with those with AD dementia.<sup>29,30</sup> Patients who are amyloid-positive and mild  $\tau$ -positive who are most likely in an asymptomatic or mild cognitive impairment stage may also require more frequent follow-up scans to monitor for disease progression.

Unlike the use of PET for cancer monitoring, patients with dementia may have much longer periods than patients with cancer in which to accrue the negative effects of medical radiation, especially if the use of image monitoring expands, beginning in the asymptomatic or minimally symptomatic stages. Reducing the PET tracer dose can lead to safer scans and increase the utility

of hybrid PET/MR imaging for screening, clinical diagnoses, and longitudinal studies (improved follow-up adherence). With the increasing availability of data and research participation, researchers can also better understand the pathogenesis and identify targets for pharmacotherapy. At the population level, reducing dosing has the

potential to decrease health care costs to individual patients as well as research and health care institutions.

## MATERIALS AND METHODS

Forty-four total participants were recruited for this study, approved by the Stanford University institutional review board. Written informed consent was obtained from all participants or an authorized surrogate decision-maker. Older healthy controls were recruited through the Stanford Aging and Memory Study (SAMS; <https://www.alzheimers.gov/clinical-trials/stanford-memory-and-aging-study>). Patients with cognitive impairment (either a clinical diagnosis of mild cognitive impairment or AD dementia) and semantic-variant primary-progressive aphasia were recruited through the Stanford Alzheimer Disease Research Center or the Stanford Center for Memory Disorders. Demographics of the patient group, including their clinical diagnoses (determined by clinical consensus of a panel of neurologists and neuropsychologists), are shown in Table 1. In particular, 7 participants from the healthy controls were amyloid-positive as determined by CSF (details in Trelle et al<sup>31</sup>).

### PET/MR Imaging Data Acquisition

T1-weighted and T2-FLAIR MR imaging data and  $\tau$  PET data were simultaneously acquired on an integrated 3T PET/MR imaging scanner (Signa; GE Healthcare); 221 [SD, 61] MBq of the  $\tau$  radiotracer [<sup>18</sup>F]-PI-2620 was injected, and imaging was performed between 60 and 90 minutes after injection. The raw list-mode PET data were reconstructed for the full-dose ground truth image and were also randomly undersampled by a factor of 20 (approximately 5% of original count level) and then reconstructed to produce an ultra-low-dose PET image. Previous studies have suggested that this method of simulation of ultra-low-dose imaging is a good representation of the true injected ultra-low-dose.<sup>23</sup> TOF ordered subsets expectation maximization, with 2 iterations and 28 subsets and accounting for randoms, scatter, dead-time, and attenuation, was used for all PET image reconstructions. MR imaging attenuation correction was performed using the vendor's zero TE-based method, and a 4-mm postreconstruction Gaussian filter was used for all reconstructions.

### Image Preprocessing

To account for any positional offset of the patient during different acquisitions, we coregistered MR images to the PET images using the FMRIB Linear Image Registration Tool (FLIRT; <http://www.fmrib.ox.ac.uk/fsl/fslwiki/FLIRT>),<sup>32</sup> with 6 *df* and the correlation ratio as the cost function. All images were resliced to the dimensions of the acquired PET volumes: eighty-nine 2.78-mm-thick slices with 256-by-256 1.17 × 1.17 mm<sup>2</sup> pixels. A head mask

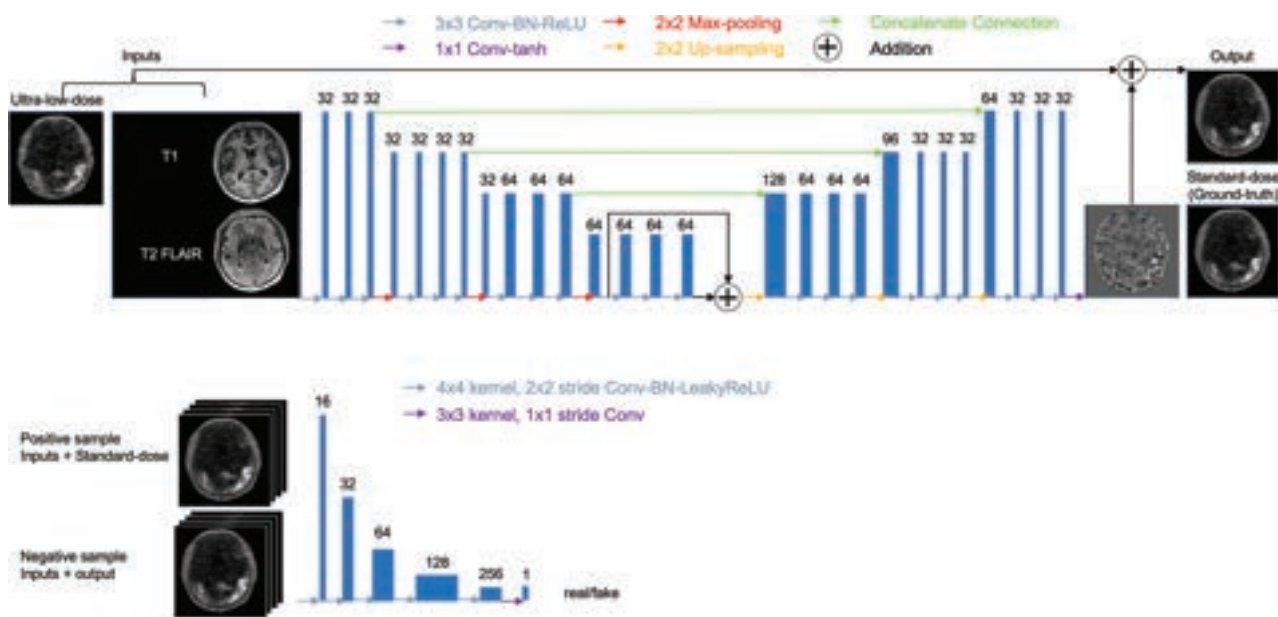


**FIG 1.** A schematic of the GAN (generator network, upper image; discriminator network, lower image) used in this work and its input and output channels. The *arrows* denote computational operations, and the tensors are denoted by *boxes*, with the number of channels indicated above each box. BN indicates batch normalization; Conv, convolution; Max, maximum; ReLU, rectified linear unit; tanh, hyperbolic tangent.

was made from the T1-weighted image through intensity thresholding and hole filling and applied to the PET and MR images. The voxel intensities of each volume were normalized using its *z* score (mean divided by SD within a FreeSurfer-based brain mask [http://surfer.nmr.mgh.harvard.edu] derived from the T1-weighted images) and used as inputs to the CNN.

### CNN Implementation

The ultra-low-dose  $\tau$  network was trained using a GAN structure<sup>28</sup> with 3916 input slices (44 data sets with 89 slices each). The generator portion of the GAN used the proposed structure in Chen et al,<sup>22,23</sup> which included an encoder-decoder CNN with the U-Net<sup>33</sup> structure (Fig 1, upper image) where the inputs were the concatenation of multicontrast MR images (T1 and T2 FLAIR-weighted) and the ultra-low-dose PET image. The full-dose PET image was treated as the ground truth and the network was trained through residual learning.<sup>11</sup> Briefly, the encoder portion is composed of layers that perform 2D convolutions (using  $3 \times 3$  filters) on input 256-by-256 transverse slices, batch normalization, and rectified linear unit activation operations. We used 2-by-2 max pooling to reduce the dimensionality of the data. In the decoder portion, the data in the encoder layers are concatenated with those in the decoder layers. Linear interpolation is performed to restore the data to its original dimensions. In addition, a discriminator (Fig 1, lower image) was added to distinguish whether the output image is realistic or not. The discriminator portion of the GAN consists of 5 convolution blocks, which are composed of convolution layers with  $4 \times 4$  filters and  $2 \times 2$  stride, batch normalization, and leaky rectified linear activation with the slope of 0.2. A convolution layer with a  $3 \times 3$  filter is added to map the features to 1 channel as the output. The final objective for the encoder-decoder network is the combination of a pixel-wise L1 loss and an adversarial loss:

$$L_G = E_{x,y}[\log D(x,y)] + E_x[\log(1 - D(x,G(x)))] + \lambda E_{x,y}[\|y - G(x)\|_1],$$

where  $x$  is the input images,  $y$  is the standard dose image, and  $G(x)$  is the enhanced image. The GAN was trained with an initial learning rate of 0.0001 and a batch size of 16 over 50 epochs. The training, validation, and testing data were split at the participant level for an approximate 7:1:2 ratio, and 5-fold cross-validation was used to employ all the data for training and testing.

### Assessment of Image Quality

The reconstructed images were first visually inspected for artifacts. For each data set, the region within the brain mask was considered for voxel-based analyses. For each axial section, the image quality of the enhanced PET images and the original ultra-low-dose PET images within the brain mask were compared with the full-dose image using the peak SNR, structural similarity,<sup>34</sup> and root mean square error. The metrics for each subject were obtained by a weighted average (by voxel number) of the slices.

### Clinical Readings

The enhanced PET images, the ultra-low-dose PET image, and the full-dose PET image of each data set were anonymized, and their series numbers were randomized and then presented by series number to 3 physicians (M.E.I.K., a dual-boarded nuclear medicine and diagnostic radiology physician; S.S., a neuroradiology fellow; G.Z., a neuroradiologist) for independent reading (reading protocol for the identification of regional uptake is available in the Online Supplemental Data). Ten random full-dose PET images were also presented to the physicians to evaluate intrareader reproducibility. The consensus  $\tau$  status read from the 3 reviewers on the full-dose images was treated as the ground truth. For each PET image, the physicians also assigned a

subjective image-quality score on a 5-point scale: 1 = uninterpretable, 2 = poor, 3 = adequate, 4 = good, 5 = excellent. Also, image-quality scores were dichotomized into 1–2 (low) versus 3–5 (high), with the percentage of images with high scores calculated for each method. The agreement of the 3 readers was assessed using the Gwet's agreement coefficient 1 (AC1)<sup>35</sup> on the full-dose readings, and if high agreement was found, the readings of the 3 readers were pooled for further analysis.

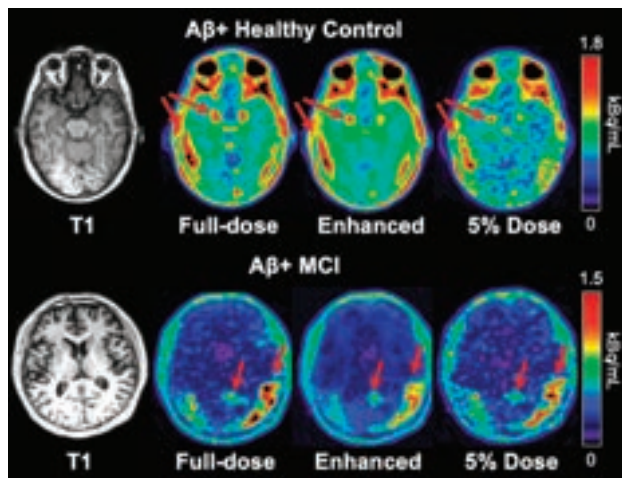


**FIG 2.** Representative  $\tau$  PET images and their corresponding T1-weighted MR image in 2 individuals positive for amyloid. The enhanced PET image shows greatly reduced noise compared with the ultra-low-dose PET image. Arrows correspond to regions of abnormal elevated  $\tau$  uptake. MCI indicates mild cognitive impairment.

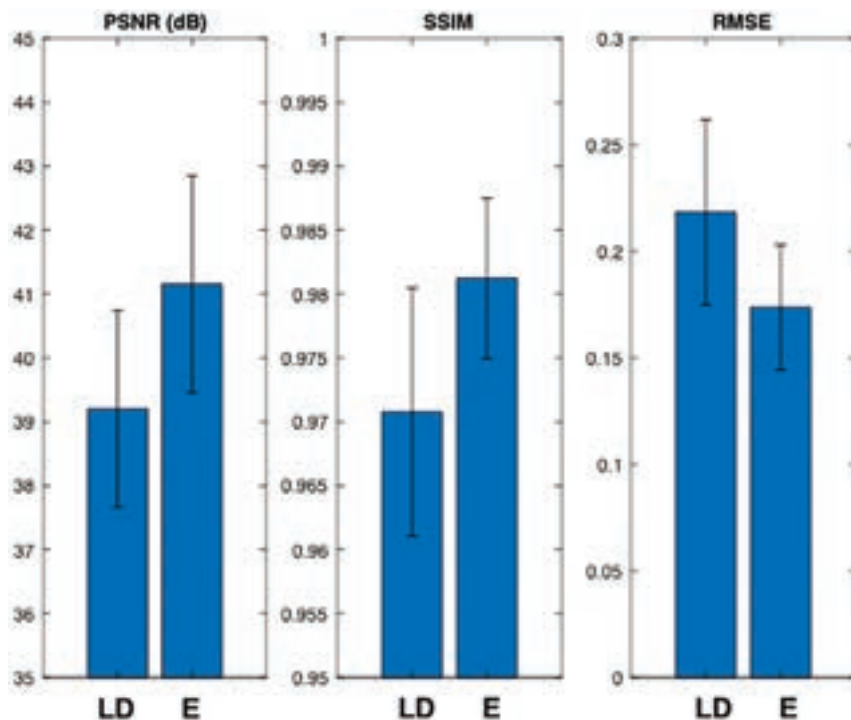


**FIG 3.** Image-quality metrics comparing the ultra-low-dose PET (LD) and the ultra-low-dose enhanced PET (E) images with the ground truth full-dose PET image. PSNR indicates peak signal-to-noise ratio; SSIM, structural similarity; RMSE, root mean square error.

### Region-Based Analysis

Region-based analyses were performed to assess the agreement of the tracer uptake among images. Cortical parcellations and cerebral segmentations based on the Desikan-Killiany Atlas<sup>36</sup> were derived from FreeSurfer and analyses focused on the medial temporal lobe, comprising the entorhinal cortex and amygdala and the inferior temporal cortex. The inferior cerebellum was used as the reference region for standard uptake value ratio (SUVr) calculations for all 3 (full-dose, ultra-low-dose, and enhanced) image types. The SUVrs were compared between methods (full-dose to ultra-low-dose and full-dose to enhanced) and evaluated by Bland-Altman plots. Focus was on the healthy controls positive for amyloid, and these participants were labeled separately on the plots. The coefficient of variation (SD divided by the mean uptake) in the medial temporal lobe and the inferior temporal cortex were also calculated to assess image noise in the image types.

### Statistical Analysis

For quantitative tests, paired *t* tests at the  $P = .05$  level were performed to compare peak SNR, structural similarity, and root mean square error metrics between the ultra-low-dose images and their CNN-enhanced counterparts.

Pair-wise *t* tests were also performed to compare the values of the image-quality metrics across the different image-processing methods. The accuracy, sensitivity, and specificity were calculated for the readings of the ultra-low-dose and enhanced PET images. Symmetry tests were also performed to examine whether the readings produced an equal number of false-positives and -negatives. The agreement of the 3 readers was assessed using Gwet's AC1.<sup>35</sup> Average image scores for each method are presented. The

95% confidence interval for the difference in the proportions of high scores was constructed and compared with a predetermined noninferiority benchmark of 15%. Tests were conducted at the  $P = .05$  level (Bonferroni correction to account for multiple comparisons when necessary).

### RESULTS

The enhanced  $\tau$  images showed apparent noise reduction with smoother image texture compared with the ultra-low-dose images (Fig 2). Quantitatively, the 3 image-based metrics all improved significantly ( $P < .05/3$ , Fig 3) after enhancement of the ultra-low-dose images. The regional coefficient of variation in regional SUVrs was reduced in the enhanced image types ( $P < .001$  for all comparisons with the enhanced images), indicating noise reduction in the images (Fig 4). The regional SUVrs showed generally low bias and variability between the full-dose images and other image types. While there is an underestimation in the SUVrs for both

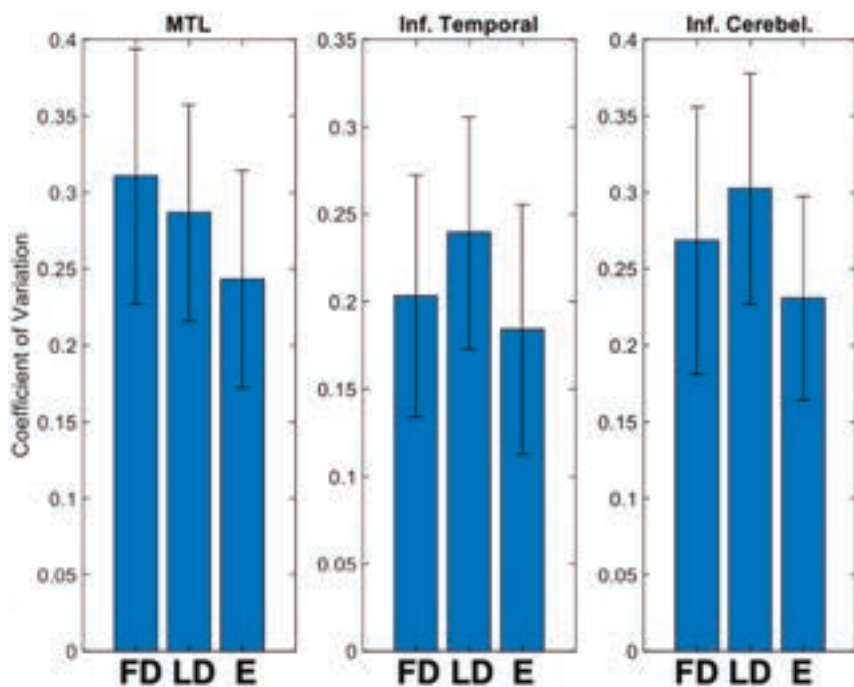


**FIG 4.** Mean (SD) of SUVR coefficient of variation in selected brain regions. E indicates enhanced images; FD, full-dose images; Inf. Cerebel, inferior cerebellum; MTL, medial temporal lobe; LD, ultra-low-dose image; Inf. Temporal, inferior temporal cortex

image types on average (influenced by regions with higher uptake, though the slight overestimation by the ultra-low-dose images contributed to a smaller coefficient of variation than that of the full-dose images) when focusing on the healthy-but-amyloid-positive population (with generally lower  $\tau$  uptake), this bias was reduced ( $P < .025$ , paired  $t$  tests corrected for 2 comparisons) in the enhanced images (average SUVR difference: 0.0101 [SD, 0.0312] in the inferior cortex and  $-0.0014$  [SD, 0.1238] in the medial temporal lobe) relative to that in the ultra-low-dose images (average SUVR difference:  $-0.0153$  [SD, 0.0374] in the inferior cortex and  $-0.0566$  [SD, 0.1451] in the medial temporal lobe) (Fig 5).

While the 3 readers have discussed and agreed to a reading protocol for the identification of regional uptake, they exhibited different preferences in reading the images based on the 5-point scale (Fig 6). However, when using the dichotomized scale, the readers showed agreement in their ratings of the 3 image types. Noninferiority tests at the predetermined threshold of  $-15\%$  for subjective image quality showed that both the ultra-low-dose and enhanced images were inferior to the full-dose images.

The intrareader reproducibility and interreader agreement was high in reading the full-dose images (Tables 2 and 3). Among image types, the readers also had high agreement in evaluating the status of  $\tau$  uptake in the regions (Gwet's AC1  $> 0.65$ , Table 1); the uptake in the ultra-low-dose and ultra-low-dose enhanced images was read accurately (accuracy  $> 0.84$  for all relevant regions, Table 2) compared with their full-dose counterparts.

## DISCUSSION

In this study, we have proposed a GAN structure to produce diagnostic-quality  $\tau$  PET images from input representing a

simulated 5% dose PET acquisition. There are many reasons to reduce the dose for dementia PET imaging, including enabling more frequent follow-up scans (under current radiation safety levels) to monitor for disease progression, especially in individuals who are asymptomatic or in the mild cognitive impairment stage. Another value is to extend the access of advanced tracers to more rural regions that are not within current service regions for radiotracer delivery, a problem that affects up to 10% of the US population. Because  $\tau$  PET images generally show reduced and focal uptake compared with other radiotracers such as amyloid and also contain more image noise, we have chosen a GAN structure for training to generate images with more similar image texture compared with those generated with only a U-Net such as in Chen et al.<sup>22</sup> We have shown in a previous study that directly using a U-Net trained on amyloid images to generate images is inferior to using a network trained with  $\tau$

images, which took the image properties of the different radiotracers into account during training.<sup>27</sup>

The generated images show that the noise in the PET images is greatly reduced through network training. The lower coefficient of variation in selected regions relevant to the participant population also reflects this finding. In addition, the peak SNR, structural similarity, and root mean square error metrics show that the generated images also resemble the full-dose images more than their ultra-low-dose counterparts.

The Bland-Altman plots showed that the ultra-low-dose and enhanced images were similar in their regional SUVR biases compared with the full-dose images (Fig 5). In general, in participants with high uptake in the inferior temporal cortex, SUVR underestimation was present compared with the values in the full-dose images. However, when we examined the healthy control population positive for amyloid, a demographic that needs close attention in tracking the participants' progression, the enhanced images showed less bias when calculating the SUVRs in regions relevant to neurodegeneration. This finding shows the potential of using deep learning-based enhancement of ultra-low-dose PET images in subjects needing more frequent PET follow-up and is a first step in translating this method to routine clinical and scientific use for these subjects.

For the reader study, the readers rated 2 aspects of each image: subjective image quality and whether the images provide clinical information related to the  $\tau$  imaging. For the former, a 5-point Likert scale was used; for the latter, because there is no official rating scale established for this particular  $\tau$  radiotracer, the readers evaluated whether there is increased uptake in a number of regions relevant to  $\tau$  imaging.

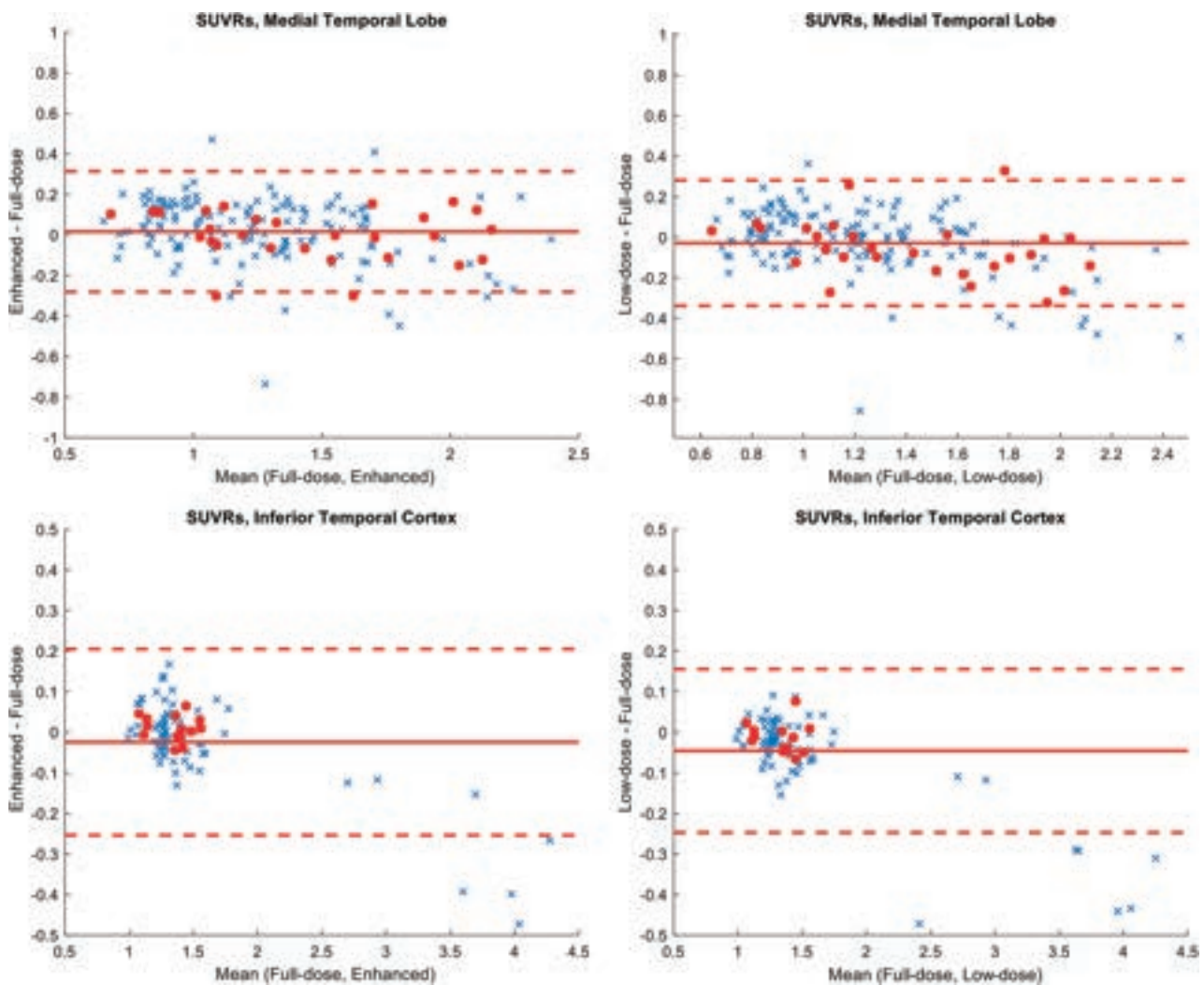


**FIG 5.** Bland-Altman plots comparing mean SUVRs in the ultra-low-dose PET and the enhanced PET with the full-dose PET images. The *red dots* denote healthy controls positive for amyloid, and the regions selected are the FreeSurfer labels, which make up the bilateral medial temporal lobe (entorhinal, amygdala) and the bilateral inferior temporal cortex.

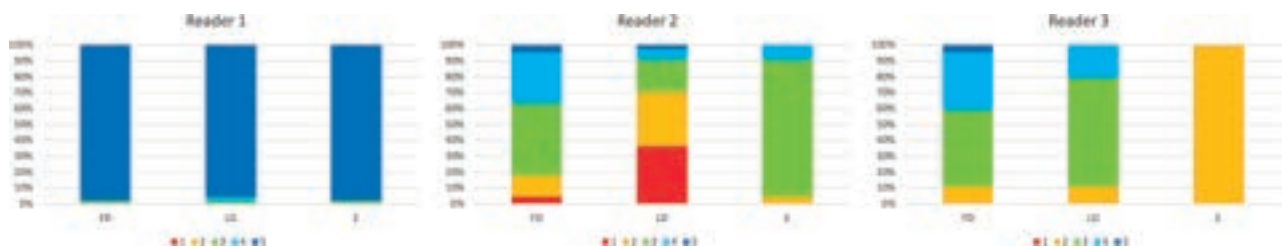


**FIG 6.** Quality scores of different image types as rated by 3 expert readers. Image quality scores: 1, uninterpretable; 2, bad; 3, adequate; 4, good; 5, excellent. FD indicates full-dose; LD, ultra-low-dose; E, enhanced.

The results from subjective image quality showed that the readers had different preferences in reading the images. In fact, the readers each had a different preference: Reader 1 was generous in assigning quality scores for all image types; reader 2 showed a preference against the ultra-low-dose images, where there was more image noise; reader 3, on the contrary, did not prefer the enhanced images where more image-smoothing occurred. However, when we examined the dichotomized scale, the ratings from all 3 readers

showed that there are more full-dose images scored as “high-quality” than the other 2 image types, in which the proportion of high-quality images for the ultra-low-dose and enhanced images fell below the noninferiority threshold. This finding also highlights the challenge of deep learning enhancement of PET images that have a weak focal uptake. It is possible that 95% undersampling is too great for the current GAN to synthesize similar quality, given the number of cases to which we had access.

**Table 2: Gwet's AC1 between and within readers of 10 randomly selected full-dose images on the tracer uptake in relevant brain regions and on the subjective image quality**

Gwet's AC1	Interreader	Reproducibility (Reader 1)	Reproducibility (Reader 2)	Reproducibility (Reader 3)
Normal	0.677	0.727	0.628	1
Entorhinal cortex	0.813	1	1	0.883
Hipp./Amyg./Parahipp.	0.677	0.771	1	1
Inferior/mesial temporal	0.901	1	1	1
Other cortex	0.830	0.872	0.669	1
Primary eloquent cortex	0.967	1	1	1
Quality (high vs low)	0.797	1	0.599	0.760

**Note:**—Normal indicates no abnormal uptake in any of the selected regions; Hipp., hippocampus; Amyg., amygdala; Parahipp., parahippocampal gyrus.

**Table 3: Accuracy, sensitivity, and specificity of ultra-low-dose images and enhanced images compared with the full-dose images**

Metric	Full-Dose vs Ultra-Low-Dose			Full-Dose vs Enhanced		
	Accuracy (%)	Sensitivity (%)	Specificity (%)	Accuracy (%)	Sensitivity (%)	Specificity (%)
Normal	86.4	89.7	77.1	84.8	87.6	77.1
Entorhinal cortex	92.4	50.0	97.5	93.9	42.9	98.3
Hipp./Amyg./Parahipp.	87.9	54.2	95.4	88.6	66.7	93.5
Inferior/mesial temporal	95.5	83.3	97.4	93.2	77.8	95.6
Other cortex	87.9	73.9	90.8	88.6	87.0	89.0
Primary eloquent cortex	95.5	80.0	96.1	99.2	80.0	100

**Note:**—Normal indicates no abnormal uptake in any of the selected regions; Hipp., hippocampus; Amyg., amygdala; Parahipp., parahippocampal gyrus.

In reading the uptake in relevant regions, Gwet's AC1 showed intrareader agreement (reproducibility) as well as interreader agreement in the radiotracer uptake of selected regions. Most interesting, the readings of different image types across the 3 readers also showed high agreement, indicating that both the enhanced images and the ultra-low-dose images could provide uptake information, similar to the full-dose images, with slight benefit for the enhanced images. Therefore, the enhanced ultra-low-dose images provide a tool for readers who do not prefer noisy images.

This study has several limitations. Because there is no official guideline on how to read  $\tau$  images and how to evaluate their image quality, we evaluated the uptake patterns on the basis of criteria agreed to by the 3 readers, using a positive/negative scale in several important ROIs. Most (31/44) of the participants in this study were healthy controls, which would contribute to an imbalance in our training data. On the other hand, healthy controls are an important focus. We have shown, in a previous study, that matching target populations in the training and testing data is important for optimal results;<sup>37</sup> if the training data were overweighted to patients with AD, the performance of the GAN might be suboptimal in a healthy control test set. Moreover, healthy controls are increasingly becoming the focus of research studies<sup>38</sup> and early prevention clinical trials, highlighting the value of tracking  $\tau$  in at-risk healthy controls in addition to patients with AD (when cognitive decline symptoms have already manifested).

In the future, more sophisticated networks will be evaluated to better replicate the image texture of the full-dose images. More complex networks could potentially allow further dose reduction to show differences between the ultra-low-dose and the enhanced images and minimize the effects of the network for reader preference. On the other hand, we did not experiment with simpler, non-deep-learning-based methods such as image filtering and their results in noise reduction. However, from our experience in training PET-only networks (which does not provide as much

morphologic information as the results indicate),<sup>22</sup> such methods tend to produce inferior results, and we suspect that this finding would be more likely for  $\tau$  because its uptake is weaker and more focal. A larger and more diverse population in the participant population for the training and testing sets would also likely improve performance. Through data-acquisition of participants with higher  $\tau$  uptake or those with more advanced dementia, we could expand our analyses to regions relevant to those populations, instead of solely focusing on the 3 regions in this work. We examined only 1 dose-reduction level, which was estimated on the basis of earlier work with FDG and amyloid tracers, partially to mitigate the demands on the 3 clinical readers. The use of low-dose images with less undersampling could produce improved results, and the results could be further confirmed with actual low-dose studies and region-based validation of SUVRs between the 2 low-dose regimens.

## CONCLUSIONS

The deep learning-enhanced images could be read clinically for regional uptake patterns of  $\tau$  accumulation, similar to the full-dose images. With further refinements, this technique can potentially increase the utility of hybrid PET/MR imaging in clinical diagnoses and longitudinal studies.

Disclosure forms provided by the authors are available with the full text and PDF of this article at [www.ajnr.org](http://www.ajnr.org).

## REFERENCES

- Gallucci M, Limbucci N, Catalucci A, et al. **Neurodegenerative diseases.** *Radiol Clin North Am* 2008;46:799–817, vii CrossRef Medline
- Mormino EC, Toueg TN, Azevedo C, et al. **Tau PET imaging with <sup>18</sup>F-Pi-2620 in aging and neurodegenerative diseases.** *Eur J Nucl Med Mol Imaging* 2021;48:2233–44 CrossRef Medline
- Nelson PT, Braak H, Markesbery WR. **Neuropathology and cognitive impairment in Alzheimer disease: a complex but coherent relationship.** *J Neuropathol Exp Neurol* 2009;68:1–14 CrossRef Medline

4. Nelson PT, Alafuzoff I, Bigio EH, et al. **Correlation of Alzheimer disease neuropathologic changes with cognitive status: a review of the literature.** *J Neuropathol Exp Neurol* 2012;71:362–81 CrossRef Medline
5. Sperling R, Mormino E, Johnson K. **The evolution of preclinical Alzheimer's disease: implications for prevention trials.** *Neuron* 2014;84:608–22 CrossRef Medline
6. Ossenkoppele R, Smith R, Mattsson-Carlgen N, et al. **Accuracy of tau positron emission tomography as a prognostic marker in preclinical and prodromal Alzheimer disease: a head-to-head comparison against amyloid positron emission tomography and magnetic resonance imaging.** *JAMA Neurol* 2021;78:961–71 CrossRef Medline
7. Judenhofer MS, Wehr HF, Newport DF, et al. **Simultaneous PET-MRI: a new approach for functional and morphological imaging.** *Nat Med* 2008;14:459–65 CrossRef Medline
8. Catana C, Drzezga A, Heiss W-D, et al. **PET/MRI for neurologic applications.** *J Nucl Med* 2012;53:1916–25 CrossRef Medline
9. Drzezga A, Barthel H, Minoshima S, et al. **Potential clinical applications of PET/MR imaging in neurodegenerative diseases.** *J Nucl Med* 2014;55:47S–55S CrossRef Medline
10. He KM, Xhand X, Ren S, et al. **Delving deep into rectifiers: surpassing human-level performance on ImageNet classification.** In: *Proceedings of the 2015 IEEE International Conference on Computer Vision (ICCV)*, December 7–13, 2015:1026–34. Santiago, Chile
11. Chen H, Zhang Y, Kalra MK, et al. **Low-dose CT with a residual encoder-decoder convolutional neural network (RED-CNN).** *IEEE Transactions on Medical Imaging* 2017;36:2524–35 CrossRef Medline
12. Shen D, Wu G, Suk HI. **Deep learning in medical image analysis.** *Annu Rev Biomed Eng* 2017;19:221–48 CrossRef Medline
13. Yu Y, Xie Y, Thamm T, et al. **Use of deep learning to predict final ischemic stroke lesions from initial magnetic resonance imaging.** *JAMA Netw Open* 2020;3:e200772 CrossRef Medline
14. Liu F, Jang H, Kijowski R, et al. **Deep learning MR imaging-based attenuation correction for PET/MR imaging.** *Radiology* 2018;286:676–84 CrossRef Medline
15. Torrado-Carvajal A, Vera-Olmos J, Izquierdo-Garcia D, et al. **Dixon-VIBE deep learning (DIVIDE) pseudo-CT synthesis for pelvis PET/MR attenuation correction.** *J Nucl Med* 2019;60:429–35 CrossRef Medline
16. Bland J, Mehranian A, Belzunce MA, et al. **MR-guided kernel EM reconstruction for reduced dose PET imaging.** *IEEE Trans Radiat Plasma Med Sci* 2018;2:235–43 CrossRef Medline
17. Chaudhari AS, Mittra E, Davidzon GA, et al. **Low-count whole-body PET with deep learning in a multicenter and externally validated study.** *NPJ Digit Med* 2021;4:127 CrossRef Medline
18. Hosch R, Weber M, Sraieb M, et al. **Artificial intelligence guided enhancement of digital PET: scans as fast as CT? *Eur J Nucl Med Mol Imaging* 2022;49:4503–15 CrossRef Medline**
19. Lei Y, Dong X, Wang T, et al. **Whole-body PET estimation from low count statistics using cycle-consistent generative adversarial networks.** *Phys Med Biol* 2019;64:215017 CrossRef Medline
20. Sanaat A, Arabi H, Mainta I, et al. **Projection-space implementation of deep learning-guided low-dose brain PET imaging improves performance over implementation in image-space.** *J Nucl Med* 2020;61:1388–96 CrossRef Medline
21. Xiang L, Qiao Y, Nie D, et al. **Deep auto-context convolutional neural networks for standard-dose PET image estimation from low-dose PET/MRI.** *Neurocomputing* 2017;267:406–16 CrossRef Medline
22. Chen KT, Gong E, de Carvalho Macruz FB, et al. **Ultra-low-dose <sup>18</sup>F-florbetaben amyloid PET imaging using deep learning with multi-contrast MRI inputs.** *Radiology* 2019;290:649–56 CrossRef Medline
23. Chen KT, Toueg TN, Koran ME, et al. **True ultra-low-dose amyloid PET/MRI enhanced with deep learning for clinical interpretation.** *Eur J Nucl Med Mol Imaging* 2021;48:2416–25 CrossRef Medline
24. Janelidze S, Mattsson N, Palmqvist S, et al. **Plasma P- $\tau$ 181 in Alzheimer's disease: relationship to other biomarkers, differential diagnosis, neuropathology and longitudinal progression to Alzheimer's dementia.** *Nat Med* 2020;26:379–86 CrossRef Medline
25. Palmqvist S, Janelidze S, Quiroz YT, et al. **Discriminative accuracy of plasma phospho-tau217 for Alzheimer disease vs other neurodegenerative disorders.** *JAMA* 2020;324:772–81 CrossRef Medline
26. Ossenkoppele R, Rabinovici GD, Smith R, et al. **Discriminative accuracy of [<sup>18</sup>F] flortaucipir positron emission tomography for Alzheimer disease vs other neurodegenerative disorders.** *JAMA* 2018;320:1151–62 CrossRef Medline
27. Chen KT, Adeyeri O, Toueg TN, et al. **Generalizing ultra-low-dose PET/MRI networks across radiotracers: from amyloid to tau.** In: *Proceedings of the Annual Meeting and Exhibition of the International Society for Magnetic Resonance in Medicine*, May 15–20, 2021; Virtual
28. Goodfellow IJ, Pouget-Abadie J, Mirza M, et al. **Generative adversarial nets.** In: *Proceedings of the 27th International Conference on Neural Information Processing Systems*, Montreal, Canada. December 8–13, 2014:2672–80
29. Braak H, Del Tredici K. **The preclinical phase of the pathological process underlying sporadic Alzheimer's disease.** *Brain* 2015;138:2814–33 CrossRef Medline
30. Hanseeuw BJ, Betensky RA, Jacobs HIL, et al. **Association of amyloid and tau with cognition in preclinical Alzheimer disease: a longitudinal study.** *JAMA Neurol* 2019;76:915–24 CrossRef Medline
31. Trelle AN, Carr VA, Wilson EN, et al. **Association of CSF biomarkers with hippocampal-dependent memory in preclinical Alzheimer disease.** *Neurology* 2021;96:e1470–81 CrossRef Medline
32. Jenkinson M, Beckmann CF, Behrens TE, et al. **FSL.** *Neuroimage* 2012;62:782–90 CrossRef Medline
33. Ronneberger O, Fischer P, Brox T. **U-Net: convolutional networks for biomedical image segmentation.** In: *Proceedings of Medical Image Computing and Computer-Assisted Intervention, MICCAI 2015*, Munich, Germany. October 5–9, 2015
34. Wang Z, Bovik AC, Sheikh HR, et al. **Image quality assessment: from error visibility to structural similarity.** *IEEE Trans Image Process* 2004;13:600–12 CrossRef Medline
35. Gwet KL. **Computing inter-rater reliability and its variance in the presence of high agreement.** *Br J Math Stat Psychol* 2008;61:29–48 CrossRef Medline
36. Desikan RS, Ségonne F, Fischl B, et al. **An automated labeling system for subdividing the human cerebral cortex on MRI scans into gyral based regions of interest.** *Neuroimage* 2006;31:968–80 CrossRef Medline
37. Guo J, Gong E, Fan AP, et al. **Predicting (15)O-Water PET cerebral blood flow maps from multi-contrast MRI using a deep convolutional neural network with evaluation of training cohort bias.** *J Cereb Blood Flow Metab* 2020;40:2240–53 CrossRef Medline
38. Ozlen H, Pichet Binette A, Köbe T, et al; Alzheimer's Disease Neuroimaging Initiative, the Harvard Aging Brain Study, the Presymptomatic Evaluation of Experimental or Novel Treatments for Alzheimer Disease Research Group. **Spatial extent of amyloid-beta levels and associations with tau-PET and cognition.** *JAMA Neurol* 2022;79:1025–35 CrossRef Medline

# Deep Learning Segmentation of the Nucleus Basalis of Meynert on 3T MRI

D.J. Doss, G.W. Johnson, S. Narasimhan, J.S. Shless, J.W. Jiang, H.F.J. González, D.L. Paulo, A. Lucas, K.A. Davis, C. Chang, V.L. Morgan, C. Constantinidis, B.M. Dawant, and D.J. Englot



## ABSTRACT

**BACKGROUND AND PURPOSE:** The nucleus basalis of Meynert is a key subcortical structure that is important in arousal and cognition and has been explored as a deep brain stimulation target but is difficult to study due to its small size, variability among patients, and lack of contrast on 3T MR imaging. Thus, our goal was to establish and evaluate a deep learning network for automatic, accurate, and patient-specific segmentations with 3T MR imaging.

**MATERIALS AND METHODS:** Patient-specific segmentations can be produced manually; however, the nucleus basalis of Meynert is difficult to accurately segment on 3T MR imaging, with 7T being preferred. Thus, paired 3T and 7T MR imaging data sets of 21 healthy subjects were obtained. A test data set of 6 subjects was completely withheld. The nucleus was expertly segmented on 7T, providing accurate labels for the paired 3T MR imaging. An external data set of 14 patients with temporal lobe epilepsy was used to test the model on brains with neurologic disorders. A 3D-Unet convolutional neural network was constructed, and a 5-fold cross-validation was performed.

**RESULTS:** The novel segmentation model demonstrated significantly improved Dice coefficients over the standard probabilistic atlas for both healthy subjects (mean, 0.68 [SD, 0.10] versus 0.45 [SD, 0.11],  $P = .002$ ,  $t$  test) and patients (0.64 [SD, 0.10] versus 0.37 [SD, 0.22],  $P < .001$ ). Additionally, the model demonstrated significantly decreased centroid distance in patients (1.18 [SD, 0.43] mm, 3.09 [SD, 2.56] mm,  $P = .007$ ).

**CONCLUSIONS:** We developed the first model, to our knowledge, for automatic and accurate patient-specific segmentation of the nucleus basalis of Meynert. This model may enable further study into the nucleus, impacting new treatments such as deep brain stimulation.

**ABBREVIATIONS:** DBS = deep brain stimulation; DnSeg = deep nuclei segmentation network; NBM = nucleus basalis of Meynert; TLE = temporal lobe epilepsy

The nucleus basalis of Meynert (NBM) is a basal forebrain nucleus and is one of the major sources of cholinergic signal in the brain.<sup>1,2</sup> It has been implicated as abnormal in several disorders with cognitive decline such as Parkinson disease dementia,

Alzheimer disease, and temporal lobe epilepsy (TLE).<sup>3,4</sup> These abnormal changes include prediction of cognitive impairment in Parkinson disease, neuronal loss and atrophy in Alzheimer disease, and abnormal functional connectivity in TLE.<sup>3-7</sup> Furthermore, there has recently been increased interest in studying the functional and structural network abnormalities involving NBM connections in these and other disease states.<sup>3,6,7</sup> Finally, several studies have started investigating neurostimulation of the NBM to improve cognitive outcomes in Alzheimer disease using deep brain stimulation (DBS).<sup>8,9</sup>

While the NBM is thought to be important in several disease states, study into it has been limited because it exhibits patient-

Received November 11, 2022; accepted after revision June 25, 2023.

From the Department of Biomedical Engineering (D.J.D., G.W.J., S.N., H.F.J.G., C. Chang, V.L.M., C. Constantinidis, D.J.E.), Institute of Imaging Science (D.J.D., G.W.J., S.N., J.S.S., J.W.J., H.F.J.G., C. Chang, V.L.M., B.M.D., D.J.E.), and Departments of Electrical and Computer Engineering (C. Chang, B.M.D., D.J.E.), Computer Science (C. Chang), and Neuroscience (C. Constantinidis), Vanderbilt University, Nashville, Tennessee; Vanderbilt Institute for Surgery and Engineering (D.J.D., G.W.J., S.N., H.F.J.G., C. Chang, V.L.M., B.M.D., D.J.E.), Nashville, Tennessee; Departments of Neurological Surgery (S.N., J.S.S., J.W.J., D.L.P., V.L.M., D.J.E.), Neurology (V.L.M.), Radiological Sciences (V.L.M., D.J.E.), and Ophthalmology and Visual Sciences (C. Constantinidis), Vanderbilt University Medical Center, Nashville, Tennessee; and Departments of Bioengineering (A.L.) and Neuroscience (K.A.D.), Center for Neuroengineering and Therapeutics (K.A.D.), and Department of Neurology (K.A.D.), University of Pennsylvania, Philadelphia, Pennsylvania.

This work was supported by the National Institutes of Health (grant Nos. T32GM007347, T32EB001628-17, T32EB021937, F31NS106735, F31NS120401, R01NS112252, R01NS108445, R01NS110130, and R01NS116504).

Please address correspondence to Derek J. Doss, Vanderbilt University, 1500 21st Ave South, VAV 4340, Nashville, TN 37212; e-mail: derekjdos@gmail.com; @DerekDoss

Indicates open access to non-subscribers at www.ajnr.org

Indicates article with online supplemental data.

<http://dx.doi.org/10.3174/ajnr.A7950>

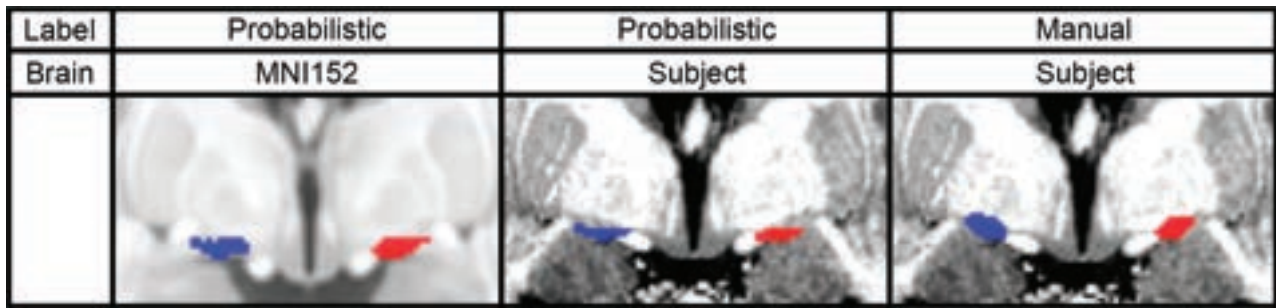


**FIG 1.** Comparison of the probabilistic and manual labels on a similar coronal section of the Montreal Neurological Institute 152 atlas space brain and a subject's 7T brain. The left NBM is shown in blue, and the right NBM is shown in red.

#### Data set demographics<sup>a</sup>

Healthy subjects, Vanderbilt	
No.	11
Sex	3 Female
Age (yr)	38.3 (SD, 10.9)
Healthy subjects, Amsterdam	
No.	10
Sex	8 Female
Age (yr)	25.9 (SD, 5.8)
Patients with TLE	
No.	14
Age (yr)	30.0 (SD, 7.5)
Sex	7 Female
Disease duration (yr)	11.0 (SD, 11.7)
Number lesional	7

<sup>a</sup>Demographics of both the healthy subject data set and the TLE data set. Data are counts or mean (SD).

specific changes and no accurate patient-specific segmentation exists.<sup>10</sup> Patient-specific changes may be accounted for with manual segmentation, but the NBM is difficult to visualize on commonly available 3T T1-weighted MR imaging. More accurate manual segmentations can be performed on high-resolution 7T MR imaging; however, these high-resolution scans are rare (Online Supplemental Data). To overcome this limitation, previous groups have developed a probabilistic atlas of the NBM, derived from postmortem histologic staining of 10 healthy subject's brains.<sup>11</sup> The segmented histologic slices were then aligned to the Montreal Neurological Institute 152 atlas space to provide a probabilistic atlas of the NBM. The probabilistic atlas has gained popularity and is the most used atlas of the NBM.<sup>12</sup> While the probabilistic atlas provides an accurate segmentation for most cases, it does not capture patient-specific anatomic variability (Fig 1). Considering that the anatomy of the NBM varies among patients and changes throughout the disease states of interest, this limitation substantially impacts nearly all studies of the NBM.<sup>3-7,13-16</sup> Furthermore, recent studies have demonstrated that the probabilistic atlas is unable to capture the patient-specific differences, and atlas innovation is needed to address this limitation.<sup>17</sup>

Deep learning methods can learn subtle features for medical imaging segmentation that are beyond human perception.<sup>18</sup> Thus, to expand study of the NBM, we propose a novel deep learning—based method for patient-specific NBM segmentation using only 3T MR imaging.

## MATERIALS AND METHODS

### Data Set

We trained the network using only 3T MR imaging and both 7T and 3T MR imaging scans of the same healthy subjects. Data from a total of 21 healthy subjects were available from 2 separate institutions (Vanderbilt University and the University of Amsterdam).<sup>19-21</sup> A total of 6 healthy subjects from this data set were completely withheld as a test data set.

An additional external data set of 14 paired 3T and 7T MR images of patients with TLE was obtained. Half of the patients had lesional changes on MR imaging, and the other half had nonlesional changes. This data set was withheld from the training and validation process and was used only for testing of the deep learning network on brains with neurologic disorders. The demographics of both data sets can be seen in the Table.

### Manual Segmentation

Although the anatomic borders of the NBM cannot be easily discerned on 3T MR imaging, 7T MR imaging enables enhanced contrast in the NBM. According to the landmarks described in the literature, the anatomic borders of the NBM were identified for manual segmentation.<sup>1,22</sup> The left and right NBMs were segmented for each subject and patient using our in-house CRANial Vault Explorer (CRAVE) software (<https://www.sciencedirect.com/science/article/abs/pii/S1361841510001015>).<sup>23</sup> The segmentations of the NBM were completed by 2 authors and were verified by 2 neurological surgeons.

### Data Preprocessing

The 7T and 3T paired images were converted to Right Anterior Superior (RAS) orientation, were skull-stripped, and were rigidly registered to the same patient's 7T scan with SPM8 (<https://www.fil.ion.ucl.ac.uk/spm/software/spm8/>).<sup>24,25</sup> The registration accuracy was then individually verified for every patient (Fig 2).

### Data Augmentation

To enhance model generalization and promote learning of anatomic variability, we augmented the healthy subject data set from 21 to 210 samples. Augmentations were performed with torchIO (<https://torchio.readthedocs.io/>) and included random rigid affine transformations, random elastic transformations, and random bias field additions, examples of which can be seen in the Online Supplemental Data.<sup>26</sup>

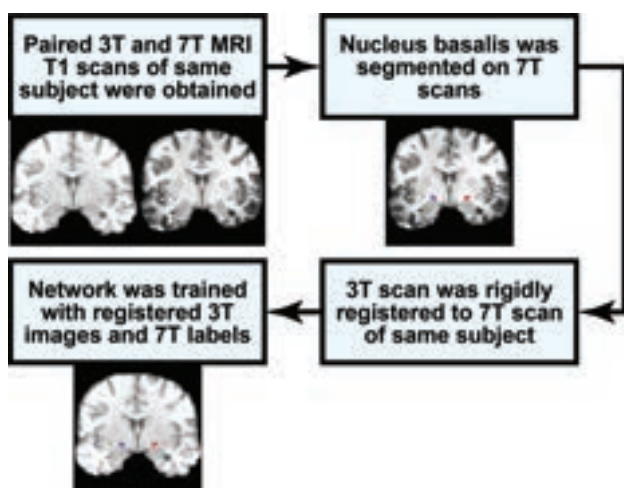


**FIG 2.** Flow chart describing how the 7T NBM segmentation is used for training the network to segment the NBM on 3T MR imaging.

### Volume Reduction

Considering the large amount of video RAM required to train a deep learning network using the whole brain, the size of the images was reduced for ease of training. Given that the mamillary bodies are the posterior anatomic borders of the NBM, we used the patient-specific segmentation package implemented in FreeSurfer ScLimbic ([surfer.nmr.mgh.harvard.edu/fswiki/ScLimbic](http://surfer.nmr.mgh.harvard.edu/fswiki/ScLimbic)) to segment the mamillary bodies.<sup>15</sup> The mamillary bodies were used as the center of a  $64 \times 64 \times 64$  mm region, which includes the entire NBM in all cases. The final network performs this step automatically, allowing for an end-to-end network that requires only 3T MR imaging for accurate segmentation.

### Convolutional Neural Network

The modified 3D U-Net architecture for biomedical image segmentation was used.<sup>27</sup> A complete visualization of the architecture can be seen in the Online Supplemental Data. The network was trained using the soft Dice loss function.<sup>28</sup>

The data were divided into train, test, and validation sets. The data sets were split on the subject level. The train data set consisted of 12 subjects (120 scans), the validation data set consisted of 3 subjects (30 scans), and the test data set consisted of 6 subjects (60 scans). The test data set was completely held out from model selection and only used for the evaluation after the final model was selected.

A 5-fold cross-validation was used on the train and validation data sets. The average Dice performance from each fold on the validation data set was used as the performance measure for model selection. Hyperparameter tuning during model selection was performed.<sup>29</sup> The final network comprised an ensemble of 5 trained and optimized models.

### Evaluation Metrics

Evaluation of the deep nuclei segmentation network (DnSeg) encompassed methods to assess volumetric overlap of the NBM and localization of the NBM. The Dice coefficient, mean surface distance, and centroid distance were calculated between the

predicted and ground truth segmentation, defined as the overlap of both rater segmentations.<sup>13,14,30</sup>

The performance of DnSeg was compared against that of the probabilistic atlas. The probabilistic atlas was thresholded such that all voxels with a  $>50\%$  probability of being the NBM were assigned as NBM. The probabilistic atlas was registered from Montreal Neurological Institute 152 atlas space to patient-specific space using SPM8 (<https://www.fil.ion.ucl.ac.uk/spm/software/spm8/>). The same metrics were then computed on the probabilistic atlas segmentation of the NBM.

## RESULTS

All results were computed in the patient's 3T MR imaging space on nonaugmented data with 1-mm isotropic slices. The results were all computed on the test data sets of 6 healthy subjects, which were held out from the training and validation of the DnSeg. Results were also computed on held-out external data sets of 14 subjects with diagnosed TLE that were not used in development of the DnSeg.

### Dice Coefficient

The Dice coefficient was computed between the predicted and ground truth–segmented NBM.<sup>30</sup> The Dice coefficient is known to underestimate the performance of small, complex structures, for example, segmentation studies of other small structures such as the ventral tegmental area and the interposed nuclei report Dice coefficients of 0.52 and 0.69, respectively.<sup>13-16,31</sup> The Dice coefficient of the NBM computed from the DnSeg (mean, 0.68 [SD, 0.10]) significantly outperformed that of the probabilistic atlas (0.45 [SD, 0.11]) in the completely withheld data sets of 6 healthy subjects (paired *t* test,  $P = .001$ ), as seen in Fig 3B. Additionally, the Dice coefficient was significantly increased in DnSeg (mean, 0.64 [SD, 0.10]) compared with the probabilistic atlas Dice coefficient (mean, 0.37 [SD, 0.22]) for the TLE data set (paired *t* test,  $P < .001$ ). The probabilistic atlas demonstrated substantial variability in the Dice coefficient for the TLE data set, likely due to anatomic changes that have been noted in the NBM for TLE.

### Mean Surface Distance

The mean surface distance between the predicted surface and the ground truth surface of the NBM segmentation was calculated for the test data set and the TLE data set (Fig 3C). For healthy subjects, DnSeg demonstrated significantly lower mean surface distance (mean, 0.65 [SD, 0.24] mm) computed with the probabilistic atlas (mean, 1.18 [SD, 0.35] mm) in the completely withheld data set of 6 healthy subjects (paired *t* test,  $P = .002$ ). Furthermore, the mean surface distance was significantly lower with DnSeg (0.69 [SD, 0.15] mm) compared with the probabilistic atlas (mean, 1.91 [SD, 2.03] mm) in the TLE data set (paired *t* test  $P = .027$ ). The variability of the probabilistic atlas on the TLE data set was far more exaggerated than that of the healthy subject data set, as seen with the 95% confidence intervals of 1.2 and 0.2 mm, respectively.

### Centroid Distance

The centroid distance represents the error in localization of the NBM that can occur due to patient-specific anatomic variability.

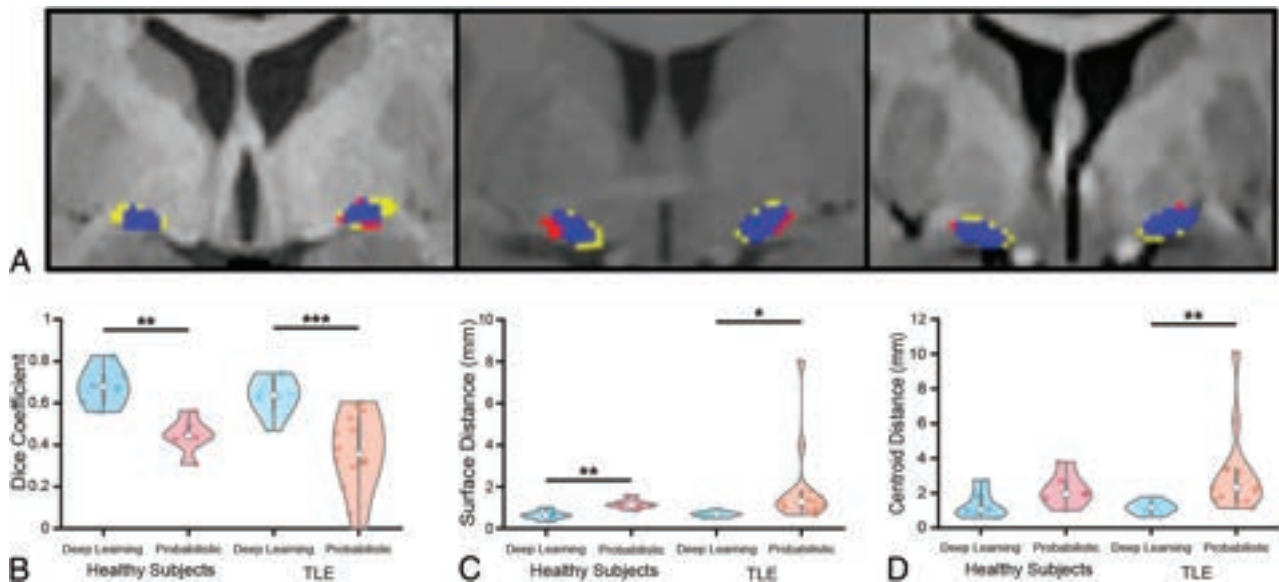


**FIG 3.** Example of favorable (A, right), average (A, middle), and poor (A, left) performance. Blue is the correct prediction of NBM, red is the over-predicted NBM (false-positive), and yellow is the ground truth label that was not predicted (false-negative). The Dice coefficient of the favorable example (right) was 0.82, the Dice coefficient of the average example (middle) was 0.63, and the Dice coefficient of the poor example (left) was 0.55. B, The Dice coefficient. C, The mean surface distance. D, The centroid distance of DnSeg versus the probabilistic atlas for both healthy subjects and patients with TLE. The healthy subjects included the nonaugmented held-out test data set ( $n = 6$ ). The patients with TLE were also not augmented and were held out until final analysis ( $n = 14$ ). Paired  $t$  test: single asterisk indicates  $P < .05$ ; double asterisks,  $P < .01$ ; triple asterisks,  $P < .001$ .

It is most relevant for DBS applications because it could contribute to a targeting error. The centroid distance performance of DnSeg (mean, 1.35 [SD, 0.86] mm) was not significantly different from the probabilistic atlas (mean, 2.19 [SD, 1.36] mm) in the completely withheld data sets of 6 healthy subjects (paired  $t$  test,  $P = .014$ ), as can be seen in Fig 3D. However, the centroid distance of DnSeg (mean, 1.18 [SD, 0.43] mm) was significantly lower than that of the probabilistic atlas (mean, 3.09 [SD, 2.56] mm) in the TLE data set (paired  $t$  test,  $P = .007$ ).

### Qualitative Comparison

Because localization and overlap are difficult to quantify for small structures, the results were also analyzed qualitatively. An evaluation of NBM prediction of DnSeg compared with the ground truth manual segmentation was completed qualitatively by visual inspection (Fig 3A). The poor-performance example demonstrates that even the poor-performing examples perform relatively well. Additionally, it is seen that the NBM shape differs slightly from patient to patient and that DnSeg successfully accounts for heterogeneous patient anatomy (Online Supplemental Data).

## DISCUSSION

The purpose of this work was to enable study of the NBM by accounting for patient-specific differences. DnSeg may have widespread impact across several diseases, perhaps enabling new treatment modalities targeting the NBM.

### DnSeg Can Distinguish Subject-Specific Anatomic Differences

The NBM has anatomic variability among healthy subjects and has been shown to change in size in patients with Parkinson

disease, Alzheimer disease, and TLE.<sup>32–40</sup> This variability presents a substantial challenge in studying the NBM and a barrier for possible treatment innovations such as DBS. Manual segmentation to capture these differences would be preferable; however, the NBM cannot be accurately visualized on 3T MR imaging. Thus, current research is limited by the non-patient-specific atlas that does not capture variability in the NBM, as seen by the wide 95% confidence intervals for patients with TLE (Fig 3). DnSeg was able to capture patient-specific differences in the NBM and accurately segment it using only 3T T1-weighted MR imaging. The results of DnSeg in patients with TLE were comparable with those of healthy subjects, indicating that it can accurately segment the NBM despite anatomic changes (Fig 3B–D), demonstrating that DnSeg can capture pathologic changes in the NBM in at least 1 disease state.

### DBS Targeting

DBS targeting for the NBM has been explored in several studies with mixed results.<sup>8,9</sup> One possible factor in these studies is DBS targeting accuracy. In this investigation, DnSeg localized the NBM with far more accuracy than the probabilistic atlas, which can have a substantial impact on targeting (Fig 3). The impact of this distance can be seen in Fig 4, where an electrode planned with DnSeg seems to target the NBM accurately, while an electrode planned with the center of the 50% thresholded probabilistic atlas targets the border of the true NBM.

In addition to this practical application, DnSeg also has 10× faster run-time than standard registration methods required for applying a Montreal Neurological Institute 152 atlas space to patient-specific space. With a modern CPU, it takes approximately 1 minute per scan if skull-stripping is not required and

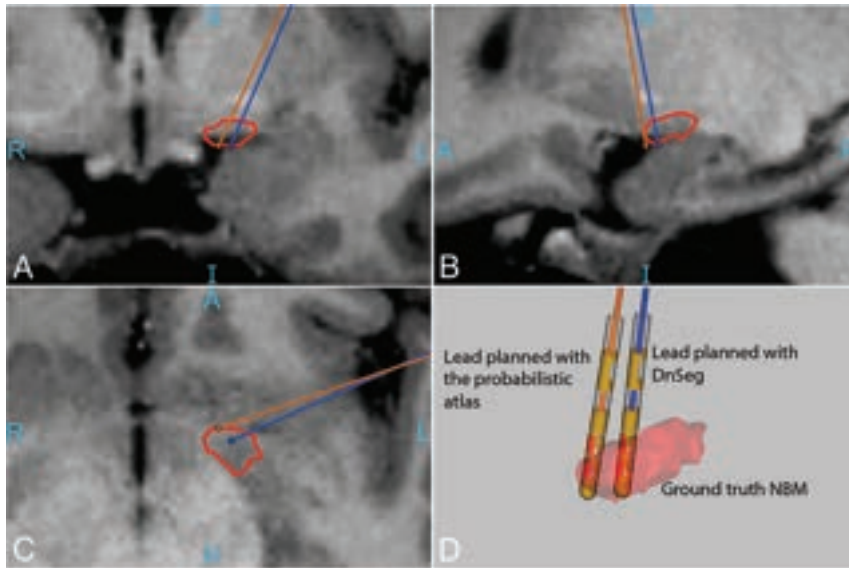


**FIG 4.** Increased accuracy of NBM electrode targeting with DnSeg. The orange electrode was placed in the center of the NBM segmentation generated by the probabilistic atlas. The blue electrode was placed in the center of the segmentation generated by DnSeg. *D*, Both electrode positions compared with the ground truth segmentation mesh. The ground truth NBM (manually segmented on 7T MR imaging) is shown in red. The outline of the ground truth NBM as well as the lead trajectories can be seen in *A*, *B*, and *C*. The sample DBS planning for this figure was generated using CRAnial Vault Explorer.<sup>23</sup>

approximately 2 minutes if skull stripping is required. The pipeline does not require the patient data to be registered to any standard space; thus, it is much faster than other methods that require a registration step.

### Limitations

Despite these benefits of the deep learning pipeline, there are some limitations. Most notably, the expert segmentations could not be verified with a postmortem histologic analysis. While the segmentations were verified by 2 neurological surgeons, a histologic analysis would be ideal. Furthermore, the current analysis validates only DnSeg in one disease state. The NBM is both of interest and has pathologic changes in several disease states. Thus, it would be preferred to validate DnSeg in other disease states. However, paired 7T and 3T MR imaging scans of the same patients needed to achieve this goal are rare. Furthermore, DnSeg is limited by the small sample size used for training. Although this limitation is common among studies of paired 3T and 7T MR imaging, it has the potential to limit the generalizability of DnSeg. Aggressive augmentation was used to attenuate this limitation and increase generalizability.

### CONCLUSIONS

In this work, we have presented an accurate, patient-specific method of segmenting the NBM using only 3T T1-weighted MR imaging. The NBM has been implicated in Alzheimer disease, Parkinson disease dementia, and TLE.<sup>3,6,7</sup> It has been shown to change in neuronal density and gray matter volume across age and disease states.<sup>32-40</sup> With the use of an expertly segmented NBM and aggressive data augmentation, we have trained a deep learning network to capture anatomic differences when segmenting the

NBM. We have presented evidence that DnSeg is a powerful and accurate NBM segmentation model.

Methodologically, this work represents an innovative approach to the segmentation of regions with little contrast enhancement. The NBM represents a small region of the brain with little contrast on commonly used 3T MR imaging but with high importance to several disease states. Paired 3T and 7T MR imaging of the same subjects is a useful approach to providing accurate labels for training a deep learning network to segment structures that cannot be accurately visualized on 3T imaging. However, this approach is intrinsically limited by the rarity of paired 3T-7T data sets.

DnSeg, therefore, opens the possibility of further study of the NBM. The NBM has long been considered a region of key interest, but study of the NBM in vivo has been difficult, in part because of the lack of an adaptive, patient-specific atlas. The presented model is available (<https://github.com/DerekDoss/DnSeg>) and may greatly assist in novel studies of the NBM.

DerekDoss/DnSeg) and may greatly assist in novel studies of the NBM.

### ACKNOWLEDGMENTS

The authors would like to thank Laurie Cutting, PhD, for providing paired 7T-3T MR imaging scans of healthy subjects. The authors would also like to thank William (Bill) Rodriguez, MED for his assistance with CRAVE and data set curation. A preprint of this article was originally released on bioRxiv.

Disclosure forms provided by the authors are available with the full text and PDF of this article at [www.ajnr.org](http://www.ajnr.org).

### REFERENCES

1. Liu AK, Chang RC, Pearce RK, et al. **Nucleus basalis of Meynert revisited: anatomy, history and differential involvement in Alzheimer's and Parkinson's disease.** *Acta Neuropathol* 2015;129:527-40 CrossRef Medline
2. Mesulam MM, Mufson EJ, Levey AI, et al. **Cholinergic innervation of cortex by the basal forebrain: cytochemistry and cortical connections of the septal area, diagonal band nuclei, nucleus basalis (substantia innominata), and hypothalamus in the rhesus monkey.** *J Comp Neurol* 1983;214:170-97 CrossRef Medline
3. Gonzalez HFJ, Narasimhan S, Johnson GW, et al. **Role of the nucleus basalis as a key network node in temporal lobe epilepsy.** *Neurology* 2021;96:e1334-46 CrossRef Medline
4. Schulz J, Pagano G, Fernández Bonfante JA, et al. **Nucleus basalis of Meynert degeneration precedes and predicts cognitive impairment in Parkinson's disease.** *Brain* 2018;141:1501-16 CrossRef Medline
5. Whitehouse PJ, Price DL, Clark AW, et al. **Alzheimer disease: evidence for selective loss of cholinergic neurons in the nucleus basalis.** *Ann Neurol* 1981;10:122-26 CrossRef Medline

6. Schumacher J, Thomas AJ, Peraza LR, et al. **Functional connectivity of the nucleus basalis of Meynert in Lewy body dementia and Alzheimer's disease.** *Int Psychogeriatr* 2021;33:89–94 CrossRef Medline
7. Oswal A, Gratwicke J, Akram H, et al. **Cortical connectivity of the nucleus basalis of Meynert in Parkinson's disease and Lewy body dementias.** *Brain* 2021;144:781–88 CrossRef Medline
8. Chen YS, Shu K, Kang HC. **Deep brain stimulation in Alzheimer's disease: targeting the nucleus basalis of Meynert.** *J Alzheimers Dis* 2021;80:53–70 CrossRef Medline
9. Kuhn J, Hardenacke K, Lenartz D, et al. **Deep brain stimulation of the nucleus basalis of Meynert in Alzheimer's dementia.** *Mol Psychiatry* 2015;20:353–60 CrossRef Medline
10. Wilson H, de Natale ER, Politis M. **Nucleus basalis of Meynert degeneration predicts cognitive impairment in Parkinson's disease.** *Handb Clin Neurol* 2021;179:189–205 CrossRef Medline
11. Zaborszky L, Hoemke L, Mohlberg H, et al. **Stereotaxic probabilistic maps of the magnocellular cell groups in human basal forebrain.** *Neuroimage* 2008;42:1127–41 CrossRef Medline
12. Eickhoff SB, Stephan KE, Mohlberg H, et al. **A new SPM toolbox for combining probabilistic cytoarchitectonic maps and functional imaging data.** *Neuroimage* 2005;25:1325–35 CrossRef Medline
13. Kim J, Duchin Y, Shamir RR, et al. **Automatic localization of the subthalamic nucleus on patient-specific clinical MRI by incorporating 7 T MRI and machine learning: application in deep brain stimulation.** *Hum Brain Mapp* 2019;40:679–98 CrossRef Medline
14. Kim J, Patriat R, Kaplan J, et al. **Deep cerebellar nuclei segmentation via semi-supervised deep context-aware learning from 7T diffusion MRI.** *IEEE Access* 2020;8:101550–68 CrossRef Medline
15. Greve DN, Billot B, Cordero D, et al. **A deep learning toolbox for automatic segmentation of subcortical limbic structures from MRI images.** *Neuroimage* 2021;244:118610 CrossRef Medline
16. Billot B, Bocchetta M, Todd E, et al. **Automated segmentation of the hypothalamus and associated subunits in brain MRI.** *Neuroimage* 2020;223:117287 CrossRef Medline
17. Wang Y, Zhan M, Roebroek A, et al. **Inconsistencies in atlas-based volumetric measures of the human nucleus basalis of Meynert: a need for high-resolution alternatives.** *Neuroimage* 2022;259:119421 CrossRef
18. Niazi MK, Parwani AV, Gurcan MN. **Digital pathology and artificial intelligence.** *Lancet Oncol* 2019;20:e253–61 CrossRef Medline
19. Isaacs BR, Mulder MJ, Groot JM, et al. **3 versus 7 Tesla magnetic resonance imaging for parcellations of subcortical brain structures in clinical settings.** *PLoS One* 2020;15:e0236208 CrossRef Medline
20. Liu Y, D'Haese PF, Newton AT, et al. **Generation of human thalamus atlases from 7T data and application to intrathalamic nuclei segmentation in clinical 3T T1-weighted images.** *Magn Reson Imaging* 2020;65:114–28 CrossRef Medline
21. Ramadass K, Rheault F, Cai LY, et al. **Ultra-high-resolution mapping of cortical layers 3T-guided 7T MRI.** *Proc SPIE Int Soc Opt Eng* 2022;12032:120321G CrossRef Medline
22. Jethwa K, Aphihatthanasumet K, Mougins O, et al. **Phase enhanced PSIR T1-weighted imaging improves contrast resolution of the nucleus basalis of Meynert at 7T: a preliminary study.** *Magn Reson Imaging* 2019;61:296–99 CrossRef Medline
23. D'Haese PF, Pallavaram S, Li R, et al. **CranialVault and its CRAVE tools: a clinical computer assistance system for deep brain stimulation (DBS) therapy.** *Med Image Anal* 2012;16:744–53 CrossRef Medline
24. Brett M, Markiewicz CJ, Hanke M, et al. **nipy/nibabel: 4.0.0rc0.** 2022/6/2022 CrossRef
25. Iglesias JE, Liu CY, Thompson PM, et al. **Robust brain extraction across datasets and comparison with publicly available methods.** *IEEE Trans Med Imaging* 2011;30:1617–34 CrossRef Medline
26. Pérez-García F, Sparks R, Ourselin S. **TorchIO: a Python library for efficient loading, preprocessing, augmentation and patch-based sampling of medical images in deep learning.** *Comput Methods Programs Biomed* 2021;208:106236 CrossRef Medline
27. Ronneberger O, Fischer P, Brox T. **U-net: Convolutional networks for biomedical image segmentation.** In: Navab N, Hornegger J, Wells WM, et al, eds. *Medical Image Computing and Computer-Assisted Intervention–MICCAI 2015.* Springer; 2015: 234–41
28. Taha AA, Hanbury A. **Metrics for evaluating 3D medical image segmentation: analysis, selection, and tool.** *BMC Med Imaging* 2015;15:29 CrossRef Medline
29. Bergstra J, Yamins D, Cox D. **Making a science of model search: hyperparameter optimization in hundreds of dimensions for vision architectures.** *Proceedings of the 30th International Conference on Machine Learning.* 2013. <https://proceedings.mlr.press/v28/bergstra13.html>. Accessed November 11, 2022
30. Dice LR. **Measures of the amount of ecologic association between species.** *Ecology* 1945;26:297–302 CrossRef
31. Trutti AC, Fontanesi L, Mulder MJ, et al. **A probabilistic atlas of the human ventral tegmental area (VTA) based on 7 Tesla MRI data.** *Brain Struct Funct* 2021;226:1155–67 CrossRef Medline
32. Cantero JL, Zaborszky L, Atienza M. **Volume loss of the nucleus basalis of Meynert is associated with atrophy of innervated regions in mild cognitive impairment.** *Cereb Cortex* 2017;27:3881–89 CrossRef Medline
33. Grothe M, Heinsen H, Teipel SJ. **Atrophy of the cholinergic basal forebrain over the adult age range and in early stages of Alzheimer's disease.** *Biol Psychiatry* 2012;71:805–13 CrossRef Medline
34. Kilimann I, Grothe M, Heinsen H, et al. **Subregional basal forebrain atrophy in Alzheimer's disease: a multicenter study.** *J Alzheimers Dis* 2014;40:687–700 CrossRef Medline
35. Kim HJ, Lee JE, Shin SJ, et al. **Analysis of the substantia innominata volume in patients with Parkinson's disease with dementia, dementia with Lewy bodies, and Alzheimer's disease.** *J Mov Disord* 2011;4:68–72 CrossRef Medline
36. Lammers F, Borchers F, Feinkohl I, et al; BioCog consortium. **Basal forebrain cholinergic system volume is associated with general cognitive ability in the elderly.** *Neuropsychologia* 2018;119:145–56 CrossRef Medline
37. Ray NJ, Bradburn S, Murgatroyd C, et al. **In vivo cholinergic basal forebrain atrophy predicts cognitive decline in de novo Parkinson's disease.** *Brain* 2018;141:165–76 CrossRef Medline
38. Rong S, Li Y, Li B, et al. **Meynert nucleus-related cortical thinning in Parkinson's disease with mild cognitive impairment.** *Quant Imaging Med Surg* 2021;11:1554–66 CrossRef Medline
39. Scheef L, Grothe MJ, Koppa A, et al. **Subregional volume reduction of the cholinergic forebrain in subjective cognitive decline (SCD).** *Neuroimage Clin* 2019;21:101612 CrossRef Medline
40. Wolf D, Grothe M, Fischer FU, et al. **Association of basal forebrain volumes and cognition in normal aging.** *Neuropsychologia* 2014;53:54–63 CrossRef Medline

# Longitudinal Changes in Cerebral Perfusion, Perivascular Space Volume, and Ventricular Volume in a Healthy Cohort Undergoing a Spaceflight Analog

J.B. Tidwell, J.A. Taylor, H.R. Collins, J.H. Chamberlin, G. Barisano, F. Sepehrband, M.D. Turner, G. Gauthier, E.R. Mulder, D.A. Gerlach, and D.R. Roberts



## ABSTRACT

**BACKGROUND AND PURPOSE:** A global decrease in brain perfusion has recently been reported during exposure to a ground-based spaceflight analog. Considering that CSF and glymphatic flow are hypothesized to be propelled by arterial pulsations, it is unknown whether a change in perfusion would impact these CSF compartments. The aim of the current study was to evaluate the relationship among changes in cerebral perfusion, ventricular volume, and perivascular space volume before, during, and after a spaceflight analog.

**MATERIALS AND METHODS:** Eleven healthy participants underwent 30 days of bed rest at 6° head-down tilt with 0.5% atmospheric CO<sub>2</sub> as a spaceflight analog. For each participant, 6 MR imaging brain scans, including perfusion and anatomic-weighted T1 sequences, were obtained before, during, and after the analog period. Global perfusion, ventricular volume, and perivascular space volume time courses were constructed and evaluated with repeated measures ANOVAs.

**RESULTS:** Global perfusion followed a divergent time trajectory from ventricular and perivascular space volume, with perfusion decreasing during the analog, whereas ventricular and perivascular space volume increased ( $P < .001$ ). These patterns subsequently reversed during the 2-week recovery period.

**CONCLUSIONS:** The patterns of change in brain physiology observed in healthy participants suggest a relationship between cerebral perfusion and CSF homeostasis. Further study is warranted to determine whether a causal relationship exists and whether similar neurophysiologic responses occur during spaceflight.

**ABBREVIATIONS:** BDC = baseline data collection; HDT = head-down tilt; ICP = intracranial pressure; PVS = perivascular spaces; R = recovery; VaPER = Visual Impairment Intracranial Pressure and Psychological :envihab Research

Spaceflight is associated with various environmental stressors including the absence of normal gravity, chronic exposure to altered atmospheric compositions, and reduced sensory input. Study of the body's physiologic responses to these challenges will advance future space exploration and may provide insight into normal function on Earth. Following spaceflight, brain MR imaging has revealed structural changes such as upward shift of the

brain,<sup>1,2</sup> narrowing of the vertex CSF spaces,<sup>3</sup> increased ventricular volume,<sup>3-6</sup> enlargement of perivascular spaces (PVS),<sup>7,8</sup> and redistribution of free water.<sup>9</sup>

Modeling the spaceflight environment on Earth is challenging. Space agencies have commonly used a 6° head-down tilt (HDT) bed rest as an earth-based analog to study the effects of microgravity on the body. By reversing the gravitational vector in the *z*-direction toward the head compared with toward the feet in the normal daily upright position, HDT simulates certain physiologic changes of spaceflight including the following: unloading of the lower body, altered sensory input, and cephalad fluid shifts.<sup>10,11</sup> However, many have noted shortcomings of HDT as a direct spaceflight analog.<sup>10,12</sup> In 2017, the National Aeronautics and Space Administration (NASA) and the German Space Agency performed a 30-day bed rest study, known as the Visual Impairment Intracranial Pressure and Psychological :envihab Research (VaPER) study, which improved on past bed rest protocols by exposing participants to elevated CO<sub>2</sub> levels to mimic the International Space Station conditions and enforcing a "strict" HDT position throughout the intervention.<sup>13</sup> In the multi-investigator VaPER bed rest

Received September 16, 2022; accepted after revision June 25, 2023.

From the Department of Radiology and Radiological Science (J.B.T., J.A.T., H.R.C., J.H.C., M.D.T., G.G., D.R.R.), Medical University of South Carolina; Charleston, South Carolina; Laboratory of Neuroimaging (F.S.), University of Southern California, Los Angeles, California; Department of Neurosurgery (G.B.), Stanford University, Stanford, California; and German Aerospace Center (DLR, Institute of Aerospace Medicine) (E.R.M., D.A.G.), Cologne, Germany.

This study was funded by the National Aeronautics and Space Administration (NASA), grant No. NNX13AJ92G.

Please address correspondence to Donna R. Roberts, MD, 96 Jonathan Lucas St, Department of Radiology, Medical University of South Carolina, Charleston, SC 29425; e-mail: robertdr@musc.edu; @BrainsOnMars

Indicates open access to non-subscribers at [www.ajnr.org](http://www.ajnr.org)

Indicates article with online supplemental data.

<http://dx.doi.org/10.3174/ajnr.A7949>

study, several researchers have documented alterations in brain function and behavioral performance.<sup>14-17</sup> Of relevance to the current study, Roberts et al<sup>16</sup> documented a mean decrease in global relative brain perfusion during the bed rest period.

However, the relationship between reduced brain perfusion and other physiologic variables such as ventricular volume and PVS has not been examined in participants in VaPER. Previous work has shown that both parameters are sensitive to spaceflight<sup>3,5,7,8</sup> and additionally, that PVS has evidence of links to decreased cerebral perfusion.<sup>18,19</sup> Therefore, the purpose of this study was to expand on previous findings by examining concurrent changes in perfusion, ventricular volume, and PVS during HDT and recovery. We hypothesized that decreased perfusion would be accompanied by an increase in ventricular and PVS volumes, like that seen in astronauts. Understanding changes in cerebral physiology that occur in response to the unique physiologic stressor of altered gravity is vital for ensuring optimal performance and safety for continued space exploration, while also providing insight to better understand fundamental cerebral structure and function in patients on Earth.

## MATERIALS AND METHODS

### Participants

Eleven healthy participants (6 men, 5 women; median age, 33 years; median absolute deviation = 6) participated in the VaPER study conducted in Cologne, Germany, at the :envihab facility of the German Aerospace Center (Deutsches Zentrum für Luft-und Raumfahrt). Participants provided written informed consent, and the study was approved by the ethics commission of the local medical association (Ärzttekammer Nordrhein) and institutional review boards at NASA and the Medical University of South Carolina. All participants underwent routine health screening as previously reported, and all were nonsmokers for at least 6 months before the start of the study.<sup>14</sup>

### Study Protocol

A detailed protocol of the multi-investigator study has been described previously.<sup>13,16,17</sup> Briefly, participants began their stay at the :envihab facility 14 days before the bed rest portion of the study for baseline data collection (BDC), while remaining ambulatory under normal atmospheric conditions. Next, they underwent 30 days of 6° HDT bed rest in a 0.5% CO<sub>2</sub> environment (HDT + CO<sub>2</sub>). Participants maintained the HDT position at all times, including while eating, and were continually monitored via video to ensure compliance. Finally, they recovered (R) in the facility for 14 days postbed rest, returning to normal atmospheric and ambulatory conditions. MR imaging was performed at 6 time points: 13 (BDC-13) and 7 (BDC-7) days before bed rest, on days 7 (HDT7) and 29 (HDT29) during bed rest, and 5 (R + 5) and 12 (R + 12) days after bed rest during recovery. Throughout the study, participants were given standardized meals to maintain body weight and standardized daily water consumption levels based on their weight.<sup>20</sup> Participants were not allowed to have caffeinated beverages.<sup>20</sup> For scans during the analog period, participants were placed on a foam wedge on the MR imaging table to strictly maintain the HDT position and supplied CO<sub>2</sub> at 0.5% via a mask to maintain the same CO<sub>2</sub> exposure throughout the

MR imaging examinations. Following the precedent of prior reports, BDC-13 was considered an acclimation time point, and BDC-7 was considered the pre-bed rest time point.<sup>14,15,17</sup>

### MR Imaging Protocol

MR imaging was performed at 3T (Biograph mMR, software, Version VE11P; Siemens). The protocol included a 3D T1-weighted gradient-echo pulse sequence for anatomy (192 slices, 0.94 × 0.94 × 0.90 mm, FOV = 270 × 270 mm, TR = 1.9 seconds, TE = 2.49 ms, flip angle = 9°) and pulsed ASL using 3D gradient/spin-echo sequences with background suppression, flow-sensitive alternating inversion recovery (FAIR) labeling, and quantitative imaging of perfusion with a single subtraction with thin-section T1 periodic saturation (Q<sub>2</sub>-TIPS) bolus saturation (40 slices, 1.5 × 1.5 × 3 mm voxel resolution, FOV = 192 × 192, TR = 4600 ms, TE = 16.38 ms, flip angle = 180°). Four control-label pairs were acquired with a 700-ms pulse duration and a 1990-ms postlabeling delay. This sequence, which was the only ASL perfusion sequence available on the :envihab MR scanner, did not include calibration imaging needed for CBF quantification. Thus, perfusion-weighted maps were globally scaled with an arbitrary value of M<sub>0</sub> = 1000. Therefore, as previously, relative perfusion values are reported.<sup>16</sup>

### Image Processing

Detailed image-processing methods are included with Online Supplemental Data and briefly described here.

PWIs were created from ASL data using the FMRIB Software Library (FSL, Version 6.0.3; (<http://www.fmrib.ox.ac.uk/fsl>) as previously described.<sup>16</sup> Global whole-brain PWI values were extracted from the masked perfusion maps to statistically evaluate the mean perfusion of each subject. Segmentation and calculation of ventricular volumes were performed using FreeSurfer Reconnall (Version 6.0.0; (<http://surfer.nmr.mgh.harvard.edu>) on T1-weighted structural brain images.<sup>21</sup> A sum of the lateral and third ventricle volumes was calculated and hereafter is referred to as our measure of ventricle volume. The fourth ventricle was omitted due to previous work showing that its volume was unchanged by spaceflight.<sup>5,6</sup> WM perivascular space (WM-PVS) segmentation was performed on the parcellations in native space previously obtained from FreeSurfer via an automated pipeline,<sup>22</sup> as in previous studies.<sup>22-24</sup> In this study, we focused solely on WM-PVS and not the basal ganglia PVS because the widespread orientation of WM-PVS aligned more closely with our interest in global perfusion.

### Statistical Analyses

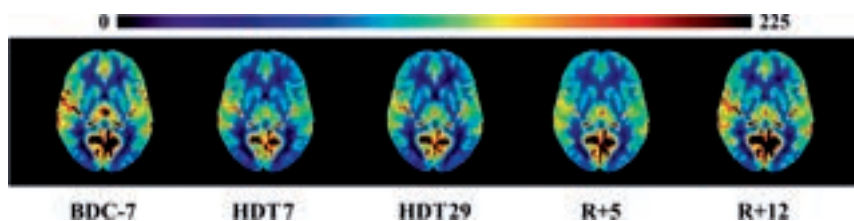
Age is described with median and median absolute deviation. Z-scores [ $z = (x - \text{mean}) / (SD)$ ] were calculated across time for each subject to account for individual differences and facilitate comparisons between metrics measured on different scales. A repeated measures ANOVA was performed on the subjects' z-scores for each time point for global relative perfusion, ventricular volume, and PVS volume. Partial eta-squared ( $\eta^2_p$ ) effect sizes were reported. We evaluated 5 time points: BDC-7, HDT7, HDT29, R + 5, and R + 12. Pair-wise comparisons were used to evaluate changes in brain metrics for the following a priori

**Table 1: Raw values for brain metrics at each time point<sup>a</sup>**

	BDC-7	HDT7	HDT29	R + 5	R + 12
Ventricular volume (mL)	16.32 (3.14)	17.08 (3.12)	17.39 (3.41)	16.86 (3.24)	16.24 (3.12)
Global perfusion (arbitrary units)	99.25 (15.4)	82.04 (17.53)	81.56 (8.75)	92.47 (15.41)	98.31 (20.36)
Perivascular space (mL)	1.78 (0.39)	2.12 (0.40)	2.14 (0.45)	2.14 (0.61)	1.88 (0.50)

<sup>a</sup>Data are mean and SD.**Table 2: Z-score scaled brain metrics at each time point<sup>a</sup>**

	BDC-7	HDT7	HDT29	R + 5	R + 12
Ventricular volume	-0.71 (0.73)	0.56 (0.30)	1.00 (0.34)	0.07 (0.55)	-0.92 (0.64)
Perfusion	0.72 (0.74)	-0.51 (0.96)	-0.75 (0.56)	0.08 (0.52)	0.45 (0.79)
PVS	-0.91 (0.41)	0.47 (0.77)	0.55 (0.57)	0.41 (0.88)	-0.52 (0.76)

<sup>a</sup>Data are mean and SD.**FIG 1.** Mean perfusion-weighted images using masks of all participants at each time point throughout the study. Yellow/red indicates greater perfusion on arbitrary scaled units.

comparisons of interest: from baseline to the end of bed rest (BDC-7 versus HDT29), from baseline to recovery (BDC-7 to R + 12), and between brain metrics at these times (BDC-7, HDT29, R + 12). Pair-wise effect sizes were calculated with the Hedges' *g* and were interpreted as very small ( $g=0.01$ ), small ( $g=0.20$ ), medium ( $g=0.50$ ), large ( $g=0.80$ ), very large ( $g=1.20$ ), and huge ( $g=2.00$ )<sup>25</sup> and were reported with 95% CIs. Because arterial pulsations are thought to propel CSF along the PVS, a Spearman rank correlation was performed between individual changes in perfusion and changes in PVS z-scores from baseline (BDC-7) to the end of bed rest (HDT29). Statistical significance was set at the  $\alpha < .05$  threshold, and analyses were conducted with R statistical and computing software, Version 4.1.2 (<http://www.r-project.org/>) and SPSS, Version 27 (IBM).

## RESULTS

Mean raw perfusion, ventricle volume, and PVS values are provided in Table 1 and participant examples are provided in Figures 1–3. A significant interaction revealed differing trajectories for perfusion, PVS volume, and ventricular volume as time progressed from before HDT + CO<sub>2</sub> to recovery, ( $F(8, 80) = 11.08; P < .001; \eta^2_p = 0.53$ ) (Table 2 and Fig 4).

### Baseline Differences among Perfusion, Ventricular Volume, and PVS

Relative to the mean level across time for each metric, at baseline, perfusion was greater than ventricular volume ( $P < .001; g = 1.49; 95\% \text{ CI}, 0.61\text{--}2.33$ ) and PVS volume ( $P < .001; g = 1.57; 95\% \text{ CI}, 0.67\text{--}2.43$ ), and PVS volume did not differ from ventricular volume ( $P = .440; g = 0.23; 95\% \text{ CI}, -0.35\text{--}0.81$ ).

### Brain Changes during HDT

By the end of the HDT + CO<sub>2</sub> period, there was an increase in ventricular volume ( $P < .001; g = 1.92; 95\% \text{ CI}, 0.90\text{--}2.92$ ; Fig 2) and PVS volume ( $P < .001; g = 2.64; 95\% \text{ CI}, 1.36\text{--}3.90$ ; Fig 3), whereas perfusion decreased ( $P < .001; g = 1.78; 95\% \text{ CI}, 0.81\text{--}2.72$ ; Fig 1) compared with baseline. A negative change-change correlation with perfusion and PVS was observed from BDC-7 to HDT29, indicating that a larger increase in PVS volume was associated with a larger decrease in perfusion ( $r_{s[9]} = -0.77, P = .008$ ).

### Brain Recovery from HDT

The divergent trajectories of brain metrics continued during recovery as ventricular volume ( $P < .001; g = 2.67; 95\% \text{ CI}, 1.38\text{--}3.95$ ) and PVS volume ( $P = .012; g = 0.89; 95\% \text{ CI}, 0.19\text{--}1.56$ ) decreased from HDT29 to R + 12, whereas global perfusion

increased during recovery ( $P = .006; g = 1.01; 95\% \text{ CI}, 0.28\text{--}1.71$ ; Table 2 and Fig 4). At the end of recovery (R + 12), their relative positions shifted with global perfusion significantly greater than both PVS volume ( $P = .025; g = 0.76; 95\% \text{ CI}, 0.09\text{--}1.41$ ) and ventricular volume ( $P = .004; g = 1.07; 95\% \text{ CI}, 0.32\text{--}1.78$ ) with no difference between PVS and ventricular volume ( $P = .146; g = 0.46; 95\% \text{ CI}, -0.15\text{--}1.05$ ).

### HDT Differences between Perfusion, Ventricular Volume, and PVS

At HDT29, ventricular volume was greater, relative to its mean across time, than both PVS volume ( $P = .017; g = 0.83; 95\% \text{ CI}, 0.14\text{--}1.49$ ) and perfusion ( $P < .001; g = 2.05; 95\% \text{ CI}, 0.99\text{--}3.09$ ), and PVS volume was greater than perfusion ( $P < .001; g = 1.47; 95\% \text{ CI}, 0.60\text{--}2.30$ ).

### Recovery versus Baseline Differences

At the end of recovery, we found no differences compared with the baseline values for ventricular volume ( $P = .619; g = 0.15; 95\% \text{ CI}, -0.43\text{--}0.72$ ), PVS volume ( $P = .275; g = 0.33; 95\% \text{ CI}, -0.26\text{--}0.91$ ), or global perfusion ( $P = .503; g = 0.20; 95\% \text{ CI}, -0.20\text{--}0.38$ ). The brain metrics revealed a double dissociation in which ventricular volume and PVS volume increased during HDT+CO<sub>2</sub> with a decrease to baseline levels during recovery, whereas global perfusion decreased during the HDT + CO<sub>2</sub> period and increased to baseline levels during recovery, suggesting distinct neurophysiological responses to simulated microgravity.

## DISCUSSION

The purpose of this study was to investigate changes in cerebral perfusion, ventricular volume, and PVS volume in healthy

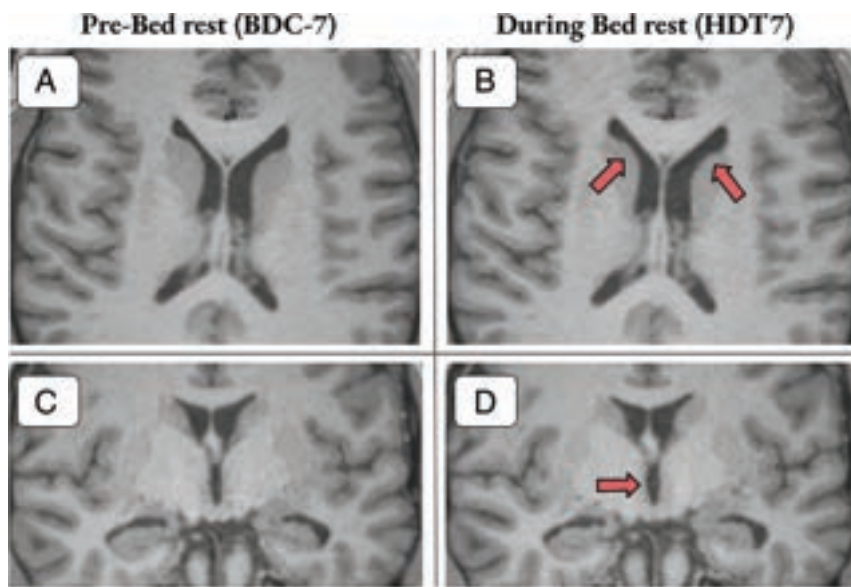


**FIG 2.** T1 images with examples of ventricular volume enlargement for 2 participants 7 days into bed rest. A and B, Axial section with *arrows* highlighting areas of gross ventricular enlargement in the lateral ventricles. C and D, Coronal section with *arrows* highlighting enlargement of the third ventricle. Participants shown experienced a 9.12% and 12.31% increase in ventricular volume, respectively.

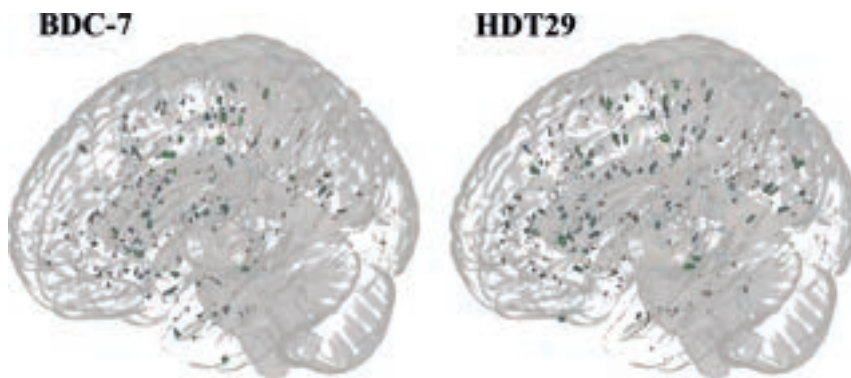


**FIG 3.** 3D mask representation of WM-PVS of a sample participant from pre-bed rest (BDC-7) to the end of bed rest (HDT29). The following participant experienced a 12% increase in PVS volume.

participants in response to 30 days of HDT + CO<sub>2</sub>. The main finding was statistically significant changes in brain metrics of opposite directionality, with global perfusion decreasing and ventricular/PVS volumes increasing during HDT + CO<sub>2</sub> and subsequent reversal during recovery.

While 2 recent studies found alterations in PVS volumes in astronauts postspaceflight,<sup>7,8</sup> this is the first study to report a change in PVS volumes in an HDT microgravity analog setting, and in general, transient PVS dilation and reversal in a cohort of healthy participants. Furthermore, decreased global perfusion in VaPER participants presented by Roberts et al<sup>16</sup> is the only previous study examining longitudinal changes in perfusion by MR imaging in a prolonged microgravity analog. A short-duration study found a 17%–20% decrease in CBF after 26.5 hours of 12° HDT measuring carotid and vertebral artery blood flow using a cine phase-contrast MR image, but it did not extrapolate to multiple time points.<sup>26</sup> Other HDT studies have investigated measurements

of CBF velocity via transcranial Doppler. However, the results of these studies are inconclusive, likely due to limitations of this technique based on the assumption that the cross-sectional area of the interrogated vessel is fixed, which might not be the case, particularly in an environment with altered CO<sub>2</sub> levels.<sup>16,27</sup> Although a perfusion-PVS link has not been explored in a longitudinal study, the inverse relationship observed in this study is in line with previous results that showed that greater PVS volumes may be associated with decreased CBF in healthy participants and patients with intracranial and extracranial atherosclerosis.<sup>18,19</sup> Moreover, the ventricular volume changes presented here align with previous findings after HDT (a 2%–3% increase in lateral ventricle volume was found after 26.5 hours of HDT)<sup>26</sup> and long-duration spaceflight (increases of ~11% have been found in both astronauts and cosmonauts.)<sup>2,3,5</sup>

The mechanisms driving decreased cerebral perfusion and ventricular/PVS enlargement in healthy participants during the 30 days of HDT + CO<sub>2</sub> are unknown. However, it is becoming clear that real and simulated microgravity elicit changes in cerebral hemodynamics and CSF dynamics.<sup>27,28</sup> In spaceflight and HDT, normal hydrostatic pressure gradients, usually experienced along the head-to-foot axis during upright posture, are reduced, resulting in the observed cephalad fluid shifts.<sup>27-29</sup> It has been hypothesized that this upward fluid shift may lead to venous congestion in the head and possibly elevated intracranial pressure (ICP).<sup>5,16,28</sup> From a hemodynamic perspective, venous congestion could lead to venous hypertension, elevated ICP, and decreased cerebral perfusion. Indeed, impaired venous outflow has been linked to reduced cerebral perfusion in patients with chronic cerebrospinal venous insufficiency.<sup>30-32</sup> Following surgical restoration of normal internal jugular venous flow, patients demonstrated improved brain perfusion and a 9.6% reduction in ventricular size.<sup>30</sup> Most interesting, this change in ventricular volume related to venous insufficiency is similar to the ventricular volume change previously reported in astronauts following long-duration spaceflight.<sup>1,25</sup> In an astronaut population, a recent article showed postflight increases in superior sagittal, transverse, and sigmoid sinus volumes.<sup>33</sup> The authors suggest improper venous drainage due to the absence of gravitational gradients and that this may explain thrombosis and abnormal internal jugular venous flow reported in astronauts.<sup>34,35</sup> As an additional contributing factor, cardiac output and stroke volume are

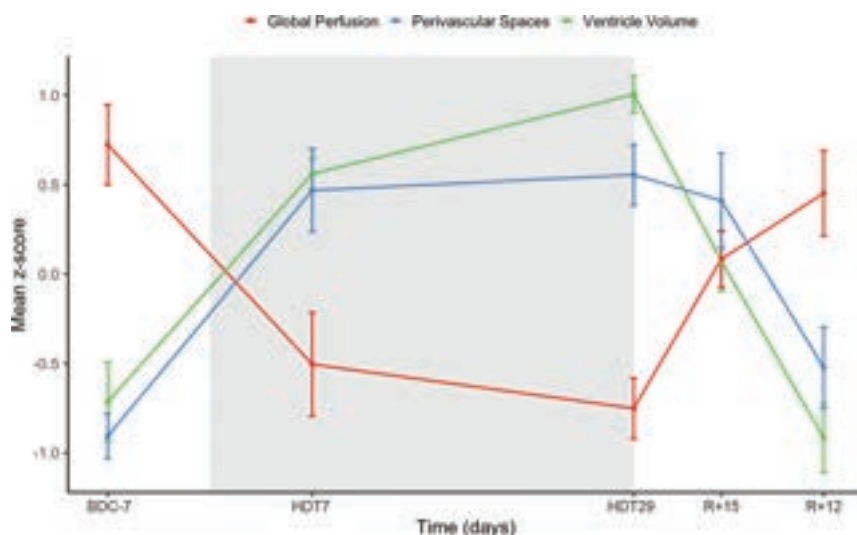


**FIG 4.** Global relative perfusion, ventricular volume, and PVS time courses. *Gray shaded area* represents the duration of the HDT + CO<sub>2</sub> intervention. Data points for scanning days include pre- (BDC-7), during (HDT7 & HDT29), and post- (R + 5 & R + 12) HDT + CO<sub>2</sub> period and are represented with mean z-scores (standard error of the mean). A divergent trajectory is observed with perfusion decreasing while ventricular and perivascular space volume increase during the HDT + CO<sub>2</sub> period.

likely affected by microgravity. Reviewing the current literature, Bateman and Bateman<sup>36</sup> surmised that both are reduced in HDT but increased during spaceflight, which may point to a key physiologic difference between the environments.

Similarly, it is likely CSF homeostasis is altered by reversal of the gravitational gradient. Upward shift of the brain itself has been suggested to impair CSF resorption by compression of the superior sagittal sinus.<sup>5,33</sup> In this theory, the ventricular system may then act as a buffer for excess CSF resulting in ventricular enlargement. Similarly, an increase in PVS volume may reflect obstruction or inefficiency in the exchange of CSF and interstitial fluid that occurs in perivascular channels. CSF flow is intrinsically connected to hemodynamics in that transmission of arterial pulsations are a driving force for CSF movement.<sup>37</sup> In this view, decreased perfusion could reduce the ability to circulate CSF, with resulting consequences for the perivascular and ventricular compartments. Indeed, cross-sectional studies showing an inverse relationship between cerebral perfusion and PVS size have hypothesized that decreased blood flow leads to increased interstitial fluid around the PVS and subsequent PVS dilation.<sup>18</sup> This hypothesis is in line with the negative correlation between perfusion and PVS volume seen in this study. Measurements of ICP could help elucidate the interplay between perfusion and CSF changes, but no direct measurement of ICP during long-duration HDT or microgravity has been performed. However, several studies have reported elevated ICP in the acute stages of HDT or in the transition from upright to supine.<sup>38,39</sup> Additionally, several astronauts presented with mildly elevated opening pressures via lumbar puncture (21–28.5 cm H<sub>2</sub>O) months after spaceflight.<sup>40</sup>

A study limitation was the necessary use of an ASL sequence that did not provide absolute CBF values. The small sample size ( $n = 11$ ) and large number of relevant study variables reduced our statistical

power, though several group-level findings had robust effect sizes. Additionally, various methods for PVS quantification exist, and the automated method used here based on PVS morphologic features has potential limitations, such as partial voluming effects of the enclosed vessel.<sup>41</sup> Most important, it is not clear that HDT bed rest represents an accurate terrestrial analog for spaceflight.<sup>12</sup>

Here, we document an association among patterns of cerebral perfusion, ventricular volume, and PVS volume that occur over a HDT + CO<sub>2</sub> intervention and recovery. The findings contribute to our understanding of the relationships among the circulatory, glymphatic, and ventricular systems of the brain, specifically, revealing a possible direct link between PVS volumes and cerebral perfusion demonstrated by a prolonged perturbation of CBF in healthy participants. The results also provide additional evidence of changes in cerebral physiology in response to

simulated microgravity. The significance of these changes, if any, should be further explored. For example, alterations in vision and ophthalmologic findings following spaceflight have been reported in astronauts, known as the spaceflight-associated neuro-ocular syndrome and thought to be linked to cephalad fluid shifts and venous congestion.<sup>40</sup> Altered cerebral physiology may also play a role in cognitive and performance decrements previously reported in astronauts.<sup>3,14,42</sup> Most important, given the increasing number of commercial spaceflight participants who may not be as physically fit as career astronauts and who may have mild forms of cerebrovascular disease, a pronounced decrease in cerebral perfusion without adequate reserve raises the possibility of spaceflight-induced ischemic events. While these data represent one step forward in developing a comprehensive model of the neurophysiologic response to microgravity, ultimately in-flight evaluation of cerebral perfusion and ICP in astronauts is greatly needed.

## ACKNOWLEDGMENTS

Research reported in this study was facilitated by the Spaceflight Standard Measures Cross-Cutting Project of the Human Research Program of the National Aeronautics and Space Administration. We also thank the entire VaPER study staff.

Disclosure forms provided by the authors are available with the full text and PDF of this article at [www.ajnr.org](http://www.ajnr.org).

## REFERENCES

1. Koppelmans V, Bloomberg JJ, Mulavara AP, et al. **Brain structural plasticity with spaceflight.** *NPI Microgravity* 2016;2:2–8 CrossRef Medline
2. Roberts DR, Albrecht MH, Collins HR, et al. **Effects of spaceflight on astronaut brain structure as indicated on MRI.** *N Engl J Med* 2017;377:1746–53 CrossRef Medline

3. Roberts DR, Asemani D, Nietert PJ, et al. **Prolonged microgravity affects human brain structure and function.** *AJNR Am J Neuroradiol* 2019;40:1878–85 CrossRef Medline
4. Van Ombergen A, Jillings S, Jeurissen B, et al. **Brain tissue–volume changes in cosmonauts.** *N Engl J Med* 2018;379:1678–80 CrossRef Medline
5. Van Ombergen A, Jillings S, Jeurissen B, et al. **Brain ventricular volume changes induced by long-duration spaceflight.** *Proc Natl Acad Sci U S A* 2019;116:10531–36 CrossRef Medline
6. Roberts DR, Inglesby DC, Brown TR, et al. **Longitudinal change in ventricular volume is accelerated in astronauts undergoing long-duration spaceflight.** *Aging Brain* 2021;1:100017 CrossRef Medline
7. Barisano G, Seppehrband F, Collins HR, et al. **The effect of prolonged spaceflight on cerebrospinal fluid and perivascular spaces of astronauts and cosmonauts.** *Proc Natl Acad Sci U S A* 2022;119:e2120439119 CrossRef Medline
8. Hupfeld KE, Richmond SB, McGregor HR, et al. **Longitudinal MRI-visible perivascular space (PVS) changes with long-duration spaceflight.** *Sci Rep* 2022;12:7238 CrossRef Medline
9. Lee JK, Koppelmans V, Riascos RF, et al. **Spaceflight-associated brain white matter microstructural changes and intracranial fluid redistribution.** *JAMA Neurol* 2019;76:412–19 CrossRef Medline
10. Hargens AR, Vico L. **Long-duration bed rest as an analog to microgravity.** *J Appl Physiol (1985)* 2016;120:891–903 CrossRef Medline
11. Traon PL, Heer M, Narici MV, et al. **From space to Earth: advances in human physiology from 20 years of bed rest studies (1986–2006).** *Eur J Appl Physiol* 2007;101:143–94 CrossRef Medline
12. Ong J, Lee AG, Moss HE. **Head-down tilt bed rest studies as a terrestrial analog for spaceflight associated neuro-ocular syndrome.** *Front Neurol* 2021;12:648958 CrossRef Medline
13. Koppelmans V, Erdeniz B, De Dios YE, et al. **Study protocol to examine the effects of spaceflight and a spaceflight analog on neurocognitive performance: extent, longevity, and neural bases.** *BMC Neurol* 2013;13:205 CrossRef Medline
14. Lee JK, De Dios Y, Kofman I, et al. **Head down tilt bed rest plus elevated CO<sub>2</sub> as a spaceflight analog: effects on cognitive and sensorimotor performance.** *Front Hum Neurosci* 2019;13:355 CrossRef Medline
15. Hupfeld KE, Lee JK, Gadd NE, et al. **Neural correlates of vestibular processing during a spaceflight analog with elevated carbon dioxide (CO<sub>2</sub>): a pilot study.** *Front Syst Neurosci* 2020;13:80 CrossRef Medline
16. Roberts DR, Collins HR, Lee JK, et al. **Altered cerebral perfusion in response to chronic mild hypercapnia and head-down tilt bed rest as an analog for spaceflight.** *Neuroradiology* 2021;63:1271–81 CrossRef Medline
17. McGregor HR, Lee JK, Mulder ER, et al. **Brain connectivity and behavioral changes in a spaceflight analog environment with elevated CO<sub>2</sub>.** *Neuroimage* 2021;225:117450 CrossRef Medline
18. Liu S, Hou B, You H, et al. **The association between perivascular spaces and cerebral blood flow, brain volume, and cardiovascular risk.** *Front Aging Neurosci* 2021;13:599724 CrossRef Medline
19. Wang H, Nie ZY, Liu M, et al. **Clinical characteristics of perivascular space and brain CT perfusion in stroke-free patients with intracranial and extracranial atherosclerosis of different extents.** *Ann Transl Med* 2020;8:215 CrossRef Medline
20. Laurie SS, Christian K, Kysar J, et al. **Unchanged cerebrovascular CO<sub>2</sub> reactivity and hypercapnic ventilatory response during strict head-down tilt bed rest in a mild hypercapnic environment.** *J Physiol* 2020;598:2491–2505 CrossRef Medline
21. Fischl B. **FreeSurfer.** *Neuroimage* 2012;62:774–81 CrossRef Medline
22. Seppehrband F, Barisano G, Sheikh-Bahaei N, et al. **Image processing approaches to enhance perivascular space visibility and quantification using MRI.** *Sci Rep* 2019;9:1–12 CrossRef Medline
23. Barisano G, Sheikh-Bahaei N, Law M, et al. **Body mass index, time of day and genetics affect perivascular spaces in the white matter.** *J Cereb Blood Flow Metab* 2021;41:1563–78 CrossRef Medline
24. Donahue EK, Murdos A, Jakowec MW, et al. **Global and regional changes in perivascular space in idiopathic and familial Parkinson's disease.** *Mov Disord* 2021;36:1126–36 CrossRef Medline
25. Sawilowsky SS. **New effect size rules of thumb.** *Journal of Modern Applied Statistical Methods* 2009;8:597–99 CrossRef
26. Kramer LA, Hasan KM, Sargsyan AE, et al; SPACECOT Investigators Group. **Quantitative MRI volumetry, diffusivity, cerebrovascular flow, and cranial hydrodynamics during head-down tilt and hypercapnia: the SPACECOT study.** *J Appl Physiol (1985)* 2017;122:1155–66 CrossRef Medline
27. Kawai Y, Doi M, Setogawa A, et al. **Effects of microgravity on cerebral hemodynamics.** *Yonago Acta Med* 2003;46:1–8
28. Nelson ES, Mulugeta L, Myers JG. **Microgravity-induced fluid shift and ophthalmic changes.** *Life (Basel)* 2014;4:621–65 CrossRef Medline
29. Hans P. **Hydrostatic pressure and neurosurgical pathology** [in French]. *Ann Fr Anesth Reanim* 1994;13:123–26 CrossRef Medline
30. Zamboni P, Menegatti E, Cittanti C, et al. **Fixing the jugular flow reduces ventricle volume and improves brain perfusion.** *J Vasc Surg Venous Lymphat Disord* 2016;4:434–45 CrossRef Medline
31. Zamboni P, Menegatti E, Weinstock-Guttman B, et al. **Hypoperfusion of brain parenchyma is associated with the severity of chronic cerebrospinal venous insufficiency in patients with multiple sclerosis: a cross-sectional preliminary report.** *BMC Med* 2011;9:22 CrossRef Medline
32. Zhou D, Ding J, Asmaro K, et al. **Clinical characteristics and neuroimaging findings in internal jugular venous outflow disturbance.** *Thromb Haemost* 2019;119:308318 CrossRef Medline
33. Rosenberg MJ, Coker MA, Taylor JA, et al. **Comparison of dural venous sinus volumes before and after flight in astronauts with and without spaceflight-associated neuro-ocular syndrome.** *JAMA Netw Open* 2021;4:e2131465 CrossRef Medline
34. Marshall-Goebel K, Laurie SS, Alferova IV, et al. **Assessment of jugular venous blood flow stasis and thrombosis during spaceflight.** *JAMA Netw Open* 2019;2:e1915011 CrossRef Medline
35. Auñón-Chancellor SM, Pattarini JM, Moll S, et al. **Venous thrombosis during spaceflight.** *N Engl J Med* 2020;382:89–90 CrossRef Medline
36. Bateman GA, Bateman AR. **A perspective on spaceflight associated neuro-ocular syndrome causation secondary to elevated venous sinus pressure.** *NPJ Microgravity* 2022;8:3 CrossRef Medline
37. Khasawneh AH, Garling RJ, Harris CA. **Cerebrospinal fluid circulation: what do we know and how do we know it?** *Brain Circ* 2018;4:14–18 CrossRef Medline
38. Murthy G, Marchbanks RJ, Watenpaugh DE, et al. **Increased intracranial pressure in humans during simulated microgravity.** *Physiologist* 1992;35:S184–85 Medline
39. Petersen LG, Petersen JC, Andresen M, et al. **Postural influence on intracranial and cerebral perfusion pressure in ambulatory neurosurgical patients.** *Am J Physiol Regul Integr Comp Physiol* 2016;310:R100–04 CrossRef Medline
40. Mader TH, Gibson CR, Pass AF, et al. **Optic disc edema, globe flattening, choroidal folds, and hyperopic shifts observed in astronauts after long-duration space flight.** *Ophthalmology* 2011;118:2058–69 CrossRef Medline
41. Barisano G, Lynch KM, Sibia F, et al. **Imaging perivascular space structure and function using brain MRI.** *Neuroimage* 2022;257:119329 CrossRef Medline
42. Strangman G, Bevan G. **Review of human cognitive performance in spaceflight.** In: *Proceedings of the 84th Annual Scientific Meeting of the Aerospace Medical Association*, Chicago, Illinois. May 12–16, 2013

# Long-Term Follow-up of Multinodular and Vacuolating Neuronal Tumors and Implications for Surveillance Imaging

S. Dogra, D. Zagzag, M. Young, J. Golfinos, D. Orringer, and R. Jain



## ABSTRACT

**BACKGROUND AND PURPOSE:** Most multinodular and vacuolating neuronal tumors (MVNTs) are diagnosed and followed radiologically without any change across time. There are no surveillance guidelines or quantitative volumetric assessments of these tumors. We evaluated MVNT volumes during long follow-up periods using segmentation tools with the aim of quantitative assessment.

**MATERIALS AND METHODS:** All patients with MVNTs in a brain MR imaging report in our system were reviewed. Patients with only 1 brain MR imaging or in whom MVNT was not clearly the most likely diagnosis were excluded. All MVNTs were manually segmented. For all follow-up examinations, absolute and percentage volume change from immediately prior and initial examinations were calculated.

**RESULTS:** Forty-eight patients (32 women; median age, 50.5 years at first scanning) underwent 158 brain MRIs. The median duration between the first and last scan was 15.6 months (interquartile range, 5.7–29.6 months; maximum, 6.4 years) and between consecutive scans, it was 6.7 months (interquartile range, 3.3–12.4 months; maximum, 4.9 years). Pearson correlation coefficients between days since immediately prior scan versus absolute and percentage volume change from immediately prior scan were  $r = 0.05$  ( $P = .60$ ) and  $r = 0.07$  ( $P = .45$ ), respectively. For the relationship between days since the first scan versus absolute and percentage volume change from the first scan, values were  $r = -0.06$  ( $P = .53$ ) and  $r = -0.04$  ( $P = .67$ ), respectively.

**CONCLUSIONS:** MVNT segmentation across follow-up brain MR imaging examinations did not demonstrate significant volume differences, suggesting that these tumors do not enlarge with time. Hence, frequent surveillance imaging of newly diagnosed MVNTs may not be necessary.

**ABBREVIATIONS:** DNET = dysembryoplastic neuroepithelial tumor; IQR = interquartile range; MVNT = multinodular and vacuolating neuronal tumor

Multinodular and vacuolating neuronal tumors (MVNTs) are relatively newly described entities, having been introduced in the literature first in 2013, included as an architectural pattern in the World Health Organization (WHO) Classification of CNS tumors in 2016, and officially admitted as a grade 1 tumor in the 2021 Classification.<sup>1–3</sup> Although the number of reported cases in the literature overall remains low, most patients appear to be middle-aged at the time of presentation. Three of the largest studies and reviews of MVNTs report median ages at presentation of 44 and 45 years and a mean age of 39, though diagnoses verified by histopathology have been made in ages as young as 10 years.<sup>4–7</sup>

The most common presenting symptoms in patients found to have MVNTs are headaches and seizures, but a significant portion of lesions are discovered incidentally.<sup>5,8–11</sup> Histopathology typically demonstrates neuroepithelial cells with stromal vacuolation and nodular arrangement located principally in the deep cortical ribbon and superficial subcortical white matter (Fig 1).<sup>7,12,13</sup> On MR imaging, these lesions typically present as a cluster of juxtacortical nodules that are iso- to mildly hypointense on T1 with rare post-contrast enhancement and hyperintense on T2 and FLAIR and do not demonstrate diffusion restriction.<sup>5,7</sup> Alternative diagnoses most often include enlarged perivascular spaces, low-grade gliomas, focal cortical dysplasia, or dysembryoplastic neuroepithelial tumors (DNETs), and indeed, many MVNTs were initially misdiagnosed as one of these entities before the 2016 description of MVNTs in the WHO Classification.<sup>7</sup>

On the basis of numerous case reports and series with stable clinical and radiologic follow-up, MVNTs have been suggested to be benign lesions and have consequently been described as “do not touch” and “leave me alone,” despite being a grade 1 tumor

Received May 2, 2023; accepted after revision June 16.

From the Departments of Radiology (S.D., M.Y., R.J.), Pathology (D.Z.), and Neurosurgery (J.G., D.O., R.J.), New York University Grossman School of Medicine, New York, New York.

Please address correspondence to Rajan Jain, MD, Department of Radiology, New York University Grossman School of Medicine, 660 First Ave, New York, NY 10016; e-mail: Rajan.Jain@nyulangone.org; @siddograMD

<http://dx.doi.org/10.3174/ajnr.A7946>

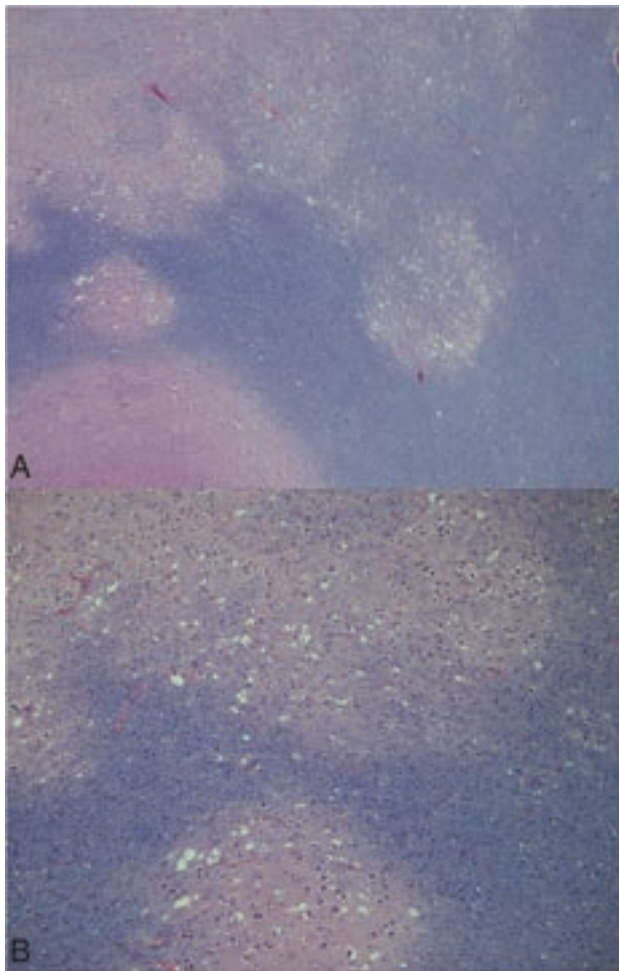


**FIG 1.** A, Low-power view shows multiple discrete nodules and the typical multinodular and vacuolating features of the tumor. The Luxol fast blue stain helps delineate the nodules of various sizes, and the pale staining indicates the variable loss of myelin in tumor nodules present in the white matter. Mitotic figures, necrosis, or microvascular proliferation are not seen (Luxol fast blue stain,  $\times 50$ ). B, A higher power reveals variously shaped vacuoles and variably sized cellular elements within the nodules. A few larger pleomorphic cellular elements are more evident in the lower nodule. Some tumor cells show an ambiguous neuronlike appearance (Luxol fast blue stain,  $\times 100$ ).

by WHO classification.<sup>7,8,14</sup> In particular, 1 study reported that 6.7% of lesions categorized as MVNT showed progression on follow-up MR imaging, while the others were stable for up to 93 months, and another followed patients up to 144 months (using MVNT diagnoses made retrospectively on older cases that previously had alternative diagnoses) with a mean follow-up of 36.8 months and did not find any significant interval change.<sup>5,7</sup> Given the reassuring course of patients with MVNTs, consensus holds that these lesions do not require biopsy or resection and can be safely followed with MR imaging surveillance; however, no uniform guidelines exist regarding the frequency of these surveillance scans. Moreover, these studies relied on qualitative evaluation of MVNT size to document stability, and no MVNT studies have included tumor segmentation and volumetric assessment.

The purpose of this study was to analyze serial imaging of patients with MVNTs using manual segmentation to quantitatively

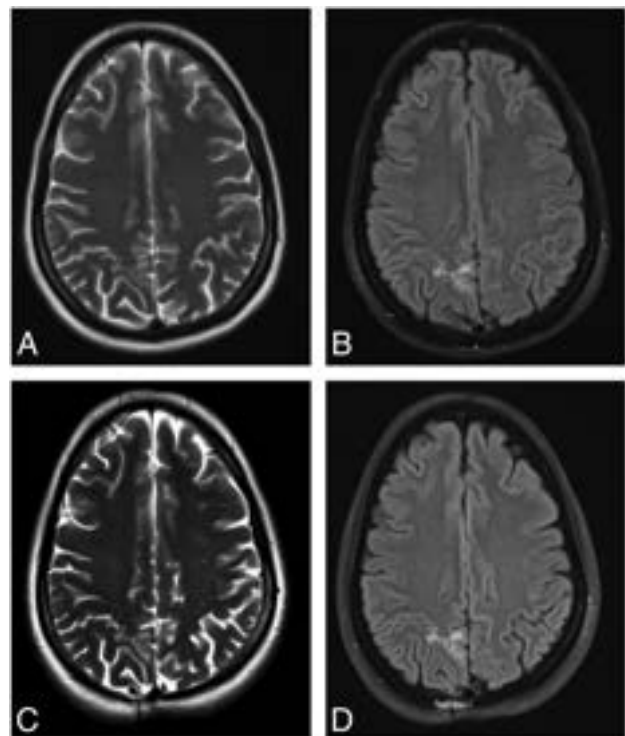


**FIG 2.** T2-weighted and FLAIR images from the baseline (A and B) and 6.4-year follow-up (C and D) MR imaging of a representative patient with a right superior parietal lobule MVNT.

evaluate tumor volume changes with time and to suggest guidelines regarding optimal MR imaging surveillance, with the hope that such guidelines reduce unnecessary imaging and stress in these patients.

## MATERIALS AND METHODS

This single-institutional retrospective study was approved by the institutional review board. A waiver of consent was obtained due to the anonymized and retrospective nature of the study.

### Subject Selection

We used the search function on our PACS to select all brain MR imaging reports through November 4, 2022, that mentioned “multinodular and vacuolating neuronal tumor” or “MVNT” in the report body. All reports were evaluated by fellowship-trained neuroradiologists at the original time of dictation. Search results were manually reviewed, and if MVNT was thought by the original reading neuroradiologist to be the most likely diagnosis for a particular patient, that patient was considered for inclusion. Exclusion criteria included having only 1 brain MR imaging examination available, lack of T2 and/or FLAIR sequences, and the presence of other structural lesions precluding MVNT segmentation.

One hundred twenty-eight patients had a mention of “multinodular and vacuolating neuronal tumor” or “MVNT” in at least 1 brain MR imaging report on our PACS. Of these patients, 39 patients had only 1 brain MR imaging and were excluded. Of the remainder, 41 patients were excluded because MVNT was not the clear top differential diagnosis, resulting in the final cohort of 48 patients.

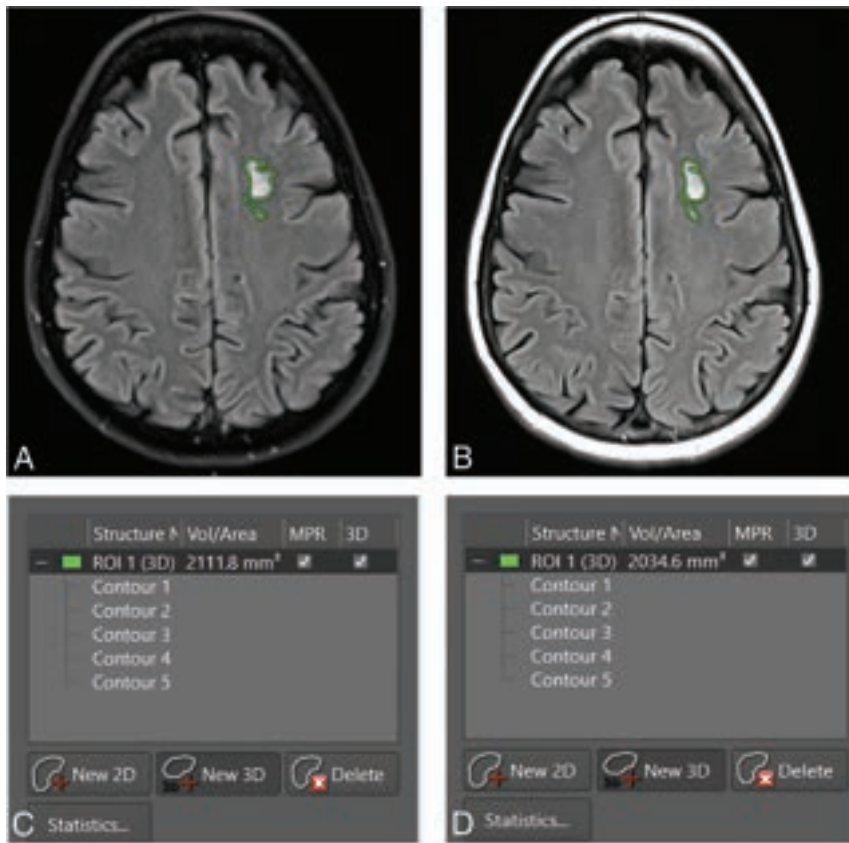


**FIG 3.** Representative FLAIR images from the baseline (A) and the second (B) MR imaging of a patient with a left-frontal MVNT (segmented in green). C and D, Images corresponding to the MR imaging examinations shown in A and B, respectively, show what the segmentation volume window looks like in our PACS.

### Clinical Data

The electronic health record for every included patient was reviewed. Demographic and clinical data were collected, including the indication for initial imaging, age at time of the initial examination, and any histopathologic data.

### MR Imaging and Analysis

MR imaging was performed on a variety of 1.5T or 3T scanners at our institution, with exact scanning parameters varying among scanners.

The MVNT location was noted. MVNT signal characteristics were recorded for T1 pre- and postcontrast, T2, FLAIR, DWI, and ADC sequences across all examinations. All MVNTs were manually segmented on the FLAIR sequence from every MR imaging using a free-form segmentation tool on our PACS. Segmentation was performed on a randomized order of examination accession numbers so that consecutive segmentations were not necessarily performed on imaging even from the same subject, to minimize the risk of subconscious bias. Because many examinations, for example generally the initial examination, had 2D FLAIR sequences but not 3D FLAIR sequences, segmentation was preferentially performed on the FLAIR sequences (section thickness ranging from 3 to 5 mm) to allow optimal comparison. A small number of examinations had only 3D FLAIR sequences (1-mm section thickness), which were consequently used for segmentation.

Following segmentation, 3D volume was automatically generated for every MVNT.

For every follow-up MR imaging examination, we calculated the following: number of days since the immediately prior and original examinations, absolute MVNT volume change (in cubic centimeters) since the immediately prior and original examinations, and percentage MVNT volume change since the immediately prior and original examinations.

### Statistical Analysis

All statistical analyses were performed by using R statistical and computing software (Version 4.0.5; <http://www.r-project.org/>). All *P* values were calculated as 2-tailed with significance set at a level of  $P < .05$ .

Pearson correlation coefficients and 2-tailed *P* values were calculated between the number of days since the immediately prior examinations and both absolute and percentage volume changes since the immediately prior examinations. They were also calculated between the number of days since the original examination and the absolute and percentage volume changes since the original examination. The Wilcoxon

signed-rank test was used to compare median MVNT volumes at the original and terminal scans.

### RESULTS

Forty-eight patients (32 women; median age, 50.5 years at the time of first scan with a range of 10–76 years) underwent a total of 158 brain MRIs between June 28, 2014, and November 4, 2022. The median duration between the first and last scan was 15.6 months (interquartile range [IQR], 5.7–29.6 months; maximum, 6.4 years). The median duration between consecutive scans was 6.7 months (IQR, 3.3–12.4 months; maximum, 4.9 years). Two patients had confirmed MVNT on histopathology.

Clinically, 1 patient has had new migraines since sustaining a concussion, and another patient has developed suspected autoimmune encephalitis, but neither symptom is suspected to be related to their MVNT. Otherwise, all patients with initial neurologic symptoms are stable or improving.

All MVNTs were T2- and FLAIR-hyperintense on every examination (Fig 2). None were intrinsically T1-hyperintense, and none demonstrated enhancement after contrast administration on both baseline and follow-up studies. None exhibited true restricted diffusion (ADC hypointense and DWI hyperintense), but 77% (37/48) exhibited T2 shinethrough (ADC and DWI both hyperintense) on the baseline MR imaging. The most common location was the frontal lobe (35.4%, 17/48), closely followed by

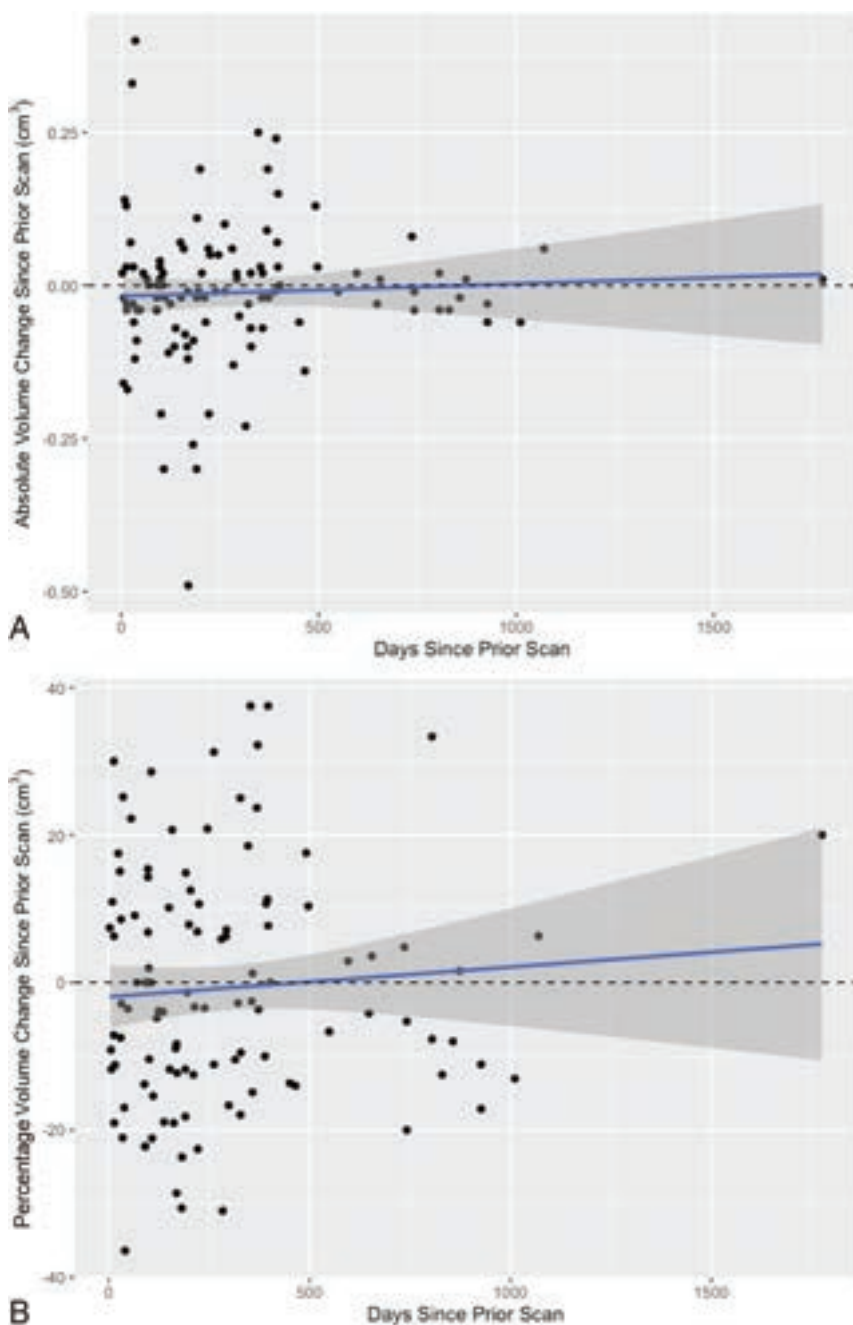


**FIG 4.** Days since prior scan versus absolute (A) and percentage (B) volume changes since the prior scan across 110 follow-up scans. Note the trendline (blue) with the 95% confidence interval (gray areas).

the parietal lobe (33.3%, 16/48). Other locations were the temporal lobe (10.4%, 5/48), cerebellum (8.3%, 4/48), and occipital lobe (6.3%, 3/48). Three MVNTs were in both the frontal and parietal lobes. No lesion had any mass effect. The most common indications for the original examination were headache (33.3%, 16/48), seizures (10.4%, 5/48), and dizziness (10.4%, 5/48).

All MVNTs were read as stable by the neuroradiologists interpreting the scan. For every follow-up brain MR imaging ( $n = 110$ ) for all subjects ( $n = 48$ ), the MVNTs were manually segmented (Fig 3) and the absolute and percentage changes in volume from the immediately prior scan as well as from the original scan were

calculated. Across all 48 individual patients, the median MVNT volume on the original scan was  $0.40 \text{ cm}^3$  (IQR,  $0.16\text{--}0.77 \text{ cm}^3$ ), while the median MVNT volume on the last scan was  $0.34 \text{ cm}^3$  (IQR,  $0.14\text{--}0.75 \text{ cm}^3$ ;  $P = .94$ ).

In comparison with the immediately prior scan, the median absolute change in volume across every follow-up scan was  $-0.02 \text{ cm}^3$  (IQR,  $-0.06\text{--}0.02 \text{ cm}^3$ ), while the median percentage change in volume was  $-5.0\%$  (IQR,  $-13.7\%\text{--}7.9\%$ ) (Fig 4). Pearson correlation coefficients and  $P$  values for the relationship between days since the immediately prior scan versus absolute and percentage changes in volumes from the immediately prior scan were  $r = 0.05$ ,  $P = .60$  and  $r = 0.07$ ,  $P = .45$  respectively.

In comparison with the original scan, the median absolute change in volume across every follow-up scan was  $-0.01 \text{ cm}^3$  (IQR,  $-0.06\text{--}0.03 \text{ cm}^3$ ), while the median percentage change in volume was  $-3.1\%$  (IQR,  $-12.3\%\text{--}10.2\%$ ) (Fig 5). Pearson correlation coefficients and  $P$  values for the relationship between days since the first scan versus absolute and percentage changes in volumes from the first scan were  $r = -0.06$ ,  $P = .53$ , and  $r = -0.04$ ,  $P = .67$ , respectively.

## DISCUSSION

Multiple case series have now suggested the long-term stability of the MVNT based on qualitative evaluation of serial imaging. However, there remain no publicly available guidelines regarding surveillance imaging of a newly diagnosed MVNT. As of 2021, MVNT is officially classified as a WHO grade 1 tumor, which only increases the need for consensus follow-up guidelines to avoid exposing patients to unnecessary imaging examinations and stress regarding

their new diagnosis. We provide quantitative evidence, based on volumetric segmentation across all follow-up examinations of patients with MVNT, that there is no significant change in tumor volume between consecutive examinations or between any individual follow-up examination and the initial examination.

In addition to volumetric stability, our other results agree with the larger retrospective studies in the existing literature, most of which are based on only qualitative assessment. By far, the single most common symptom in our cohort was headache, as in Alsufayan et al<sup>5</sup> and Nunes et al,<sup>7</sup> though like those analyses, we also had multiple patients initially imaged for seizures. Although 7

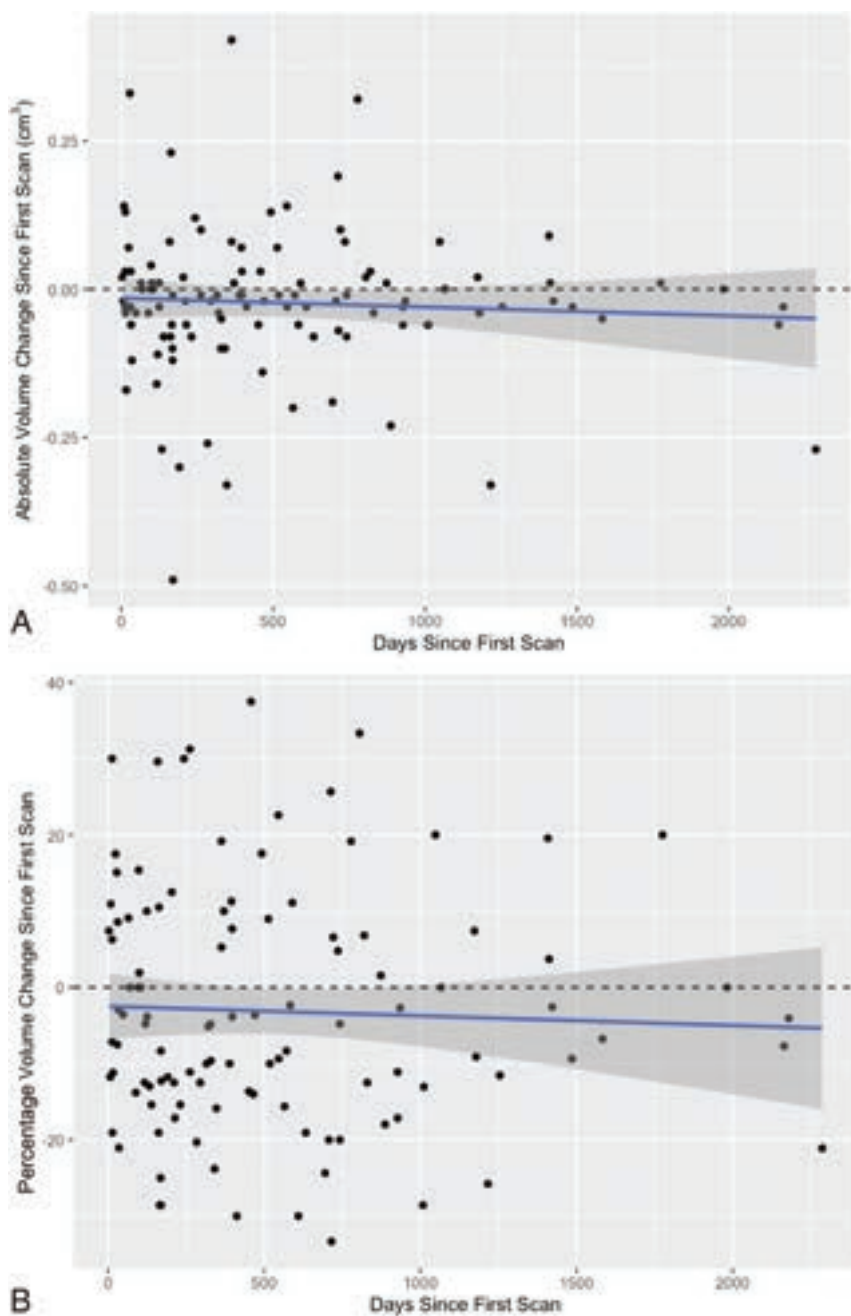


**FIG 5.** Days since first scan versus absolute (A) and percentage (B) volume changes since the first scan, across 110 follow-up scans. Note the trendline (blue) with the 95% confidence interval (gray areas).

of the initial 10 cases of MVNT were found in the temporal lobes,<sup>1</sup> the literature suggests that these lesions are most commonly found in the frontal and parietal lobes, as in our study.<sup>5,7,8</sup> MVNT signal characteristics in our cohort also are in consensus with the literature: All of our MVNT cases showed T2 and FLAIR hyperintensity and T1 iso- or hypointensity. None of our lesions demonstrated contrast enhancement, though there are very scant reports of contrast enhancement in existing studies.<sup>7</sup> Finally, none of our cases showed true restricted diffusion, though most showed T2 shthrough, highlighting the need to scrutinize ADC maps in these cases.

With respect to surveillance imaging suggestions, because MVNTs themselves are benign and, as we have shown, do not change in volume, follow-up imaging should be targeted to rule out other entities in the differential diagnosis. In the literature, other considered diagnoses most commonly have included DNET,<sup>5</sup> focal cortical dysplasia, low-grade glioma,<sup>4</sup> and enlarged perivascular spaces.<sup>5</sup>

Many of these lesions should be distinguishable on a single study alone and do not necessarily merit follow-up solely to differentiate them from an MVNT. Perivascular spaces should not be hyperintense on FLAIR and are typically found in areas of perforator vessels. DNETs are located in the cortex, demonstrate a relatively brighter rim of FLAIR signal, often have calcifications, and present symptomatically with seizures at a young age.<sup>15</sup> Focal cortical dysplasia type IIb often has a characteristic transmante sign of T2 FLAIR hyperintensity extending linearly between the ventricle and cortex and has cortical thickening not seen in MVNT.<sup>16</sup> Most low-grade gliomas should be distinguishable from MVNT on imaging, but there may be diagnostic confusion in cases of large-sized MVNTs or small gliomas. In this case, differentiating low-grade gliomas from MVNTs even with serial imaging may be difficult or require extensive follow-up because certain subgroups of WHO grade 1 or 2 gliomas show very slow progression across several years. In this specific scenario, consultation with neurosurgery colleagues is appropriate.

For incidentally discovered MVNT, we propose a follow-up MR imaging with contrast at approximately 6 months to 1 year. Further follow-up can be performed with annual MR imaging without contrast for an additional 2–3 years, and, after that, imaging intervals can be increased to 3–5 years based on patient comfort level. Of course, individual clinical circumstances may merit more frequent imaging.

We believe no further contrast is needed after a stable follow-up contrast-enhanced examination. The primary utility of surveillance imaging then becomes recognizing slow increases in size; contrast is unnecessary and introduces needless risk. Although the nephrogenic systemic fibrosis incidence has decreased due to a switch to macrocyclic gadolinium-based contrast agents,<sup>17</sup> there is now increased attention given to gadolinium deposition in the

brain.<sup>18</sup> While studies suggest that macrocyclic agents are less likely to cause noticeable MR imaging changes even in patients with moderate renal dysfunction,<sup>19</sup> postmortem studies show deposition in the brain even with macrocyclic agents.<sup>20</sup> Although the clinical significance of gadolinium deposition remains unclear, administering unnecessary contrast should be avoided.

The psychological effects of a delayed diagnosis of benign-versus-malignant tumors should not be underestimated, particularly now that MVNT is officially a WHO grade 1 tumor. Patients with malignant brain tumors are significantly more likely to report posttraumatic stress disorder symptoms than patients with benign tumors.<sup>21</sup> In women with a breast mass awaiting biopsy, all patients exhibited elevated stress-related biomarkers and anxiety symptoms, but women diagnosed with a benign tumor returned to a normal baseline while women with a malignant diagnosis did not.<sup>22</sup> A stable first follow-up scan at 7–12 months should reassure the patient about a benign MVNT diagnosis.

Limitations of our study include the lack of histopathologic confirmation of MVNT cases, because only 2 subjects underwent biopsy. Unfortunately, lack of pathology is a problem common to all large MVNT analyses,<sup>5,7,8</sup> because the lesions have now been recognized as “touch me not” and, therefore, do not undergo biopsy unless there is considerable doubt regarding the diagnosis. Second, natural limits on the precision of manual segmentation provide another source of error, particularly given the small volume of many of our lesions. For example, an increase from 0.05 to 0.06 cm<sup>3</sup> is a 20% increase in volume, but it, more than likely, is within segmentation error. Similarly, differences in scanners may provide heterogeneity across scans of the same lesion, producing small changes affecting segmentation volume. Although our quantitative results align with qualitative observations of other studies, we did not test intra- or interobserver agreement for the manual segmentations. In a similar vein, the single-institution nature of this study is another inherent limitation, and a multi-institution quantitative analysis would add even more strength to our conclusion.

## CONCLUSIONS

Volumetric assessment of MVNTs across serial follow-up brain MR imaging examinations did not demonstrate any significant difference in absolute or percentage volume changes from either immediately prior or baseline scans. Uniform recommendations regarding surveillance imaging of newly diagnosed MVNTs are needed, particularly considering the new classification of MVNT as a WHO grade 1 tumor. However, most of these patients with a definitive imaging diagnosis can be reassured of a very benign course, can avoid surgery, and, more important, can be followed up with less frequent imaging. Moreover, MR imaging follow-up studies could skip or avoid gadolinium contrast injections.

Disclosure forms provided by the authors are available with the full text and PDF of this article at [www.ajnr.org](http://www.ajnr.org).

## REFERENCES

1. Huse JT, Edgar M, Halliday J, et al. **Multinodular and vacuolating neuronal tumors of the cerebrum: 10 cases of a distinctive seizure-associated lesion.** *Brain Pathol* 2013;23:515–24 CrossRef Medline
2. Louis DN, Perry A, Reifenberger G, et al. **The 2016 World Health Organization Classification of Tumors of the Central Nervous System: a summary.** *Acta Neuropathol* 2016;131:803–20 CrossRef Medline
3. Louis DN, Perry A, Wesseling P, et al. **The 2021 WHO Classification of Tumors of the Central Nervous System: a summary.** *Neuro Oncol* 2021;23:1231–51 CrossRef Medline
4. Alizada O, Ayman T, Akgun MY, et al. **Multinodular and vacuolating neuronal tumor of the cerebrum: two cases and review of the literature.** *Clin Neurol Neurosurg* 2020;197:106149 CrossRef Medline
5. Alsufayan R, Alcaide-Leon P, de Tilly LN, et al. **Natural history of lesions with the MR imaging appearance of multinodular and vacuolating neuronal tumor.** *Neuroradiology* 2017;59:873–83 CrossRef Medline
6. Nunes Dias L, Candela-Cantó S, Jou C, et al. **Multinodular and vacuolating neuronal tumor associated with focal cortical dysplasia in a child with refractory epilepsy: a case report and brief review of literature.** *Childs Nerv Syst* 2020;36:1557–61 CrossRef Medline
7. Nunes RH, Hsu CC, da Rocha AJ, et al. **Multinodular and vacuolating neuronal tumor of the cerebrum: a new “leave me alone” lesion with a characteristic imaging pattern.** *AJNR Am J Neuroradiol* 2017;38:1899–904 CrossRef Medline
8. Buffa GB, Chaves H, Serra MM, et al. **Multinodular and vacuolating neuronal tumor of the cerebrum (MVNT): a case series and review of the literature.** *J Neuroradiol* 2020;47:216–20 CrossRef Medline
9. Makrakis D, Veneris S, Papadaki E. **Multinodular and vacuolating neuronal tumor incidentally discovered in a young man: conventional and advanced MRI features.** *Radiol Case Rep* 2018;13:960–64 CrossRef Medline
10. Hongo T, Nakajima H, Kishizaki H, et al. **Multinodular and vacuolating neuronal tumor (MVNT) diagnosed asymptotically by characteristic MRI findings [in Japanese].** *Brain Nerve* 2022;74:817–18 CrossRef Medline
11. Arbuiso S, Roster K, Gill A, et al. **Multinodular and vacuolating neuronal tumor: incidental diagnosis of a rare brain lesion.** *Cureus* 2021;13:e20674 CrossRef Medline
12. Lecler A, Broquet V, Bailleux J, et al. **Advanced multiparametric magnetic resonance imaging of multinodular and vacuolating neuronal tumor.** *Eur J Neurol* 2020;27:1561–69 CrossRef Medline
13. Choi E, Kim SI, Won JK, et al. **Clinicopathological and molecular analysis of multinodular and vacuolating neuronal tumors of the cerebrum.** *Hum Pathol* 2019;86:203–12 CrossRef Medline
14. De Wandeler T, De Brucker Y, Jansen A, et al. **Multinodular and vacuolating neuronal tumor of the cerebrum (MVNT): do not touch.** *Acta Neurol Belg* 2020;120:747–48 CrossRef Medline
15. Parmar HA, Hawkins C, Ozelame R, et al. **Fluid-attenuated inversion recovery ring sign as a marker of dysembryoplastic neuroepithelial tumors.** *J Comput Assist Tomogr* 2007;31:348–53 CrossRef Medline
16. Kimura Y, Shioya A, Saito Y, et al. **Radiologic and pathologic features of the transmantle sign in focal cortical dysplasia: the T1 signal is useful for differentiating subtypes.** *AJNR Am J Neuroradiol* 2019;40:1060–66 CrossRef Medline
17. Mathur M, Jones JR, Weinreb JC. **Gadolinium deposition and nephrogenic systemic fibrosis: a radiologist’s primer.** *Radiographics* 2020;40:153–62 CrossRef Medline
18. Radbruch A, Weberling LD, Kieslich PJ, et al. **Gadolinium retention in the dentate nucleus and globus pallidus is dependent on the class of contrast agent.** *Radiology* 2015;275:783–91 CrossRef Medline
19. Dogra S, Borja MJ, Lui YW. **Impact of kidney function on CNS gadolinium deposition in patients receiving repeated doses of gadobutrol.** *AJNR Am J Neuroradiol* 2021;42:824–30 CrossRef Medline

20. Murata N, Gonzalez-Cuyar LF, Murata K, et al. **Macrocyclic and other non-group 1 gadolinium contrast agents deposit low levels of gadolinium in brain and bone tissue: preliminary results from 9 patients with normal renal function.** *Invest Radiol* 2016;51:447–53 CrossRef Medline
21. Fehrenbach MK, Brock H, Mehnert-Theuerkauf A, et al. **Psychological distress in intracranial neoplasia: a comparison of patients with benign and malignant brain tumours.** *Front Psychol* 2021;12:664235 CrossRef Medline
22. Bai LJ, Liu Q, Wang M, et al. **Evaluation of the psychological and biological changes of patients diagnosed with benign and malignant breast tumors.** *Int J Biol Markers* 2012;27:e322v30 CrossRef Medline

# Prospective Comparison of T1-SPACE and MPRAGE for the Identification of Intrinsic T1 Hyperintensity in Patients with Intracranial Melanoma Metastases

Arian Lasocki, Stephen L. Stuckey, Lauren Caspersz, Jing Xie, and Grant A. McArthur

## ABSTRACT

**BACKGROUND AND PURPOSE:** Volumetric TSE (3D-TSE) techniques are increasingly replacing volumetric magnetization-prepared gradient recalled-echo (3D-GRE) sequences due to improved metastasis detection. In addition to providing a baseline for assessing postcontrast enhancement, precontrast T1WI also identifies intrinsic T1 hyperintensity, for example, reflecting melanin or blood products. The ability of precontrast 3D-TSE to demonstrate intrinsic T1 hyperintensity is not clear from the literature; thus, this study compares precontrast 3D-TSE and 3D-GRE sequences for identifying intrinsic T1 hyperintensity in patients with metastatic melanoma.

**MATERIALS AND METHODS:** Patients with metastatic melanoma and previously reported intrinsic T1 hyperintensity were identified. MRIs were performed at 3T including both 3D-GRE (MPRAGE) and 3D-TSE T1 sampling perfection with application-optimized contrasts by using different flip angle evolution (T1-SPACE) sequences precontrast. Axial 1-mm slices of both T1WI sequences were independently reviewed by 2 neuroradiologists, comparing the conspicuity of each lesion between the 2 sequences according to a 5-point scale and assessing whether the intrinsic T1 hyperintensity was attributable to melanin, blood products, or both.

**RESULTS:** Twenty examinations were performed, with a total of 214 lesions demonstrating intrinsic T1 hyperintensity. Both readers found that intrinsic T1 hyperintensity was less conspicuous with T1-SPACE compared with MPRAGE for most lesions assessed (81.8%, averaged across both readers), including for lesions with intrinsic T1 hyperintensity attributable to melanin and blood products. Intrinsic T1 hyperintensity was rarely more conspicuous on T1-SPACE (1.4%).

**CONCLUSIONS:** Precontrast intrinsic T1 hyperintensity is more conspicuous with MPRAGE than T1-SPACE. In patients with metastatic melanoma, 3D-GRE should be preferred as the precontrast T1WI sequence when both 3D-TSE and 3D-GRE are performed postcontrast and when not administering IV contrast.

**ABBREVIATIONS:** 3D-GRE = volumetric magnetization-prepared gradient recalled-echo; 3D-TSE = volumetric TSE; IMM = intracranial melanoma metastases; T1H = intrinsic T1 hyperintensity; T1-SPACE = T1 sampling perfection with application-optimized contrasts by using different flip angle evolution

Volumetric TSE (3D-TSE) techniques are increasingly replacing volumetric magnetization-prepared gradient recalled-echo (3D-GRE) sequences such as MPRAGE for postcontrast T1WI, due to their improved ability to detect small intracranial

metastases.<sup>1</sup> For example, 1 important advantage of 3D-TSE over 3D-GRE is inherently greater suppression of normal vessels, which can otherwise obscure small metastases adjacent to vessels.<sup>2</sup> Performing precontrast T1WI is important to confirm that hyperintensity demonstrated on postcontrast T1WI truly reflects enhancement rather than intrinsic T1 hyperintensity (T1H), and providing such a baseline is arguably the most important role of precontrast T1WI. The pre- and postcontrast sequences are typically performed with the same imaging parameters, to most accurately assess postcontrast enhancement.

The identification of T1H on precontrast T1WI is also important, given the limited number of possible causes, including melanin, blood products (methemoglobin), lipid, protein, and minerals (including calcification).<sup>3</sup> Given its ability to identify melanin, precontrast T1WI plays a more important role in the assessment of metastatic melanoma as opposed to metastatic disease from other

Received August 2, 2022; accepted after revision July 17, 2023.

From the Department of Cancer Imaging (A.L., S.L.S., L.C.), Centre for Biostatistics and Clinical Trials (J.X.), and Department of Medical Oncology (G.A.M.), Peter MacCallum Cancer Centre, Melbourne, Victoria, Australia; Sir Peter MacCallum Department of Oncology (A.L., S.L.S., G.A.M.), and Department of Radiology (A.L.), The University of Melbourne, Parkville, Victoria, Australia; School of Clinical Sciences at Monash Health (S.L.S.), and Department of Medical Imaging and Radiation Sciences (S.L.S.), Monash University, Clayton, Victoria, Australia.

Arian Lasocki was supported by a Peter MacCallum Cancer Foundation Discovery Partner Fellowship.

Please address correspondence to Arian Lasocki, MD, Department of Cancer Imaging, Peter MacCallum Cancer Centre, Grattan St, Melbourne, Victoria 3000, Australia; e-mail: arian.lasocki@petermac.org

<http://dx.doi.org/10.3174/ajnr.A7975>

primaries. This role may be particularly relevant when using 3D-GRE because intracranial melanoma metastases (IMM) can occasionally be obscured by normal vessels on postcontrast imaging but be visible precontrast on the basis of T1H. T1H attributable to melanin occurs in approximately one-third of IMM,<sup>4,5</sup> and the frequency of T1H attributable to melanin may be slightly higher in metastases with a *BRAF* mutation compared with *BRAF* wild-type disease.<sup>5</sup> IMM also have a particular propensity to hemorrhage, which is more frequent than metastases from most other primaries.<sup>6</sup> Both melanin and blood products may contribute to T1H within a given intracranial melanoma metastasis; thus, it is important to correlate precontrast T1WI with a susceptibility-sensitive sequence to aid in this distinction.<sup>5,7</sup> Blood products will result in low signal on SWI,<sup>7</sup> while melanin will produce either high signal due to the T1 shine-through effect<sup>8</sup> or intermediate signal.

With the transition from 3D-GRE to 3D-TSE for postcontrast T1WI, it follows that a similar transition will also occur for precontrast T1WI. However, the ability of precontrast 3D-TSE to detect T1H, in particular T1H attributable to melanin or hemorrhage, has not been assessed to our knowledge. If a single postcontrast T1WI sequence is performed, the precontrast T1WI sequence would generally be performed with the same parameters. There is, however, value in performing both 3D-TSE and 3D-GRE postcontrast, to optimize both the sensitivity and specificity for the detection of metastases.<sup>9</sup> With such an imaging protocol, 1 precontrast T1WI sequence is adequate, but it is not clear from the literature whether 3D-TSE or 3D-GRE should be selected. In addition, gadolinium administration is contraindicated in some patients, and some patients may decline contrast administration, for example due to concerns regarding gadolinium accumulation. Therefore, the relative performance of the 2 T1WI sequences is an important consideration in clinical practice. The purpose of the study was to compare the identification of T1H in IMM on precontrast 3D-GRE and 3D-TSE.

## MATERIALS AND METHODS

### Patient Identification

Approval from the Peter MacCallum Cancer Centre ethics committee was obtained. Patients were identified prospectively on the basis of an upcoming MR imaging booking and a history of metastatic melanoma. All were adult patients. The preceding MR imaging report for each patient was reviewed by the lead study neuroradiologist (with 10 years of subspecialty expertise in neuro-oncology), and patients in whom T1H was reported were identified. Verbal consent for the additional sequence was obtained from each patient following an institutional ethics committee–approved procedure. A total of 20 examinations were planned.

### Image Acquisition

All MR imaging examinations were performed on 3T MR imaging (Magnetom Skyra; Siemens) using a standardized protocol, including pre- and postcontrast 3D-GRE (MPRAGE), precontrast 3D-TSE (T1 sampling perfection with application-optimized contrasts by using different flip angle evolution [SPACE sequence; Siemens]), axial T2WI, axial FLAIR, DWI, and SWI. T2WI was performed between contrast administration and postcontrast MPRAGE. MPRAGE was performed in the axial plane.

The parameters for MPRAGE were the following: TR = 1900 ms; TE = 2.44 ms; TI = 944 ms; flip angle = 8°; frequency = 6; phase = 256; number of excitations = 1; FOV = 256 mm; section thickness = 1 mm; fat suppression = water excitation; parallel imaging acceleration factor = 2; bandwidth = 250 Hz/px. Initially, T1-SPACE was also performed in the axial plane (for the first 7 examinations), but wrap-around artifacts occurred in the superior aspect of the FOV in some patients. As a result, the acquisition plane was changed to sagittal (for the remaining 13 examinations), though images were primarily assessed in the axial plane with 1.0-mm section thickness, to be equivalent to MPRAGE. The parameters for T1-SPACE were the following: TR = 700 ms; TE = 11 ms; frequency = 256; phase = 256; number of excitations = 1.4; FOV = 256 mm; section thickness = 1 mm; fat suppression = fat saturation strong; blood suppression = free; parallel imaging acceleration factor = 2; bandwidth = 630 Hz/px. Both sequences were similar in duration: 3 minutes and 44 seconds for MPRAGE and 4 minutes and 4 seconds for T1-SPACE. Examinations were performed between February and October 2020.

### Imaging Review

All MR imaging examinations were first assessed by the lead study neuroradiologist, either at the time of the initial report ( $n = 5$ ) or later, but blinded to the report (by nonstudy radiologists;  $n = 15$ ). Axial 1-mm slices of both T1WI sequences were reviewed, comparing the conspicuity of each lesion between the 2 sequences according to a 5-point scale: similar to that used previously by Goncalves Filho et al<sup>10</sup> for the detection of gadolinium-enhancing lesions with different T1-SPACE sequences: only visualized on T1-SPACE; visible on MPRAGE but better visualized on T1-SPACE; similar conspicuity on both sequences; visible on T1-SPACE but better visualized on MPRAGE; or only visible on MPRAGE. SWI was also assessed to determine whether the T1H could potentially be solely attributed to blood products, solely attributed to melanin, or mixed (with both magnetic susceptibility and at least a portion demonstrating T1H without associated magnetic susceptibility). Examples are shown in Fig 1. Lesion locations (anatomic locations and image numbers) were noted, and the MRIs were subsequently reviewed by a second neuroradiologist (with >20 years of experience) in the same way, blinded to the first reader's assessment and the clinical report. Assessment was performed using the standard clinical PACS in a typical reading room environment. The window and level were determined by each reader on a case-by-case basis.

### Statistical Analysis

The Fleiss  $\kappa$  was computed to assess the agreement between the 2 MR imaging readers for determining the nature of T1H and the relative conspicuity between the 2 sequences, according to categorical scales (nominal and ordinal, respectively). When determining the nature of T1H, lesions that could not be confidently characterized due to artifacts were excluded. T1-SPACE and MPRAGE were compared using the exact binomial test, considering together lesions better seen on 1 particular sequence and only seen on that sequence. All statistical analyses were performed in R statistical and computing software (Version 4.0.3; <http://www.r-project.org/>) using standard and validated statistical procedures.

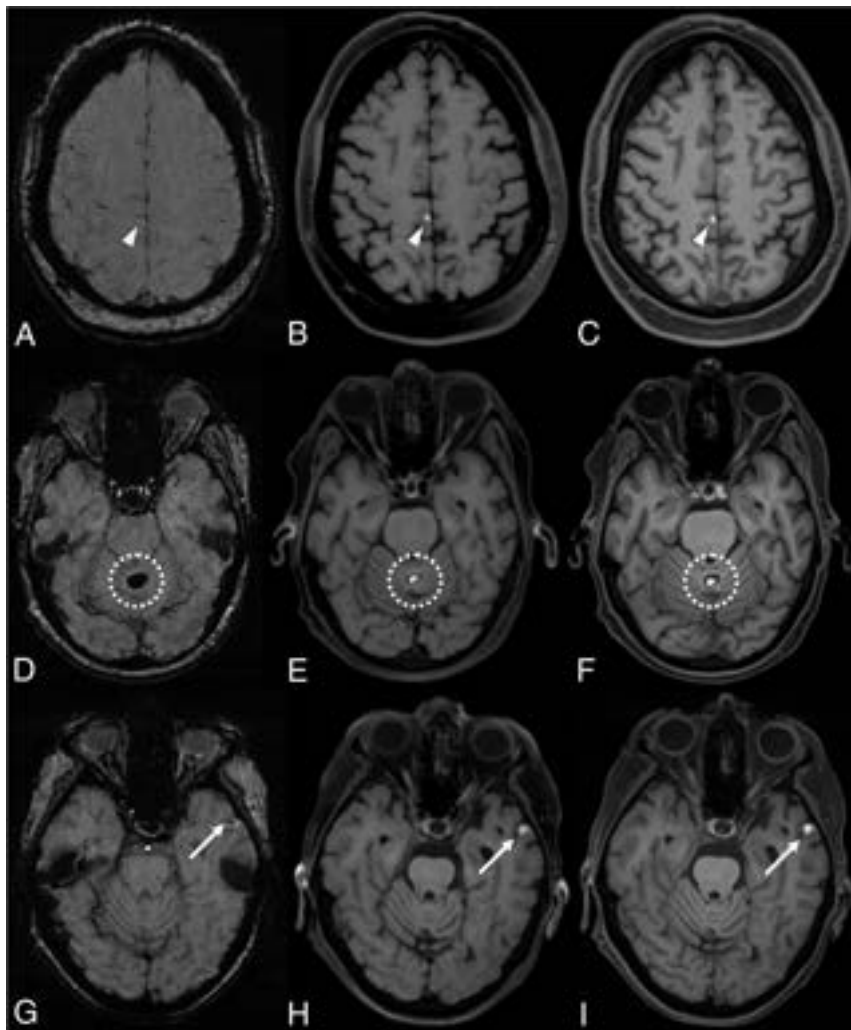


**FIG 1.** SWI (left column), precontrast T1-SPACE (middle column), and precontrast MPRAGE (right column) images demonstrating the determination of the cause of T1H. In the first patient (A–C), there is a small intracranial melanoma metastasis (arrowheads) at the medial margin of the right paracentral lobule demonstrating T1H (B and C), but no magnetic susceptibility (A), thus consistent with melanin. A cerebellar vermian lesion (dotted circles) with central T1H in the second patient (D–F) demonstrates magnetic susceptibility throughout the lesion (D), thus the T1H is potentially entirely attributable to blood products. In the third patient (G–I), there is a small area of magnetic susceptibility at the anteromedial aspect of the lesion (G, arrow), but the remainder of the T1H (H and I, arrows) does not have associated magnetic susceptibility, consistent with a combination of melanin and blood products. In all 3 examples, the T1H is similarly conspicuous on T1-SPACE as MPRAGE.

## RESULTS

Twenty MRIs including precontrast 3D-TSE were performed, in a total of 18 patients (2 patients had 3D-TSE on 2 separate occasions within the study period). There were a total of 214 lesions demonstrating T1H, with a median of 2 per examination (range, 1–141 lesions). The median age of the 18 patients (obtained at the time of the first examination for the 2 patients with 2 study examinations) was 58 years (range, 27–87 years), with an equal number of men and women. Five patients had presented with metastatic disease of unknown primary; 4 had lower limb primaries; 2 each had primaries on their neck, back, and chest wall; and the remaining 3 patients had primaries in other locations (shoulder, ear, and conjunctiva). These background data are summarized in Table 1.

Both readers determined that T1H was attributable solely to melanin for most lesions (179 and 170 lesions, respectively, for the 2 readers). Both melanin and blood products were demonstrated in 4.7% of lesions (taking the average of the 2 readers' results), while T1H could be entirely attributed to blood products in an average of 11.2% of the lesions. Only in a minority of lesions was SWI unable to adequately characterize the T1H due to artifacts, generally due to a peripheral location. Further detail is provided in Table 2. There was good interobserver agreement for assessing the cause of T1H (Fleiss  $\kappa = 0.71$ ,  $P < .001$ ).

Both readers determined that more than half of the lesions were better visualized on MPRAGE but were visible on T1-SPACE (57.2% of the lesions averaged across the 2 readers), with a further 24.5% seen only on MPRAGE. Overall, 81.8% of lesions were better visualized on MPRAGE than on T1-SPACE ( $P < .0001$ ), while conspicuity was similar on both sequences for 16.8% of lesions. It was rare for lesions to be better seen on T1-SPACE: According to reader 1, one lesion was more conspicuous on T1-SPACE and another was seen only on T1-SPACE; and for reader 2, four lesions were more conspicuous on T1-SPACE and none were seen only on T1-SPACE. These results are also summarized in Table 2. Some examples of the differences in conspicuity are shown in Fig 2. Interobserver agreement was moderate (Fleiss  $\kappa = 0.59$ ,  $P < .001$ ) for comparing the conspicuity of T1H on T1-SPACE and MPRAGE. The discrepancies were largely one reader assessing the lesion as being better seen with MPRAGE

and the other reader assessing the lesion as seen only on MPRAGE, or one reader assessing the lesion as being better seen with MPRAGE and the other reader reporting similar conspicuity. Table 3 has additional data on the interobserver agreement for comparing T1-SPACE and MPRAGE.

Lesions were also divided into those with evidence of only melanin or only blood products (excluding lesions with evidence of both or indeterminate due to artifacts). For lesions with T1H attributable to melanin, reader 1 assessed 88.8% of lesions as being more conspicuous with MPRAGE (including those only seen on MPRAGE), with 81.8% for reader 2. For lesions with T1H attributable to blood products, reader 1 reported that MPRAGE better visualized the lesion in 73.1%, and reader 2, in

69.6%. These results are also included in Table 2. In all 12 examinations demonstrating >1 lesion with T1H, the conspicuity of individual lesions varied to some extent, as assessed by both readers.

## DISCUSSION

Both readers independently determined that MPRAGE is overall better than T1-SPACE for identifying T1H. Not infrequently, the difference between the 2 sequences was quite marked (Fig 2), supporting the well-accepted recommendation of using the same T1WI sequence both before and after contrast administration. Nevertheless, some centers may perform more limited T1WI pre-contrast (eg, single-plane axial or sagittal acquisition), and it is important to be aware of potential differences in signal due to technical factors. The lower conspicuity with T1-SPACE was

particularly pronounced for lesions containing melanin but was also evident in most lesions with T1H due to blood products. The latter may be an advantage in some settings: The presence of T1H often makes it more difficult to appreciate postcontrast enhancement. This feature suggests that 3D-TSE may facilitate assessment of enhancement in hemorrhagic lesions, though we have not specifically investigated this possibility. Ultimately, our results provide valuable insights into the differences between the 2 sequences, in turn allowing the optimal sequence to be selected for the given scenario.

Despite the greater conspicuity on MPRAGE, the choice of the T1WI sequence is, in large part, dependent on the postcontrast T1WI sequence being used, and 3D-TSE has other important advantages over 3D-GRE as outlined above. However, if IV gadolinium is contraindicated or declined, our results indicate that unenhanced 3D-GRE is better than unenhanced 3D-TSE for detecting IMM. In addition to 3D-TSE producing generally lower conspicuity of T1H, its key advantages of over 3D-GRE for the assessment of metastatic disease, namely vascular suppression and more pronounced enhancement,<sup>2</sup> are negated in the absence of IV contrast. Also, while more pronounced T1H from blood products that occurs with 3D-GRE may be a disadvantage when trying to assess postcontrast enhancement, it may be beneficial when IV contrast is not administered, especially if a susceptibility-sensitive sequence is not used.

Our findings are also relevant when contrast is administered. While a single postcontrast T1WI sequence is performed in many centers, there are benefits in performing both 3D-TSE and 3D-GRE postcontrast. 3D-TSE improves detection of intracranial metastases, especially small metastases,<sup>1,11</sup> but has a higher false-positive rate due to incompletely suppressed vessels mimicking metastases,<sup>12</sup> which is particularly relevant in patients without known intracranial metastatic disease.<sup>9</sup> In contrast, the more pronounced vascular enhancement with 3D-GRE can obscure small

metastases, but it allows the equivocal findings on 3D-TSE to be resolved, being able to distinguish between metastases and normal vessels.<sup>9,12</sup> In our routine practice, we currently perform both 3D-TSE and 3D-GRE postcontrast, for the reasons outlined above, and consider performing a single pre-contrast T1WI sequence to assess enhancement adequately. For small IMM demonstrating T1H, it is not uncommon for these to be best identified on precontrast 3D-GRE due to relative obscuration by enhancing vessels on postcontrast 3D-GRE and the presence of less marked hyperintensity on postcontrast 3D-TSE (Fig 3). Therefore, when performing both 3D-GRE and 3D-TSE postcontrast in patients with metastatic melanoma, we recommend 3D-GRE precontrast rather than 3D-TSE. We also suggest value in performing 3D-GRE rather than 3D-TSE

**Table 1: Background data**

Data	
Total patients	18
Total examinations	20
Male	9 (50.0%)
Female	9 (50.0%)
Age (yr)	
Median	58
Range	27–87
Total IMM	214
Median	2
Range	1–141
Primary site	
Metastases of unknown primary	5
Lower limb	4
Neck	2
Back	2
Chest wall	2
Shoulder	1
Ear	1
Conjunctiva	1

**Table 2: MR imaging assessment results for both readers**

	Reader 1	Reader 2	Average (%)
Cause of T1H			
Melanin only	179 (83.6%)	170 (79.4%)	81.5%
Blood products only	26 (12.1%)	22 (10.3%)	11.2%
Both melanin and blood	7 (3.3%)	13 (6.1%)	4.7%
Artifacts	2 (0.9%)	9 (4.2%)	2.6%
Relative conspicuity (overall)			
Only seen on T1-SPACE	1 (0.5%)	0 (0%)	0.2%
Better on T1-SPACE	1 (0.5%)	4 (1.9%)	1.2%
Similar conspicuity	31 (14.5%)	41 (19.2%)	16.8%
Better on MPRAGE	123 (57.5%)	122 (57.0%)	57.2%
Only seen on MPRAGE	58 (27.1%)	47 (22.0%)	24.5%
Relative conspicuity (melanin)			
Only seen on T1-SPACE	0 (0%)	0 (0%)	0.0%
Better on T1-SPACE	1 (0.6%)	2 (1.2%)	0.9%
Similar conspicuity	19 (10.6%)	29 (17.1%)	13.8%
Better on MPRAGE	114 (63.7%)	98 (57.6%)	60.7%
Only seen on MPRAGE	45 (25.1%)	41 (24.1%)	24.6%
Relative conspicuity (blood)			
Only seen on T1-SPACE	1 (3.8%)	0 (0%)	1.9%
Better on T1-SPACE	0 (0%)	1 (4.3%)	2.2%
Similar conspicuity	6 (23.1%)	6 (26.1%)	24.6%
Better on MPRAGE	7 (26.9%)	12 (52.2%)	39.5%
Only seen on MPRAGE	12 (46.2%)	4 (17.4%)	31.8%

precontrast in patients with metastatic disease from an unknown primary because the greater conspicuity of T1H when using MPRAGE may allow melanoma to be suggested as the likely primary with greater confidence.

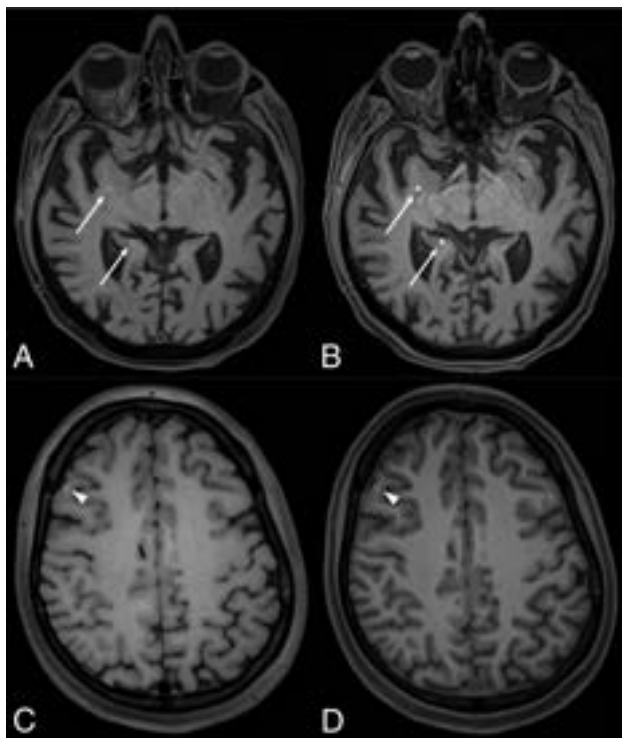


**FIG 2.** Precontrast TI-SPACE (left column) and precontrast MPRAGE (right column) images demonstrating differing conspicuity of IMM. In the first patient (A and B), 2 IMM (arrows) are less conspicuous on TI-SPACE (A) compared with MPRAGE (B). In another patient (C and D), a right frontal cortical intracranial melanoma metastasis (arrowhead) is more conspicuous on TI-SPACE (C) than on MPRAGE (D), albeit subtle on both sequences.

The reasons for the differences in the conspicuity of some lesions between the 2 sequences are not clear. They may not be entirely related to a visible difference in the T1 signal of the lesions, but, in part, to differences in the signal of the background brain parenchyma. Specifically, most small IMM are located at the interface between the cortex and the leptomeninges,<sup>13</sup> in contrast to the gray-white matter junction more typical of metastases from other primaries;<sup>14</sup> and 3D-GRE inherently produces better gray-white matter differentiation than 3D-TSE.<sup>2</sup> Thus, the relatively lower signal of the cortex with 3D-GRE facilitates the identification of T1H located within it, which may account for some of the differences in conspicuity, especially when lesions exhibit more subtle T1H. In some lesions, the coexistence of melanin and blood products may have also been a factor, given that a GRE technique is inherently more sensitive to blood products. We note that 3D-TSE was performed with fat saturation, as recommended in the aforementioned consensus guidelines.<sup>2</sup> While it is not feasible to perform fat saturation with 3D-GRE sequences,<sup>2</sup> a similar effect was achieved by performing MPRAGE with a water excitation technique.<sup>15</sup> We consider it unlikely that the differences in fat-suppression techniques would affect the conspicuity of T1H, though we cannot be certain. Despite these additional considerations, our impression is that a component of the difference does indeed reflect greater sensitivity to melanin using a 3D-GRE technique.

There is the potential for selection bias in our study because patients were identified on the basis of T1H having been identified on previous 3D-GRE imaging, though we think that this feature would have had little effect, if at all. This was necessary logistically, given that only a minority of MR imaging examinations had evidence of T1H. Nevertheless, we think that identifying patients prospectively, before the study examination had been performed, would have been less prone to bias than a purely retrospective analysis.

**Table 3: Interobserver agreement for comparing the conspicuity of T1H between TI-SPACE and MPRAGE**

		Reader 2			Total
		Better or Only on MPRAGE	Similar Conspicuity	Better or Only on TI-SPACE	
Reader 1	Better or only on MPRAGE	164 (76.6%)	17 (7.9%)	0	181 (84.6%)
	Similar conspicuity	5 (2.3%)	24 (11.2%)	2 (0.9%)	31 (14.4%)
	Better or only on TI-SPACE	0	0	2 (0.9%)	2 (0.9%)
Total		169 (79.0%)	41 (19.2%)	4 (1.9%)	214

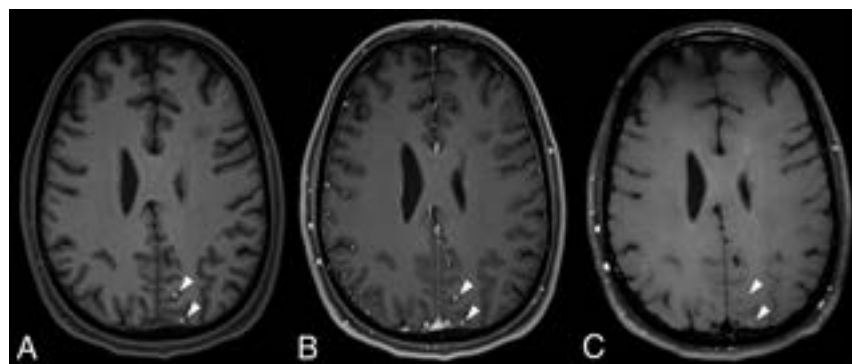


**FIG 3.** Precontrast MPRAGE (A), postcontrast MPRAGE (B), and postcontrast TI-SPACE (C) images showing 2 left parietal IMM demonstrating T1H (arrowheads), which are most conspicuous on the precontrast MPRAGE images (A). They are relatively less obvious on the postcontrast MPRAGE image (B) due to the enhancement of normal vessels and are barely visible on postcontrast TI-SPACE (C).

## CONCLUSIONS

T1H is overall more conspicuous with MPRAGE than T1-SPACE, both for melanin and blood products. Therefore, precontrast 3D-GRE should be preferred over 3D-TSE in patients with metastatic melanoma in whom both 3D-GRE and 3D-TSE are performed postcontrast or when not administering IV contrast, and it may aid in the diagnosis in patients with metastatic disease from an unknown primary. It is also important to be aware of potential differences in the appearances if using different T1WI sequences pre- and postcontrast.

Disclosure forms provided by the authors are available with the full text and PDF of this article at [www.ajnr.org](http://www.ajnr.org).

## REFERENCES

1. Suh CH, Jung SC, Kim KW, et al. **The detectability of brain metastases using contrast-enhanced spin-echo or gradient-echo images: a systematic review and meta-analysis.** *J Neurooncol* 2016;129:363–71 CrossRef Medline
2. Kaufmann TJ, Smits M, Boxerman J, et al. **Consensus recommendations for a standardized brain tumor imaging protocol for clinical trials in brain metastases.** *Neuro Oncol* 2020;22:757–72 CrossRef Medline
3. Ginat DT, Meyers SP. **Intracranial lesions with high signal intensity on T1-weighted MR images: differential diagnosis.** *Radiographics* 2012;32:499–516 CrossRef Medline
4. Bordia R, Zhong H, Lee J, et al. **Melanoma brain metastases: correlation of imaging features with genomic markers and patient survival.** *J Neurooncol* 2017;131:341–48 CrossRef Medline
5. Lasocki A, McArthur GA. **Correlation of MRI signal characteristics of intracranial melanoma metastases with BRAF mutation status.** *Melanoma Res* 2022;32:373–78 CrossRef Medline
6. Byrne TN, Cascino TL, Posner JB. **Brain metastasis from melanoma.** *J Neurooncol* 1983;1:313–17 CrossRef Medline
7. Ong BC, Stuckey SL. **Susceptibility weighted imaging: a pictorial review.** *J Med Imaging Radiat Oncol* 2010;54:435–49 CrossRef Medline
8. Hsu CC, Haacke EM, Heyn CC, et al. **The T1 shine through effect on susceptibility weighted imaging: an under recognized phenomenon.** *Neuroradiology* 2018;60:235–37 CrossRef Medline
9. Lasocki A, Caspersz L, McArthur GA. **Prospective comparison of volumetric post-contrast T1-sampling perfection with application optimized contrasts by using different flip angle evolutions and magnetization-prepared rapid acquisition with gradient echo in patients with metastatic melanoma.** *Neuroradiol J* 2023;36:169–75 CrossRef Medline
10. Goncalves Filho AL, Longo MG, Conklin J, et al. **MRI highly accelerated wave-CAIPI T1-SPACE versus standard T1-SPACE to detect brain gadolinium-enhancing lesions at 3T.** *J Neuroimaging* 2021;31:893–901 CrossRef Medline
11. Kammer NN, Copenrath E, Treitl KM, et al. **Comparison of contrast-enhanced modified T1-weighted 3D TSE black-blood and 3D MP-RAGE sequences for the detection of cerebral metastases and brain tumours.** *Eur Radiol* 2016;26:1818–25 CrossRef Medline
12. Nagao E, Yoshiura T, Hiwatashi A, et al. **3D turbo spin-echo sequence with motion-sensitized driven-equilibrium preparation for detection of brain metastases on 3T MR imaging.** *AJNR Am J Neuroradiol* 2011;32:664–70 CrossRef Medline
13. Lasocki A, Khoo C, Lau PK, et al. **High-resolution MRI demonstrates that more than 90% of small intracranial melanoma metastases develop in close relationship to the leptomeninges.** *Neuro-oncology* 2020;22:423–32 CrossRef Medline
14. Smirniotopoulos JG, Murphy FM, Rushing EJ, et al. **Patterns of contrast enhancement in the brain and meninges.** *Radiographics* 2007;27:525–51 CrossRef Medline
15. Altun E, Semelka RC, Dale BM, et al. **Water excitation MPRAGE: an alternative sequence for postcontrast imaging of the abdomen in noncooperative patients at 1.5 Tesla and 3.0 Tesla MRI.** *J Magn Reson Imaging* 2008;27:1146–54 CrossRef Medline

# CT Perfusion Does Not Modify the Effect of Reperfusion in Patients with Acute Ischemic Stroke Undergoing Endovascular Treatment in the ESCAPE-NA1 Trial

N.B. Rex, R.V. McDonough, J.M. Ospel, N. Kashani, A. Sehgal, J.C. Fladt, R.A. McTaggart, R. Nogueira, B. Menon, A.M. Demchuk, M. Tymianski, M.D. Hill, and M. Goyal, on behalf of the ESCAPE-NA1 Investigators



## ABSTRACT

**BACKGROUND AND PURPOSE:** Although reperfusion is associated with improved outcomes in patients with acute ischemic stroke undergoing endovascular treatment, many patients still do poorly. We investigated whether CTP modifies the effect of near-complete reperfusion on clinical outcomes, ie, whether poor clinical outcomes despite near-complete reperfusion can be partly or fully explained by CTP findings.

**MATERIALS AND METHODS:** Data are from the Safety and Efficacy of Nerinetide in Subjects Undergoing Endovascular Thrombectomy for Stroke (ESCAPE-NA1) trial. Admission CTP was processed using RAPID software, generating relative CBF and CBV volume maps at standard thresholds. CTP lesion volumes were compared in patients with-versus-without near-complete reperfusion. Associations between each CTP metric and clinical outcome (90-day mRS) were tested using multivariable logistic regression, adjusted for baseline imaging and clinical variables. Treatment-effect modification was assessed by introducing CTP lesion volume  $\times$  reperfusion interaction terms in the models.

**RESULTS:** CTP lesion volumes and reperfusion status were available in 410/1105 patients. CTP lesion volumes were overall larger in patients without near-complete reperfusion, albeit not always statistically significant. Increased CBF <34%, CBV <34%, CBV <38%, and CBV <42% lesion volumes were associated with worse clinical outcome (ordinal mRS) at 90 days. CTP core lesion volumes did not modify the treatment effect of near-complete recanalization on clinical outcome.

**CONCLUSIONS:** CTP did not modify the effect of near-complete reperfusion on clinical outcomes. Thus, CTP cannot explain why some patients with near-complete reperfusion have poor clinical outcomes.

**ABBREVIATIONS:** AIS = acute ischemic stroke; eTICI = expanded TICI; EVT = endovascular treatment; LVO = large-vessel occlusion; rCBF = relative CBF

The goal of endovascular treatment (EVT) of stroke is reperfusion of ischemic brain tissue via recanalization of the occluded blood vessel, the latter of which is measured by the expanded TICI (eTICI) score. While recanalization is almost

always required to achieve good clinical outcomes, it is by no means a guarantee for favorable outcome.<sup>1</sup> On the contrary, many patients in whom near-complete recanalization can be achieved (final eTICI 2c–3) still do poorly. The reasons for this apparent discrepancy are manifold and may include “futile” recanalization (leading to reperfusion of tissue that is already irreversibly damaged), postprocedural complications (eg, pulmonary embolism, aspiration, and urinary tract infections), as well as lacking reperfusion at the tissue level despite angiographic vessel recanalization as assessed by the eTICI score.

CTP is often performed as part of acute ischemic stroke (AIS) imaging in addition to noncontrast CT and CTA alone.<sup>2–4</sup> It relies on tracking of a contrast bolus after IV injection of iodinated contrast via repeat imaging (45–90 times). These repeat measurements are then used to generate time-to-maximum, relative CBF (rCBF), and CBV maps. These various CTP measures are thought to capture the “depth” of ischemia and may explain the discrepancy between near-complete angiographic reperfusion and poor clinical outcomes in some patients undergoing EVT.

Received March 28, 2023; accepted after revision June 27.

From the Department of Diagnostic Imaging (N.B.R., R.A.M.), Brown University, Providence, Rhode Island; Departments of Diagnostic Imaging (N.B.R., R.V.M., J.M.O., B.M., A.M.D., M.D.H., M.G.), and Clinical Neurosciences (J.M.O., A.S., J.C.F., B.M., A.M.D., M.D.H., M.G.), University of Calgary, Calgary, Alberta, Canada; Department of Neurosurgery (N.K.), University of Saskatchewan, Saskatoon, Saskatchewan, Canada; Department of Neurology and Stroke Center (J.C.F.), University Hospital Basel, Basel, Switzerland; Department of Neurology and Neurosurgery (R.N.), University of Pittsburgh School of Medicine, Pittsburgh, Pennsylvania; and NoNO Inc (M.T.), Toronto, Ontario, Canada.

The ESCAPE-NA1 trial was funded by the Canadian Institutes of Health Research, Alberta Innovates and NoNO Inc.

Please address correspondence to Mayank Goyal, MD, Departments of Diagnostic Imaging and Clinical Neurosciences, Foothills Medical Centre, 1403 29th St NW, University of Calgary, Calgary, Alberta, T2N2T9, Canada; e-mail: mgoyal@ucalgary.ca; @johanna\_ospel; @rosevcmd; @mayank\_GO; @joachimfladt

Indicates open access to non-subscribers at www.ajnr.org

<http://dx.doi.org/10.3174/ajnr.A7954>

We therefore, investigated whether CTP parameters modify the effect of reperfusion status on clinical outcomes in patients with AIS undergoing EVT and whether CTP information improves prognostic performance regarding clinical outcome in patients with EVT with near-complete reperfusion.

## MATERIALS AND METHODS

### Patient Sample

This study is a post hoc analysis of the Safety and Efficacy of Nerinetide in Subjects Undergoing Endovascular Thrombectomy for Stroke (ESCAPE-NA1), trial (clinicaltrials.gov: NCT02930018), a double-blind, multicenter, randomized controlled trial that evaluated the efficacy of nerinetide in patients with AIS who underwent EVT.<sup>5</sup> Patients were randomly allocated to receive either IV nerinetide versus a placebo in addition to best medical management, including IV alteplase if indicated. Inclusion criteria were as follows: the presence of a large-vessel occlusion (LVO), moderate-to-good collateral circulation, ASPECTS of  $\geq 5$ , at least 18 years of age, NIHSS score of  $> 5$ , functional independence before the stroke (Barthel index  $> 90$ ), and time since last known well of  $< 12$  hours. Perfusion imaging was performed as part of clinical routine at each respective site, but it was not mandated by the trial. Appropriate ethics and local regulatory approval were required at each site, as was signed informed consent from participants, a legally authorized representative, or the investigators using 2-physician consent when required by national laws or regulations.

**Imaging Analysis.** All imaging was assessed by a Central Imaging Core Lab that was blinded to treatment allocation and clinical outcomes.

The ASPECTS was assessed on baseline NCCT. Occlusion location on multiphase CTA was reported as either the terminal ICA or the M1 or M2 segment of the MCA.

Perfusion source images, when available, were processed using RAPID perfusion software, Version 5.2.2 (iSchemaView) to generate standard rCBF and CBV volumes. The standard RAPID workflow followed for each patient in this study generated 4 rCBF volumes ( $< 20\%$ ,  $< 30\%$ ,  $< 34\%$ ,  $< 38\%$ ), and 3 CBV volumes ( $< 34\%$ ,  $< 38\%$ ,  $< 42\%$ ). These thresholds were chosen because they are the values provided in the standard RAPID output that have been previously validated<sup>6</sup> and are commonly used in clinical practice. All output DICOMs were converted to NIFTI using `dcm2niix` (<http://www.github.com/rordenlab/dcm2niix>) and then underwent automated segmentation using color-based thresholding in Python, Version 3.10 (<http://www.python.org>). Segmentation volumes for each threshold were extracted using 3D Slicer, Version 5.0.2 (<http://www.slicer.org>). Segmentation volumes were extracted using the built-in Segmentation Statistics functionality of 3D Slicer. All Slicer-generated output volumes were confirmed and rounded to the nearest milliliter of the original RAPID generated output, validating the fidelity of this approach. Key Python functions necessary for reproduction of feature extraction and processing are detailed on Github ([https://github.com/naterex23/RAPID\\_Perfusion\\_Processing](https://github.com/naterex23/RAPID_Perfusion_Processing)), and the additional Python source code is available on reasonable request.

eTICI was assessed on the final intracranial DSA run. Near-complete reperfusion was defined as eTICI 2c–3, ie,  $> 90\%$  reperfusion of the target territory.

**Outcome Measures.** The primary outcome was functional outcome as measured by the mRS at 90 days, which was assessed blinded to treatment allocation. To perform receiver operating characteristic analysis, we dichotomized the mRS into good outcome (mRS 0–2) versus no good outcome (mRS 3–6).

**Statistical Analysis.** Baseline characteristics, clinical outcomes, and CTP lesion volumes in patients with-versus-without near-complete recanalization were reported using descriptive statistics as appropriate.

We then performed adjusted ordinal logistic regression using the ordinal mRS at 90 days as a dependent variable and the following, prespecified independent variables: age (in years), sex, NIHSS score, treatment allocation (nerinetide versus placebo), alteplase treatment, baseline ASPECTS, collateral score (poor versus moderate versus good), time from onset to CT, final eTICI (eTICI 2c–3 versus none), and CTP lesion volume. Separate models were constructed for each CTP parameter (ie, CBF  $< 20\%$ , CBF  $< 30\%$ ,  $< \text{CBF} < 34\%$ , CBF  $< 38\%$ , CBV  $< 34\%$ , CBV  $< 38\%$ , CBV  $< 42\%$ ). Each model included a multiplicative two-by-two CTP lesion volume  $\times$  near-complete reperfusion interaction term to investigate whether CTP lesion volumes modify the effect of near-complete reperfusion on outcome.

To further investigate whether CTP lesion volumes could explain the variance in clinical outcomes in patients with near-complete reperfusion, we compared CTP lesion volumes in patients with eTICI 2c–3 with versus without good clinical outcomes. We further compared the prognostic performance of logistic regression models containing prespecified baseline variables (age, sex, NIHSS score, treatment allocation, alteplase treatment, baseline ASPECTS, collateral score [poor versus moderate versus good], time from onset to CT imaging) versus those containing additional CTP lesion volumes. Model performance was assessed using the area under the curve and the Akaike and Bayesian information criterion.

In case the initial interaction analyses were not significant, the above-mentioned subgroup analyses in patients with eTICI 2c–3 were considered purely exploratory.

Statistical analysis was conducted using STATA 17 (StatCorp), and *P* values  $< .05$  were considered statistically significant.

## RESULTS

### Patient Characteristics

Of the 1105 patients enrolled in ESCAPE-NA1, 426 had available CTP imaging. CTP quality was judged to be insufficient for analysis in 13 patients, and final reperfusion status could not be assessed in 3 patients, leaving 410 patients for the analysis. Table 1 compares baseline and treatment characteristics of patients with versus without near-complete reperfusion, which did not differ significantly between the groups. Although CTP lesion volumes were nominally larger in patients without near-complete reperfusion irrespective of the CTP threshold used, this difference

**Table 1: Baseline and treatment characteristics of patients with-versus-without near-complete reperfusion (eTICI 2c-3)**

Variable	Near-Complete Reperfusion (n = 186)	No Near-Complete Reperfusion (n = 224)	P Value
Age (median) (IQR) (yr)	71.1 (61.2–80.1), n = 186	69.3 (58.4–79.6), n = 224	.12
Baseline NIHSS (median) (IQR)	18 (12–21), n = 186	17 (13–20), n = 224	.29
History of diabetes (No.) (%)	31/186 (16.7%)	46/224 (20.5%)	.55
History of past stroke/TIA (No.) (%)	24/186 (12.9%)	33/224 (14.7%)	.67
History of prior cardiac disease (No.) (%)	49/186 (26.3%)	47/224 (21.0%)	.24
Baseline ASPECTS (median) (IQR)	8 (7–9), n = 186	8 (6–8), n = 224	.13
Collateral score (No.) (%)			.06
Poor	2/186 (1.1%)	11/218 (5.1%)	
Moderate	154/186 (82.8%)	178/218 (81.7%)	
Good	30/186 (16.1%)	29/218 (13.3%)	
Study drug to reperfusion time (median) (IQR) (min)	22 (9–39), n = 182	26 (12–52), n = 170	.17
Terminal ICA occlusion (No.) (%)	28/186 (15.1%)	44/223 (19.7%)	.24
IV alteplase (No.) (%)	110/186 (59.1%)	122/224 (54.5%)	.37
IV nerinete (No.) (%)	89/186 (47.9%)	107/224 (47.8%)	1.00
Stent retriever as first-line device (No.) (%)	150/204 (73.5)	142/176 (80.7)	.103
Carotid stent placement during EVT	22/110 (20.0)	12/81 (14.8)	.445

Note:—IQR indicates interquartile range.

**Table 2: CTP lesion volumes in patients with-versus-without near-complete reperfusion<sup>a</sup>**

CTP Parameter (Median) (IQR)	Near-Complete Reperfusion (n = 186)	No Near-Complete Reperfusion (n = 224)	P Value
CBF <20%	0 (0–0)	0 (0–7.5)	<.01
CBF <30%	7.6 (0–28.1)	12.0 (0–32.1)	.06
CBF <34%	14.3 (2.7–39.4)	19.1 (5.2–47.2)	.10
CBF <38%	21.3 (7.1–54.8)	26.4 (9.9–60.9)	.20
CBV <34%	5.1 (0–28.1)	9.8 (0–33.3)	.07
CBV <38%	6.7 (0–35.6)	13.3 (0–39.0)	.048
CBV <42%	10.1 (0–41.2)	17.9 (4.6–46.0)	.06

Note:—IQR indicates interquartile range.

<sup>a</sup>Data in columns 2 and 3 are medians and interquartile ranges.

**Table 3: CTP lesion volumes in patients with near-complete reperfusion who did and did not achieve good outcome at 90 days<sup>a</sup>**

CTP Parameter (Median) (IQR)	Near-Complete Reperfusion with No Good Outcome (n = 54)	No Near-Complete Reperfusion with Good Outcome (n = 132)	P Value
CBF <20%	0 (0–6.9)	0 (0–0)	.02
CBF <30%	12.2 (4.4–38.6)	6.0 (0–22.2)	.01
CBF <34%	20.6 (8.1–53.0)	13.0 (0–33.6)	.02
CBF <38%	33.4 (13.4–73.0)	18.4 (6.6–46.4)	.0495
CBV <34%	12.2 (2.9–43.2)	0 (0–20.6)	<.01
CBV <38%	19.0 (4.9–54.2)	4.7 (0–23.1)	<.01
CBV <42%	21.8 (6.4–66.7)	6.5 (0–28.5)	<.01

Note:—IQR indicates interquartile range.

<sup>a</sup>When comparing the performance of multivariable logistic regression models in predicting good outcome at 90 days in patients with near-complete recanalization, model performance slightly increased and information loss decreased when CTP lesion volumes were added in addition to baseline variables, though the area under the curve confidence intervals overlapped (Table 4). Data in columns 2 and 3 are medians and interquartile ranges.

reached statistical significance only when using the CBF <20% threshold (Table 2).

### Multivariable Logistic Regression with Two-by-Two Interaction Terms

In the adjusted analysis, none of the CTP lesion volume × reperfusion status interaction terms were significant; thus, the subgroup analyses below were considered exploratory. Of all the CTP lesion volumes, CBF <34% (adjusted OR = 1.01; 95% CI, 1.0001–1.017 per milliliter increase), CBV <34% (adjusted OR =

1.01; 95% CI, 1.001–1.02 per milliliter increase), CBV <38% (adjusted OR = 1.01; 95% CI, 1.001–1.02 per milliliter increase), and CBV <42% (adjusted OR = 1.01; 95% CI, 1.000–1.02 per milliliter increase) were predictors of clinical outcome (ordinal mRS) at 90 days.

### Exploratory Subgroup Analyses in Patients with Near-Complete Reperfusion

In patients with near-complete reperfusion (eTICI 2c-3), CTP lesion volumes were higher in patients without-versus-with good outcome (Table 3). Model performance as measured by the AUC, AIC, BIC and pseudo-R squared improved slightly when CTP parameters were included in the model, although the AUC 95% CI overlapped (Table 4).

### DISCUSSION

This post hoc analysis of the ESCAPE-NA1 trial suggests that patients having undergone EVT with small CTP lesion volumes at baseline generally do better compared with those with larger CTP lesions, but CTP did not modify the effect of near-complete reperfusion on

clinical outcomes. In other words, CTP is a prognostic marker for post-EVT outcomes, but it cannot explain why some patients have poor outcomes despite near-complete recanalization.

There are many reasons why patients undergoing successful EVT with near-complete recanalization still do not do well. For example, reperfusion injury may lead to formation of reactive oxygen species, apoptosis may be induced by oxidative stress, and edema progression or poststroke complications such as pulmonary embolism or pneumonia may occur.<sup>7,8</sup> Another potential explanation is futile reperfusion, ie, reperfusion of tissue that is already irreversibly damaged. Establishing reperfusion in such

**Table 4: Performance of multivariable logistic regression models without and with CTP lesion volumes in predicting good outcome at 90 days in patients with near-complete recanalization**

Model	Pseudo-R <sup>2</sup>	BIC	AIC	AUC (95% CI)
Baseline variables only <sup>a</sup>	0.302	203.6	174.5	0.766 (0.718–0.813)
Baseline variables + CBF <20% volume	0.336	201.1	168.9	0.782 (0.735–0.829)
Baseline variables + CBF <30% volume	0.357	196.4	164.2	0.785 (0.739–0.831)
Baseline variables + CBF <34% volume	0.359	196.0	163.8	0.784 (0.738–0.830)
Baseline variables + CBF <38% volume	0.359	195.8	163.6	0.781 (0.735–0.828)
Baseline variables + CBV <34% volume	0.343	199.5	167.2	0.778 (0.731–0.824)
Baseline variables + CBV <38% volume	0.346	198.8	166.5	0.779 (0.732–0.825)
Baseline variables + CBV <42% volume	0.349	198.1	165.9	0.779 (0.732–0.825)

**Note:**—AIC indicates Akaike information criterion; BIC, Bayesian information criterion; AUC, area under the curve; Pseudo-R<sup>2</sup>, pseudo-R squared.

<sup>a</sup>Baseline variables were prespecified and included age (in years), sex, NIHSS, treatment allocation (nerinetide versus placebo), alteplase treatment, baseline ASPECTS, collateral score (poor versus moderate versus good), and time from onset to CT imaging.

tissue only exposes the patient to risk of hemorrhage, without restoring brain function. The single most important parameter that determines the infarct progression rate and hence the time-point at which recanalization becomes futile is collateral blood supply, which, in turn, is influenced by a number of factors including patient age, pre-existing vascular conditions, as well as other comorbidities (eg, hypertension, hyperglycemia).<sup>9</sup>

So-called fast progressors with poor collateral status are more likely to show completed infarcts before treatment is initiated (and thus do not benefit from recanalization) compared with slow progressors. Noncontrast CT is not able to accurately delineate irreversibly damaged tissue from ischemic tissue that can be salvaged. Advanced imaging methods such as MR imaging and CTP provide additional information on brain tissue hemodynamics over and beyond noncontrast CT and CTA.<sup>10</sup> Of note, CTP provides estimates about tissue viability rather than precise measurements and, therefore, should not be used to exclude patients from treatment in the early time window. However, it undoubtedly contains more information about tissue viability than NCCT and CTA alone. One may, therefore, argue that the depth of ischemia as characterized by CTP imaging findings may be able to explain the discrepancy between technical EVT success (near-complete reperfusion) and poor clinical outcomes. Patients with “deep” and extensive ischemia on CTP maps (large CTP core volumes with low CBV and CBF values compared with the unaffected hemisphere) may not benefit as much from near-complete reperfusion compared with patients with less severe and less extensive ischemia.

If this was the case, CTP would modify the effect of reperfusion on clinical outcomes. In our study, we did not find evidence of such an interaction effect for any of the CTP lesion thresholds tested. In other words, CTP is unlikely to explain the discrepancy between technical EVT success and poor clinical outcomes, perhaps due to the inability of a single CTP threshold to accurately distinguish between irreversibly and reversibly damaged tissue. Because tissue tolerance to ischemia is influenced by many factors including patient and tissue heterogeneity, a single universal CTP threshold (as it is used in clinical practice and hence also in this analysis) seems unlikely to accurately delineate the “true infarct core.”<sup>11</sup> In fact, it has been shown that such binary CTP maps often overestimate ischemic changes (“ghost core”).<sup>12</sup>

It has previously been suggested that IV thrombolysis, which is still explicitly recommended in addition to EVT by the current European and North American guidelines,<sup>2,13</sup> may restore tissue perfusion by dissolving microscopic thrombi in the microcirculation that persist even after macroscopic recanalization has been achieved, thereby exerting a “clearing” effect that improves clinical outcomes.<sup>14</sup> In other words, IV thrombolysis treatment could help to reduce the discrepancy between recanalization success and poor clinical outcomes, though the current study was underpowered to determine whether

such an effect truly exists. Ultimately, the reasons why some patients do poorly despite technical EVT success remain unclear and may include postprocedural complications such as poststroke pneumonia and pulmonary embolism and potentially reduced brain reserve (“brain frailty”) in some patients. The exact underlying reasons and extent to which they contribute to this phenomenon should be investigated in future studies.

### Limitations

This study has several limitations. First, we batch-processed perfusion studies from multiple sites with different sequence acquisition settings and CT machines through the RAPID software algorithm, which has introduced some heterogeneity into our data. Second, most of the patient population included in this study presented within 6 hours from onset and, therefore, did not meet guideline-based recommendations for CTP imaging, the latter being restricted to patients in the late window. CTP was simply part of the acute stroke imaging protocol in many participating sites, irrespective of the time of patient presentation. Thus, the generalizability of our results is mostly limited to patients presenting in the early time window. Furthermore, the ESCAPE-NA1 trial was a pragmatic trial that allowed sites to use their locally established imaging protocols, and, thus, no standardization of imaging parameters (eg, section thickness, contrast volume, and so forth) was required, which led to heterogeneity of the available imaging data. Third, just like any randomized trial, the ESCAPE-NA1 trial had rather stringent inclusion and exclusion criteria, and our patient sample is, therefore, not representative of the general EVT population.

### CONCLUSIONS

Large baseline CTP lesion volumes are associated with worse outcomes in patients with AIS-LVO undergoing EVT, but CTP does not modify the effect of near-complete reperfusion on clinical outcomes in these patients. Therefore, CTP cannot explain why some patients with LVO have poor outcomes despite near-complete recanalization following EVT.

Disclosure forms provided by the authors are available with the full text and PDF of this article at [www.ajnr.org](http://www.ajnr.org).

## REFERENCES

1. Cho TH, Nighoghossian N, Mikkelsen IK, et al. **Reperfusion within 6 hours outperforms recanalization in predicting penumbra salvage, lesion growth, final infarct, and clinical outcome.** *Stroke* 2015;46:1582–89 CrossRef Medline
2. Powers WJ, Rabinstein AA, Ackerson T, et al. **Guidelines for the Early Management of Patients with Acute Ischemic Stroke: 2019 Update to the 2018 Guidelines for the Early Management of Acute Ischemic Stroke—A Guideline for Healthcare Professionals from the American Heart Association/American Stroke Association.** *Stroke* 2019;50:e344–418 CrossRef Medline
3. Albers GW, Marks MP, Kemp S, et al; DEFUSE 3 Investigators. **Thrombectomy for stroke at 6 to 16 hours with selection by perfusion imaging.** *N Engl J Med* 2018;378:708–18 CrossRef Medline
4. Nogueira RG, Jadhav AP, Haussen DC, et al; DAWN Trial Investigators. **Thrombectomy 6 to 24 hours after stroke with a mismatch between deficit and infarct.** *N Engl J Med* 2018;378:11–21 CrossRef Medline
5. Hill MD, Goyal M, Menon BK, et al; ESCAPE-NA1 Investigators. **Efficacy and safety of nerinetide for the treatment of acute ischaemic stroke (ESCAPE-NA1): a multicentre, double-blind, randomised controlled trial.** *Lancet* 2020;395:878–87 CrossRef Medline
6. Mokin M, Levy EI, Saver J, et al; SWIFT PRIME Investigators. **Predictive value of RAPID assessed perfusion thresholds on final infarct volume in SWIFT PRIME (Solitaire With the Intention for Thrombectomy as Primary Endovascular Treatment).** *Stroke* 2017;48:932–38 CrossRef Medline
7. Ospel J, Rex N, Kandregula S, et al. **The vessel has been recanalized: now what?** *Neurotherapeutics* 2023;20:679–92 CrossRef Medline
8. Broocks G, McDonough R, Meyer L, et al. **Reversible ischemic lesion hypodensity in acute stroke CT following endovascular reperfusion.** *Neurology* 2021;97:e1075–84 CrossRef Medline
9. Saber H, Liebeskind DS. **Infarct progression in the early and late phases of acute ischemic stroke.** *Neurology* 2021;97:S60–67 CrossRef Medline
10. DiBiasio EL, Jayaraman MV, Goyal M, et al. **Dismantling the ability of CT and MRI to identify the target mismatch profile in patients with anterior circulation large vessel occlusion beyond six hours from symptom onset.** *Emerg Radiol* 2019;26:401–08 CrossRef Medline
11. Goyal M, Ospel JM, Menon B, et al. **Challenging the ischemic core concept in acute ischemic stroke imaging.** *Stroke* 2020;51:3147–55 CrossRef Medline
12. Martins N, Aires A, Mendez B, et al. **Ghost infarct core and admission computed tomography perfusion: redefining the role of neuroimaging in acute ischemic stroke.** *Interv Neurol* 2018;7:513–21 CrossRef Medline
13. Turc G, Tsivgoulis G, Audebert HJ, et al. **European Stroke Organisation: European Society for Minimally Invasive Neurological Therapy expedited recommendation on indication for intravenous thrombolysis before mechanical thrombectomy in patients with acute ischaemic stroke and anterior circulation large vessel occlusion.** *Eur Stroke J* 2022;7:1–XXVI CrossRef Medline
14. Desilles JP, Loyau S, Syvannarath V, et al. **Alteplase reduces downstream microvascular thrombosis and improves the benefit of large artery recanalization in stroke.** *Stroke* 2015;46:3241–48 CrossRef Medline

# Intra-Arterial Thrombolysis is Associated with Delayed Reperfusion of Remaining Vessel Occlusions following Incomplete Thrombectomy

A. Mujanovic, C.C. Kurmann, B.L. Serrallach, T. Dobrocky, T.R. Meinel, D. Windecker, L. Grunder, M. Beyeler, D.J. Seiffge, S. Pilgram-Pastor, M. Arnold, E.I. Piechowiak, J. Gralla, U. Fischer, and J. Kaesmacher



## ABSTRACT

**BACKGROUND AND PURPOSE:** Intra-arterial thrombolytics may be used to treat distal vessel occlusions, which cause incomplete reperfusion following mechanical thrombectomy. Because immediate reperfusion after intra-arterial thrombolytics occurs rarely, the aim of this study was to assess the delayed effect of intra-arterial thrombolytics using follow-up perfusion imaging.

**MATERIALS AND METHODS:** We included patients from a prospective stroke registry (February 2015 to September 2022) who had undergone mechanical thrombectomy and had incomplete reperfusion (expanded TICI 2a–2c) and available 24 hour perfusion imaging. Perfusion imaging was rated as delayed reperfusion if time-sensitive perfusion maps did not show wedge-shaped delays suggestive of persisting occlusions corresponding to the post-mechanical thrombectomy angiographic deficit. Patients treated with intra-arterial thrombolytics were compared with controls using multivariable logistic regression and inverse probability of treatment weighting matching for baseline differences and factors associated with delayed reperfusion.

**RESULTS:** The median age of the final study population ( $n = 459$ ) was 74 years (interquartile range, 63–81 years), and delayed reperfusion occurred in 61% of cases. Patients treated with additional intra-arterial thrombolytics ( $n = 40$ ) were younger and had worse expanded TICI scores. After matching was performed, intra-arterial thrombolytics was associated with higher rates of delayed reperfusion (adjusted OR = 2.7; 95% CI, 1.1–6.4) and lower rates of new infarction in the residually hypoperfused territory after mechanical thrombectomy (adjusted OR = 0.3; 95% CI, 0.1–0.7). No difference was found in the rates of functional independence (90-day mRS, 0–2; adjusted OR = 1.4; 95% CI, 0.4–4.1).

**CONCLUSIONS:** Rescue intra-arterial thrombolytics is associated with delayed reperfusion of remaining vessel occlusions following incomplete mechanical thrombectomy. The value of intra-arterial thrombolytics as a potential therapy for incomplete reperfusion after mechanical thrombectomy should be assessed in the setting of randomized controlled trials.

**ABBREVIATIONS:** aOR = adjusted OR; DR = delayed reperfusion; eTICI = expanded TICI; IA = intra-arterial; IAT = intra-arterial thrombolytics; IPTW = inverse probability of treatment weighting; IQR = interquartile range; MT = mechanical thrombectomy; sICH = symptomatic intracranial hemorrhage

Rates of complete reperfusion (expanded TICI [eTICI] score 3) are continuously improving, yet more than one-half of endovascularly treated patients with stroke either have no reperfusion or reperfusion is incomplete ( $< eTICI$  3).<sup>1,2</sup> One potential adjunctive strategy in patients with incomplete reperfusion after mecha-

nical thrombectomy (MT) is the application of intra-arterial thrombolytics (IAT).<sup>3–5</sup>

Data from several older randomized clinical trials suggested that IAT increase the chances of partial or complete reperfusion by 50% compared with a placebo.<sup>6</sup> However, a recent trial that aimed to evaluate the added benefit of intra-arterial (IA) alteplase after MT showed better clinical outcomes, but no increase in the rates of early reperfusion.<sup>7</sup> A potential explanation for this discrepancy might be the time point of the reperfusion evaluation.<sup>7–9</sup>

A recent observational report stated that delayed reperfusion (DR) is associated with better clinical outcome and a lower chance for infarct growth.<sup>10</sup> However, studies on the effect of IAT post-MT and the occurrence of DR are sparse.<sup>11</sup>

We hypothesized that adjunctive IAT are associated with DR of the remaining vessel occlusions following incomplete reperfusion

Received April 14, 2023; accepted after revision June 22.

From the Departments of Diagnostic and Interventional Neuroradiology (A.M., C.C.K., B.L.S., T.D., D.W., L.G., S.P.-P., E.I.P., J.G., J.K.), Diagnostic, Interventional and Pediatric Radiology (C.C.K.), and Neurology (T.R.M., M.B., D.J.S., M.A., U.F.), University Hospital Bern, Inselspital, University of Bern, Bern, Switzerland; and Department of Neurology (U.F.), University Hospital Basel, University of Basel, Basel, Switzerland.

Please address correspondence to Johannes Kaesmacher, MD, PhD, Department of Diagnostic and Interventional Neuroradiology, University Hospital Bern Inselspital, Freiburgstrasse 10, 3001 Bern, Switzerland; e-mail: johannes.kaesmacher@insel.ch

Indicates article with online supplemental data.

<http://dx.doi.org/10.3174/ajnr.A7943>

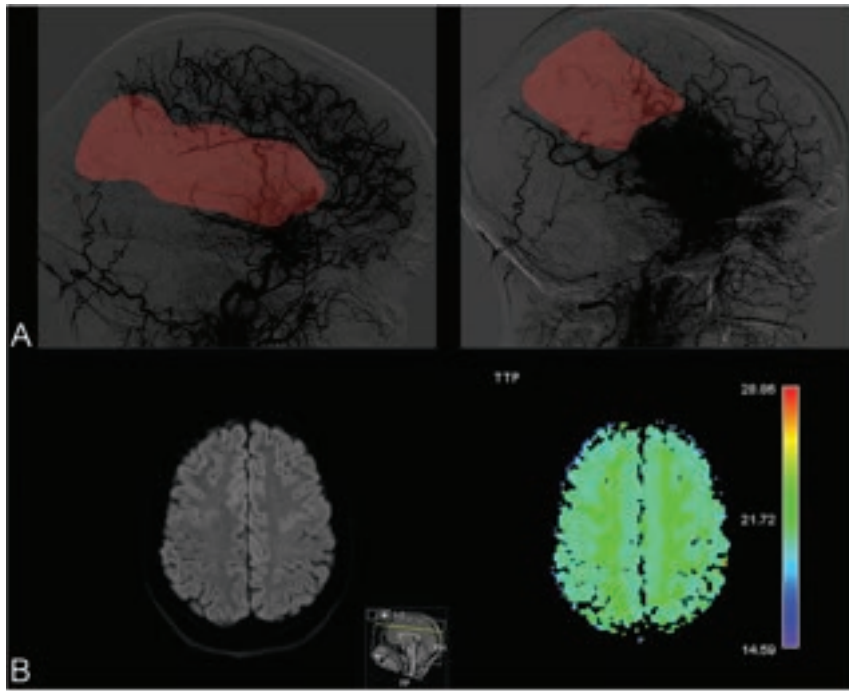


**FIG 1.** Patients with DR after IA urokinase. *A*, The first DSA shows right-sided occlusions of the MI MCA segment (*left panel*). The last DSA after MT shows that the patient has achieved reperfusion in 50% of the initial target territory (eTICI 2b50) (*right panel*). DSA runs are shown with high contrast in order to emphasize the capillary phase deficits. *Areas in red* show nonreperfused territory. *B*, Follow-up MR imaging performed 24 hours after the end of the intervention. DWI shows no signs of a new infarct despite incomplete reperfusion on the final DSA series (*left panel*). Postprocessed perfusion imaging shows DR with no residual perfusion deficit (*right panel*).

with thrombectomy, and we assessed the potential delayed effects of IAT on follow-up perfusion imaging.

## MATERIALS AND METHODS

### Study Design

This was a retrospective analysis of a prospective stroke registry for all patients admitted to our institution between February 2015 and September 2022 with acute ischemic stroke. This study follows the Strengthening the Reporting of Observational Studies in Epidemiology (STROBE) reporting guidelines. Design and conduct of the study were performed in accordance with the Helsinki Declaration, and the study was approved by the ethics committee (reference ID 231/2014 and ID 2020-01696). The data set used in this study is available from the corresponding author on reasonable request and clearance by the ethics committee.

### Patient Selection and Intervention

All patients in the stroke registry were screened for eligibility. Patients who refused use of their data, did not undergo MT, or had posterior vessel occlusion were excluded. Only patients with final eTICI scores of 2a–2c and available follow-up perfusion imaging 24 (SD, 12) hours after the index stroke were included in the final analysis (Online Supplemental Data).

The indication to perform IAT was at the discretion of the neurointerventionalist. According to internal protocols,<sup>5</sup> IAT were considered when the occluded branch was supplying an eloquent area (ie, the precentral gyrus, visual cortex) and the branch

was deemed too distal for a mechanical maneuver. The same microcatheter used during MT was then navigated into the occluded vessel. The tip of the microcatheter was embedded within or just proximal to the thrombus and urokinase was infused through an injection pump for 20–30 minutes. Details on the availability and indications for IA urokinase in Switzerland have been described previously.<sup>5</sup>

### Neuroimaging Evaluation

Reperfusion was graded on the eTICI scale, according to the consensus statement.<sup>12</sup> Grades 2a, 2b50, 2b67, and 2c correspond to reperfusion of 1%–49%, 50%–66%, 67%–89%, and 90%–99% of the initially hypoperfused area, respectively. For patients who have received IAT, eTICI was graded on the last angiography run before the introduction of the microcatheter, which was used for IAT administration. On the other hand, for patients in the non-IAT group, eTICI was graded on the final angiography that was performed at the end of the intervention. Reperfusion grading was performed by a neuroradiology core lab blinded to clinical data. The American

Society of Interventional and Therapeutic Neuroradiology/Society of Interventional Radiology scale was used for collateral grading, which was performed on the initial DSA series. The grading system ranges from 0 to 4, in which the former represents no visible collaterals, and the latter, complete and rapid blood flow in the ischemic area.<sup>12</sup>

Details and methods used for perfusion imaging evaluation have been previously described (Online Supplemental Data).<sup>10</sup> Briefly, DR was rated if time-sensitive perfusion maps did not show a wedge-shaped delay suggestive of persisting occlusion, which would correspond to the postprocedural angiographic deficit (Fig 1). Inversely, if time-sensitive perfusion maps did show a wedge-shaped delay suggestive of persisting occlusion that directly corresponded to the area of a postprocedural angiographic deficit, this would be rated as a persistent perfusion deficit (Fig 2). It could be suggested that these wedge-shaped delays represent microvascular occlusions in the presence of macrovascular reperfusion (this discrepancy has been named the “no-reflow” phenomenon). However, all DR and persistent perfusion deficit evaluations were performed on TTP and time-to-maximum maps because they have been suggested to be more sensitive to macrovascular obstructions, while CBV and CBF are more informative for microvascular status.<sup>10,13</sup> Even though the probability of no-reflow might still exist, we would be hesitant to name these wedge-shaped delays as no-reflow, given the many uncertainties and discrepancies in definitions and methods of no-reflow that are currently being reported.<sup>14</sup> Four independent neuroradiologists blinded to clinical data and not involved in patient treatment

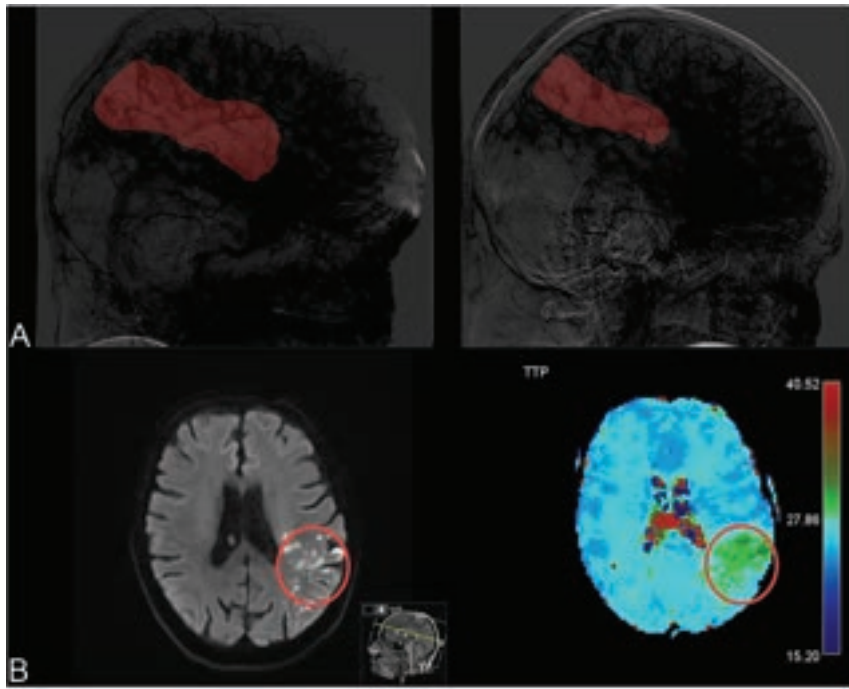


**FIG 2.** A patient with a persistent perfusion deficit after receiving IA urokinase. *A*, The first DSA shows left-sided occlusions of the M2 MCA segment (*left panel*). The last DSA series after MT shows that the patient has achieved reperfusion of 50% of the initial target territory (eTICI 2b50) (*right panel*). DSA runs are shown with high contrast in order to emphasize the capillary phase deficits. *Areas in red* show nonreperfused territory. *B*, Follow-up MR imaging performed 24 hours after the end of the intervention. DWI shows a newly developed distal infarct (*left panel*). Postprocessed perfusion imaging shows a persistent perfusion deficit that directly corresponds to the nonreperfused territory from the final DSA series (*right panel*).

performed perfusion imaging evaluation. Interrater agreement on a random sample of 50 patients was excellent (Krippendorff  $\alpha = 0.82$ ; 95% CI, 0.80–0.84).

### Primary and Secondary Outcomes

The primary outcome of this analysis was the association between IAT and DR. Secondary outcomes included the association among IAT, functional outcome at 3 months, the presence of a new infarct, and symptomatic intracranial hemorrhage (sICH) on 24-hour follow-up imaging. The mRS score 0–2 at 3 months was defined as functional independence. Functional outcome was evaluated by an independent research nurse at the scheduled follow-up visit or during the structured telephone interview 3 months after the intervention. To match the residual occlusion location with the perfusion outcome, we defined the new infarct as the infarcted area on follow-up imaging, which directly corresponds to the same area of capillary hypoperfusion observed on the final DSA run. All follow-up imaging data were also compared with the initial preinterventional imaging to confirm that the area of interest did not undergo infarction before the intervention. The definition of sICH was intracranial hemorrhage on the 24-hour follow-up imaging with an increase of  $\geq 4$  points on the NIHSS.

### Statistical Analysis

Results are reported as either No. (%) or median (interquartile range, [IQR]). Statistical analysis was performed in 2 steps. First,

multivariable logistic regression was used to report the association between perfusion imaging outcome and IAT. Regression results are reported as adjusted ORs (aORs) with corresponding 95% CIs. However, due to the limitations associated with multivariable logistic regressions when estimating causal effects in observational data,<sup>15</sup> propensity scores were calculated and the inverse probability of treatment weighting (IPTW) method was used in the second step of our analysis (Online Supplemental Data).<sup>16,17</sup>

We have performed full IPTW matching to optimize the study power and minimize the sum of within-pair differences in the propensity scores.<sup>18</sup> To reduce bias of unmeasured confounders, we included only weights distributed between the 5th and 95th percentiles.

IPTW matching was performed for all confounders that have been previously reported as associated with perfusion imaging outcome and clinical outcome: age (continuous variable), sex (binary variable), atrial fibrillation (binary variable), anticoagulants prestroke (binary variable) and antiplatelets prestroke (binary variable), onset-to-door

time (continuous variable, aOR referring to a 1-hour delay), NIHSS on admission (continuous variable, aOR referring to a 1-point increase), IV thrombolysis (binary variable), collateral status (ordinal variable with a stepwise increase), eTICI score (ordinal variable with a stepwise increase), and intervention-to-follow-up imaging time (continuous variable, aOR referring to a 1-hour delay). Intervention-to-follow-up time was defined as the time window between the final DSA series and the time of the first follow-up imaging series. All secondary outcome analyses were adjusted for the same confounders and additionally for perfusion imaging outcome (binary variable). All statistical analyses were performed in R statistical and computing software, Version 4.0.0 (<http://www.r-project.org/>). Propensity scoring and IPTW were performed with the package MatchIt, Version 4.5.0 (<https://www.rdocumentation.org/packages/MatchIt/versions/4.5.0/topics/matchit>).

### RESULTS

The final study population constituted 459 patients. The median age of the cohort was 74 (IQR = 63–81) years, 237 (51.6%) were men, and the median NIHSS score on admission was 12 (IQR = 7–18). Of 459 patients, 40 (8.7%) had received IA urokinase during the intervention (median dose, 250,000 IU; IQR = 250,000–500,000 IU). Patients who received IA urokinase were on average younger, 68.4 years (IQR = 59.9–76.1 years) versus 74 years (IQR = 63.6–81.5 years;  $P = .02$ ), were less likely to have a history of

### Baseline characteristics of study population

	Overall	IA Urokinase -	IA Urokinase +	P	Missing (%)
No.	459	419	40		
Age (median) (IQR) (yr)	74 (63–81)	74 (63–81)	68 (60–76)	.02	0
Sex male (%)	237 (51.6)	211 (50.4)	26 (65.0)	.109	0
AFib = yes (%)	151 (32.9)	141 (33.7)	10 (25.0)	.349	0
Hypertension = yes (%)	317 (69.1)	291 (69.5)	26 (65.0)	.687	0
ODT (median) (IQR) (h)	3.03 (1.68–6.62)	3.20 (1.71–7.22)	2.42 (1.37–3.60)	.021	
NIHSS on admission (median) (IQR)	12 (7–18)	13 (7–18)	11 (6–16)	.07	
SBP (median) (IQR)	151 (133–171)	151 (133–172)	148 (131–161)	.332	
DBP (median) (IQR)	80 (70–93)	80 (70–93)	82 (73–89)	.539	
Anticoagulants prestroke = yes (%)	60 (13.1)	53 (12.6)	7 (17.5)	.533	0
Antiplatelets prestroke = yes (%)	125 (27.2)	115 (27.4)	10 (25.0)	.884	0
ASPECTS (median) (IQR)	8 (7–9)	8 (6–9)	9 (7–9)	.032	18.5
ASITN/SIR collateral score (median) (IQR)	2 (1–3)	2 (1–3)	2 (2–3)	.772	0

**Note:**—AFib indicates atrial fibrillation; ODT, onset-to-door time; SBP, systolic blood pressure; DBP, diastolic blood pressure; ASITN/SIR, American Society of Interventional and Therapeutic Neuroradiology/Society of Interventional Radiology.

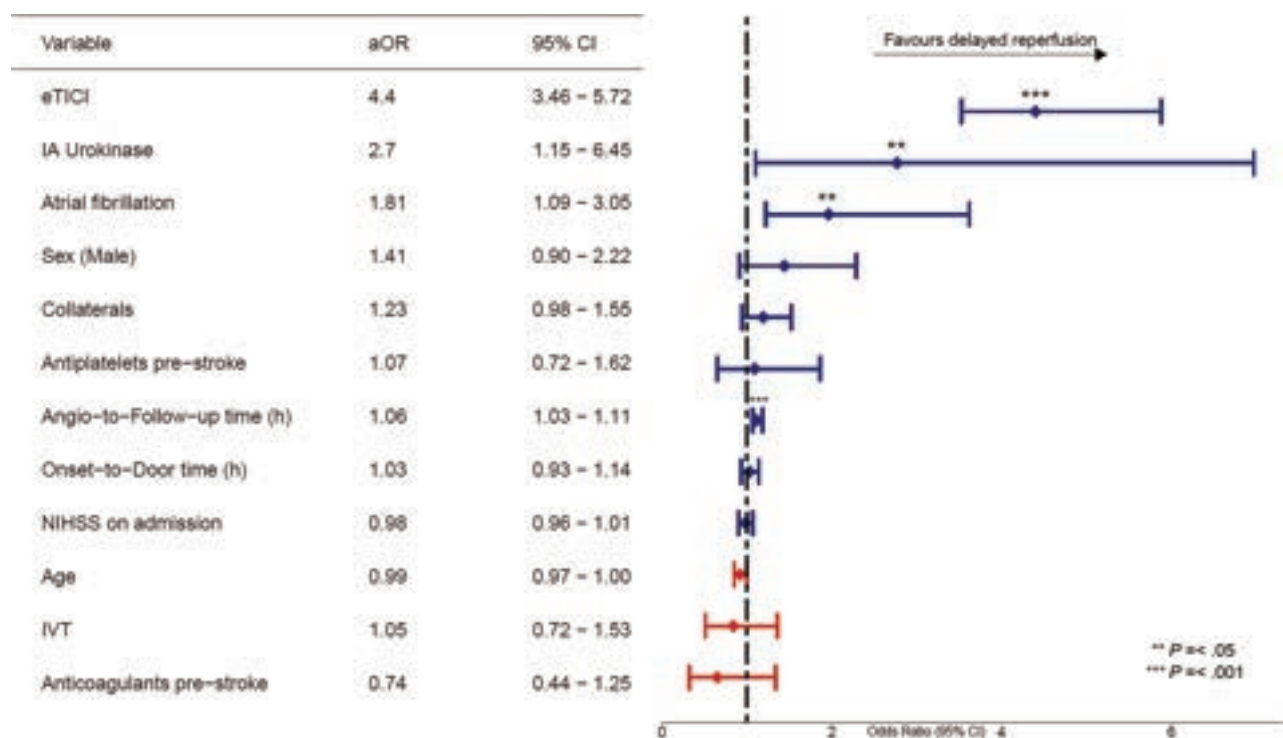


**FIG 3.** Analysis of the IPTW matched cohort. aORs of the independent variables are plotted in decreasing order as forest plots. In the IPTW fully matched cohort, DR was associated with receiving IA urokinase (aOR = 2.7; 95% CI, 1.1–6.4) and having atrial fibrillation (aOR = 1.8; 95% CI, 1.1–3.1), a higher eTICI score (aOR = 4.4; 95% CI, 3.4–5.7), and a longer intervention-to-follow-up time (aOR = 1.1; 95% CI, 1.0–1.1). IVT indicates IV thrombolysis.

hyperlipidemia (42.5% versus 64%;  $P = .01$ ), and had a shorter onset-to-door time (2 hours 24 minutes [IQR = 1 hour 22 minutes to 3 hours 36 minutes] versus 3 hours 12 minutes [IQR = 1 hour 42 minutes to 7 hours 13 minutes];  $P = .02$ ) (Table and Online Supplemental Data). Due to the indication bias, patients who received IA urokinase had worse reperfusion scores compared with patients not receiving IA urokinase (eg, rates of eTICI 2c: 5% versus 39.9%,  $P < .001$ ).

### Primary Outcome

DR occurred in 60.1% of all analyzed cases. After we adjusted for prespecified confounders in the initial, unmatched cohort, DR

was associated with IA urokinase (aOR = 2.8; 95% CI, 1.2–6.7), atrial fibrillation (aOR = 1.9; 95% CI, 1.1–3.4), eTICI (aOR = 4.4; 95% CI, 3.5–5.8), and intervention-to-follow-up time (aOR = 1.1; 95% CI, 1.0–1.1), as shown in the Online Supplemental Data.

Full IPTW matching was performed on prespecified confounders and yielded good matching results (Online Supplemental Data). In the IPTW fully-matched data set, DR was again associated with IA urokinase (aOR = 2.7; 95% CI, 1.1–6.4), atrial fibrillation (aOR = 1.8; 95% CI, 1.1–3.1), eTICI (aOR = 4.4; 95% CI, 3.4–5.7), and intervention-to-follow-up time (aOR = 1.1; 95% CI, 1.0–1.1, Fig 3). Other confounders in the IPTW data set showed a comparable association with IA urokinase as in the initial,

unmatched cohort. IA urokinase showed 0.5 (95% CI, 0.2–0.7, Online Supplemental Data) average treatment effect points on DR, ie, receiving IA urokinase resulted in approximately a 50% increase in the probability of having DR.

### Secondary Outcomes

When we analyzed the new infarct occurrence in the IPTW fully matched cohort adjusted for all prespecified confounders, having no new infarcted tissue on follow-up imaging was associated with receiving IA urokinase (aOR = 0.3; 95% CI, 0.1–0.7). Furthermore, receiving IA urokinase did not seem to impact the rates of functional independence (aOR = 1.4; 95% CI, 0.4–4.1) or sICH rates (aOR = 0.8; 95% CI, 0.2–3.1), even though point estimates favored patients who had received IA urokinase (Online Supplemental Data).

## DISCUSSION

The main findings of this study are the following: 1) IAT is associated with DR of the remaining vessel occlusions following incomplete thrombectomy. 2) Patients who received IAT were unlikely to have newly infarcted tissue and had a tendency toward better outcomes compared with patients without IAT.

### Early-versus-Delayed Reperfusion

The full efficacy of IAT evaluated within an extended timeframe from IAT initiation until reperfusion assessment is presently unknown. Investigators of the Prolyse in Acute Cerebral Thromboembolism trial (PROACT I and II) found higher reperfusion rates in the IAT-versus-placebo treatment arm when reperfusion was evaluated 120 minutes after IAT application (thrombolysis in myocardial infarction [TIMI] score 2–3 for PROACT I: 57.7% versus 14.3%,  $P = .017$ ; and for PROACT II: 66% versus 18%,  $P < .001$ ).<sup>8,9</sup> The Middle Cerebral Artery Embolism Local Fibrinolytic Intervention Trial (MELT) has also reported high reperfusion results in patients receiving IAT (73.7% of patients had reperfusion of >50% of the affected territory) when evaluated within the 2-hour timeframe.<sup>19</sup> However, the recently completed Chemical Optimization of Cerebral Embolectomy (CHOICE) trial reported no significant improvement in reperfusion rates between patients in the IAT and control groups (8.5% versus 7.7%; risk difference = 0.6%; 95% CI, –9.5%–10.7%).<sup>7</sup> Disparate findings between CHOICE and other trials might be explained by different timing of when reperfusion was assessed (10 versus 120 minutes, respectively). Multicenter observational registries have also reported improvement in angiographic reperfusion in half of treated patients (116/228, 50.9%) when IAT were administered;<sup>20</sup> however, these reperfusion improvements were not always associated with a change of the TICI score, and results should be interpreted cautiously due to possible indication and operator-rating biases.

To fully understand the efficacy of IAT, one should consider the effects over an extended timeframe from IAT initiation until reperfusion assessment. All these trials have reported only rates of early reperfusion and did not report the delayed effect that IAT might have on reperfusion rates. In this study, receiving IAT has shown an association with DR through both unmatched and matched analyses despite lower raw rates of DR in the IAT group.

Preclinical studies have already shown the delayed effects of IA urokinase in MCA occlusions.<sup>21,22</sup> When the pharmacologic effect was evaluated at 24 hours, IA urokinase resulted in higher reperfusion rates and also had an added benefit of preserving the integrity of the blood-brain barrier.<sup>21</sup> IA urokinase has also been shown to reduce microthrombi in secondary distal occlusions and capillary beds, aiding in the reperfusion of microcirculation within the 24-hour time window.<sup>22</sup> Therefore, the full thrombolytic efficiency of IA urokinase might be understood only when observed within an extended time window (ie, 24 hours).

### Functional Outcome

The effects of IAT on functional outcome have been reported across the studies. PROACT I failed to show differences in rates of 90-day excellent outcome (mRS 0–1;  $P = .48$ ), though the number of patients in the treatment and control groups was too small to test for differences ( $n = 8$  and 3, respectively).<sup>8</sup> While PROACT II reported higher rates of 90-day functional independence in patients receiving IAT (mRS 0–2; OR = 2.1; 95% CI, 1.0–4.4),<sup>9</sup> the MELT trial could not replicate these results (mRS 0–2 for IAT versus the control group, 49.1% versus 38.6%;  $P = .34$ ).<sup>19</sup> Different findings in these 2 trials are most likely caused by early termination of the MELT trial and the inability to achieve the pre-specified number of enrolled patients for complete analyses. A meta-analysis of IAT trials showed an association between IAT and increased odds of both excellent (OR = 2.1; 95% CI, 1.3–3.5) and functional independent (OR = 2.1; 95% CI, 1.3–3.1) outcomes.<sup>6</sup> The authors of the CHOICE trial have reported higher rates of excellent outcome in the treatment-versus-placebo group (mRS 0–1; adjusted risk difference = 18.4%; 95% CI, 0.3%–36.4%).<sup>7</sup> However, results from multicenter observational registries reported no improvement in functional outcome among patients receiving IAT.<sup>20,23</sup>

After adjusting for confounders, we have not observed a significant increase in the rates of functional independence among patients who received IAT, even though point estimates seemed to favor these patients. Administration of additional IAT might promote microvascular reperfusion of capillary beds because persistent occlusions of the microvasculature can be observed despite successful thrombi removal from the main blood vessels. This effect of “open capillaries” might translate into higher rates of functional outcome because the association between microvascular reperfusion and 90-day outcome has already been established.<sup>24,25</sup> The nested substudy of the CHOICE trial showed a lower prevalence of microvascular perfusion abnormalities at 48 hours in patients who received IAT versus placebo (24% versus 58%;  $P = .03$ ).<sup>11</sup> This also translated into improved rates of functional independence among patients without microvascular perfusion abnormalities compared with those who still had them (mRS 0–2, 100% versus 67%;  $P = .004$ ).<sup>11</sup> Areas with reperfed principal blood vessels that still experience microvascular occlusions (ie, the no-reflow phenomenon) may be salvageable if microvascular reperfusion is established in a timely manner.

Previous studies have reported conflicting findings between atrial fibrillation and DR.<sup>13,26</sup> Atrial fibrillation might represent a surrogate for another factor that might increase DR rates (eg, anticoagulants); however, these factors were already taken into account in the initial and IPTW analysis. Compared with other stroke etiologies, cardioembolic stroke appears to be more

susceptible to IAT treatment;<sup>27</sup> hence, it is possible that cardioembolic origin may be the cause of increased DR rates rather than atrial fibrillation. Presently, we are not able to draw any definitive conclusions because this study design is insufficient to test this association and evidence in available literature is modest.

### **Is There a Place for IAT?**

IAT have already been suggested as an adjunctive therapy for patients with incomplete reperfusion ( $eTICI < 3$ )<sup>3-5</sup> because IAT are usually considered for secondary distal occlusions, which are not amendable by MT. Other therapeutic options (eg, antiplatelets, secondary MT) have also been proposed for this scenario,<sup>28,29</sup> but they all require a careful application and selection of patient subgroups who would be most likely to benefit. One of the safety concerns when administering IAT is the occurrence of sICH.<sup>3-5</sup> PROACT I reported comparable sICH rates in the treatment and control arms (15.4% versus 7.1%,  $P > .1$ ).<sup>8</sup> Conversely, PROACT II reported higher 24-hour hemorrhage rates in the intervention group compared with the control group (35% versus 13%,  $P = .003$ ).<sup>9</sup> However, this difference was not significant over time (on 10-day follow-up: 68% versus 57%,  $P = .23$ ). MELT also reported no difference in sICH rates between patients with and without IAT (9% versus 2%,  $P = .21$ ).<sup>19</sup> Investigators of the CHOICE trial reported no sICH rates in their treatment group (IAT versus placebo: 0% versus 3.8%; risk difference =  $-3.8$ ; 95% CI,  $-13.2\%$ – $2.5\%$ ).<sup>7</sup> A recently conducted meta-analysis showed that receiving IAT did not increase sICH rates (OR = 0.8; 95% CI, 0.6–1.3) and IAT had safety and efficacy comparable with those of intravenous thrombolysis.<sup>30</sup> Here we also report comparable sICH rates between patients with and without IAT. Because the relationship between IAT and sICH has already been reported across several studies, we aimed to disentangle the association between IAT and the presence of new infarcts on 24-hour follow-up imaging. Present data show a minimal likelihood of new infarcts in residually hypoperfused territory after MT among patients who receive additional IAT. These results are corroborated by the CHOICE trial substudy, which showed that infarct expansion was less likely to occur in patients receiving IAT compared with a placebo (35% versus 74%,  $P = .02$ ).<sup>11</sup>

There might be several reasons for consistent findings on safety outcomes across this and previous studies on IAT. First, even minimal improvements in the TICI score produced by IAT are associated with reduced sICH rates.<sup>31</sup> Second, IA urokinase shows a neuroprotective effect on injured neurons and promotes synaptic recovery in the ischemic area.<sup>32,33</sup> Third, IAT might be able to improve microvascular reperfusion by dissolution of the microthrombi, which persist in the capillary beds and are not directly targeted during the macrovascular reperfusion approach.<sup>22</sup> This concept is further mitigated by the idea that not all areas of tissue injury are permanently lost to ischemia and IAT might help provide a more comprehensive treatment approach in patients with incomplete reperfusion.<sup>34</sup>

### **Limitations**

The design of this single-center retrospective study limits the generalizability of the present study results. IA urokinase was administered at the discretion of the treating neurointerventionalist,

prompting inherent selection bias. Even though steps have been taken to ensure minimal bias of unmeasured confounders, propensity score-matching can be used to balance out only those confounders included in estimating the propensity score and cannot overcome any bias caused by confounders that were not observed. The association between IAT and DR should be interpreted cautiously, because part of the DR rates could be partially attributed to early reperfusion rates, which have been shown to occur occasionally.<sup>5</sup> However, it would be difficult to evaluate early reperfusion rates in patients without IAT because there are usually no control angiography runs performed 20 minutes after the end of the intervention in this patient subgroup. Therefore, DR was chosen as the primary study outcome because patients both with and without additional IAT would have an imaging end point at 24 hours per standard protocol. Last, this study was not powered to show the true effects of IA urokinase on imaging and clinical outcomes; therefore, all presented results should be interpreted carefully.

### **CONCLUSIONS**

IAT is associated with DR of remaining vessel occlusions following incomplete thrombectomy, potentially promoting higher rates of functional outcome with comparable safety aspects. The value of IAT as a potential therapy for patients with stroke with incomplete reperfusion should be assessed in the setting of a randomized controlled trial.

Disclosure forms provided by the authors are available with the full text and PDF of this article at [www.ajnr.org](http://www.ajnr.org).

### **REFERENCES**

1. Goyal M, Menon BK, Van Zwam WH, et al; HERMES Collaborators. **Endovascular thrombectomy after large-vessel ischaemic stroke: a meta-analysis of individual patient data from five randomised trials.** *Lancet* 2016;387:1723–31 CrossRef Medline
2. Fischer U, Kaesmacher J, Strbian D, et al; SWIFT DIRECT Collaborators. **Thrombectomy alone versus intravenous alteplase plus thrombectomy in patients with stroke: an open-label, blinded-outcome, randomised non-inferiority trial.** *Lancet* 2022;400:104–15 CrossRef Medline
3. Chen VH, Lee GK, Tan CH, et al. **Intra-arterial adjunctive medications for acute ischemic stroke during mechanical thrombectomy: a meta-analysis.** *Stroke* 2021;52:1192–202 CrossRef Medline
4. Kaesmacher J, Meinel TR, Kurmann C, et al. **Safety and efficacy of intra-arterial fibrinolytics as adjunct to mechanical thrombectomy: a systematic review and meta-analysis of observational data.** *J Neurointerv Surg* 2021;13:1073–80 CrossRef Medline
5. Kaesmacher J, Bellwald S, Dobrocky T, et al. **Safety and efficacy of intra-arterial urokinase after failed, unsuccessful, or incomplete mechanical thrombectomy in anterior circulation large-vessel occlusion stroke.** *JAMA Neurol* 2020;77:318–26 CrossRef Medline
6. Lee M, Hong K, Saver JL, et al. **Efficacy of intra-arterial fibrinolysis for acute ischemic stroke meta-analysis of randomized controlled trials.** *Stroke* 2010;41:932–37 CrossRef Medline
7. Renu A, Millan M, San Roman L, et al; CHOICE Investigators. **Effect of intra-arterial alteplase vs placebo following successful thrombectomy on functional outcomes in patients with large vessel occlusion acute ischemic stroke: the CHOICE Randomized Clinical Trial.** *JAMA* 2022;327:826–35 CrossRef Medline
8. Del Zoppo GJ, Higashida RT, Furlan AJ, et al. **PROACT: a Phase II randomized trial of recombinant pro-urokinase by direct arterial**

- delivery in acute middle cerebral artery stroke. *Stroke* 1998;29:4–11 CrossRef Medline
9. Furlan AJ, Higashida RT, Wechsler LR. Intra-arterial prourokinase for acute ischemic stroke. The PROACT II study: a randomized controlled trial. Prolyse in Acute Cerebral Thromboembolism. *JAMA* 1999;82:203–11
  10. Mujanovic A, Jungi N, Kurmann CC, et al. Importance of delayed reperfusion in patients with incomplete thrombectomy. *Stroke* 2022;53:3350–58 CrossRef Medline
  11. Laredo C, Rodríguez A, Oleaga L, et al. Adjunct thrombolysis enhances brain reperfusion following successful thrombectomy. *Ann Neurol* 2022;92:860–70 CrossRef Medline
  12. Zaidat OO, Yoo AJ, Khatri P, et al; STIR Thrombolysis in Cerebral Infarction (TICI) Task Force. Recommendations on angiographic revascularization grading standards for acute ischemic stroke: a consensus statement. *Stroke* 2013;44:2650–63 CrossRef Medline
  13. Mujanovic A, Kammer C, Kurmann CC, et al. Association of intravenous thrombolysis with delayed reperfusion after incomplete mechanical thrombectomy. *Clin Neuroradiol* 2023;33:87–98 CrossRef Medline
  14. Mujanovic A, Ng F, Meinel TR, et al. No-reflow phenomenon in stroke patients: a systematic literature review and meta-analysis of clinical data. *Int J Stroke* 2023 Jun 8 [Epub ahead of print] CrossRef Medline
  15. Kurth T, Walker AM, Glynn RJ, et al. Results of multivariable logistic regression, propensity matching, propensity adjustment, and propensity-based weighting under conditions of nonuniform effect. *Am J Epidemiol* 2006;163:262–70 CrossRef Medline
  16. Shiba K, Kawahara T. Using propensity scores for causal inference: pitfalls and tips. *J Epidemiol* 2021;31:457–63 CrossRef Medline
  17. Robins JM, Hernán MA, Brumback B. Marginal structural models and causal inference in epidemiology. *Epidemiology* 2000;11:550–60 CrossRef Medline
  18. Raad H, Cornelius V, Chan S, et al. An evaluation of inverse probability weighting using the propensity score for baseline covariate adjustment in smaller population randomised controlled trials with a continuous outcome. *BMC Med Res Methodol* 2020;20:1–12 CrossRef Medline
  19. Ogawa A, Mori E, Minematsu K, et al; MELT Japan Study Group. Randomized trial of intraarterial infusion of urokinase within 6 hours of middle cerebral artery stroke: the Middle Cerebral Artery Embolism Local Fibrinolytic Intervention Trial (MELT) Japan. *Stroke* 2007;38:2633–39 CrossRef Medline
  20. Kaesmacher J, Abdullayev N, Maamari B, et al. Safety and angiographic efficacy of intra-arterial fibrinolytics as adjunct to mechanical thrombectomy: results from the INFINITY registry. *J Stroke* 2021;23:91–102 CrossRef Medline
  21. Cui W, Liu R, Jin H, et al. The protective effect of polyethylene glycol-conjugated urokinase nanogels in rat models of ischemic stroke when administered outside the usual time window. *Biochem Biophys Res Commun* 2020;523:887–93 CrossRef Medline
  22. Nan D, Jin H, Yang D, et al. Combination of polyethylene glycol-conjugated urokinase nanogels and urokinase for acute ischemic stroke therapeutic implications. *Transl Stroke Res* 2021;12:844–57 CrossRef Medline
  23. Zaidi SF, Castonguay AC, Jumaa MA, et al. Intraarterial thrombolysis as rescue therapy for large vessel occlusions. *Stroke* 2019;50:1003–06 CrossRef Medline
  24. De Silva DA, Fink JN, Christensen S, et al; Echoplanar Imaging Thrombolytic Evaluation Trial (EPITHET) Investigators. Assessing reperfusion and recanalization as markers of clinical outcomes after intravenous thrombolysis in the Echoplanar Imaging Thrombolytic Evaluation Trial (EPITHET). *Stroke* 2009;40:2872–74 CrossRef Medline
  25. Albers GW, Thijs VN, Wechsler L, et al. Magnetic resonance imaging profiles predict clinical response to early reperfusion: the Diffusion and Perfusion Imaging Evaluation for Understanding Stroke Evolution (DEFUSE) study. *Ann Neurol* 2006;60:508–17 CrossRef Medline
  26. Xu Y, Qian G, Wei L, et al. Predictive factors for the spontaneous recanalization of large and middle cerebral arteries after acute occlusion. *J Stroke Cerebrovasc Dis* 2016;25:1896–900 CrossRef Medline
  27. Kaesmacher J, Peschi G, Abdullayev N, et al. Factors associated with early reperfusion improvement after intra-arterial fibrinolytics as rescue for mechanical thrombectomy. *Clinical and Translational Neuroscience* 2021;5:2514183X2110173 CrossRef
  28. Jang SH, Park H, Lee S, et al. The safety of intra-arterial tirofiban during endovascular therapy after intravenous thrombolysis. *AJNR Am J Neuroradiol* 2021;42:1633–37 CrossRef Medline
  29. Meyer L, Stracke CP, Wallocha M, et al; TOPMOST Study Group. Thrombectomy for secondary distal, medium vessel occlusions of the posterior circulation: Seeking complete reperfusion. *J Neurointerv Surg* 2021;14:654–59 CrossRef Medline
  30. Kharel S, Nepal G, Joshi PR, et al. Safety and efficacy of low-cost alternative urokinase in acute ischemic stroke: a systematic review and meta-analysis. *J Clin Neurosci* 2022;106:103–09 CrossRef Medline
  31. Wang DT, Churilov L, Dowling R, et al. Successful recanalization post endovascular therapy is associated with a decreased risk of intracranial haemorrhage: a retrospective study. *BMC Neurol* 2015;15:185 CrossRef Medline
  32. Cho E, Lee KJ, Seo JW, et al. Neuroprotection by urokinase plasminogen activator in the hippocampus. *Neurobiol Dis* 2012;46:215–24 CrossRef Medline
  33. Diaz A, Merino P, Manrique LG, et al. A cross talk between neuronal urokinase-type plasminogen activator (uPA) and astrocytic uPA receptor (uPAR) promotes astrocytic activation and synaptic recovery in the ischemic brain. *J Neurosci* 2017;37:10310–22 CrossRef Medline
  34. Goyal M, Ospel JM, Menon B, et al. Challenging the ischemic core concept in acute ischemic stroke imaging. *Stroke* 2020;51:3147–55 CrossRef Medline

# Contrast Injection from an Intermediate Catheter Placed in an Intradural Artery is Associated with Contrast-Induced Encephalopathy following Neurointervention

M. Fuga, T. Tanaka, R. Tachi, S. Yamana, K. Irie, I. Kajiwara, A. Teshigawara, T. Ishibashi, Y. Hasegawa, and Y. Murayama



## ABSTRACT

**BACKGROUND AND PURPOSE:** Contrast-induced encephalopathy can result from neurotoxicity of contrast medium in the affected area. The development of intermediate catheters has allowed guidance of catheters to more distal arteries. This study focused on the association between contrast-induced encephalopathy and contrast injection from an intermediate catheter guided into a distal intradural artery during neurointervention for cerebral aneurysms.

**MATERIALS AND METHODS:** We retrospectively reviewed 420 consecutive aneurysms in 396 patients who underwent neurointervention for extracranial aneurysms and unruptured intracranial aneurysms at our institution from February 2012 to January 2023. Patients were divided into a group with contrast-induced encephalopathy and a group without. To identify risk factors for contrast-induced encephalopathy, we compared clinical, anatomic, and procedural factors between groups by multivariate logistic regression analysis and stepwise selection.

**RESULTS:** Among the 396 patients who underwent neurointervention for cerebral aneurysms, 14 (3.5%) developed contrast-induced encephalopathy. Compared with the group without contrast-induced encephalopathy, the group with contrast-induced encephalopathy showed significantly higher rates of patients on hemodialysis, previously treated aneurysms, intradural placement of a catheter for angiography, nonionic contrast medium, and flow-diversion procedures in univariate analyses. Stepwise multivariate logistic regression analysis revealed intradural placement of a catheter for angiography (OR = 40.4; 95% CI, 8.63–189) and previously treated aneurysms (OR = 8.20; 95% CI, 2.26–29.6) as independent predictors of contrast-induced encephalopathy.

**CONCLUSIONS:** Contrast injection from an intradural artery and retreatment of recurrent aneurysms were major risk factors for contrast-induced encephalopathy. Attention should be paid to the location of the intermediate catheter for angiography to avoid developing contrast-induced encephalopathy.

**ABBREVIATIONS:** CIE = contrast-induced encephalopathy; VA = vertebral artery

Contrast-induced encephalopathy (CIE) after neurointervention is a rare-but-important complication.<sup>1–7</sup> CIE can cause a variety of neurologic abnormalities, including motor, sensory, and visual impairments, aphasia, and seizures, depending on the affected area of cerebrum.<sup>1,5,6,8</sup> The symptoms are generally temporary and curable but may occasionally persist.<sup>1,9</sup> Risk factors

for CIE have previously been considered to include prior stroke, renal dysfunction, hemodialysis, hypertension, diabetes mellitus, posterior circulation aneurysms, higher dosage of contrast medium, and injection of contrast medium under elevated blood pressure.<sup>1–4,6,7,10</sup>

To clarify the mechanisms underlying CIE, animal studies have demonstrated that the BBB is temporarily overcome by either elevated blood pressure or hyperosmolality and that the penetration of contrast medium (including nonionic monomeric contrast medium) causes neuronal cell death in the affected area.<sup>10–14</sup> Furthermore, in clinical practice, Uchiyama et al<sup>15</sup> detected large amounts of iodine in the CSF on neuroimaging after coil embolization for a ruptured intracranial aneurysm, probably due to temporary leakage or destruction of the BBB. Because neurointervention involves repeat injection of contrast medium into a single intracranial artery, the risk of contrast-induced neurotoxicity might be elevated.

Received March 22, 2023; accepted after revision June 22.

From the Department of Neurosurgery (M.F., T.T., R.T., S.Y., A.T., Y.H.), Jikei University School of Medicine, Kashiwa Hospital, Chiba, Japan; Department of Neurosurgery (T.T., S.Y., T.I., Y.M.), Jikei University School of Medicine, Tokyo, Japan; Department of Neurosurgery (K.I.), Japanese Red Cross Medical Center, Tokyo, Japan; and Department of Neurosurgery (I.K.), National Center for Global Health and Medicine, Kohnodai Hospital, Chiba, Japan.

Please address correspondence to Michiyasu Fuga, MD, Department of Neurosurgery, Jikei University School of Medicine, Kashiwa Hospital, 163-1 Kashiwashita, Kashiwa-shi, Chiba 277-8567, Japan; e-mail: fugamichiyasu@icloud.com



Indicates article with online supplemental data.

<http://dx.doi.org/10.3174/ajnr.A7944>

Large-bore intermediate catheters have recently been used extensively in neurointerventional procedures for cerebral aneurysms. The development of intermediate catheters has helped guide catheters to more distal arteries, improved the maneuverability of microcatheters, and facilitated high-density coil packing.<sup>16</sup> One of the problems with contrast injection from a distally guided catheter is thought to be higher pressures and volume loading on distal arteries, which might destroy the BBB and cause neurotoxicity and CIE by leakage of contrast medium.

To verify this hypothesis, we investigated the association between CIE and contrast injection from an intermediate catheter guided into a distal intradural artery during neurointervention for cerebral aneurysms.

## MATERIALS AND METHODS

### Study Population

This study included 420 consecutive aneurysms in 396 patients who underwent neurointervention for extracranial aneurysms and unruptured intracranial aneurysms at our institution between February 2012 and January 2023. By retrospective review, patients were divided into those with CIE (CIE group; 14 patients, 14 aneurysms) and those without it (Non-CIE group; 382 patients, 406 aneurysms). Groups were compared in terms of clinical, anatomic, and procedural factors. The present study was approved by our institutional review board, and the need for informed consent was waived on the basis of the retrospective design.

### Anatomic Classification of the ICA and Vertebral Artery

Segments of the ICA in the present study were categorized according to the classification of Gibo et al.<sup>17</sup> The extracranial ICA was classified as the C1 segment, and the extracranial ICA was subdivided into petrous (C2) and cavernous (C3) segments, ending at the distal dural ring. The entire intradural ICA was categorized as the supraclinoid (C4) segment, including the ophthalmic, communicating, and choroidal subsegments.

The vertebral artery (VA) was classified into 4 segments: V1, representing the preforaminal segment and ranging from the origin of the VA to the transverse foramen of the sixth cervical vertebra; V2, representing the foraminal segment and ranging from the transverse foramen of the sixth cervical vertebra to the transverse foramen of the second cervical vertebra; V3, representing the atlantic, extradural segment and ranging from the transverse foramen of the second cervical vertebra to the penetration of the dura mater; and V4, representing the intradural segment and ranging from after the penetration of the dura mater to the confluence with the contralateral VA.

An intradural artery was defined as the intradural segment of a major artery, including distal to the C4 segment of the ICA in the anterior circulation and distal to the V4 segment of the VA in the posterior circulation.

### Contrast Medium Usage and Endovascular Treatment

All coil embolization procedures were performed solely by certified interventional neurosurgeons (M.F., R.T., A.T., K.I., I.K.) in a standardized manner. Dual antiplatelet therapy with aspirin (100 mg/day) and clopidogrel (75 mg/day) was initiated 1–4 weeks before coil embolization to prepare for unintended rescue

stenting. All coil embolizations were performed with the patient under general anesthesia. Heparin was administered during treatment to maintain an activated clotting time of at least 250 seconds during the procedure. Guiding catheters used included Optimo (Tokai Medical Products), Asahi Fubuki (Asahi Intecc), Shuttle (Cook Medical), FlowGate2 (Stryker Neurovascular), Axcelguide (Medikit), and Envoy (Codman & Shurtleff); and intermediate catheters used included Sofia (MicroVention-Terumo), Navien (Medtronic), Cerulean (Medikit), Asahi Fubuki, and Destination (MicroVention-Terumo). Until July 2017, unless the patient had an allergy to contrast medium, the ionic dimeric contrast medium ioxaglate (Hexabrix 320; Mallinckrodt) was routinely used. After this time, the nonionic monomeric contrast medium iohexol (Omnipaque 300; GE Healthcare) was used. 3D DSA was performed using a biplane flat panel detector C-arm angiography system (Artis zee BA Twin Large Display; Siemens) before and after embolization by injecting a 2:1 diluted contrast medium with an injector through a guiding catheter placed in C1 of the ICA or V1 or V2 of the VA. Control and working projection angiograms were also obtained by manually injecting 2:1 diluted contrast medium from the guiding catheter or intermediate catheter as appropriate during neurointervention.

### Diagnostic Criteria for CIE

On the basis of previous studies,<sup>4,5,7</sup> CIE was diagnosed when all 3 of the following criteria were met. 1) Unequivocal postoperative neurologic deterioration compared with the preoperative neurologic status that could not be explained by other reasons. Patients underwent neurologic assessment immediately after waking from general anesthesia and at the onset of any new symptoms. 2) Neurologic symptoms persisting for >24 hours and differentiated from TIA. When imaging findings typical of CIE were present, such as cortical or subcortical contrast enhancement on noncontrast CT or cortical gyriiform hyperintensity on a FLAIR sequence or T2-weighted MR imaging, CIE was diagnosed even if symptoms improved within 24 hours.<sup>8,18</sup> 3) Symptoms improved within 1 week after treatment and with re-evaluation on CT or MR imaging showing no obvious abnormality if imaging findings had been abnormal at onset. Noncontrast CT or MR imaging analysis was blinded to the clinical features of the patient and independently reviewed and evaluated by 2 certified interventional neurosurgeons (2 of the following: M.F., R.T., A.T., K.I., and I.K.) who were not the responsible interventional neurosurgeons for the aneurysm treatment. In cases of discrepancies in assessment, a third certified interventional neurosurgeon (One of M.F., R.T., A.T., K.I., and I.K.) other than the initial reviewers verified the consistency of the data and reached a consensus. In addition, the time courses from neurointervention to CIE onset and from CIE onset to recovery and the mRS at 1 month after treatment were also recorded.

### Statistical Analyses

The Mann-Whitney *U* test or Fisher exact test was administered to compare baseline characteristics between the CIE and non-CIE groups. Multivariate logistic regression analysis and stepwise selection were used to assess whether contrast injection from an intermediate catheter guided into an intradural artery was a

**Table 1: Baseline clinical characteristics in CIE and non-CIE groups<sup>a</sup>**

	CIE	Non-CIE	P Value
No. of patients	14 (3.5)	382 (96)	
Age (yr)	73 [66–79]	68 [57–75]	.054
Sex, female	8 (57)	254 (67)	.57
Body mass index (kg/m <sup>2</sup> )	23.5 [21.4–26.3]	22.9 [20.3–25.7]	.29
Race			
Asian	14 (100)	382 (100)	NA
Medical history			
Hypertension	10 (71)	245 (64)	.78
Diabetes mellitus	3 (21)	35 (9.2)	.14
Hyperlipidemia	6 (43)	174 (46)	1
Prior stroke <sup>b</sup>	4 (29)	45 (12)	.081
Ischemic stroke	3 (21)	17 (4.5)	
Hemorrhagic stroke	2 (14)	28 (7.3)	
Cerebral hemorrhage	0 (0)	6 (1.6)	
SAH	2 (14)	22 (5.8)	
Renal dysfunction (eGFR <45) <sup>c</sup>	2 (14)	19 (5.0)	.17
Hemodialysis	2 (14)	5 (1.3)	.022 <sup>d</sup>
eGFR, (mL/min per 1.73 m <sup>2</sup> )	79.1 [55.5–92.2]	79.9 [66.1–92.4]	.58
Smoking	9 (64)	155 (41)	.098
Drinking	5 (36)	146 (38)	1
Allergy <sup>e</sup>	1 (7.1)	82 (22)	.32
Allergy to contrast medium	1 (7.1)	20 (5.2)	.54

**Note:**—eGFR indicates estimated glomerular filtration rate; NA, not applicable.

<sup>a</sup> Unless otherwise indicated, values represent the number of aneurysms (%) or median [interquartile range]. Not all percentage totals reach 100% because of rounding.

<sup>b</sup> Patients with a history of both ischemic and hemorrhagic stroke were counted in each category.

<sup>c</sup> Renal dysfunction was defined as an eGFR of <45 mL/min/1.73 m<sup>2</sup>.

<sup>d</sup>  $P < .05$ .

<sup>e</sup> History of allergy included allergy to any food or drug.

predictor of the development of CIE. This analysis was adjusted not only for factors that appeared significant in univariate analyses in the present study but also for the following previously reported risk factors for CIE: prior stroke, renal dysfunction, hemodialysis, hypertension, diabetes mellitus, posterior circulation aneurysm, and total volume of contrast medium.<sup>1–4,6,7</sup> Because renal dysfunction and hemodialysis were strongly correlated, only variables with lower *P* values in univariate analyses were included in the multivariate analysis. All statistical analyses were performed with Easy R (EZR) (Saitama Medical Center, Jichi Medical University, Saitama, Japan), which is based on R and R commander [Bone Marrow Transplant].<sup>19</sup> Values of  $P < .05$  were considered significant.

## RESULTS

### Background of Aneurysms

Among the 396 patients who underwent neurointervention for cerebral aneurysms, 14 (3.5%) fulfilled the diagnostic criteria for CIE. Of the 420 aneurysms, 417 (99%) were unruptured cerebral aneurysms, including 5 (1.2%) dissecting aneurysms. The remaining 3 (0.7%) were ruptured extracranial cerebral aneurysms, 2 of which caused epistaxis and 1 that caused otorrhagia.

### Baseline Clinical Characteristics

The baseline clinical characteristics of patients are shown in Table 1. No significant differences between groups were seen with respect to age, sex, body mass index, smoking or drinking history, or allergies. In terms of medical history, no significant difference was observed between groups in hypertension,

diabetes mellitus, hyperlipidemia, prior stroke, or renal dysfunction. Compared with the non-CIE group, the CIE group showed a significantly higher rate of hemodialysis ( $P = .022$ ).

### Anatomic and Procedural Characteristics

No significant differences were found between groups for aneurysm characteristics, including aneurysm size, neck size, aneurysm volume, aneurysm location, access site, or size of catheter used for angiography (Online Supplemental Data). The rate of retreatment for previously treated aneurysms was significantly higher in the CIE group than in the non-CIE group ( $P = .017$ ).

Distributions of locations of the guiding catheter used for angiography in the CIE and non-CIE groups were 0 (0%) and 3 (0.8%) for the common carotid artery, 8 (100%) and 325 (87%) for the ICA C1 segment, 0 (0%) and 8 (2.1%) for the VA V1 segment, and 0 (0%) and 37 (9.9%) for the VA V2 segment, respectively. Distributions of locations of the intermediate catheter used for angiography in the CIE and non-CIE groups were 1 (17%) and 13 (39%) for the ICA C2 segment, 1 (17%) and 9 (27%) for the ICA C3 segment, 3 (50%) and 3 (9.1%) for the ICA C4 segment, 1 (17%) and 0 (0%) for the horizontal (M1) segment of the MCA, 0 (0%) and 1 (3%) for the VA V1 segment, 0 (0%) and 3 (9.1%) for the VA V2 segment, 0 (0%) and 1 (3%) for the VA V3 segment, 0 (0%) and 2 (6.1%) for the VA V4 segment, and 0 (0%) and 1 (3%) for the basilar artery, respectively. The rate of intradural placement of catheters used for angiography was significantly higher in the CIE group than in the non-CIE group ( $P < .001$ ).

No significant differences between the CIE and non-CIE groups were seen regarding procedure time, fluoroscopy duration, total volume of contrast medium, embolization result, or volume embolization ratio. On the other hand, compared with the non-CIE group, the CIE group significantly used nonionic monomeric contrast medium more frequently, underwent a higher proportion of flow diverter treatment, and required a longer hospital stay ( $P = .002$ ,  $P = .026$ , and  $P = .028$ , respectively) (Online Supplemental Data).

### Contrast-Induced Encephalopathy

Of the 14 patients who developed CIE, the median age was 73 years (interquartile range, 66–79 years), with a predominance of female patients ( $n = 8$ , 57%). All patients presenting with CIE showed normal laboratory values with the exception of 2 patients undergoing hemodialysis with severely impaired renal function. The location of the aneurysm was the ICA in 10 patients (71%), the MCA in 3 (21%), and the anterior cerebral artery in 1 (7.1%).

**Table 2: Multivariate logistic regression analysis and stepwise selection of risk factors for CIE**

Parameter	OR (95% CI)	P Value
Variables with $P < .05$ or previously reported as risk factors for CIE		
Intradural placement of catheter for angiography	50.2 (7.25–347)	<.001 <sup>a</sup>
Previously treated aneurysm	7.46 (1.47–37.9)	.015 <sup>a</sup>
Prior stroke	4.30 (0.756–24.5)	.1
Hemodialysis	7.91 (0.504–124)	.14
Hypertension	0.985 (0.233–4.17)	.98
Diabetes mellitus	1.64 (0.241–11.1)	.62
Posterior circulation aneurysm	$7.52 \times 10^{-10}$ (0–Inf)	.995
Total contrast medium volume (mL)	0.997 (0.988–1.01)	.58
Nonionic contrast medium	$7.85 \times 10^7$ (0–Inf)	.99
Endovascular technique (flow diversion)	7.15 (0.642–79.7)	.11
After the stepwise selection using the $P$ value (until $P < .05$ )		
Intradural placement of catheter for angiography	40.4 (8.63–189)	<.001 <sup>a</sup>
Previously treated aneurysm	8.20 (2.26–29.6)	.001 <sup>a</sup>

Note:—Inf indicates infinitesimal or infinity.

<sup>a</sup> $P < .05$ .

In addition, 5 (36%) of the 14 aneurysms had been previously treated. The catheter used for angiography was a Sofia in 4 patients (29%), an Optimo in 4 patients (29%), an Asahi Fubuki in 3 patients (21%), and Navien, Axcelguide, and Destination in 1 patient each (7.1%) (Online Supplemental Data).

The location of the catheter used for angiography was the ICA C1 in 8 patients (57%), ICA C2 in 1 (7.1%), ICA C3 in 1 (7.1%), ICA C4 in 3 (21%), and MCA M1 in 1 (7.1%), with the left side predominating (64%), and 4 catheters (29%) were placed intradurally. The contrast medium used was iohexol (Omnipaque 300) in 13 cases and iopamidol (Iopamiron 370; Bayer) in 1 case. The median volume of contrast used was 173 mL (interquartile range, 131–208 mL). There was a higher percentage of hypertension in 10 patients (71%), prior stroke in 4 (29%), diabetes mellitus in 3 (21%), and hemodialysis in 2 (14%) patients with CIE. Most patients presented with a disturbance of consciousness (12/14; 86%) and cortical symptoms (13/14; 93%), including hemiparesis, aphasia, agnosia, hemispatial neglect, and cortical blindness. The most frequent cortical symptoms were hemiparesis (10/14; 71%) and aphasia (6/14; 43%).

Imaging findings were abnormal in 8 (89%) of 9 patients on CT and 5 (38%) of 13 patients on MR imaging. Treatment for CIE mainly comprised anticonvulsants and adequate hydration, and patients with end-stage renal failure were treated with hemodialysis to remove contrast medium from the body. The median time from neurointervention to CIE onset was 1 hour (interquartile range, 0.5–1 hour), and the median time from CIE onset to recovery was 4 days (interquartile range, 2–5.75 days). One month after neurointervention, 12 (86%) of the 14 patients showed normalization of mRS compared with pre-neurointervention, while 1 patient showed mild sequelae (mRS 1) and 1 patient showed severe sequelae (mRS 5) due to CIE.

#### Risk Factors for CIE

Intradural placement of a catheter for angiography (OR = 40.4; 95% CI, 8.63–189) and a previously treated aneurysm (OR = 8.20; 95% CI, 2.26–29.6) were identified as independent predictors of

CIE by multivariate logistic regression analysis and stepwise selection (Table 2).

#### Illustrative Case

A 70-year-old man with hemodialysis due to end-stage renal failure was scheduled for coil embolization of a right MCA aneurysm with a maximum diameter of 9 mm (Fig 1A). The aneurysm was treated by guiding a 6F Sofia catheter as an intermediate catheter into the right MCA M1; then coil embolization was performed using a stent-assisted technique (Fig 1B). Contrast medium was injected through the intermediate catheter to examine the embolization status.

Coil embolization achieved complete occlusion, with a volume embolization ratio of 30% (Fig 1C). A total of 120 mL of iohexol (Omnipaque 300) was used. Half an hour after completion of treatment, the patient presented progressively with stupor, disorientation, and severe left upper- and lower-extremity paralysis. MR imaging found no obvious ischemic or hemorrhagic lesions (Fig 1D, -E), and MR angiography did not detect any arterial occlusion, dissection, or vasospasm. Noncontrast CT showed enhancement in the right cerebral cortex and subcortex (Fig 1F).

On the basis of the above, CIE was diagnosed and the patient was administered anticonvulsant and underwent emergency hemodialysis to drain the contrast medium. After hemodialysis, disturbance of consciousness and left hemiparesis gradually improved. Noncontrast CT 5 days after treatment demonstrated disappearance of contrast-induced enhancement from the right cerebral cortex and subcortex (Fig 1G). Six days after coil embolization, neurologic abnormalities had completely resolved (mRS 0).

#### DISCUSSION

In the present study, contrast injection from an intradural artery and retreatment of a previously treated aneurysm were identified as risk factors for CIE by multivariate analysis.

Contrast medium can cross the BBB and leak into brain tissue, resulting in neurotoxicity.<sup>10–14,20</sup> Uchiyama et al<sup>15</sup> proposed that CIE might be caused by temporary disruption of the BBB as evidenced by elevated concentrations of iodine levels in the CSF of patients with CIE. Recently, large-bore, flexible intermediate catheters such as the Navien and Sofia have become available for neurointervention. Guiding the intermediate catheter into an intradural artery is expected to improve maneuverability of the microcatheter.<sup>16</sup> However, the present study demonstrated that direct contrast injection from an intermediate catheter guided into an intradural artery might raise the risk of CIE. Diamandis et al<sup>21</sup> experienced CIE after multiple angiograms from an intermediate catheter (AXS Catalyst6; Stryker Neurovascular) placed in an intradural artery during flow-diverter treatment of an aneurysm of the left ICA C4 segment. Close attention may need to be

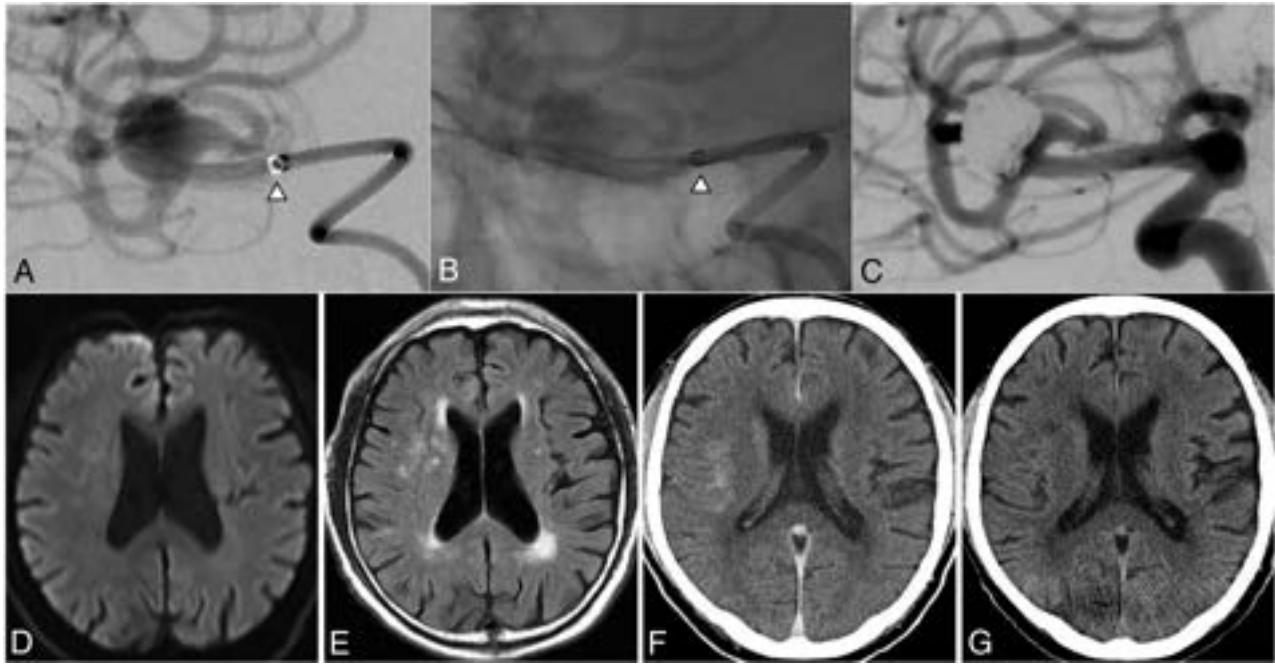


**FIGURE.** A 70-year-old man undergoing hemodialysis due to end-stage renal failure underwent coil embolization for a right MCA aneurysm with a maximum diameter of 9 mm. Right middle cerebral arteriography (A) and fluoroscopic view (B) show contrast of the right MCA aneurysm from the 6F Sofia catheter, an intermediate catheter guided to the right MCA horizontal segment. Right middle cerebral arteriography (C) shows complete embolization of aneurysm achieved by a stent-assisted technique. Half an hour after completion of the treatment, the patient's condition with stupor, disorientation, and severe left upper and lower extremity paralysis progressively deteriorated. No obvious ischemic and hemorrhagic lesions were seen on MR imaging (D, DWI; E, FLAIR sequence). MRA did not detect arterial occlusion, dissection, or vasospasm. Noncontrast CT (F) shows enhancement due to leakage of contrast medium into the right cerebral cortex and subcortex. After hemodialysis, disturbance of consciousness and left hemiparesis gradually improved. Noncontrast CT (G) 5 days after treatment demonstrates that the contrast-induced enhancement in the right cerebral cortex and subcortex had disappeared. The *arrowhead* indicates the tip of Sofia catheter.

paid to the location of the intermediate catheter for angiography to avoid CIE.

The present study also revealed retreatment of a previously treated aneurysm as a risk factor for CIE. Prior stroke may pose a risk factor for CIE due to disruption of the BBB in the same or adjacent vascular territories,<sup>4</sup> resulting in tissue damage and cerebral edema via leakage of contrast medium into a wide range of cerebral parenchyma.<sup>22</sup> Recent SAH might compromise the BBB via endothelial cell damage.<sup>6,23</sup> In the present study, 3 of the 4 patients with recurrent aneurysms who developed CIE had previously undergone treatment of a ruptured aneurysm (2 after coil embolization, 1 after clipping). In addition, the remaining case involved a recurrent aneurysm after coil embolization of an unruptured cerebral aneurysm, with complications of cerebral infarction at the time of initial treatment. These results suggest previous SAH or cerebral infarction as a potential cause of damage to the BBB, allowing direct neurotoxicity and CIE via leakage of contrast medium into the cerebral parenchyma. Predisposing surgical insults of craniotomy or neuroendovascular surgery including brain injury, SAH, and cerebral infarction might thus represent key risk factors for CIE, especially when repeating treatment for recurrent aneurysms. This issue warrants investigation in the future.

In addition to prior stroke, factors of renal dysfunction, hemodialysis, hypertension, diabetes mellitus, posterior circulation aneurysms, and a higher dosage of contrast medium might

contribute to the risk of CIE.<sup>1-4,6,7,10</sup> Unexpectedly, multivariate analysis in the present study failed to identify any of those factors as significant, along with the class of contrast medium, in comparisons between patients with and without CIE. Some researchers have found no relationship between contrast volume and CIE.<sup>3,24</sup> Lantos<sup>24</sup> reported CIE in 4 patients who received <40 mL of contrast medium (ionic and nonionic). Unlike the field of interventional cardiology, repeat injection of contrast medium into a single intracranial artery during neurointervention, regardless of the total volume of contrast medium injected, could cause local increases in intravascular pressure and contrast concentration, resulting in transient disruption of the BBB and subsequent CIE. Furthermore, CIE can develop regardless of the type of contrast medium. Animal studies have demonstrated that iodixanol and iopamidol can cross the BBB at comparable rates.<sup>25</sup> CIE occurred even with the use of iodoxanol, which shows the same osmotic pressure as physiologic saline.<sup>26</sup>

Renal dysfunction may decrease contrast clearance, which may, in turn, exacerbate the osmotic accumulation and neurotoxicity of contrast medium. Patients with renal dysfunction requiring hemodialysis should be carefully followed up for CIE.<sup>2</sup> Similarly, in the present study, hemodialysis was a significant risk factor for the development of CIE in univariate analysis after neurointervention. One of the 2 patients receiving hemodialysis had developed frequent generalized seizures. The day after the procedure, MR imaging showed no abnormal findings and

noncontrast CT demonstrated cortical and subcortical contrast enhancement throughout the left hemisphere, meeting the criteria for CIE. However, the delayed treatment of CIE using hemodialysis to remove contrast medium resulted in severe neurologic sequelae due to brain damage secondary to generalized seizures. As shown in the illustrative case, the other patient in whom CIE was suspected from the onset underwent hemodialysis to remove contrast medium immediately after onset, resulting in complete neurologic recovery. CIE that develops in patients with hemodialysis can be improved by rapid induction of hemodialysis to remove contrast medium from the body.<sup>2,27,28</sup>

Our study has several limitations. First, uniform diagnostic criteria for CIE are lacking. As a result, potential underdiagnosis of CIE in our study cohort could not be ruled out. However, patients with SAH were not included in the present study, and only patients with cerebral aneurysms without impaired consciousness were included, allowing more sensitive judgments regarding potential discrepancies between postoperative neurologic changes and imaging findings. These inclusion choices may have contributed to an improved diagnostic accuracy of CIE. Second, control and working-projection angiography from the guiding or intermediate catheter during neurointervention was performed by injecting contrast medium manually, rather than with an injector. Injection pressure varied individually, and the pressures used for injection of contrast medium in each operation were not precisely measured. Third, this study was performed exclusively on East Asian patients. Further validation studies are needed before our findings can be generalized to other ethnic groups. Finally, this study was conducted as a retrospective, single-center study of a moderate-sized cohort. The low incidence of CIE may have limited the statistical power.<sup>2-4,7</sup> Despite these limitations, the present study showed that injection of contrast from an intradural artery and retreatment of a previously treated aneurysm warrant careful follow-up for CIE.

## CONCLUSIONS

Contrast injection from an intradural artery and retreatment of recurrent aneurysms were the main risk factors for CIE. The location of the intermediate catheter for angiography may need to be considered to minimize the risk of developing CIE.

Disclosure forms provided by the authors are available with the full text and PDF of this article at [www.ajnr.org](http://www.ajnr.org).

## REFERENCES

1. Leong S, Fanning NF. **Persistent neurological deficit from iodinated contrast encephalopathy following intracranial aneurysm coiling: a case report and review of the literature.** *Interv Neuroradiol* 2012;18:33-41 CrossRef Medline
2. Matsubara N, Izumi T, Miyachi S, et al. **Contrast-induced encephalopathy following embolization of intracranial aneurysms in hemodialysis patients.** *Neurol Med Chir (Tokyo)* 2017;57:641-48 CrossRef Medline
3. Zevallos CB, Dandapat S, Ansari S, et al. **Clinical and imaging features of contrast-induced neurotoxicity after neurointerventional surgery.** *World Neurosurg* 2020;142:e316-24 CrossRef Medline
4. Chu YT, Lee KP, Chen CH, et al. **Contrast-induced encephalopathy after endovascular thrombectomy for acute ischemic stroke.** *Stroke* 2020;51:3756-59 CrossRef Medline
5. Quintas-Neves M, Araújo JM, Xavier SA, et al. **Contrast-induced neurotoxicity related to neurological endovascular procedures: a systematic review.** *Acta Neurol Belg* 2020;120:1419-24 CrossRef Medline
6. Vignano M, Mantero V, Basilico P, et al. **Contrast-induced encephalopathy mimicking total anterior circulation stroke: a case report and review of the literature.** *Neurol Sci* 2021;42:1145-50 CrossRef Medline
7. Li M, Liu J, Chen F, et al. **Contrast-induced encephalopathy following endovascular treatment for intracranial aneurysms-risk factors analysis and clinical strategy.** *Neuroradiology* 2023;65:629-35 CrossRef Medline
8. Spina R, Simon N, Markus R, et al. **Contrast-induced encephalopathy following cardiac catheterization.** *Catheter Cardiovasc Interv* 2017;90:257-68 CrossRef Medline
9. Niimi Y, Kupersmith MJ, Ahmad S, et al. **Cortical blindness, transient and otherwise, associated with detachable coil embolization of intracranial aneurysms.** *AJNR Am J Neuroradiol* 2008;29:603-07 CrossRef Medline
10. Whisson CC, Wilson AJ, Evill CA, et al. **The effect of intracarotid nonionic contrast media on the blood-brain barrier in acute hypertension.** *AJNR Am J Neuroradiol* 1994;15:95-100 Medline
11. Suzuki M, Iwasaki Y, Yamamoto T, et al. **Sequelae of the osmotic blood-brain barrier opening in rats.** *J Neurosurg* 1988;69:421-28 CrossRef Medline
12. Salahuddin TS, Kalimo H, Johansson BB, et al. **Observations on exudation of fibronectin, fibrinogen and albumin in the brain after carotid infusion of hyperosmolar solutions: an immunohistochemical study in the rat indicating longlasting changes in the brain microenvironment and multifocal nerve cell injuries.** *Acta Neuropathol* 1988;76:1-10 CrossRef Medline
13. Sokrab TE, Johansson BB, Tengvar C, et al. **Adrenaline-induced hypertension: morphological consequences of the blood-brain barrier disturbance.** *Acta Neurol Scand* 1988;77:387-96 CrossRef Medline
14. Sokrab TE, Johansson BB, Kalimo H, et al. **A transient hypertensive opening of the blood-brain barrier can lead to brain damage: extravasation of serum proteins and cellular changes in rats subjected to aortic compression.** *Acta Neuropathol* 1988;75:557-65 CrossRef Medline
15. Uchiyama Y, Abe T, Hirohata M, et al. **Blood brain-barrier disruption of nonionic iodinated contrast medium following coil embolization of a ruptured intracerebral aneurysm.** *AJNR Am J Neuroradiol* 2004;25:1783-86 Medline
16. Matsushige T, Sakamoto S, Ishii D, et al. **Safety and efficacy of a new outreach distal access catheter, tactics, for coil embolization of unruptured intracranial aneurysms.** *Interv Neuroradiol* 2018;24:482-88 CrossRef Medline
17. Gibo H, Lenkey C, Rhoton AL Jr. **Microsurgical anatomy of the supraclinoid portion of the internal carotid artery.** *J Neurosurg* 1981;55:560-74 CrossRef Medline
18. Parrilla G, García-Villalba B, Espinosa de Rueda M, et al. **Hemorrhage/contrast staining areas after mechanical intra-arterial thrombectomy in acute ischemic stroke: imaging findings and clinical significance.** *AJNR Am J Neuroradiol* 2012;33:1791-96 CrossRef Medline
19. Kanda Y. **Investigation of the freely available easy-to-use software 'EZR' for medical statistics.** *Bone Marrow Transplant* 2013;48:452-58 CrossRef Medline
20. Lalli AF. **Contrast media reactions: data analysis and hypothesis.** *Radiology* 1980;134:1-12 CrossRef Medline
21. Diamandis E, Swiatek VM, Behme D. **Fully reversible contrast-induced encephalopathy mimicking stroke after flow diverter treatment of carotid cave aneurysm.** *Neurointervention* 2023;18:58-62 CrossRef Medline
22. Zhang G, Wang H, Zhao L, et al. **Contrast-induced encephalopathy resulting from use of ioversol and iopromide.** *Clin Neuropharmacol* 2020;43:15-19 CrossRef Medline
23. Peeyush Kumar T, McBride DW, Dash PK, et al. **Endothelial cell dysfunction and injury in subarachnoid hemorrhage.** *Mol Neurobiol* 2019;56:1992-2006 CrossRef Medline

24. Lantos G. **Cortical blindness due to osmotic disruption of the blood-brain barrier by angiographic contrast material: CT and MRI studies.** *Neurology* 1989;39:567–71 CrossRef Medline
25. Wilcox J, Wilson AJ, Evill CA, et al. **A comparison of blood-brain barrier disruption by intracarotid iohexol and iodixanol in the rabbit.** *AJNR Am J Neuroradiol* 1987;8:769–72 Medline
26. Lee KK, Kang DH, Kim YS, et al. **Serious blood-brain barrier disruption after coil embolization of unruptured intracranial aneurysm: report of two cases and role of immediate postembolization CT scan.** *J Korean Neurosurg Soc* 2011;50:45–47 CrossRef Medline
27. Muruve DA, Steinman TI. **Contrast-induced encephalopathy and seizures in a patient with chronic renal insufficiency.** *Clin Nephrol* 1996;45:406–09 Medline
28. Yan J, Ramanathan V. **Severe encephalopathy following cerebral arteriogram in a patient with end-stage renal disease.** *Semin Dial* 2013;26:203–07 CrossRef Medline

# Iterative Denoising Accelerated 3D FLAIR Sequence for Hydrops MR Imaging at 3T

R. Quint, A. Vaussy, A. Stemmer, C. Hautefort, E. Houdart, and M. Eliezer

## ABSTRACT

**BACKGROUND AND PURPOSE:** 3D FLAIR sequences have become the criterion standard for identifying endolymphatic hydrops, but scan time remains an important limitation to their widespread use. Our purpose was to evaluate the diagnostic performance and image quality of an accelerated 3D FLAIR sequence combined with an iterative denoising algorithm.

**MATERIALS AND METHODS:** This was a retrospective study performed on 30 patients with clinical suspicion of endolymphatic hydrops who underwent 3T MR imaging 4 hours after gadolinium injection using two 3D FLAIR sequences. The first (conventional FLAIR) was accelerated with a conventional turbo factor of 187. The second was accelerated with an increased turbo factor of 263, resulting in a 33% scan time reduction (5 minutes 36 seconds versus 8 minutes 15 seconds, respectively). A sequence was reconstructed in-line immediately after the accelerated 3D FLAIR acquisition from the same raw data with iterative denoising (accelerated-FLAIR iterative denoising). The signal intensity ratio image quality score and endolymphatic hydrops diagnosis were evaluated.

**RESULTS:** The mean signal intensity ratio for symptomatic and asymptomatic ears of accelerated-FLAIR iterative denoising was significantly higher than the mean SNR of conventional FLAIR (29.5 versus 19 and 25.9 versus 16.3,  $P < .001$ ). Compared with the conventional FLAIR sequence, the image-quality score was higher with accelerated-FLAIR iterative denoising (mean image-quality score, 3.8 [SD, 0.4] versus 3.3 [SD, 0.6] for accelerated-FLAIR iterative denoising and conventional FLAIR, respectively,  $P = .003$ ). There was no significant difference in the diagnosis of endolymphatic hydrops between the 2 sequences. Interreader agreement was good-to-excellent.

**CONCLUSIONS:** The iterative denoising algorithm applied to an accelerated 3D FLAIR sequence for exploration of endolymphatic hydrops enabled significantly reducing the scan time without compromising image quality and diagnostic performance.

**ABBREVIATIONS:** acc = accelerated; conv = conventional; CS = compressed sensing; DLR = deep learning reconstruction; EH = endolymphatic hydrops; GRAPPA = generalized autocalibrating partially parallel acquisition; ID = iterative denoising; PI = parallel imaging; SIR = signal intensity ratio

Since the first MR imaging study performed by Nakashima et al,<sup>1</sup> in 2007, 3D FLAIR sequences performed 4 hours after IV contrast administration have become the criterion standard in clinical practice for identifying endolymphatic hydrops (EH) in patients with suspicion of Menière disease and other inner ear disorders.<sup>2-4</sup>

Despite the significantly increased quality of these high-resolution sequences, the scan time is an important limitation to the widespread use of the hydrops protocol, with acquisition lengths up to 15 minutes in some centers.

Parallel imaging (PI) acceleration techniques, based on phased array coils, are used to significantly decrease scan time, improving patient comfort, image quality, and cost-effectiveness.<sup>5</sup> Sensitivity encoding and generalized autocalibrating partially parallel acquisition (GRAPPA) are the most commonly used techniques for clinical MR imaging systems.<sup>6,7</sup> However, by increasing the acceleration factor, the reduction of the acquisition time is limited by a significant SNR loss.

Although variable flip angle sequences are frequently used because they allow keeping the high-signal amplitude during a long readout duration,<sup>8</sup> it has been demonstrated that 3D FLAIR sequences with a constant flip angle provide a higher signal and contrast intensity ratio for EH evaluation.<sup>9</sup> Nevertheless, the use of constant flip angle sequences with a high echo-train length can compromise the SNR, compensated for by an extended scan time.

Recently, Naganawa et al<sup>10</sup> reported a 5-minute HYDROPS2-Mi2 sequence by increasing the PI factor and decreasing the

Received February 13, 2023; accepted after revision June 27.

From the Departments of Neuroradiology (R.Q., E.H., M.E.), and Head and Neck Surgery (C.H.), Lariboisière University Hospital, Paris, France; Siemens Healthineers France (A.V.), Saint-Denis, France; Siemens Healthineers (A.S.), Erlangen, Germany; and Faculté de Médecine (E.H.), Université de Paris, Paris, France.

Please address correspondence to Michael Eliezer, MD, Department of Neuroradiology, Lariboisière University Hospital, 75010 Paris, France; e-mail: michael.eliezer@aphp.fr

<http://dx.doi.org/10.3174/ajnr.A7953>

**Table 1: Imaging parameters for 3D FLAIR EH MR imaging sequences**

	Conv-FLAIR	Acc-FLAIR-ID
FOV (frequency × phase) (mm <sup>2</sup> )	154 × 154	154 × 154
Matrix	256 × 256	256 × 256
Orientation	Axial	Axial
Section thickness (mm)	0.8	0.8
GRAPPA	2	2
No. of slices	28	28
TR/TE/T1 (ms)	16,000/640/3000	16,000/640/3000
Flip angle	Constant 140°	Constant 140°
Turbo factor	187	263
Bandwidth (Hz/pixel)	279	501
Scanning time	8 minutes 15 seconds	5 minutes 36 seconds

acquisition coverage with a reduced number of slices. The signal loss was compensated for by using a deep learning reconstruction (DLR) algorithm.<sup>11</sup>

Another approach using an iterative denoising (ID) reconstruction algorithm, which works with quantitative noise information, has been proposed to compensate for the SNR loss penalty inherent in the high acceleration factor. This strategy has been evaluated for MR imaging of various organs, and these studies highlighted a significantly decreased scan time while preserving image quality and SNR.<sup>12-14</sup>

This study aimed to evaluate the diagnostic performance and image quality of an accelerated 3D FLAIR sequence with ID reconstruction for EH exploration at 3T.

## MATERIALS AND METHODS

### Study Design

This single-center retrospective study was approved by our institutional Research Ethics Board (NTC 02529475) and adhered to the tenets of the Declaration of Helsinki. Informed consent was waived. This study follows the Strengthening Reporting of Observational Studies in Epidemiology (STROBE) guidelines. The on-site institutional PACS and electronic patient medical records of our center were queried from October 2020 and May 2021, to identify patients referred for “hydrops protocol” MR imaging. A total of 924 patients with a hydrops MR imaging protocol were evaluated for inclusion.

The medical charts of all patients were systematically reviewed by 1 otoneurologist (C.H.). Demographic features were recorded as well as clinical reports including detailed neuro-otologic examinations.

### Patients

Among the 924 patients, 30 patients (60 ears) had undergone both a conventional 3D FLAIR (conv-FLAIR) and an accelerated 3D FLAIR with ID (acc-FLAIR-ID) during the implementation of this sequence in our center. These patients had various cochleovestibular symptoms and a clinical suspicion of EH after evaluation by an otolaryngologist (C.H.).

### MR Imaging Protocol

MR imaging examinations were performed on a 3T Magnetom Skyra (Siemens) scanner with a Head/Neck 64 coil (Siemens). All patients underwent MR imaging 4 hours after a single IV dose of gadobutrol (Gd-DO3A-butrol; Gadovist, 0.1 mmol/kg, 1 mmol/mL;

Bayer Schering Pharma) that provided a high contrast in the labyrinth.<sup>15</sup>

All patients underwent heavily T2-weighted sequences for an anatomic reference of the labyrinthine fluid, as well as diffusion-weighted and 3D FLAIR sequences of the brain.

Two 3D FLAIR sequences were successively performed for each patient. Detailed scan parameters are summarized in Table 1.

The first acquisition, conv-FLAIR, was accelerated with a conventional GRAPPA factor of 2 and a turbo factor of 187, as used in the clinical routine at our institution. The second acquisition was also accelerated with an increased turbo factor of 263, while the GRAPPA factor was maintained at 2, resulting in a 33% scan-time reduction (5 minutes 36 seconds versus 8 minutes 15 seconds, respectively). To maintain the same echo-train length (1212 ms), we increased the bandwidth (501 versus 279 Hz/pixel), resulting in a 25% SNR loss. A sequence was reconstructed in-line immediately after the accelerated 3D FLAIR acquisition from the same raw data with ID (acc-FLAIR-ID).

### Iterative Denoising

The ID prototype algorithm was integrated into the reconstruction pipeline of the MR imaging scanner. Data processing was performed in-line using the ID algorithm. Patient-specific noise maps were measured using the adjustment framework of the system, ensuring a precise estimation of the heterogeneous noise distribution. An additional edge enhancement was built into the ID processing, which would undo some of the SNR improvement while producing a sharper image appearance. A denoising strength of 110% was chosen to efficiently reduce the noise while maintaining a detailed level of fine anatomic structures.

### Imaging Analysis

For each patient, MR images were evaluated with Carestream Vue 12.1 (Philips Healthcare) by 1 neuroradiologist (M.E.) with 7 years of experience in inner ear imaging and 1 radiology resident (R.Q.) blinded to the clinical data and to the acquisition scheme of the different data sets.

For each examination, 2 data sets were independently evaluated: 1) the conv-FLAIR, and 2) the acc-FLAIR-ID. All images were randomly interpreted.

**Qualitative Assessment.** Overall image quality was rated on a 4-point scale as follows: 1 = “poor:” limiting diagnostic capability; 2 = “fair:” not preventing diagnostic capability but significantly decreased image quality; 3 = “good:” minor artifacts; and 4 = “excellent:” no artifacts.

**Quantitative Assessment.** Quantitative assessment was performed with the ROI method.<sup>16</sup> For the signal intensity of the perilymphatic space, a 5-mm<sup>2</sup> circular ROI was placed in the basal turn of the cochlea. For the signal intensity of the noise, a 50-mm<sup>2</sup> circular ROI was placed at the same level in the medulla. The SNR, also known as signal intensity ratio (SIR), was defined as the signal

intensity of the basal turn divided by the SD of noise in the medulla (SIR = Siperilymph / SD of SInoise).

**MR Imaging Evaluation.** For the diagnosis of EH, we used the grading systems previously described in the literature,<sup>17</sup> as follows: 1) Cochlear hydrops was reported present in case of obstruction of the scala vestibuli by the endolymphatic space; 2) saccular hydrops was reported present when the saccule appeared larger than the utricle or touched the oval window; 3) utricular hydrops was defined when there was herniation of the utricle in part of the lateral semicircular canal or when there was no surrounding perilymphatic space.

**Statistical Analysis.** Data were analyzed using R statistical and computing software, Version 3.3.2 (<http://www.r-project.org/>). Comparison of the SIR between the conv-FLAIR and acc-FLAIR-

ID sequences was assessed by a *t* test. Visual assessment between the conv-FLAIR and acc-FLAIR-ID sequences was compared using the Fisher exact test. To evaluate the reproducibility of the qualitative analysis, we calculated interreader agreement with the Cohen  $\kappa$  coefficient.<sup>18</sup> Continuous data were expressed as mean and SD. Categorical data were expressed as frequencies and percentages. Significance was set at  $P < .05$ .

## RESULTS

### Population

Thirty patients (18 women and 12 men) with a mean age of 51.6 (SD, 16.6) years (range, 23–86 years) were included in this study. A total of 60 ears were analyzed.

### MR Imaging Data

**Quantitative Analysis.** For conv-FLAIR, the mean SIR for the symptomatic and asymptomatic ears was 19 (SD, 8) and 16.3 (SD, 6.8), respectively. For acc-FLAIR-ID, the mean SIR for the symptomatic and asymptomatic ears was 29.5 (SD, 15.7) and 25.9 (SD, 10.5), respectively. The mean SIR for symptomatic and asymptomatic ears of acc-FLAIR-ID was significantly higher than the mean SNR of conv-FLAIR ( $P < .001$ ).

**Image-Quality Subjective Analysis.** Pooled image quality scores are shown in Table 2.

For the senior radiologist, the mean overall image quality was considered good for conv-FLAIR (3.3 [SD, 0.6]) and acc-FLAIR-ID (3.8 [SD, 0.4]). For conv-FLAIR, image quality of 3 patients was rated as fair; 15 patients, as good; and 12 patients, as excellent. For acc-FLAIR-ID, image quality of 6 patients was rated as good, and 24 patients, as excellent. The improved image-quality score was significantly different for acc-FLAIR-ID compared with conv-FLAIR ( $P = .003$ ) (Fig 1).

For the junior radiologist, the mean overall image quality was considered as good for conv-FLAIR (2.7 [SD, 1]) and acc-FLAIR-ID (2.8 [SD, 1]). For conv-FLAIR, image quality for 5 patients was rated as poor; 4 patients, as fair; 16 patients, as good; and 5 patients, as excellent. For acc-FLAIR-ID, image quality of 5 patients was rated as poor; 2 patients, as fair; 15 patients, as good; and 8 patients, as excellent. The image-quality score was not significantly different for acc-FLAIR-ID compared with conv-FLAIR ( $P = .38$ ).

### EH Evaluation

For conv-FLAIR, EH was observed in 18/60 ears (30%): cochlear hydrops ( $n = 15$ ), saccular hydrops ( $n = 18$ ), utricular hydrops ( $n = 8$ ) by the senior

**Table 2: Qualitative assessment independently performed by 2 blinded radiologists on a 4-point scale<sup>a</sup>**

	Conv-FLAIR		Acc-FLAIR-ID	
	Senior Radiologist	Junior Radiologist	Senior Radiologist	Junior Radiologist
Poor	0	5	0	5
Fair	3	4	0	2
Good	15	16	6	15
Excellent	12	5	24	8

<sup>a</sup>1, poor; 2, fair; 3, good; and 4, excellent.

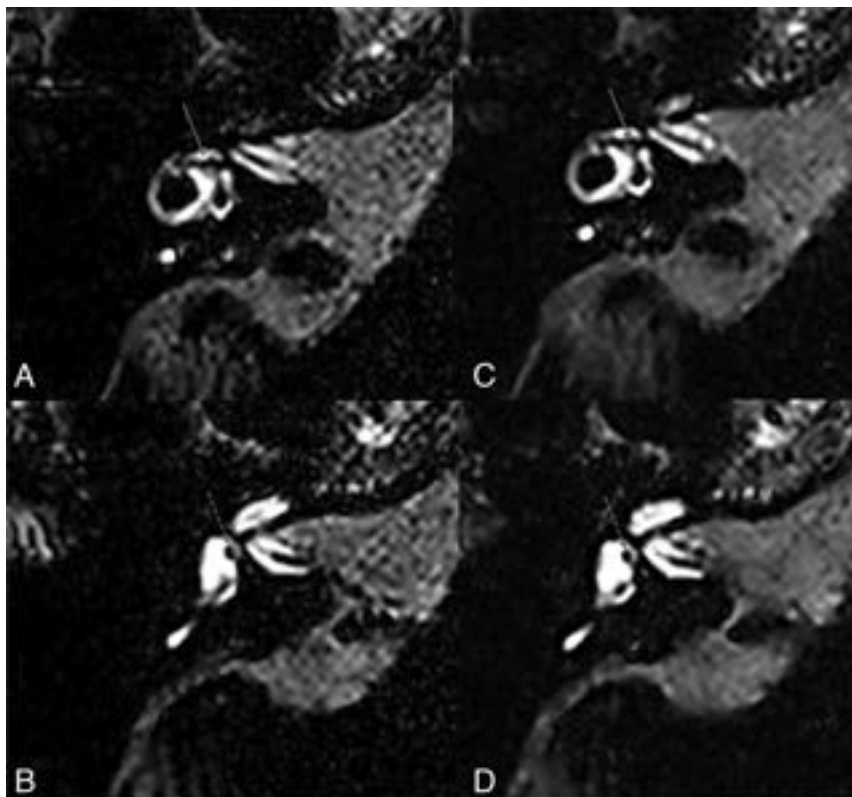


**FIG 1.** An example of conv-FLAIR (A and B) and acc-FLAIR-ID (C and D) images with normal findings in the same patient without hydrops. A and C, The level of the utricle (white arrow) and the lateral semicircular canal. B and D, The level of the saccule (dashed white arrow). Both sequences were rated as excellent. Note the sharper appearance of the acc-FLAIR-ID images, which were acquired with a 33% scan time reduction.

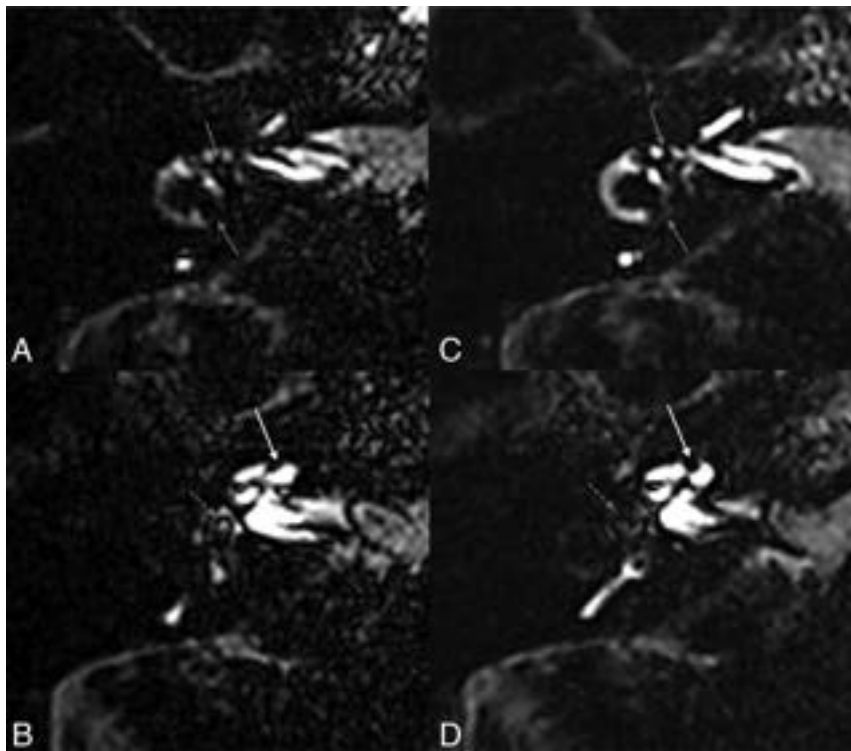


**FIG 2.** Conv-FLAIR (A and B) and Acc-FLAIR-ID (C and D) images of a patient with cochlear, saccular, and utricular hydrops. A and C, Utricular hydrops: an enlarged utricle (white arrow) with partial obstruction of the perilymphatic space and herniation in the posterior limb of the lateral semicircular canal. B and D, Cochlear and saccular hydrops: an enlarged endolymphatic space with obstruction of the scala vestibuli (white arrow) and an enlarged saccule (dashed arrow), confluent with the utricle from which it is not distinguishable.

**Table 3: Pooled diagnostic assessment of hydrops independently performed by 2 blinded radiologists<sup>a</sup>**

	Conv-FLAIR			Acc-FLAIR-ID		
	Senior	Junior	$\kappa$	Senior	Junior	$\kappa$
Cochlear hydrops	15/60	10/60	0.75 (0.57–0.93)	15/60	11/60	0.81 (0.65–0.96)
Saccular hydrops	18/60	12/60	0.74 (0.57–0.90)	18/60	13/60	0.81 (0.65–0.96)
Utricular hydrops	8/60	8/60	1 (1.00–1.00)	10/60	8/60	0.78 (0.63–0.94)

<sup>a</sup> There were no significant differences for all EH locations between the 2 sequences. The  $\kappa$  coefficients for interobserver agreement were good-to-excellent.

reader (Fig 2). For acc-FLAIR-ID, EH was also observed in 18/60 ears (30%): cochlear hydrops ( $n = 15$ ), saccular hydrops ( $n = 18$ ), utricular hydrops ( $n = 10$ ) by the senior reader. There were no significant differences for all EH locations ( $P < .001$ ) between the 2 sequences (Fig 2).

For conv-FLAIR, EH was observed in 12/60 ears (20%): cochlear hydrops ( $n = 10$ ), saccular hydrops ( $n = 12$ ), utricular hydrops ( $n = 8$ ) by the junior reader (Fig 2). For acc-FLAIR-ID, EH was observed in 13/60 ears (21.7%): cochlear hydrops ( $n = 11$ ), saccular hydrops ( $n = 13$ ), utricular hydrops ( $n = 8$ ) by the junior reader. There were no significant differences for all EH locations ( $P < .001$ ) between the 2 sequences (Table 3).

With conv-FLAIR, the interreader agreement was good for cochlear (0.75 [0.57–0.93]) and saccular (0.74 [0.57–0.90]) hydrops and excellent (1 [1.00–1.00]) for utricular hydrops. With acc-FLAIR-ID, the interreader agreement was very good for

cochlear (0.81 [0.65–0.96]) and utricular (0.81 [0.65–0.96]) hydrops, and good for saccular hydrops (0.78 [0.63–0.94]).

## DISCUSSION

In this study, we demonstrated that an accelerated 3D FLAIR sequence combined with an ID algorithm enabled reducing the scan time by 33% without compromising image quality and diagnostic performance for EH. As expected, the SNR was significantly increased with acc-FLAIR-ID compared with conv-FLAIR because a noise-reduction algorithm was used.

An MR imaging evaluation of the endolymphatic space relies on the selective enhancement of the perilymphatic space after administration of IV contrast media, which enables distinguishing the endolymphatic and perilymphatic spaces.<sup>1,3</sup> The main limiting factor is the low concentration of gadolinium obtained in the perilymphatic space. To overcome this, we optimized several parameters to increase the signal intensity. First, the administration of gadolinium-based contrast agents with higher longitudinal relaxivity and concentration has been recommended.<sup>15</sup> Second, a constant flip angle instead of a variable flip angle provides higher signal and contrast in the perilymphatic space, by shortening the longitudinal relaxation induced by gadolinium.<sup>9</sup> However, the use of a constant flip angle with a high echo-train length compromises the SNR. Third, the signal intensity of the perilymphatic space increases using a long TR (16,000 ms), which allows sufficient longitudinal magnetization

regrowth to detect minor T1-shortening related to low gadolinium concentration.<sup>19,20</sup> Yet, a long TR contributes to the long acquisition time, which is an important limitation to the wide spread of this protocol.

PI acceleration techniques, based on phased array coils, might be used to significantly decrease scan time to overcome the long acquisition time of these sequences. However, by increasing the acceleration factor, the reduction of the acquisition time is limited by a significant decrease in SNR (by a factor of the square root of the acceleration factor) because fewer data points are acquired and averaged.<sup>5,21</sup> In PI-reconstructed images, the SNR also depends on the spatially varying noise characteristics and amplification in the final images, quantified by the g-factor, which originates from the coil sensitivities. Because inner ear imaging requires reduced section acquisition coverage with activation of a few coil elements, the use of a higher acceleration

factor is limited. Moreover, PI techniques are particularly sensitive to motion artifacts that might occur between the time of the calibration scan and image acquisition. Thus, we have decided to increase the turbo factor and the receiver bandwidth instead of increasing the PI acceleration factor. 3D FLAIR sequences for EH exploration are less susceptible to signal loss due to the weaker later echoes affected by T2 decay. Indeed, inner ear imaging is particularly suitable for the use of a high turbo factor with a long echo-train because the T2 values of the labyrinthine fluid are high (similar to CSF, which is around 2000 ms at 3T). Despite the high turbo factor used, blurring is avoided because the echo-train duration remains inferior to 2–3 times the T2 values of the primary interest area.<sup>8</sup> By increasing the bandwidth, we were able to reduce interecho spacing to maintain the same readout time while increasing the number of echoes, decreasing the total scan time. Nevertheless, the inherent result of an increased bandwidth is a 25% SNR loss because of the amount of noise that is sampled due to the larger frequency range.

The ID algorithm compensated for the signal loss caused by using a constant flip angle with a long echo-train length and the increased bandwidth. Recently, Naganawa et al<sup>10</sup> achieved a 5-minute HYDROPS-Mi2 sequence with DLR. The reduction in acquisition time was mainly obtained by decreasing the number of slices (224 to 60), while the SNR loss was compensated for with the DLR. The DLR tool incorporates a deep convolutional neural network restoration process into the reconstruction flow and enables noise reduction. DLR is a nonlinear processing with behaviors potentially difficult to predict.<sup>22</sup> Thus, in our experience, ID allows better control of the denoising process, parameters, and strength, ensuring a precise estimation of the heterogeneous noise distribution.

Other acceleration approaches such as compressed sensing (CS) have been introduced to reduce the scan time. CS is based on incoherent subsampling of the Fourier space, transformation of the image into a sparse representation, and nonlinear iterative reconstruction.<sup>23</sup> It is used in various applications and is particularly suitable for indications in which images are sparse, such as MRA.<sup>24</sup> However, other applications with low sparsity, such as 3D morphologic sequences with high spatial resolution, offer little acceleration potential with CS. In addition, artifacts such as image blurring and global ringing have been described with CS, notably for MR neuroimaging,<sup>25</sup> which limits the acceleration rates achievable. CS is also limited by its extended reconstruction time, which can be reduced with the use of a graphic processing unit, though it is not available on all clinical MR imaging scanners.

Conversely, an ID algorithm can be performed on conventional computers without a significant increase of reconstruction time. The use of a quantitative noise map in ID is particularly suited to limit the g-factor penalty associated with high acceleration rates, as well as the SNR loss related to the increased bandwidth.

Our study has several limitations. EH was reported as present or absent by an anatomic system, but we did not use grading or volumetric assessment. However, our hydrops assessment was based on a previously reported anatomically-based grading system,<sup>17</sup> and the grading used should not have impacted diagnostic relevancy.

The use of a 3T system and a 64-channel phased array head coil contributed to the high image quality. The SNR improvement with ID could improve the image quality of 1.5T scanners, which are more available, and further studies should be performed at 1.5T or with lower head coil density.

Our study has several clinical implications. By reducing the scan time, patient comfort and satisfaction are increased, reducing the risk of motion artifacts. Shortening the imaging time will also allow a higher patient throughput and is expected to promote wider use of MR imaging for the evaluation of EH. In our institution, about 40 patients per week undergo inner ear MR imaging. A 33% scan time reduction of 8 minutes 15 seconds would allow 120 minutes of additional machine time.

Along with the scan time, the 4-hour delay after gadolinium injection contributes to the logistical strains of EH imaging. Our group showed in a recent work that with optimized 3D FLAIR parameters, the postinjection delay could be shortened to 2 hours with sufficient contrast for EH evaluation, which should further shorten the imaging time and promote a wider use of EH MR imaging.<sup>26</sup>

## CONCLUSIONS

3D FLAIR sequences for EH evaluation require optimal parameters to obtain sufficient signal in the perilymphatic space. The trade-off and one of the main limitations are long acquisition times. In this study, the ID algorithm was successfully applied to an accelerated 3D FLAIR sequence for EH exploration with significantly reduced scan time without compromising image quality and the diagnostic performance.

Disclosure forms provided by the authors are available with the full text and PDF of this article at [www.ajnr.org](http://www.ajnr.org).

## REFERENCES

1. Nakashima T, Naganawa S, Sugiura M, et al. **Visualization of endolymphatic hydrops in patients with Meniere's disease.** *Laryngoscope* 2007;117:415–20 CrossRef Medline
2. Eliezer M, Attyé A, Toupet M, et al. **Imaging of endolymphatic hydrops: a comprehensive update in primary and secondary hydroptic ear disease.** *J Vestib Res* 2021;31:261–68 CrossRef Medline
3. Connor SE, Pai I. **Endolymphatic hydrops magnetic resonance imaging in Ménière's disease.** *Clin Radiol* 2021;76:76.e1–19 CrossRef Medline
4. Gürkov R. **Menière and friends: imaging and classification of hydroptic ear disease.** *Otol Neurotol* 2017;38:e539–44 CrossRef Medline
5. Deshmane A, Gulani V, Griswold MA, et al. **Parallel MR imaging.** *J Magn Reson Imaging* 2012;36:55–72 CrossRef Medline
6. Pruessmann KP, Weiger M, Scheidegger MB, et al. **SENSE: sensitivity encoding for fast MRI.** *Magn Reson Med* 1999;42:952–62 Medline
7. Griswold MA, Jakob PM, Heidemann RM, et al. **Generalized autocalibrating partially parallel acquisitions (GRAPPA).** *Magn Reson Med* 2002;47:1202–10 CrossRef Medline
8. Mugler JP. **Optimized three-dimensional fast spin-echo MRI.** *J Magn Reson Imaging* 2014;39:745–67 CrossRef Medline
9. Nahmani S, Vaussy A, Hautefort C, et al. **Comparison of enhancement of the vestibular perilymph between variable and constant flip angle–delayed 3D FLAIR sequences in Ménière disease.** *AJNR Am J Neuroradiol* 2020;41:706–11 CrossRef Medline
10. Naganawa S, Ito R, Kawai H, et al. **MR imaging of endolymphatic hydrops in five minutes.** *Magn Reson Med Sci* 2021;21:401–40 CrossRef Medline

11. Naganawa S, Nakamichi R, Ichikawa K, et al. **MR imaging of endolymphatic hydrops: utility of iHYDROPS-Mi2 combined with deep learning reconstruction denoising.** *Magn Reson Med Sci* 2021;20:272–79 CrossRef Medline
12. Eliezer M, Vaussy A, Toupin S, et al. **Iterative denoising accelerated 3D SPACE FLAIR sequence for brain MR imaging at 3T.** *Diagn Interv Imaging* 2022;103:13–20 CrossRef Medline
13. Almansour H, Weiland E, Kuehn B, et al. **Accelerated three-dimensional T2-weighted turbo-spin-echo sequences with inner-volume excitation and iterative denoising in the setting of pelvis MRI at 1.5T: impact on image quality and lesion detection.** *Acda Radiol* 2022;29:e248–59 CrossRef Medline
14. Kang HJ, Lee JM, Ahn SJ, et al. **Clinical feasibility of gadoteric acid-enhanced isotropic high-resolution 3-dimensional magnetic resonance cholangiography using an iterative denoising algorithm for evaluation of the biliary anatomy of living liver donors.** *Invest Radiol* 2019;54:103–09 CrossRef Medline
15. Eliezer M, Poillon G, Gillibert A, et al. **Comparison of enhancement of the vestibular perilymph between gadoterate meglumine and gadobutrol at 3-Tesla in Meniere's disease.** *Diagn Interv Imaging* 2018;99:271–77 CrossRef Medline
16. Pakdaman MN, Ishiyama G, Ishiyama A, et al. **Blood-labyrinth barrier permeability in Menière disease and idiopathic sudden sensorineural hearing loss: findings on delayed postcontrast 3D-FLAIR MRI.** *AJNR Am J Neuroradiol* 2016;37:1903–08 CrossRef Medline
17. Kahn L, Hautefort C, Guichard JP, et al. **Relationship between video head impulse test, ocular and cervical vestibular evoked myogenic potentials, and compartmental magnetic resonance imaging classification in Menière's disease.** *Laryngoscope* 2020;130:E444–52 CrossRef Medline
18. Benchoufi M, Matzner-Lober E, Molinari N, et al. **Interobserver agreement issues in radiology.** *Diagn Interv Imaging* 2020;101:639–41 CrossRef Medline
19. Osman S, Hautefort C, Attyé A, et al. **Increased signal intensity with delayed post contrast 3D FLAIR MRI sequence using constant flip angle and long repetition time for inner ear evaluation.** *Diagn Interv Imaging* 2022;103:225–29 CrossRef Medline
20. Kato Y, Bokura K, Taoka T, et al. **Increased signal intensity of low-concentration gadolinium contrast agent by longer repetition time in heavily T2-weighted-3D FLAIR.** *Jpn J Radiol* 2019;37:431–35 CrossRef Medline
21. Robson PM, Grant AK, Madhuranthakam AJ, et al. **Comprehensive quantification of signal-to-noise ratio and g-factor for image-based and k-space-based parallel imaging reconstructions.** *Magn Reson Med* 2008;60:895–907 CrossRef Medline
22. Higaki T, Nakamura Y, Tatsugami F, et al. **Improvement of image quality at CT and MRI using deep learning.** *Jpn J Radiol* 2019;37:73–80 CrossRef Medline
23. Yang AC, Kretzler M, Sudarski S, et al. **Sparse reconstruction techniques in magnetic resonance imaging: methods, applications, and challenges to clinical adoption.** *Invest Radiol* 2016;51:349–64 CrossRef Medline
24. Lustig M, Donoho D, Pauly JM. **Sparse MRI: The application of compressed sensing for rapid MR imaging.** *Magn Reson Med* 2007;58:1182–95 CrossRef Medline
25. Sartoretti T, Reischauer C, Sartoretti E, et al. **Common artefacts encountered on images acquired with combined compressed sensing and SENSE.** *Insights Imaging* 2018;9:1107–15 CrossRef Medline
26. Barlet J, Vaussy A, Ejzenberg Y, et al. **Optimized 3D FLAIR sequences to shorten the delay between intravenous administration of gadolinium and MRI acquisition in patients with Menière's disease.** *Eur Radiol* 2022;32:6900–09 CrossRef Medline

# Early Diagnosis of Tuberous Sclerosis Complex: Prenatal Diagnosis

M. Bekiesinska-Figatowska, P. Sobieraj, M. Pasieczna, and J. Szymkiewicz-Dangel

## ABSTRACT

**BACKGROUND AND PURPOSE:** Strong emphasis has been placed recently on early (4 postnatal months) detection of tuberous sclerosis complex and the introduction of antiepileptic treatment before seizure onset. This objective can be achieved prenatally: Cardiac rhabdomyomas and the major diagnostic tuberous sclerosis complex sign are detected during fetal ultrasound, and prenatal MR imaging allows detection of cerebral major manifestations: cortical tubers, subependymal nodules, and subependymal giant cell astrocytomas.

**MATERIALS AND METHODS:** We retrospectively reviewed 50 fetuses with ultrasound-detected cardiac tumors at 19–36 gestational weeks (median, 31 weeks). MR imaging with the use of 1.5T scanners was performed at 24–37 gestational weeks (median, 34 weeks).

**RESULTS:** In 11 fetuses (22%), cardiac tumors remained the only criterion. In remaining 39 fetuses (78%), MR imaging revealed a prenatal diagnosis of tuberous sclerosis complex, having shown an additional 1–3 major criteria: subependymal nodules in all cases (39/39 = 100.0%), subependymal giant cell astrocytomas in 6 (6/39 = 15.4%), and cortical tubers in 24 (24/39 = 61.5%). Radial migration lines and cerebellar tuber, not published so far, were shown in 1 case each.

**CONCLUSIONS:** A schedule of proper care of children with tuberous sclerosis complex can be established during the perinatal period due to education of women to report for mandatory ultrasound examinations during pregnancy, the good quality of ultrasound, and referral to MR imaging if a cardiac tumor is depicted on ultrasound. Gynecologists and pediatric cardiologists performing fetal ultrasound and radiologists performing prenatal MR imaging are a key to early diagnosis of tuberous sclerosis complex in many cases.

**ABBREVIATIONS:** CT = cortical tuber; GW = gestational week; SEGA = subependymal giant cell astrocytoma; SEN = subependymal nodule; SSFSE = single-shot fast spin-echo; TSC = tuberous sclerosis complex; US = ultrasound

Epileptogenesis in tuberous sclerosis complex (TSC) starts prenatally with epilepsy, according to some authors, in 100% of TSC cases. In recent years, there has been strong emphasis on the early detection of TSC and on the early introduction of antiepileptic treatment before the seizure onset to improve the neurodevelopmental outcome of the affected children. In neurological journals, “early” means the first 4 months (16 weeks) of postnatal life because this time point is regarded as the usual time of clinical seizure onset.<sup>1</sup>

It is estimated that up to 90% of children with cardiac rhabdomyomas have TSC, at least 50% of children with TSC have cardiac rhabdomyomas, and almost 100% of fetuses with multiple rhabdomyomas have TSC.<sup>2</sup> Rhabdomyomas are the most common type of fetal primary cardiac tumors, with an incidence of 60%<sup>3</sup> to 86%.<sup>4</sup> They are detected during fetal ultrasound (US) with further characterization on fetal echocardiography.

Being 1 major diagnostic sign of TSC, cardiac rhabdomyomas require the second major feature to confirm the diagnosis. Prenatal MR imaging allows detection of cerebral TSC manifestations. These are cortical tubers, subependymal nodules (SENs), and subependymal giant cell astrocytomas (SEGAs).

If one takes the above into account, a big percentage of patients could be diagnosed prenatally by cardiac rhabdomyomas and brain lesions, which is much earlier than the first 4 months of postnatal life. If the diagnosis is confirmed by 2 major signs, an optimal perinatal strategy can be introduced.

On the basis of the experience of 2 tertiary diagnostic centers (Department of Diagnostic Imaging, Institute of Mother and

Received March 28, 2023; accepted after revision June 25.

From the Department of Diagnostic Imaging (M.B.-F., P.S.), Institute of Mother and Child, Warsaw, Poland; Second Department of Obstetrics and Gynecology (M.P.), Medical University of Warsaw, Warsaw, Poland; and Department of Perinatal Cardiology and Congenital Anomalies (J.S.-D.), Centre of Postgraduate Medical Education, Warsaw, Poland.

This work was supported by the internal grant of the Institute of Mother and Child, Warsaw, Poland, No. 510-14-03.

Please address correspondence to Monika Bekiesinska-Figatowska, MD, PhD, Department of Diagnostic Imaging, Institute of Mother and Child, Kasprzaka 17a, 01-211 Warsaw, Poland; e-mail: monika.bekiesinska@imid.med.pl

<http://dx.doi.org/10.3174/ajnr.A7952>

**Table 1: Details of MR imaging protocol**

	SSFSE/T2	FSE/T1	3D T1 LAVA-Flex	FIESTA/2D	GRE EPI	DWI
TR (ms)	1 800	400	6.4	4.5	3 000	6 120
TE (ms)	81.4	7.6	3.1	2.0	50.0	71.0
Section thickness/overlap (mm)	3.0/1.0	3.0/0.5	4.0/−2.0	5.0/0.5	5.0/0.5	3.0/0.5
FOV (cm)	39 × 35	33 × 33	39 × 39	38 × 38	38 × 38	33 × 33
Breathhold	No	Yes	Yes	Yes	Yes	No

**Note:**—GRE indicates gradient recalled echo.

**Table 2: Number of diagnostic TSC criteria in the analyzed material**

No. of Pts with 1 Criterion Only (Cardiac Tubers) on US	No. of Pts with 2 Major Criteria Only	No. of Pts with 3 Major Criteria Only	No. of Pts with 4 Major Criteria	No. of Pts with 2 Major and 1 Minor Criteria	No. of Pts with 3 Major and 1 Minor Criteria
11	17	18	2	1	1

**Note:**—Pts indicates patients.

Child, and Referral Center for Fetal Cardiology, Agatowa Sonography Clinic, Warsaw, Poland), the authors show that an early diagnosis of TSC means a prenatal diagnosis, which is feasible in the experienced hands of fetal cardiologists and radiologists. Also, the recent publication in the *American Journal of Neuroradiology*, presenting 47 published cases from PubMed and 4 cases of the authors, prompts us to publish our material.<sup>5</sup>

## MATERIALS AND METHODS

The study group consisted of 50 retrospectively reviewed fetuses with cardiac tumors detected on US and referred to MR imaging, with a diagnosis of cardiac tumors suggestive of rhabdomyomas to confirm or rule out TSC. Informed consent for clinical investigations was obtained from all patients. The Bioethical Committee's approval was waived due to the retrospective character of this study.

There were 5 fetuses with 1 cardiac tumor, 29 fetuses  $\geq 2$  cardiac tumors, and in 16 fetuses, the number of cardiac tumors was unclear (missing an exact US report and images, cardiac tubers known from the referral sheet and from MR images). In the second group, in 2 cases, we dealt with a dichorionic diamniotic pregnancy of a mother with TSC with only 1 fetus affected and a healthy co-twin. Cardiac tumors were detected on US between the gestational ages of 19 and 36 weeks (median, 31 weeks), and MR imaging was performed between 24 and 37 gestational weeks (GWs), median, 33 GWs.

In 32 cases, US was performed in the Referral Center for Fetal Cardiology, Agatowa Sonography Clinic. Each fetus had detailed fetal echocardiography using the Voluson Expert (GE Healthcare) or EPIQ7 (Philips Healthcare) machines.

MR imaging was performed without maternal and fetal sedation with the use of a 1.5T scanner in single-shot fast spin-echo (SSFSE)/T2- and FSE/T1-weighted images (and/or 3D T1 LAVA-Flex; GE Healthcare), FIESTA/2D, gradient-echo EPI, and DWI sequences in 3 planes. Details of MR imaging protocol are shown in Table 1.

## RESULTS

Among the group of 50 fetuses, in 11 cases (22%), cardiac tumors remained the only criterion of TSC, and the suspicion of TSC

was not confirmed on fetal MR imaging. Of these 11 cases, in 3, there were single cardiac tubers; in 3, cardiac tubers were multiple; and 5 belonged to the group with an unclear number of cardiac tumors. In the remaining 39 fetuses (78%), MR imaging allowed the prenatal diagnosis of TSC after having shown an additional 1–3 major criteria and in 2 cases, 1 minor criterion (multiple renal cysts) as well. These data are presented in Table 2.

SENs were detected on MR imaging in all cases of TSC (39/39 = 100.0%) and were not detected on US. In 6 fetuses (6/39 = 15.4%), SEGAs were diagnosed on MR imaging on the basis of their location near the foramen of Monro and a size of  $>10$  mm, and in half of these cases, there was already asymmetric ventriculomegaly on the side of the tumor. Cortical tubers were the only cerebral manifestation of TSC suspected on US in 6 cases and confirmed on MR imaging in 5. Cortical tubers were found on MR imaging in 24 cases (24/39 = 61.5%). In one of these cases, we could also observe migration lines on MR imaging.

The SSFSE/T2-weighted sequence was the most important one for making the diagnosis of cerebral manifestations of TSC: SENs, SEGAs, and cortical tumor (CTs) with clear hypointensity of these lesions most strongly expressed in the case of SENs and SEGAs, which were the most conspicuous lesions. Their visualization was weaker on FIESTA/2D. Gradient recalled-echo EPI was used to differentiate SENs from foci of germinal matrix/subependymal hemorrhage and calcifications. CTs were more difficult to diagnose due to weaker delineation from the surrounding brain tissue and weaker hypointensity on SSFSE/T2. It was particularly important in cases of CTs to perform and compare SSFSE/T2, FIESTA/2D, and T1-weighted images. The latter, which are always inferior in fetal studies, were, nevertheless, helpful, showing the (weak) hyperintensity of these lesions.

Failure to see SENs in at least 2 projections or the questionable images of CTs were treated as the absence of the second major criterion, and TSC was not confirmed; while on the other hand, the obvious image of SENs in at least 2 planes was a clear second major criterion, allowing a reliable prenatal diagnosis of TSC.

Detailed information on the TSC criteria detected in the study group on US and MR imaging is presented in Table 3.

Single renal cysts were found on MR imaging in 2 fetuses and, for obvious reasons, were not regarded as a diagnostic criterion.

**Table 3: Details of US and MR imaging findings in the analyzed material**

No. of Pts	US: No. of Cardiac Tumors	US: Susp. of CT	MRI: SEN	MRI: SEGAs	MRI: CT	SEGAs-Related VM	MRI: Renal Cysts
5	1	1	2	—	1	—	—
29	≥2	4	25	4	13	2	2
16	Unclear	1	12	2	10	1	—
50		6	39	6	24	3	2

**Note:**—Pts indicates patients; Susp, suspicion; VM, ventriculomegaly; en dash, none.

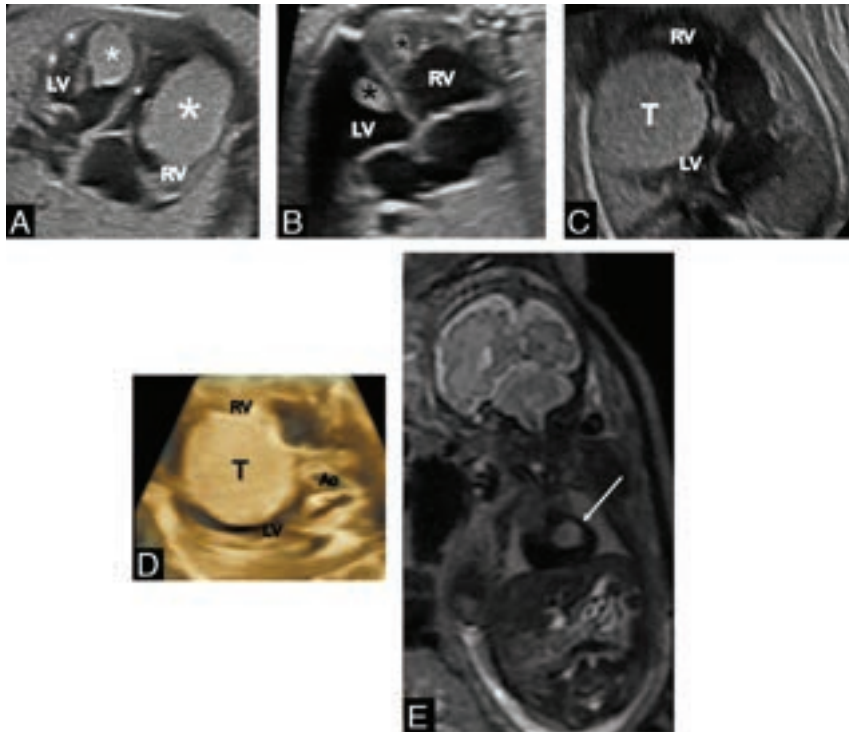


**FIG 1.** Typical echocardiographic images of multiple cardiac tumors (rhabdomyomas) in 3 different fetuses (fetus 1, 38 GWs (A); fetus 2 (B), 35 GWs; fetus 3 (C and D)). A and B, Tumors are located in both ventricles and attached to the ventricular walls and interventricular septum and do not disturb blood flow. C and D, A huge cardiac tumor located in the RV, compressing the LV, and disturbing blood flow through both ventricles (C, 2D view; D, 3D view). E, MR imaging at 30 GWs. SSFSE/T2-weighted image, coronal plane: hypointense cardiac tumor (arrow) against the background of the “black hole” of a heart. RV, right ventricle; LV, left ventricle; Ao, aorta; T and/or \* tumor.

Multiple renal angiomyolipomas were detected in mothers in 2 cases.

## DISCUSSION

Subependymal nodules, subependymal giant cell astrocytomas, multiple cortical tubers and/or radial migration lines, and cardiac rhabdomyomas are the major features of TSC as listed in the updated diagnostic criteria for TSC in 2021. Brain abnormalities are the domain of MR imaging, and cardiac ones are diagnosed on US, and it is possible to detect them in the prenatal period. Two major features are sufficient to make a definite diagnosis of TSC,<sup>6</sup> and 2 diagnostic methods (fetal US and MR imaging) are necessary to reach this diagnosis, also before birth. In the PubMed database, we found the first description of a prenatal diagnosis of TSC on MR imaging dating back to 1992.<sup>7</sup> Our interest in this topic has also been ongoing for years, with the first publication in 2007.<sup>8</sup>

Neuroimaging findings of SENs, SEGAs, and what was formerly called cortical dysplasia are often identified after an initial presentation, but we strive for an early diagnosis in this considerable group of patients whose brain involvement occurs early in fetal life. In an article by Davis et al,<sup>9</sup> 35% of 130 infants with TSC presented prenatally. It is, therefore, a large group, and it is worth fighting for an early diagnosis in this group of patients.

An early diagnosis should be reached in these cases, provided that pregnant women are required to present themselves for US during gestation. Having found cardiac tubers, a fetal US specialist should refer the expectant mother to MR imaging for a detailed assessment of the brain. This referral is to answer the question, “How to make the diagnosis before seizures.”<sup>1</sup> It is what experts have advised since at least 2014,<sup>10</sup> and this procedure is followed by the authors’ 2 centers.

Incidentally, seizures may begin before birth, not only in association with TSC. They may be felt by the mother and confirmed on US<sup>11</sup> or on MR imaging, especially in the cine mode. In our material, one pregnant woman with prenatally confirmed TSC reported the recent

change of her baby’s movement pattern, with a new onset of rhythmic, repetitive movements lasting for several seconds which, though not visualized during MR imaging, most likely represented seizures.

There are several questions: 1) Is it possible to diagnose specifically cardiac rhabdomyoma? 2) Is it possible to diagnose, specifically, SENs, SEGAs, and cortical dysplasia prenatally?

Cardiac rhabdomyomas are quite easy to detect during fetal echocardiography. They usually occur in the third trimester of pregnancy, so most of them cannot be seen during the US, which is performed around 20 weeks of gestation. The US appearance of rhabdomyomas is very characteristic (Fig 1A–D). They are histologically benign; however, they are a typical sign of TSC. It is important to check their location because sometimes they obstruct inflow or outflow of the heart. Although they occur very rarely, they are a life-threatening condition for neonates, so perinatal specialist care should be instituted.

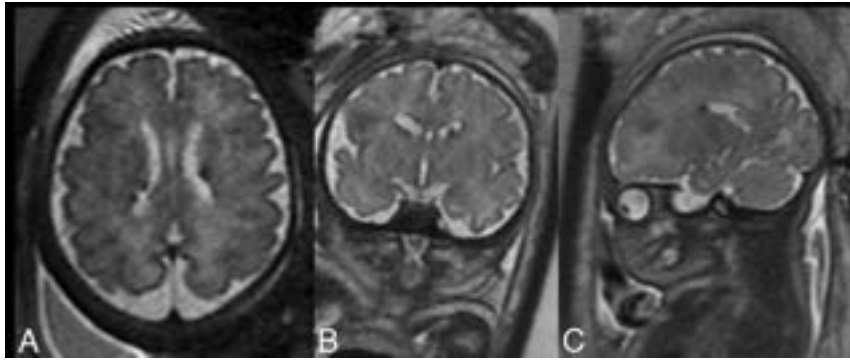


**FIG 2.** T2-hypointense subependymal nodules on the axial (A), coronal (B), and sagittal (C) planes.

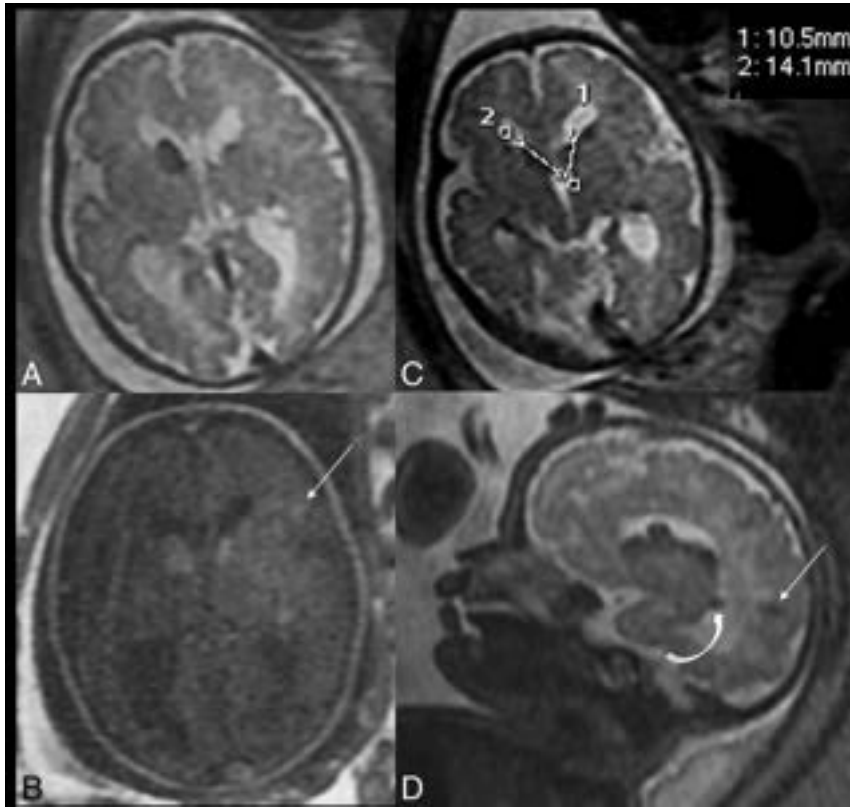


**FIG 3.** MR imaging at 32 GWs. SSFSE/T2-weighted images in the axial (A and C) and sagittal (D) planes and an axial T1-weighted image (B). A fetus with 4 major criteria: cardiac tumors (not shown here), 2 SEGAs (measured), SENs (curved arrow), and cortical tubers (straight arrows).

Cardiac rhabdomyomas have a quite typical appearance on US. They are usually firmly attached to the heart muscle, interventricular or free ventricular walls, rarely in the atria. They are always oval and have various sizes, from a few millimeters to the huge tumor that involves most of the cardiac cavity. Most commonly, their diameter is a few millimeters, and they do not disturb blood inflow or outflow. They look slightly more hyperechogenic than the heart muscle.

On MR imaging, cardiac rhabdomyomas are uniformly hyperintense on SSFSE/T2-weighted images against the background of a dark heart that is called a “black hole” (Fig 1E). Being the most common cardiac tumors in the

prenatal period, often multiple, they usually do not cause diagnostic uncertainty.

SENs are occult to US and are detected only on MR imaging in most cases. These nodules are T2-hypointense (Fig 2) and, according to the literature, display typically bright signal on T1-weighted images.<sup>12,13</sup> The latter was not obvious in our experience, most likely due to the suboptimal quality of T1WI and the small size of these nodules. SENs should not be diagnosed unless they are demonstrated in 2 different projections, eg, axial and coronal, to avoid misdiagnoses. The differential diagnosis of SENs on fetal MR imaging includes subependymal heterotopia and subependymal hemorrhage.<sup>12</sup> Nagaraj et al<sup>14</sup> added to this list abnormal nodularity of the germinal matrix that does not correspond to subependymal heterotopia postnatally. The normal germinal matrix that forms on the ventricular walls is smooth and symmetric. During development in utero, it increases in volume between 13 and 26 GWs, then loses half of its volume between 26 and 28 GWs, and decreases further thereafter. Between 26 and 28 GWs, the germinal matrix is at high risk of hemorrhage.<sup>13</sup> However, subependymal hemorrhage is often associated with ventricular bleeding, detected on US, and has a typical evolution on follow-up US.<sup>12</sup> The nodular appearance of the ventricular walls that is depicted on MR imaging early in pregnancy, eg, at 21 GWs, suggests subependymal heterotopia; late appearance in the third trimester is more suggestive of SENs in TSC. In our study group, SENs were detected on prenatal MR imaging in 78% of cases in all fetuses with prenatally diagnosed TSC and represented the second major criterion in all cases of TSC. They were not described on US in any fetus in our study group.

SEGAs also belong to the list of major features of TSC. They have an incidence of 5%–15% in TSC and tend to arise from SENs later in life, though they may also be detected prenatally. Their most common location is near the foramen of Monro; thus, they can cause obstructive hydrocephalus.<sup>6</sup> The definition of SEGAs is as follows: a tumor at the caudothalamic groove of >10 mm in any direction or any SEN that had demonstrated growth across consecutive imaging studies.<sup>15</sup> The first part of this definition was used in our study because only 1 fetus with a TSC diagnosis had the second MR imaging performed (and no

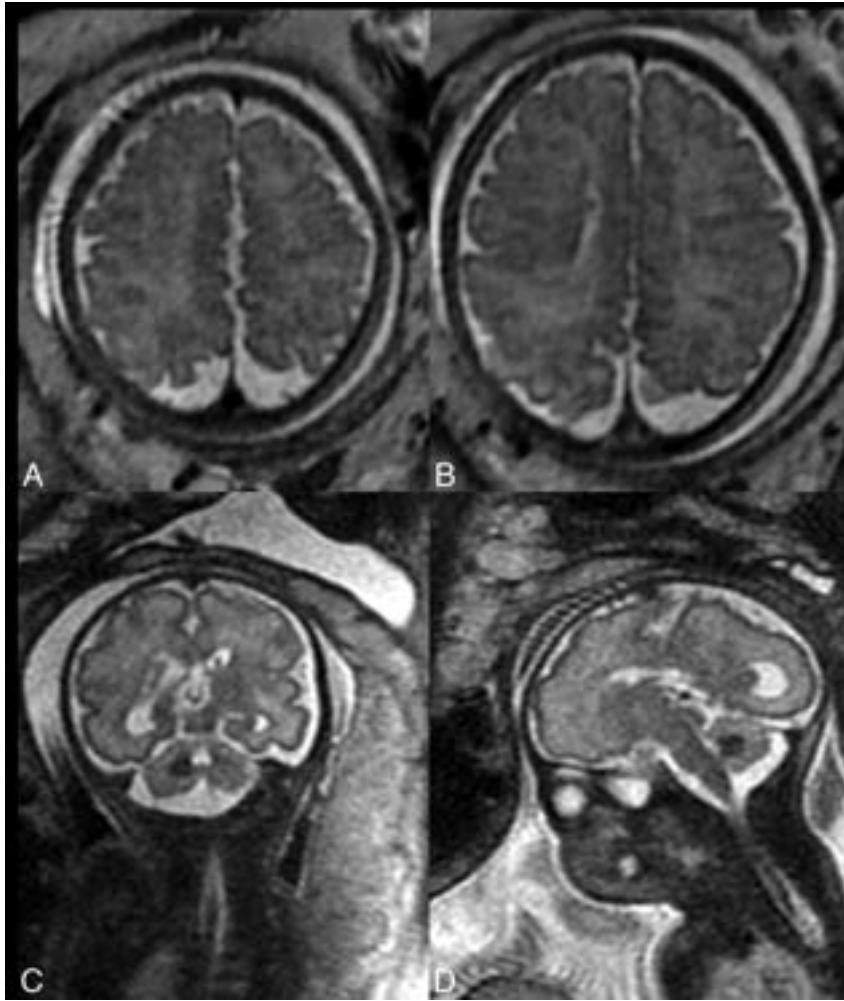


**FIG 4.** MR imaging of 2 different fetuses: at 35 GWs (A and B) and at 29 GWs (C and D). SSFSE/T2-weighted images. A and B, T2-hypointense radial migration lines. C and D, T2-hypointense tuber in the right cerebellar hemisphere.

progression of the SEGAs was noted during a 4-week period). SENs of <10 mm located near the foramen of Monro were found in 20 cases in our material, and SEGAs, in as many as 6 (Fig 3A–C).

In the published report on the prenatal diagnosis of SEGAs by Hussain et al,<sup>16</sup> there were no dimensions of the tumor reported, but it was huge. Kotulska et al<sup>17</sup> reported 2 cases of a prenatal diagnosis of SEGAs in their material but did not show the images and did not address the question of the dimensions of the tumor and growth and hydrocephalus; therefore, it is unclear on what basis SEGAs were diagnosed in these 2 cases. Most interesting, these authors reported in their retrospective study that only 10 of 452 (2.2%) patients with TSC were diagnosed with SEGAs in the first 3 months of life, while in our, much smaller material, this percentage is much higher, only in the prenatal period (15.4%).

Finally, cortical tubers, which constitute another major feature of TSC, were seen less frequently than SENs in the prenatal period on MR imaging. Similar to SENs, they are T2-hypointense and T1-hyperintense (Fig 3B, -D).<sup>18</sup> In our material, they were present in 61.5% of cases of TSC. In the literature, cortical tubers are reported as the most frequent finding in the prenatal period;<sup>10</sup> this was not confirmed in our material. In the newest updated

TSC diagnostic criteria, the new criterion has been formulated as “multiple cortical tubers and/or radial migration lines,”<sup>6</sup> and in our material, we have 1 case in which radial migration lines seem to be present as radial T2-hypointense lines (Fig 4A, -B). These lesions are described in the literature as displaying low signal intensity on T1-weighted images and high signal intensity on T2- and FLAIR; however, this MR imaging pattern is reversed in young infants (and fetuses) against the background of the surrounding unmyelinated brain with increased water content.<sup>18</sup> No reports on radial migration lines on fetal MR imaging have been found in the literature. On the contrary, statements such as “white matter abnormalities were not evaluated in this study because of their poor visibility on fetal MR imaging” were noted.<sup>19</sup> Most interesting, in our study, there is also 1 case of a cerebellar tuber that, in addition, has already been depicted on US and confirmed on MR imaging (Fig 4C, -D). No reports on cerebellar tubers on fetal MR imaging have been found in the literature either.

We cannot agree with the recently published information that “cortical tubers are occasionally detected only on the postnatal MR imaging of the brain.”<sup>20</sup> The authors of this article contradict themselves, writing a few lines earlier that US and MR imaging

“indicate that cortical tubers and SENs are the most common lesions detected prenatally.” We cannot agree with another statement from this publication that “no significant difference was found in the time of detection” of “characteristic TSC brain lesions. . .comparing the two methods”: US and MR imaging. Again, it is a well-known and documented fact that brain lesions are often sonographically occult,<sup>21</sup> and this fact was also shown in our study. Thus, despite a seemingly well-described topic and relatively extensive literature, there is still a need for research and publications on prenatal diagnosis of TSC.

In a prospective study conducted in Germany in 2015–2017 by Ebrahimi-Fakhari et al,<sup>22</sup> in a group of 86 patients who had met the inclusion criteria of definite or possible TSC, the median age at diagnosis was 6 months (range, 5 months before birth to 197 months of age). Moreover, in the prenatal period only the diagnosis of possible TSC was established on US after cardiac rhabdomyomas had been detected in 22.1% of patients (19/86). Only one of these patients had “concomitant cerebral abnormalities” that were not further characterized and did not lead to the final diagnosis. In a retrospective French study by Saada et al,<sup>23</sup> in turn, 25 of 51 fetuses with ≥1 cardiac tumor (49%) were

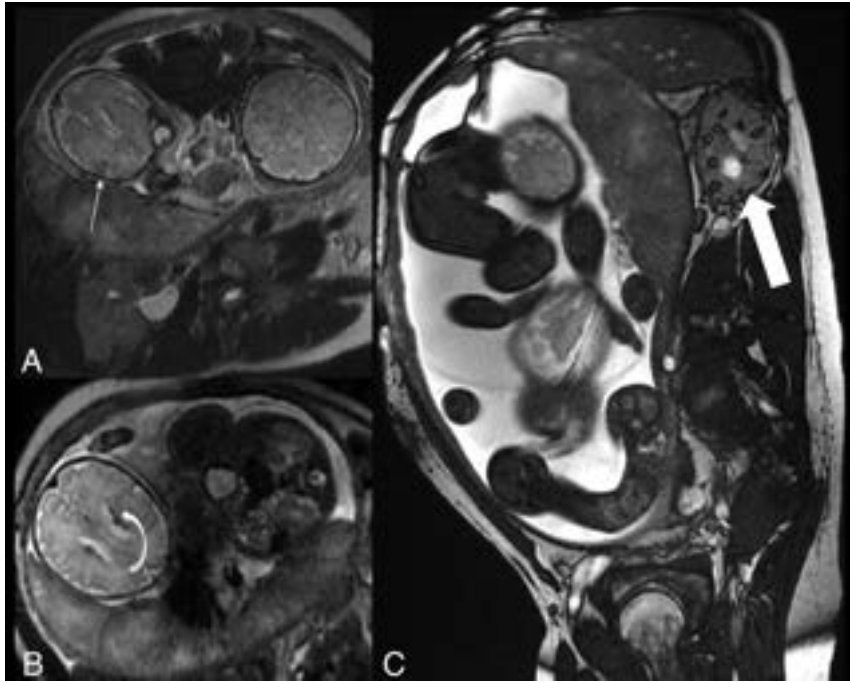


**FIG 5.** MR imaging at 34 GWs. SSFSE/T2-weighted images (A and B) and FIESTA (C). Dichorionic diamniotic pregnancy of a mother with TSC, with angiomyolipomas in the kidney (C, *Thick arrow*). Note the fetus on the left side of the images with a cortical tuber (A, *Thin arrow*) and SENs (B, *Curved arrow*).

diagnosed with TSC after fetal MR imaging. On the one hand, this finding illustrates the approach to prenatal diagnostics in general and to prenatal MR imaging in particular, and on the other hand, it indicates the quality of the diagnostics, both different in different countries.

In our material, all pregnant women with cardiac tumors diagnosed on US were referred to MR imaging. Major features of cerebral TSC were found in as many as 78% of the analyzed cases, confirming the diagnosis. In more than half of cases of TSC (22/39 = 56.4%), the fetuses showed >2 major TSC criteria that are necessary to establish the diagnosis (Fig 3).

In cases of inherited TSC, the features of maternal disease within the FOV of the fetal MR imaging may be helpful, ie, renal angiomyolipomas (Fig 5C).<sup>21</sup> Angiomyolipomas are a major TSC diagnostic criterion but are not encountered prenatally. Multiple renal cysts constitute the minor feature of the TSC diagnostic criteria and are very rarely depicted in a prenatal period. In our material, we had only 2 fetuses with small renal cysts, which is consistent with findings in the literature.<sup>20</sup>

It has been postulated since at least 2007 that TSC Consensus Conference criteria can and should be applied to fetal MR imaging and that this method should be better promoted.<sup>24</sup> Then, the diagnosis could be established much earlier than within the first 4 months of postnatal life in a significant group of patients,<sup>1</sup> a possibility that was shown in our material. In 2021, a group of experts working on TSC with the long-term, prospective study evaluating clinical and molecular biomarkers of epileptogenesis in a genetic model of epilepsy-tuberous sclerosis complex (EPISTOP) consortium finally admitted that “fetal cerebral MR imaging can be used reliably in the diagnosis of TSC.” The

authors wrote as well that “to establish TSC prenatally, it is... necessary to detect another major feature of TSC” (meaning that cardiac rhabdomyomas are the first one) “or to confirm the diagnosis with DNA testing after amniocentesis.”<sup>19</sup> The long-postulated recognition of prenatal MR images as sufficient to diagnose the disease has finally happened and will lead to a greater number of diagnoses at the right time. In this international multicenter retrospective study, 41 children with TSC who underwent prenatal MR imaging were included, a study group comparable with our material from only 2 centers.

## CONCLUSIONS

The schedule of proper care of children with TSC can and should be established during the perinatal period in a large percentage of patients. It is necessary to emphasize the education of women to report on mandatory sonographic examinations during pregnancy, on the quality of US, and on the need to refer

pregnant patients to MR imaging if a cardiac tumor is depicted on US. Gynecologists and pediatric cardiologists performing fetal US and radiologists performing prenatal MR imaging are the clue to the early diagnosis of TSC, before seizures in many cases, and many patients can win the race against time due to prenatal diagnostic imaging.

Disclosure forms provided by the authors are available with the full text and PDF of this article at [www.ajnr.org](http://www.ajnr.org).

## REFERENCES

1. Słowińska M, Józwiak S, Peron A, et al. **Early diagnosis of tuberous sclerosis complex: a race against time—how to make the diagnosis before seizures?** *Orphanet J Rare Dis* 2018;13:25 CrossRef Medline
2. Hinton RB, Prakash A, Romp RL, et al; International Tuberous Sclerosis Consensus Group. **Cardiovascular manifestations of tuberous sclerosis complex and summary of the revised diagnostic criteria and surveillance and management recommendations from the International Tuberous Sclerosis Consensus Group.** *J Am Heart Assoc* 2014;3:e001493 CrossRef Medline
3. Yuan SM. **Fetal primary cardiac tumors during perinatal period.** *Pediatr Neonatol* 2017;58:205–10 CrossRef Medline
4. Bejiqi R, Retkoceri R, Bejiqi H. **Prenatally diagnosis and outcome of fetuses with cardiac rhabdomyoma: single centre experience.** *Open Access Maced J Med Sci* 2017;5:193–96 CrossRef Medline
5. Goergen SK, Fahey MC. **Prenatal MR imaging phenotype of fetuses with tuberous sclerosis: an institutional case series and literature review.** *AJNR Am J Neuroradiol* 2022;43:633–38 CrossRef Medline
6. Northrup H, Aronow ME, Bebin EM, et al; International Tuberous Sclerosis Complex Consensus Group. **Updated international tuberous sclerosis complex diagnostic criteria and surveillance and management recommendations.** *Pediatr Neurol* 2021;123:50–66 CrossRef Medline

7. Mirlisse V, Wener H, Jacquemard F, et al. **Magnetic resonance imaging in antenatal diagnosis of tuberous sclerosis.** *Lancet* 1992;340:1163 CrossRef Medline
8. Jurkiewicz E, Bekiesińska-Figatowska M, Romaniuk-Doroszewska A, et al. **Brain MRI in fetuses with cardiac tumours.** *Neuroradiol J* 2007;20:494–99 CrossRef Medline
9. Davis PE, Filip-Dhima R, Sideridis G, et al; on behalf of the Tuberous Sclerosis Complex Autism Center of Excellence Research Network. **Presentation and diagnosis of tuberous sclerosis complex in infants.** *Pediatrics* 2017;140:e20164040 CrossRef Medline
10. Rovira À, Ruiz-Falcó ML, García-Esparza E, et al. **Recommendations for the radiological diagnosis and follow-up of neuropathological abnormalities associated with tuberous sclerosis complex.** *J Neurooncol* 2014;118:205–23 CrossRef Medline
11. Usta IM, Adra AM, Nassar AH. **Ultrasonographic diagnosis of fetal seizures: a case report and review of the literature.** *BJOG* 2007;114:1031–33 CrossRef Medline
12. Manganaro L, Saldari M, Bernardo S, et al. **Bilateral subependymal heterotopia, ventriculomegaly and cerebellar asymmetry: fetal MRI findings of a rare association of brain anomalies.** *J Radiol Case Rep* 2013;7:38–45 CrossRef Medline
13. Girard NJ, Chaumoitre K. **The brain in the belly: what and how of fetal neuroimaging?** *J Magn Reson Imaging* 2012;36:788–804 CrossRef Medline
14. Nagaraj UD, Peiro JL, Bierbrauer KS, et al. **Evaluation of subependymal gray matter heterotopias on fetal MRI.** *AJNR Am J Neuroradiol* 2016;37:720–25 CrossRef Medline
15. Roth J, Roach ES, Bartels U, et al. **Subependymal giant cell astrocytoma: diagnosis, screening, and treatment—recommendations from the International Tuberous Sclerosis Complex Consensus Conference 2012.** *Pediatr Neurol* 2013;49:439–44 CrossRef Medline
16. Hussain N, Curran A, Pilling D, et al. **Congenital subependymal giant cell astrocytoma diagnosed on fetal MRI.** *Arch Dis Child* 2006;91:520 CrossRef Medline
17. Kotulska K, Borkowska J, Mandera M, et al. **Congenital subependymal giant cell astrocytomas in patients with tuberous sclerosis complex.** *Childs Nerv Syst* 2014;30:2037–42 CrossRef Medline
18. Baskin HJ Jr. **The pathogenesis and imaging of the tuberous sclerosis complex.** *Pediatr Radiol* 2008;38:936–52 CrossRef Medline
19. Hulshof HM, Slot EM, Lequin M, et al; EPISTOP consortium. **Fetal brain magnetic resonance imaging findings predict neurodevelopment in children with tuberous sclerosis complex.** *J Pediatr* 2021;233:156–62.e2 CrossRef Medline
20. Dragoumi P, O’Callaghan F, Zafeiriou DI. **Diagnosis of tuberous sclerosis complex in the fetus.** *Eur J Paediatr Neurol* 2018;22:1027–34 CrossRef Medline
21. Goel R, Aggarwal N, Lemmon ME, et al. **Fetal and maternal manifestations of tuberous sclerosis complex: value of fetal MRI.** *Neuroradiol J* 2016;29:57–60 CrossRef Medline
22. Ebrahimi-Fakhari D, Mann LL, Poryo M, et al. **Incidence of tuberous sclerosis and age at first diagnosis: new data and emerging trends from a national, prospective surveillance study.** *Orphanet J Rare Dis* 2018;13:117 CrossRef Medline
23. Saada J, Hadj Rabia S, Fermont L, et al. **Prenatal diagnosis of cardiac rhabdomyomas: incidence of associated cerebral lesions of tuberous sclerosis complex.** *Ultrasound Obstet Gynecol* 2009;34:155–59 CrossRef Medline
24. Mühler MR, Rake A, Schwabe M, et al. **Value of fetal cerebral MRI in sonographically proven cardiac rhabdomyoma.** *Pediatr Radiol* 2007;37:467–74 CrossRef Medline

# Brain Maturation Patterns on Normalized FLAIR MR Imaging in Children and Adolescents

K. Chan, A. Ghazvanchahi, D. Rabba, L. Vidarsson, M.W. Wagner, B.B. Ertl-Wagner, and A. Khademi



## ABSTRACT

**BACKGROUND AND PURPOSE:** Signal analysis of FLAIR sequences is gaining momentum for studying neurodevelopment and brain maturation, but FLAIR intensity varies across scanners and needs to be normalized. This study aimed to establish normative values for standardized FLAIR intensity in the pediatric brain.

**MATERIALS AND METHODS:** A new automated algorithm for signal normalization was used to standardize FLAIR intensity across scanners and subjects. Mean intensity was extracted from GM, WM, deep GM, and cortical GM regions. Regression curves were fitted across the pediatric age range, and ANOVA was used to investigate intensity differences across age groups. Correlations between intensity and regional volume were also examined.

**RESULTS:** We analyzed 429 pediatric FLAIR sequences in children 2–19 years of age with a median age of 11.2 years, including 199 males and 230 females. WM intensity had a parabolic relationship with age, with significant differences between various age groups ( $P < .05$ ). GM and cortical GM intensity increased over the pediatric age range, with significant differences between early childhood and adolescence ( $P < .05$ ). There were no significant relationships between volume and intensity in early childhood, while there were significant positive and negative correlations ( $P < .05$ ) in WM and GM, respectively, for increasing age groups. Only the oldest age group showed significant differences between males and females ( $P < .05$ ).

**CONCLUSIONS:** This work presents a FLAIR intensity standardization algorithm to normalize intensity across large data sets, which allows FLAIR intensity to be used to compare regions and individuals as a surrogate measure of the developing pediatric brain.

**ABBREVIATIONS:** cGM = cortical gray matter; dGM = deep gray matter

Many diseases and disorders are associated with abnormal brain development in children, including autism spectrum disorder, attention deficit/hyperactivity disorder, and epilepsy.<sup>1</sup>

Received May 10, 2023; accepted after revision July 18.

From the Department of Electrical, Computer and Biomedical Engineering (K.C., A.G., D.R., A.K.), Toronto Metropolitan University, Toronto, Ontario, Canada; Institute for Biomedical Engineering, Science Tech (iBEST) (K.C., A.G., D.R., A.K.), a Partnership between St. Michael's Hospital and Toronto Metropolitan University, Toronto, Ontario, Canada; Keenan Research Center for Biomedical Science (A.K.), St. Michael's Hospital, Unity Health Network, Toronto, Ontario, Canada; Department of Diagnostic Imaging (L.V., M.W.W., B.B.E.-W.), Division of Neuroradiology, The Hospital for Sick Children, Toronto, Ontario, Canada; Department of Medical Imaging (L.V., M.W.W., B.B.E.-W.), University of Toronto, Toronto, Ontario, Canada; and Department of Neuroradiology (M.W.W.), University Hospital Augsburg, Augsburg, Germany.

This work was supported by a Natural Sciences and Engineering Research Council of Canada Discovery Grant (April Khademi).

Please address correspondence to Karissa Chan, MAsc, Electrical, Computer and Biomedical Engineering Department, Toronto Metropolitan University, 350 Victoria St, Toronto, ON, Canada; e-mail: karissa.chan@torontomu.ca

Indicates open access to non-subscribers at [www.ajnr.org](http://www.ajnr.org)

Indicates article with online supplemental data.

<http://dx.doi.org/10.3174/ajnr.A7966>

Maturation curves are used to identify children with normal, delayed, or abnormal brain maturation. Normative maturation trajectories have been established for various MR imaging sequences in the pediatric age range.<sup>2–5</sup> FLAIR sequences are a mainstay of brain imaging, but there is currently limited information on maturation trajectories because signal intensities vary widely across FLAIR MR imaging scanners. In a previous study,<sup>3</sup> the authors examined normal brain maturation on FLAIR for children 1 day to 4 years of age and found that FLAIR signal intensity had a biphasic pattern in WM regions in the first 48 months of life. Several other studies researched maturation patterns in young children, mainly in the first 2 years of life, using various sequences including T1, T2, FLAIR, DTI, as well as T1 and T2 mapping.<sup>2,4,5</sup> However, little is known about brain maturation patterns of FLAIR signal intensities across the entire pediatric age range.

FLAIR signal intensities have been shown to be related to lipid and water content<sup>6</sup> and may serve as good indicators of structural development and maturation-related brain development. There is wide variability of FLAIR signal intensity patterns across MR imaging scanners, making comparing intensities for large data

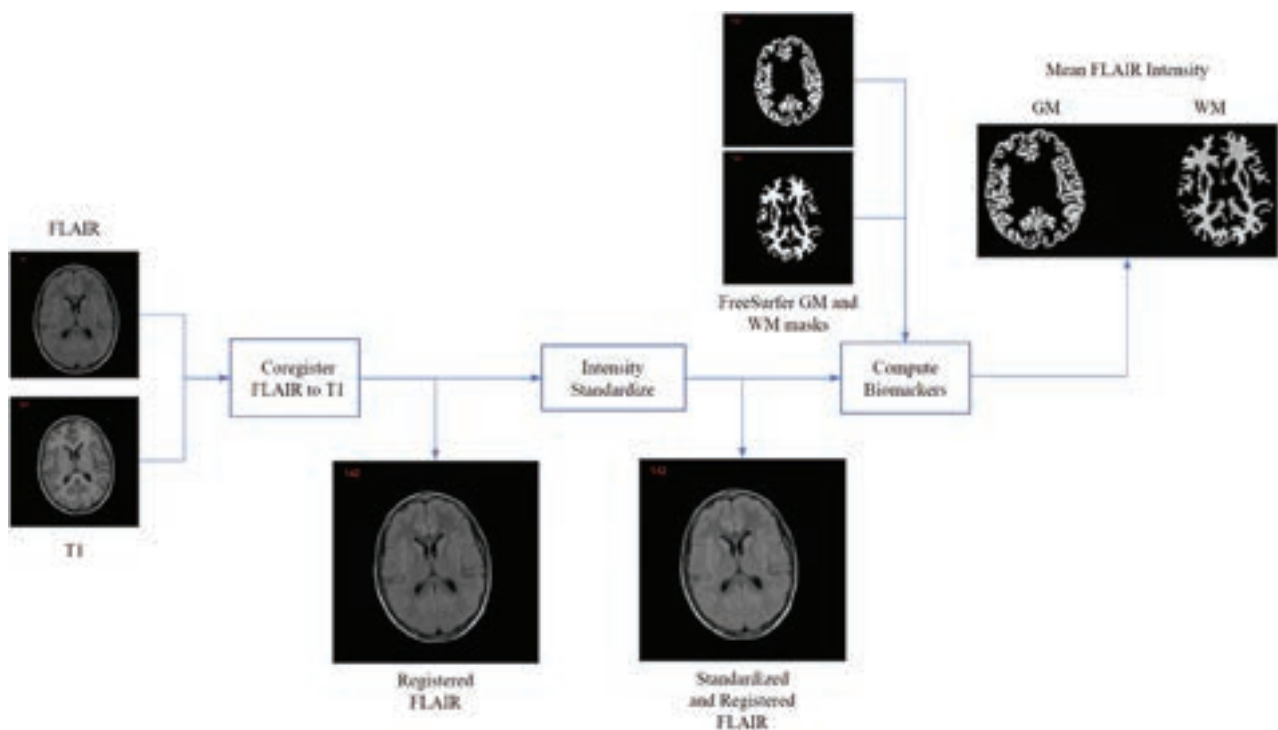


**FIG 1.** Image-processing pipeline for measuring FLAIR intensity biomarkers.

sets challenging. FLAIR intensity standardization algorithms can be used across individuals and scanners to overcome this variability. In the past, Nyúl was the most widely used MR imaging intensity normalization scheme, but this method is optimized for T1 and T2 images.<sup>7,8</sup> Reiche et al<sup>8</sup> developed a normalization algorithm specifically for FLAIR MR imaging, which outperformed Nyúl by demonstrating high alignment accuracy in large multicenter data sets.<sup>9</sup> This work applies the FLAIR normalization technique to study pediatric brain changes during childhood and adolescence. We aimed to assess T2-weighted FLAIR signal intensities in individuals 2 to 19 years of age without structural abnormalities to establish normative maturation trajectories.

## MATERIALS AND METHODS

This study was approved by the Hospital for Sick Children's local institutional review board. Due to the retrospective nature of the study, informed consent was waived by the local research ethics board. T2-weighted FLAIR and T1 MR imaging were performed in the clinical setting, and findings were reported as normal. Imaging was acquired across MR imaging scanners from 3 vendors (Sigma HDxt, GE Healthcare; Achieva, Philips Healthcare; Magnetom Skyra, Siemens), at field strengths of 1.5T or 3T. Section thicknesses of the FLAIR sequences ranged between 3 and 5 mm. Acquired in-plane voxel dimensions ranged between 0.6 and 1 mm. TR, TI, and TE ranged between 7 and 10 seconds, 2.3 and 2.9 seconds, and 85–150 ms, respectively. For the 3D T1-weighted sequence, section thickness ranged between 1 and 2 mm; the acquired in-plane voxel dimension was 1 mm; and TR, TE, and flip angle were 6–10 ms, 2–5 ms, and 7°–15°, respectively.

The various algorithms used are summarized in Fig 1 to compare FLAIR signal intensities from different scanners and

individuals. FLAIR volumes were registered to the T1 space using the Advanced Normalization Tools software package (<http://stnava.github.io/ANTs>) symmetric normalization.<sup>10</sup> Following registration, FLAIR images were N4 bias field-corrected<sup>11</sup> followed by intensity normalization. The signal intensity normalization is a patented technology developed specifically for multicenter FLAIR MR imaging.<sup>8</sup> It aligns the peaks of 2 histograms using a scaling factor defined as the ratio of the 2 histogram peaks. Given that GM comprises the largest volume, the GM histogram peaks of all volumes are aligned. The Kullback-Leibler divergence, which measures the degree of similarity between histograms, was used to quantify standardization performance.<sup>8</sup>

FreeSurfer, Version 7.2 (<http://surfer.nmr.mgh.harvard.edu>)<sup>12</sup> was used to segment WM and GM regions on 3D T1-weighted images, and the masks were verified by a pediatric neuroradiologist. GM subregions, deep GM (dGM), and cortical GM (cGM) were also segmented and verified. The segmentations were used to mask the respective regions on FLAIR images, and the mean standardized FLAIR signal intensities were measured for each region to compute intensity features. For each individual, the mean intensity biomarkers were examined across age for the WM, GM, cGM, and dGM. The difference in GM and WM intensity was also considered.

Nonlinear regression was used to fit curves for examining tissue intensity trends across the age range. Quadratic curves were generated separately for females and males. The standard errors of the curve coefficients and *P* values are reported. ANOVA and the Tukey post hoc tests were used to evaluate differences in intensities across age groups and sexes. The first comparison investigates differences in intensities among age groups. The second analysis considers each age group while comparing intensities between males and females. To investigate the dependence of

FLAIR intensity on volumetric changes, we correlated each tissue volume normalized by intracranial volume to the mean intensity of the corresponding regions using Pearson correlation tests.

## RESULTS

Axial FLAIR and sagittal 3D T1-weighted FLAIR sequences of 512 children between 2 and 19 years of age were included in the study. Forty-four data sets with marked registration errors were excluded, and sequences of 39 patients with poor segmentation masks were discarded, leading to a final data set of 429 FLAIR and T1-weighted sequences (median age of 11.2 years and 199/230 male/female split), summarized in the Table. To examine the intensity standardization on pathologic brains and demonstrate proof of concept, we have included 2 FLAIR sequences acquired at the same center of atypical teratoid/rhabdoid tumor and stroke.

### Intensity Standardization

Sample original and standardized images of WM and GM are shown in Fig 2. Before normalization, the intensity histograms demonstrated different ranges for similar tissues. The mean Kullback-Leibler divergences before and after normalization were 1.303 and

0.006, respectively (Online Supplemental Data). The variability of the data after normalization was much lower, indicating that the multiscanner variation was reduced, permitting fair comparison of intensity biomarkers across individuals. Intensity histograms of the FLAIR volumes before and after intensity normalization are shown in the Online Supplemental Data, while histograms across different age ranges are also shown in the Online Supplemental Data. To demonstrate the utility of the standardization framework, one can visualize the original and standardized images of the pathologic brains in the Online Supplemental Data. The standardized images have much better intensity alignment than the original ones.

### Intensity Biomarkers across the Pediatric Age Range

By means of the intensity-normalized FLAIR volumes and corresponding registered masks for WM, GM, dGM, and cGM, the mean intensity in each region was extracted for every individual. Figure 3 shows the fitted curves of intensity biomarkers as a function of age for all tissues. GM intensity demonstrated a quadratic profile with a slight increasing trend, while WM intensity demonstrated a biphasic pattern, with minimums in the approximate 8- to 12-year age range for both WM and GM. The absolute difference in GM and WM intensity demonstrated that WM intensity was lower than GM intensity across all age ranges, with more similar intensities in early childhood and adolescence, and the largest difference at 8–10 years of age. For most age ranges, male and female intensity profiles in both tissues were similar. In a GM subanalysis, dGM and cGM demonstrated nonlinear patterns, with slight upward trends in cGM. There was lower variability in intensities in the cGM than the dGM. The standard errors and *P* values from the models are shown in the Online Supplemental Data. All relationships were significant ( $P < .05$ ).

### Cohort summary

Age Group (yr)	Total	Percentage Female
2–4	30	42.9
4–6	39	43.2
6–8	41	37.5
8–10	59	58.5
10–12	73	46.8
12–14	67	53.5
14–16	68	69.0
16–18.2	52	59.3

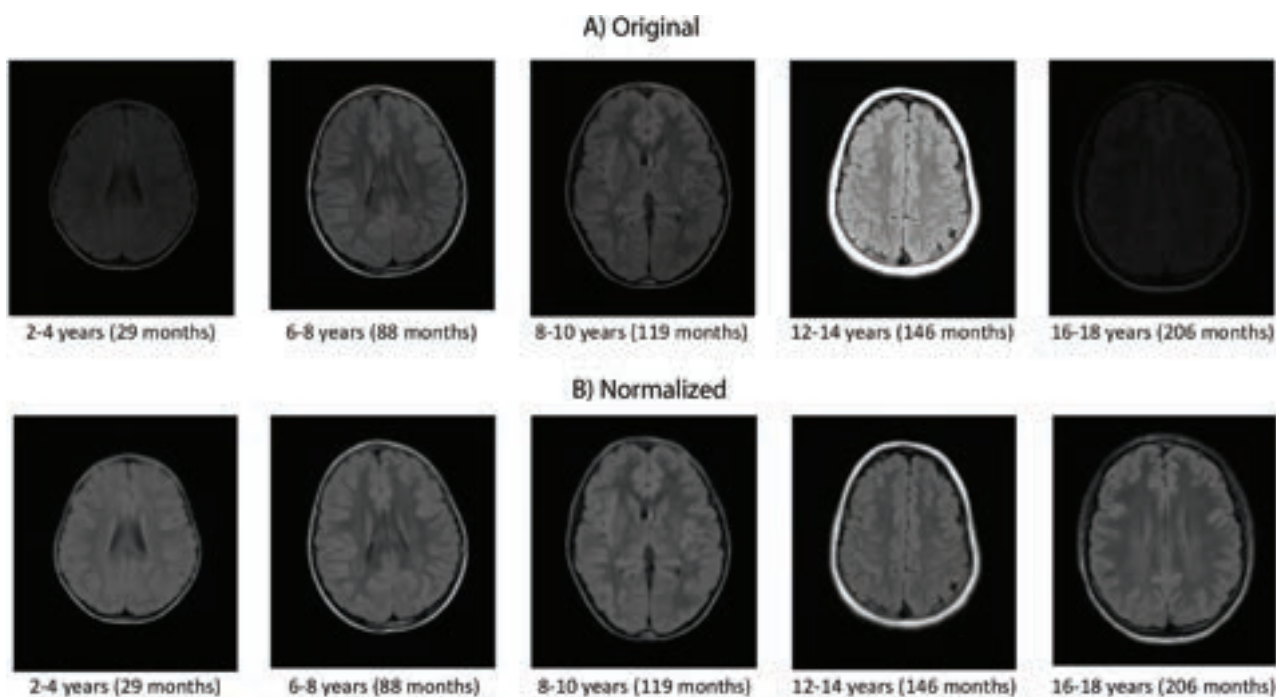


**FIG 2.** Samples from different age ranges (original images, A) and images after intensity normalization (B). Approximate middle section taken from each subject.

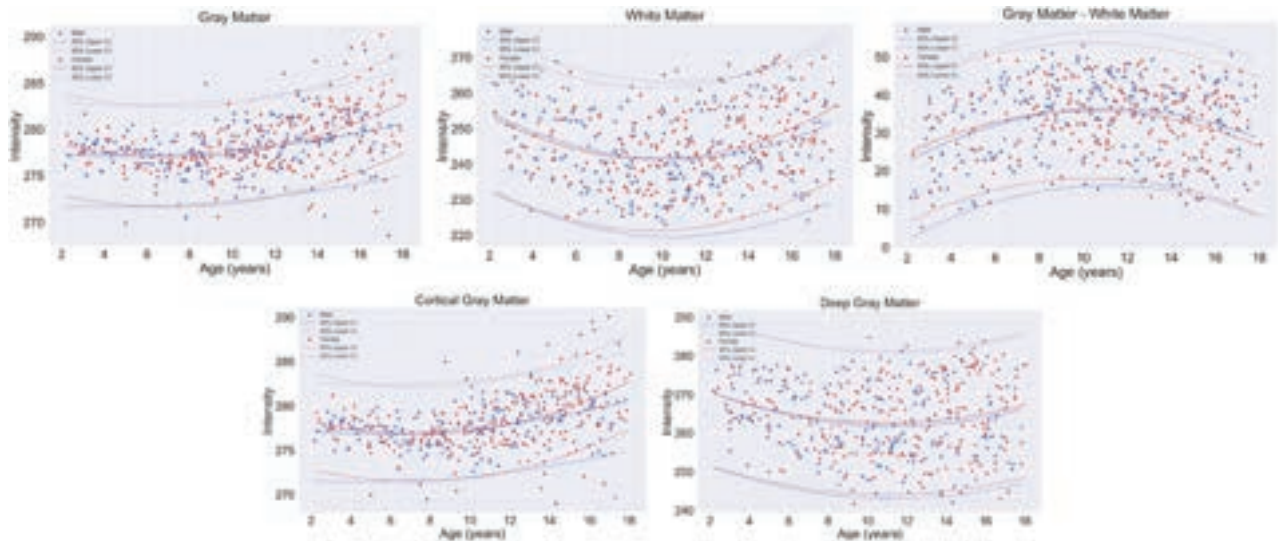


**FIG 3.** Fitted curves of mean normalized intensity by age per tissue region for all 429 healthy pediatric patients.

The distribution of FLAIR intensities of each tissue region across age groups is shown in the Online Supplemental Data, while the mean FLAIR intensity across all age ranges is summarized in the Online Supplemental Data. ANOVA demonstrated significant differences in intensity across age ranges for all tissues ( $P < .05$ ) (Online Supplemental Data). The Tukey post hoc test was used to further analyze differences among age groups (Online Supplemental Data). The mean intensities and significant differences among age groups for each region are visualized in Fig 4 and the Online Supplemental Data. In WM, there were significant differences in intensity between early childhood (2–6 years) and 6–12 years of age. Significant differences were also observed between the age ranges of 6–12 years and 14–18 years, reflecting the biphasic pattern. For GM, significant differences ( $P < .05$ ) were mostly observed when comparing intensities between the age ranges of 2–10 years and 14–18 years. The cGM followed patterns similar to those of the GM, whereas there were almost no differences across all ages for the dGM. The results of ANOVA comparing mean intensities between boys and girls for every age group are shown in the Online Supplemental Data. Significant differences ( $P < .05$ ) between boys and girls were found only in the GM for the 16- to 18-year age group.

### Volume Correlation

Correlation analysis between intensity and volume for 4 nonoverlapping age groups was performed as shown in Fig 5, while correlations across all ages are shown in the Online Supplemental Data. The 4 age ranges were the following:  $2 \leq \text{age} < 6$  years,  $6 \leq \text{age} < 10$  years,  $10 \leq \text{age} < 14$  years,  $14 \leq \text{age} \leq 18.2$  years. In GM, there was a significant negative correlation ( $P < .05$ ) between intensity and GM volume for all age groups except in the 2- to 6-year age range. The cGM had trends similar to those in the GM, and the dGM demonstrated weak insignificant correlations for all age groups. In WM, there was a significant positive correlation ( $P < .05$ ) between intensity and WM volume for the 2 older age groups, while there was no significant correlation in the 2- to 6- and 6- to 10-year age groups.

### DISCUSSION

This study analyzed normalized FLAIR signal intensity in the GM and WM regions of normative individuals across the pediatric age range. A FLAIR intensity normalization method was used to ensure that individuals could be compared across the pediatric cohort. A total of 429 children ranging from 2 years to 18.2 years of age were studied. The mean FLAIR intensity was extracted from the GM, WM, cGM, and dGM. Regression analysis was performed to fit curves across the pediatric age range, and ANOVA and post hoc analyses investigated differences in biomarkers across age groups. Correlation analysis was performed to investigate relationships between intensity and changes in brain volume.

As shown in Fig 3, a quadratic relationship between intensity and age was found in the WM, and an increasing trend was found in the GM regions. The difference in GM and WM intensity also followed a quadratic trend. In Ashikaga et al,<sup>3</sup> FLAIR signal-intensity differences between GM and WM had a biphasic pattern for the frontal and occipital deep WM and the centrum semiovale in the first 48 months of life. It was shown that WM progressed from hyper- to hypointense compared with adjacent GM during the first 2 years of life.<sup>3</sup> Similarly, in Kizildag et al,<sup>2</sup> a study of children ranging from 0 to 2 years of age showed that brain maturation can be demonstrated on FLAIR images as well as with T1-weighted and T2-weighted images. While these related works focus on early life, they showed that changes in intensity occur in the developing brain and that FLAIR can be used to measure them. Moreover, few studies investigated FLAIR signal intensities beyond the first few years of life. In this work, we automatically characterize brain changes using FLAIR intensity over the entire pediatric age range. We also use a validated standardization method to normalize the FLAIR intensities to allow comparisons across a large pediatric data set.

The first few years of life involve substantial volumetric and morphologic changes, including large increases in total brain volume along with WM and GM volume.<sup>13</sup> By 6 years of age, total

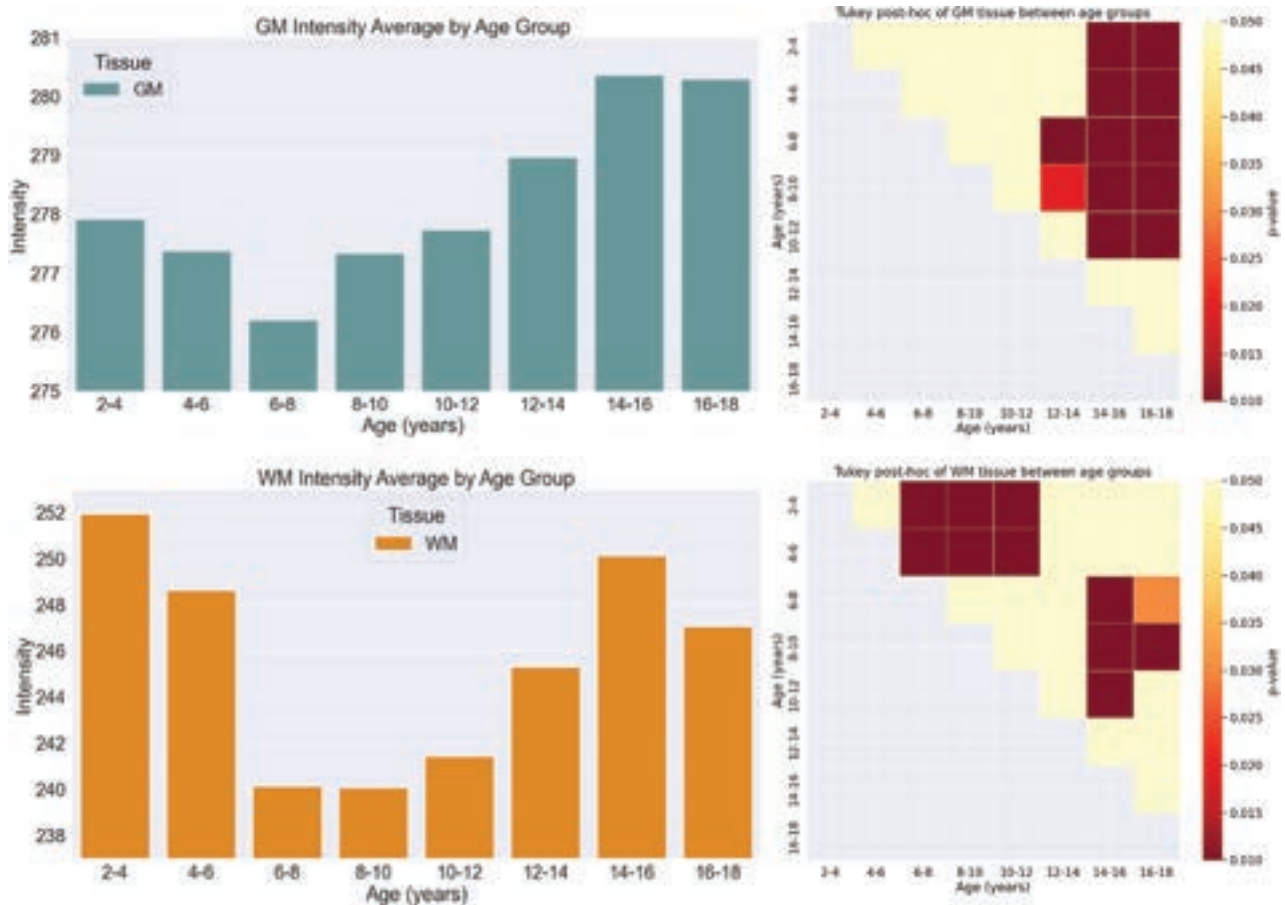


**FIG 4.** Mean intensity (left) and *P* value heatmap for intensity comparison for 2 age groups (right) for GM (upper row) and WM (lower row).

brain volume has reached approximately 90% of adult values, with incremental increases throughout the remainder of childhood and into adolescence.<sup>13</sup> Previous volumetric studies on MR imaging across the pediatric age range have shown an increase of WM and a decrease of GM with age, while the total brain volume remains fairly constant.<sup>14</sup> Our results demonstrated an increase in GM FLAIR intensity, with the highest increase after 12 years of age. The correlation between GM intensity and volume showed that GM volume decreases while FLAIR intensity increases with age. Significant negative correlations were found between intensity and volume in older children (6–18 years), with the most rapid changes occurring in the 10- to 18-year age range. In the early years of life (2–6 years), intensity and volume were not correlated. Changes in GM volume are associated with cortical thickness decreases<sup>13</sup> and cortical surface area/degree of gyrification reductions<sup>15</sup> due to arborization, axonal growth, increase in pyramidal cell somata, synaptogenesis, and synapse elimination (pruning).<sup>16</sup> Therefore, FLAIR intensity may present a novel way to measure these microstructural GM changes. When we examined GM compartments, cGM followed intensity and volume trajectories similar to those of the entire GM region, but minimal changes in the dGM were found. Neurobiologically, these tissues differ in composition. The cGM contains mostly excitatory neurons, whereas dGM contains both excitatory and inhibitory neurons. These neurobiological differences may explain the differing trends in the 2 tissue types.

Previous DTI studies also found quadratic patterns of fractional anisotropy in WM regions of children, which peak in late adolescent years<sup>15</sup> and are thought to be related to increased fiber density, axonal diameter, and myelination. Increasing WM volume over the pediatric age range is related to normal maturation processes such as myelination and increased axonal size and packing.<sup>17</sup> Increased axonal packing is accompanied by decreasing water content, while axon coherence remains stable across brain development.<sup>13</sup> Correlations between WM intensity and volume showed higher WM volume associated with higher FLAIR intensity, with significant correlations at 6–18 years of age and the highest intensity increases occurring at 10 years of age and older. This finding indicates a more rapid increase in intensity for smaller volume changes in older age groups. Because most myelination is completed early in life but continues into adulthood, FLAIR intensity may be a surrogate marker of the dynamic process of myelination, axonal packing, and water diffusion that could complement current studies. Longitudinal studies would be needed to study this effect further.

Studies are emerging showing the value of FLAIR MR imaging biomarkers<sup>18,19</sup> for dementia and cerebrovascular disease. Intensity was found to be strongly correlated with mean diffusivity in DTI,<sup>18</sup> indicating that FLAIR intensity is related to water diffusion properties of the tissue. Therefore, changes in FLAIR intensity in this study may be related to water content and tissue organization in the WM and GM regions of children, but histologic

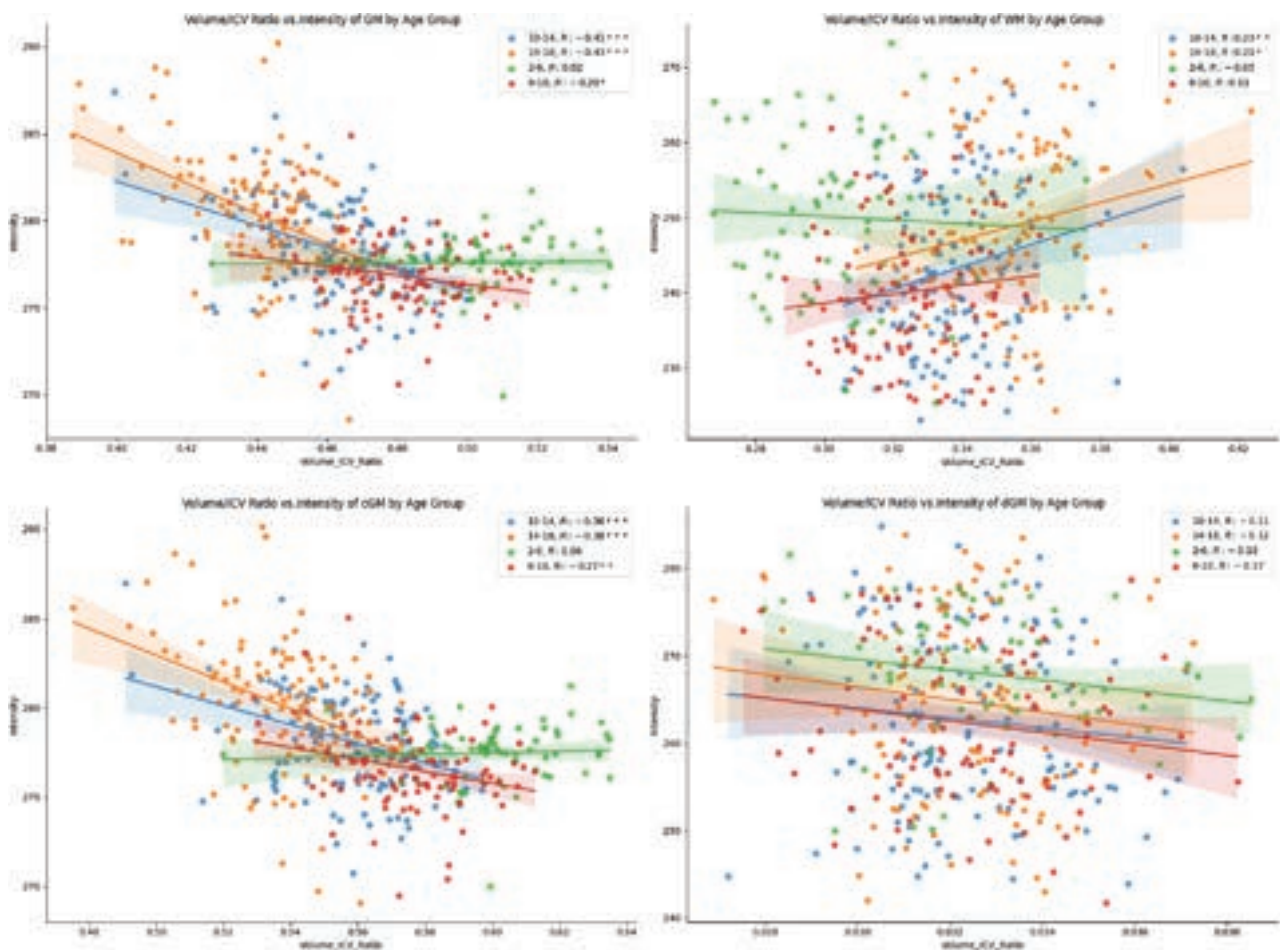


**FIG 5.** Volume versus intensity for GM, WM, cGM, and dGM. Regression is performed for 4 age groups. ICV indicates intracranial volume.

studies would be needed to confirm this hypothesis. The benefit of the current approach is that DTI volumes are not required for biomarker measurement. DTI not only has long acquisition and preprocessing times but also has wide variability in its measurements.<sup>20</sup> In contrast, the FLAIR intensity standardization framework normalizes intensities and allows robust comparison across subjects. Because FLAIR is routinely acquired in clinical brain imaging investigations, FLAIR intensity biomarkers have wide translation potential.

Possible limitations in this work include segmentation or registration errors. While segmentations and scans were examined visually to reduce errors, there could be artifacts that are difficult to detect with the human eye. Future work may include implementing a deep learning–based registration<sup>21</sup> or segmentation scheme,<sup>22</sup> with automated failure detection to reject poor-quality images. We could also improve the normalization tool by aligning specific tissue regions or making alignment less dependent on the main histogram mode. However, we wanted to avoid dependence on segmentation accuracy for the normalization scheme. Last, future work would include further validation of the FLAIR intensity biomarkers by comparing the FLAIR normative curves with biomarkers from children with neurodevelopmental disorders. Additionally, longitudinal studies will be required to investigate intensity changes on the individual level.

## CONCLUSIONS

We have explored how normalized FLAIR signal intensity changes across the pediatric age range. There was a biphasic pattern in WM, while GM intensity gradually increased. There were minimal differences noted in the dGM, whereas cGM showed similar trends to GM. There were no significant differences between females and males, except in the GM in late adolescence. There were no significant relationships between intensity and volume for the first 2–6 years of life in both GM and WM. However, with increasing age, volume was directly proportional to intensity in the WM and inversely related to GM intensity. This is one of the first large-scale studies on FLAIR intensity across the pediatric age range and can be used in future studies to analyze pathology and abnormal brain development.

Disclosure forms provided by the authors are available with the full text and PDF of this article at [www.ajnr.org](http://www.ajnr.org).

## REFERENCES

- Parenti I, Rabaneda LG, Schoen H, et al. **Neurodevelopmental disorders: from genetics to functional pathways.** *Trends Neurosci* 2020;43:608–21 CrossRef Medline
- Kızıldağ B, Düşünceli E, Fitoz S, et al. **The role of classic spin echo and FLAIR sequences for the evaluation of myelination in MR imaging.** *Diagn Interv Radiol* 2005;11:130–36 Medline

3. Ashikaga R, Araki Y, Ono Y, et al. **Appearance of normal brain maturation on fluid-attenuated inversion-recovery (FLAIR) MR images.** *AJNR Am J Neuroradiol* 1999;20:427–31 Medline
4. Murakami JW, Weinberger E, Shaw DW. **Normal myelination of the pediatric brain imaged with fluid-attenuated inversion-recovery (FLAIR) MR imaging.** *AJNR Am J Neuroradiol* 1999;20:1406–11 Medline
5. Ganzetti M, Wenderoth N, Mantini D. **Whole brain myelin mapping using T1- and T2-weighted MR imaging data.** *Front Hum Neurosci* 2014;8:671 CrossRef Medline
6. Maillard P, Carmichael O, Harvey D, et al. **FLAIR and diffusion MRI signals are independent predictors of white matter hyperintensities.** *AJNR Am J Neuroradiol* 2013;34:54–61 CrossRef Medline
7. Nyúl LG, Udupa JK. **On standardizing the MR image intensity scale.** *Magn Reson Med* 1999;42:1072–81 CrossRef Medline
8. Reiche B, Moody AR, Khademi A. **Pathology-preserving intensity standardization framework for multi-institutional FLAIR MRI datasets.** *Magn Reson Imaging* 2019;62:59–69 CrossRef Medline
9. Ghazvanchahi A, Maralani P, Moody AR, et al. **Effect of intensity standardization in deep learning for WML segmentation in multi-centre FLAIR MRI.** *arXiv* 2023 <https://arxiv.org/abs/2307.03827>. Accessed January 21, 2023
10. Avants BB, Tustison NJ, Song G, et al. **A reproducible evaluation of ANTs similarity metric performance in brain image registration.** *Neuroimage* 2011;54:2033–44 CrossRef Medline
11. Tustison NJ, Avants BB, Cook PA, et al. **N4ITK: improved N3 bias correction.** *IEEE Trans Med Imaging* 2010;29:1310–20 CrossRef Medline
12. Fischl B, Dale AM. **Measuring the thickness of the human cerebral cortex from magnetic resonance images.** *Proc Natl Acad Sci U S A* 2000;97:11050–55 CrossRef Medline
13. Lebel C, Deoni S. **The development of brain white matter microstructure.** *Neuroimage* 2018;182:207–18 CrossRef Medline
14. Brain Development Cooperative Group. **Total and regional brain volumes in a population-based normative sample from 4 to 18 years: the NIH MRI Study of Normal Brain Development.** *Cereb Cortex* 2012;22:1–12 CrossRef Medline
15. Vijayakumar N, Mills KL, Alexander-Bloch A, et al. **Structural brain development: a review of methodological approaches and best practices.** *Dev Cogn Neurosci* 2018;33:129–48 CrossRef Medline
16. Groeschel S, Vollmer B, King MD, et al. **Developmental changes in cerebral grey and white matter volume from infancy to adulthood.** *Int J Dev Neurosci* 2010;28:481–89 CrossRef Medline
17. Tamnes CK, Roalf DR, Goddings AL, et al. **Diffusion MRI of white matter microstructure development in childhood and adolescence: methods, challenges and progress.** *Dev Cogn Neurosci* 2018;33:161–75 CrossRef Medline
18. Bahsoun MA, Khan MU, Mitha S, et al. **FLAIR MRI biomarkers of the normal appearing brain matter are related to cognition.** *Neuroimage Clin* 2022;34:102955 CrossRef Medline
19. Chan K, Fischer C, Maralani P, et al. **Alzheimer's and vascular disease classification using regional texture biomarkers in FLAIR MRI.** *Neuroimage Clin* 2023;38:103385 CrossRef Medline
20. Figley CR, Uddin MN, Wong K, et al. **Potential pitfalls of using fractional anisotropy, axial diffusivity, and radial diffusivity as biomarkers of cerebral white matter microstructure.** *Front Neurosci* 2021;15:799576 CrossRef Medline
21. Mocanu S, Moody AR, Khademi A. **FlowReg: fast deformable unsupervised medical image registration using optical flow.** *Machine Learning for Biomedical Imaging* 2021;1:1–40 CrossRef
22. Khademi A, Gibicar A, Arezza G, et al. **Segmentation of white matter lesions in multicentre FLAIR MRI.** *Neuroimage* 2021;1:100044 CrossRef

# DTI of Opioid-Exposed Fetuses Using ComBat Harmonization: A Bi-Institutional Study

J.A. Dudley, U.D. Nagaraj, S. Merhar, F.T. Mangano, B.M. Kline-Fath, X. Ou, A. Acheson, and W. Yuan



## ABSTRACT

**BACKGROUND AND PURPOSE:** The underlying mechanisms leading to altered cognitive, behavioral, and vision outcomes in children with prenatal opioid exposure are yet to be fully understood. Some studies suggest WM alterations in infants and children with prenatal opioid exposure; however, the time course of WM changes is unknown. We aimed to evaluate differences in diffusion tensor imaging MRI parameters in the brain between opioid exposed fetuses and normal controls.

**MATERIALS AND METHODS:** This is a pilot, prospective cohort study in which subjects in the third trimester of pregnancy underwent fetal DTI of the brain with 20 noncolinear diffusion directions and a b-value of 500 s/mm<sup>2</sup> at 2.5-mm isotropic resolution.

**RESULTS:** The study included a total of 26 fetuses, 11 opioid-exposed (mean gestational age, 32.61 [SD, 2.35] weeks) and 15 unexposed controls (mean gestational age, 31.77 [SD, 1.68] weeks). After we adjusted for gestational age, fractional anisotropy values were significantly higher in opioid-exposed fetuses relative to controls in 8 WM tracts: the bilateral lemniscus (left:  $P = .017$ ; right:  $P = .020$ ), middle cerebellar peduncle ( $P = .027$ ), left inferior cerebellar peduncle ( $P = .026$ ), right sagittal stratum ( $P = .040$ ), right fornix stria terminalis ( $P = .022$ ), right inferior fronto-occipital fasciculus ( $P = .011$ ), and the right uncinate fasciculus ( $P = .033$ ). Significant alteration was also identified in other DTI indices involving a series of brain regions.

**CONCLUSIONS:** Our data demonstrate initial evidence of cerebral WM microstructural differences between opioid-exposed fetuses and unexposed controls. Further studies in larger patient populations will be needed to fully understand these findings.

**ABBREVIATIONS:** AD = axial diffusivity; FA = fractional anisotropy; GA = gestational age; MD = mean diffusivity; RD = radial diffusivity; SSFSE = single-shot fast spin-echo; SVR = slice-to-volume registration

Opioid use during pregnancy remains a common problem in the United States, with 7% of pregnant women reporting the use of prescription opioid pain relievers during pregnancy and 0.8% of women having an opioid-related diagnosis at the time of delivery.<sup>1,2</sup> Children with prenatal opioid exposure overall demonstrate lower educational achievement, compromised

development, and higher rates of behavioral issues by school age.<sup>3-5</sup> However, the underlying neural mechanisms leading to these poor outcomes are still unknown. There is a growing body of literature describing neonatal brain differences in opioid-exposed infants, including lower regional brain volumes, increased WM injury, and alterations in functional connectivity.<sup>6-11</sup> It is unknown whether these changes are present before birth.

Fetal MR imaging, which has become an accessible tool for the clinical evaluation of the developing brain, has the potential to answer some of these questions.<sup>12</sup> Pilot studies using fetal MR imaging have described smaller brain sizes in fetuses with prenatal opioid exposure.<sup>13</sup> DTI, a technique sensitive to WM abnormalities, has yielded growing evidence suggesting that opioid exposure may impact WM development in children as early as the neonatal period; however, WM microstructure in utero of opioid-exposed fetuses remains to be explored.<sup>14-16</sup> Fetal DTI has historically been challenging due to artifacts from excessive fetal motion. With recent advances in imaging data-processing and analysis, including slice-to-volume registration (SVR), fetal DTI has become more robust and reliable, making it possible to extend the study of WM microstructure into the prenatal

Received April 13, 2023; accepted after revision June 25.

From the Department of Radiology and Medical Imaging (J.A.D., U.D.N., B.M.K.-F., W.Y.), Perinatal Institute, Division of Neonatology (S.M.), and Department of Neurosurgery (F.T.M.), Cincinnati Children's Hospital Medical Center, Cincinnati, Ohio; University of Cincinnati College of Medicine (J.A.D., U.D.N., S.M., F.T.M., B.M.K.-F., W.Y.), Cincinnati, Ohio; and Departments of Radiology (X.O.), Pediatrics (X.O.), and Psychiatry (A.A.), University of Arkansas for Medical Sciences, Little Rock, Arkansas.

This work was supported by the Schubert Research Clinic Clinical Research Feasibility Fund, Cincinnati Children's Radiology Pilot Fund, and grants CCHMC R34-DA050268 and R34-DA050261 from Phase I of the HEALTHy Brain and Child Development Study.

J.A. Dudley and U.D. Nagaraj contributed equally to this work.

Please address correspondence to Usha D. Nagaraj, MD, Department of Radiology and Medical Imaging, Cincinnati Children's Hospital Medical Center, 3333 Burnet Ave, Cincinnati, OH 45229-3026; e-mail: usha.nagaraj@cchmc.org; @CincyKidsRad

Indicates open access to non-subscribers at www.ajnr.org

<http://dx.doi.org/10.3174/ajnr.A7951>

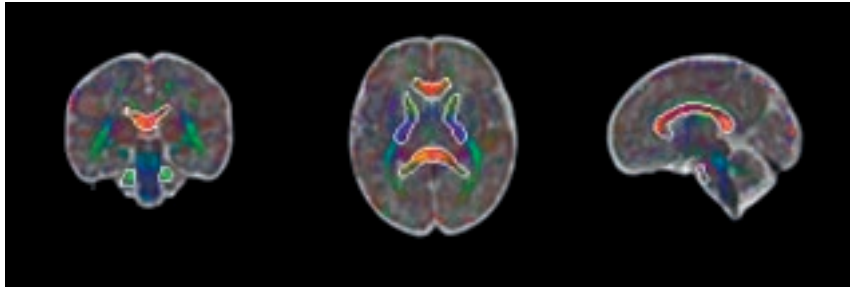


**FIG 1.** Illustration of atlas-based WM regions outlined in coronal, axial, and sagittal directions. The examples of the brain regions include the following: 1) middle cerebellar peduncle; 2) genu, body, and splenium of the corpus callosum; and 3) bilateral anterior and posterior limbs of the internal capsule.

period.<sup>17</sup> This study aimed to assess WM integrity on the basis of in utero DTI from fetuses with opioid exposure during gestation.

## MATERIALS AND METHODS

### Study Design and Patients

This prospective study was approved by the institutional review board at each institution. Written informed consent was obtained from all study participants. Participants were recruited from the Cincinnati Children's Hospital Medical Center (CCHMC) and the University of Arkansas for Medical Sciences (UAMS) from July 1, 2020, through December 31, 2021. Women in the third trimester of pregnancy with and without opioid use during the current pregnancy were recruited to undergo fetal MR imaging for investigational purposes only. Opioid and other substance use (or lack thereof) during the current pregnancy was determined by maternal self-report and maternal chart review. Substantial opioid use was defined as daily reported opioid use during most of the pregnancy to date, with most patients on a daily opioid-use disorder maintenance medication such as buprenorphine or methadone. Patients were recruited through a combination of flyers seeking volunteers in obstetrics and substance abuse clinics, e-mails to hospital employees seeking volunteers, and by connecting with previous research participants who agreed to be contacted for future research studies.

Eligibility for enrollment was determined by a study coordinator by telephone interview. Inclusion criteria included being at least 18 years of age, singleton pregnancy, and gestational age (GA) of at least 26 weeks. Exclusion criteria included an inability to supply the name of at least 1 additional person to contact if the participant could not be reached, a known genetic disorder, fetal abnormality identified on prenatal sonography, a nonviable fetus, contraindications to MR imaging, and the inability of the participant to enter the magnet bore due to body habitus. During this telephone interview, the study coordinator also informed potential participants that they would undergo a further interview regarding opioid exposure at the time of the fetal MR imaging appointment.

### MR Imaging Acquisition

Fetal MR imaging examinations were performed using a 3T MR imaging system (Ingenia; Philips Healthcare) at CCHMC and a 3T system (Magnetom Prisma; Siemens) at UAMS. Both sites used a phased array abdominal imaging coil. Sedation was not used. Patients

were placed in the left lateral decubitus position unless they reported feeling more comfortable in the supine position.

Examinations included localizer sequences followed by sagittal steady-state free precession images through the uterus with 5-mm-thick interleaved contiguous slices. T2 HASTE/single-shot fast spin-echo (SSFSE) images of the fetal brain were obtained in the axial, sagittal, and coronal planes with 2-mm-thick interleaved contiguous slices. Fetal DTI data were acquired in 20 noncollinear diffusion directions with a b-value of 500 s/mm<sup>2</sup> and resolution of 2.5 mm isotropic.

### MR Imaging Data-Processing and Analysis

Orthogonally-acquired 2D stacks of T2 HASTE/SSFSE images were motion-corrected and reconstructed into a single volumetric image with 1-mm<sup>3</sup> isotropic resolution using the niftydic toolkit deployed in a docker image (<https://hub.docker.com/r/renbem/niftymic>), which additionally calculated an affine-registration matrix to a GA-matched template.<sup>18</sup> Rigid-body transformation matrices describing the coregistration of the  $b=0$  diffusion image to the reconstructed T2 HASTE image were calculated using the FMRIB Software Library (FSL; [www.fmrib.ox.ac.uk/fsl](http://www.fmrib.ox.ac.uk/fsl)), Version 6.0.4. DTI processing was performed using FSL as well. SVR was used to correct for excessive head motion and artifacts in the fetal DTI. Each acquired EPI section was individually aligned to a target estimation of the 3D fetal brain anatomy so that all data could be projected from the scanner coordinates to anatomic coordinates that are static relative to the fetal brain. DTI measures, including fractional anisotropy (FA) and mean diffusivity (MD), axial diffusivity (AD), and radial diffusivity (RD), respectively, were extracted from WM regions derived from a nonlinear registration of the Johns Hopkins University WM atlas (Mori et al,<sup>19</sup> 2005) into a GA-matched template space (Fig 1).<sup>20</sup>

### Statistical Analysis

Before being pooled for group-difference testing, multisite DTI data were harmonized using the ComBat approach, a statistical correction strategy that minimizes the intercenter effect resulting from scanner differences while preserving physiologic features.<sup>21</sup> Group differences in FA, AD, MD, or RD in each atlas region were assessed using a FSL General Linear Model framework (<http://fsl.fmrib.ox.ac.uk/fsl/fslwiki/GLM>) with opioid exposure status as a categorical predictor variable, GA as a continuous predictor variable (mean centered), and the DTI metrics as the dependent variables.

## RESULTS

### Description of Patient Sample

Forty-one mothers completed the MR imaging session: 28 from CCHMC (13 opioid-exposed, 15 controls) and 13 from UAMS (4 opioid-exposed, 9 controls). Of these scans, fetal DTI data of 15 mothers were excluded due to poor image quality (11 from CCHMC: 4 opioid-exposed, 7 controls; 4 from UAMS: 2 opioid-exposed, 2 controls). Thus, a total of 26 fetuses, including 11

opioid-exposed (GA: 32.61 [SD, 2.35] weeks; 9 from CCHMC, 2 from UAMS) and 15 unexposed controls (GA: 31.77 [SD, 1.68] weeks;  $P = .30$ ; 8 from CCHMC, 7 from UAMS), were included in the final analyses. Other demographic characteristics are provided in the Table. No significant differences in fetal motion between the 2 groups were identified using analysis of average framewise displacement in millimeters (Wilcoxon rank-sum test,  $P = .96$ ). All fetal brain MRIs were interpreted as having normal signal and morphology by the study radiologists.

### Fetal DTI Findings

After adjusting for GA, FA values were significantly higher in opioid-exposed fetuses relative to controls in 8 WM regions (Fig 2). These significant regions included the bilateral lemniscus (left:  $P = .017$ ; right:  $P = .020$ ), the middle cerebellar peduncle ( $P = .027$ ), the left inferior cerebellar peduncle ( $P = .026$ ) and the right sagittal stratum ( $P = .040$ ), the fornix ( $P = .022$ ), the inferior fronto-occipital fasciculus ( $P = .011$ ), and the uncinate fasciculus ( $P = .033$ ). MD was significantly higher for exposed fetuses relative to controls in the left anterior limb of the internal capsule ( $P = .037$ ) and the left uncinate fasciculus ( $P = .013$ ) but significantly lower for exposed relative to controls in the left sagittal

stratum ( $P = .035$ ). AD was significantly higher for exposed fetuses relative to controls in 11 WM regions (Fig 3). These regions were the following: the middle cerebellar peduncle ( $P = .019$ ), the pontine crossing tract ( $P = .043$ ), the left medial lemniscus ( $P = .049$ ), the anterior and posterior limbs of the internal capsule ( $P = .007$ ,  $P = .018$ , respectively), the left anterior corona radiata ( $P = .002$ ), the right external capsule ( $P = .027$ ), the right cingulum hippocampus ( $P = .034$ ), the right stria terminalis of the fornix ( $P = .021$ ), the left inferior fronto-occipital fasciculus ( $P = .035$ ), and the left uncinate fasciculus ( $P = .006$ ). RD was significantly lower for exposed subjects relative to controls in the left sagittal stratum ( $P = .025$ ).

### DISCUSSION

This is a prospective study in which the use of ComBat harmonization allowed bi-institutional data use. There is a paucity of literature examining prenatal imaging of patients with in utero opioid exposure, and to the best of the authors' knowledge, there are no previously published works examining DTI data in human fetuses with in utero opioid exposure. In this study, we observed statistically significantly increased FA values in opioid-exposed fetuses compared with healthy controls in 8 WM regions in the cerebrum, cerebellum, and brainstem after adjusting for GA. We also observed statistically significant alterations in AD in 11 different WM regions, MD in 3 regions, and RD in 1 region in the exposed fetuses relative to controls.

Alterations in DTI indices in children with prenatal exposure to opioids have been described in multiple age

### Demographic information and additional substance exposure

	Controls (n = 15)	Opioid-Exposed (n = 11)	P Value
Maternal age (mean) (yr)	28.5 (SD, 4.9)	27.8 (SD, 6.1)	.73
GA (mean) (wk)	31.77 (SD, 1.68)	32.61 (SD, 2.35)	.3
Sex (% male)	80% (12/15)	54.5% (6/11)	.18
Nicotine exposure	0%	40% (4/10) <sup>a</sup>	
Other illicit drug exposure <sup>b</sup>	0%	40% (4/10) <sup>a</sup>	
Both	0%	20% (2/10) <sup>a</sup>	

<sup>a</sup> One patient in the opioid-exposed group preferred not to answer these questions.

<sup>b</sup> Illicit drug exposure inquiries included marijuana, cocaine, amphetamine or methamphetamine, barbiturates, and benzodiazepines.

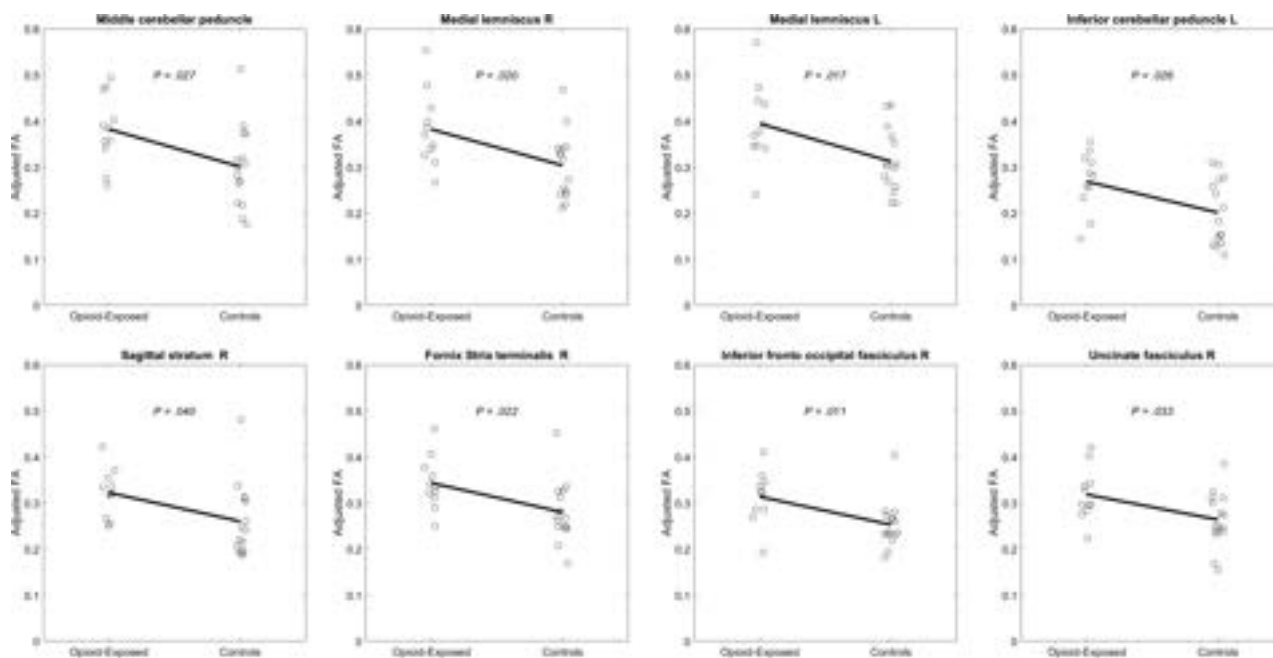


**FIG 2.** Plots of FA, adjusted for age, by group in 8 deep WM structures showing opioid-exposed fetuses with higher FA compared with controls.

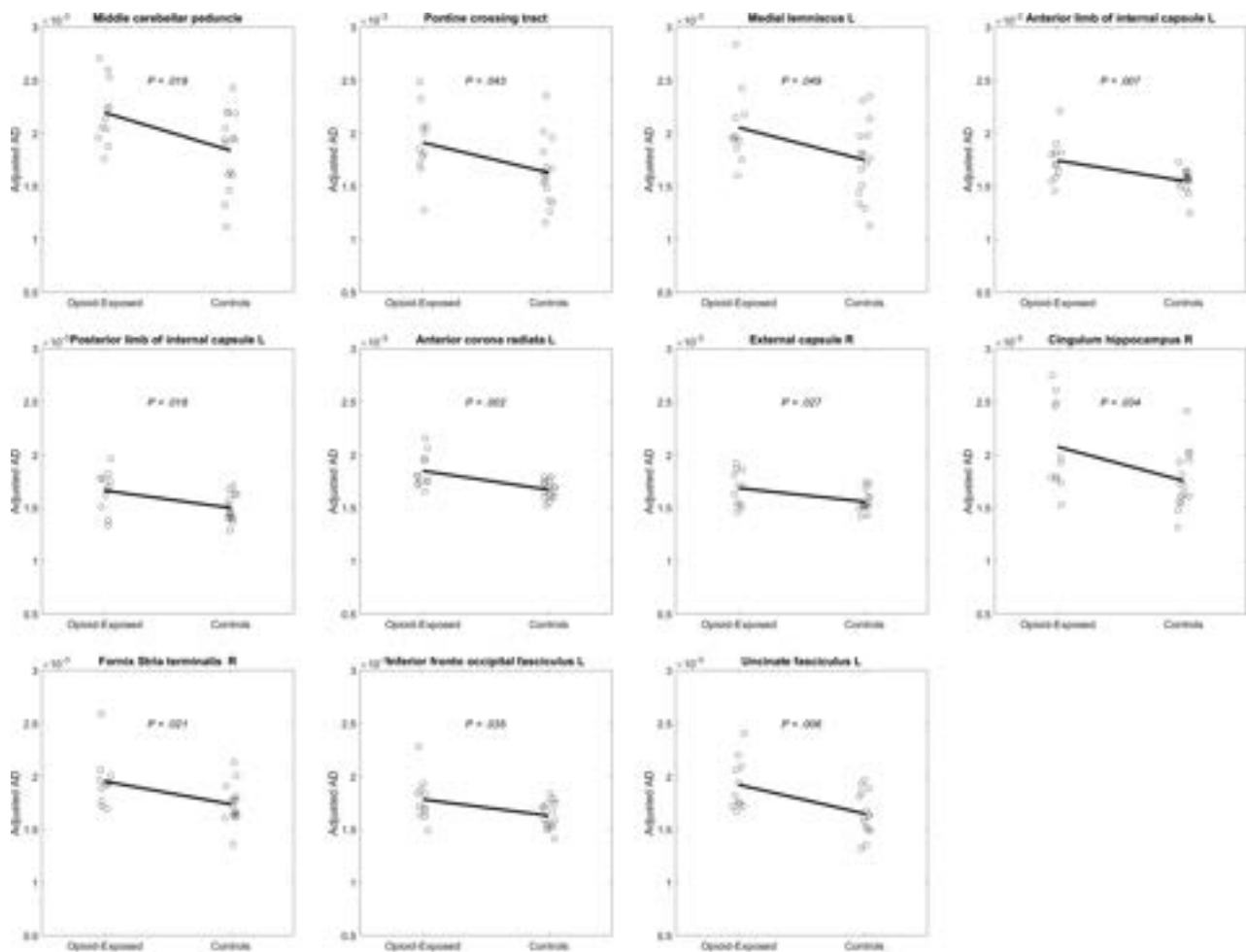


**FIG 3.** Plots of AD, adjusted for age, by group in 11 deep WM structures showing opioid-exposed fetuses with higher AD compared with controls.

ranges and in association with various substances. There are studies describing alterations in neonates, infants, and school-aged children.<sup>16,22-24</sup> However, some of these changes are not consistently found in all studies in terms of the direction of alterations. For example, 1 study described decreased FA in prenatal methadone-exposed infants compared with controls.<sup>23</sup> Another more recent study described significantly increased FA values in neonates (37- to 49-weeks' postmenstrual age) with prenatal opioid exposure.<sup>25</sup> The authors of this study also noted increased FA values in infants with prenatal exposure to cocaine and marijuana. Some of these previous works revealed region-specific direction changes in DTI parameters in the same cohort, reflecting the complexity of the underlying mechanisms of injury as a result of prenatal substance abuse on the developing brain.<sup>15,26</sup>

While our study potentially contributes one of the only descriptions of altered DTI parameters on fetal MR imaging in prenatal opioid exposure, the clinical significance of these results is preliminary in nature. Previous work examining the relationship between DTI and histology has demonstrated that, in general, abnormally lower FA values and higher MD, AD, and/or RD values are often interpreted as damage to the myelin sheath and axonal membrane. However, higher FA and lower MD, AD, and/or RD values can also be attributed to extracellular

space compression, cytotoxic edema, or inflammation.<sup>27,28</sup> In the present study, we identified multiple WM regions with abnormally higher FA, driven mainly by the increase of AD, a result that seems to be in line with the latter scenario. Increased expression of inflammatory genes has also been demonstrated in infants with prenatal opioid exposure compared with unexposed controls, making the underlying inflammatory processes a potential explanation for our findings.<sup>29</sup> However, contrary to the direction of changes observed in these studies, 1 mouse model study demonstrating increased serum inflammatory biomarkers described reduced WM FA on ex vivo DTI of the brain with decreased axial diffusivity.<sup>30</sup> Also, the interpretation of underlying neuropathology and its potential association with substance abuse during fetal life is complicated by the rapid fetal brain development and maturation process. Furthermore, our statistical analysis of group differences assumed a linear relationship in the developmental trajectory for DTI, which may not be accurate.

The current literature in fetal DTI is evolving, and while some studies have reported a linear or at least monotonic relationship between DTI and age, other studies have revealed a more complicated temporal process. For example, as reported in a study by Zanin et al,<sup>31</sup> the potential relationship between DTI and age may vary as determined by different phases during fetal brain

maturation. While no significant age correlation was found for DTI in our data, this finding could be due to the limited sample size in our study, which did not allow further exploration of this relation. Therefore, future studies with larger sample sizes are critical in elucidating underlying injury mechanisms along with spatiotemporal progression in the fetal brain with opioid exposure.<sup>32</sup>

Our study has limitations. One of the major limitations of this study is the relatively small sample size. The issue was partially addressed through bi-institutional collaboration and the use of ComBat harmonization. However, additional studies in larger patient populations will be needed to further understand and validate these results. Another limitation commonly encountered in fetal imaging is motion artifacts, which are one of main challenges faced in fetal DTI performance. Despite using SVR to improve image quality, multiple patients had to be excluded for excessive fetal motion in this study. Super resolution reconstruction methods have been shown to improve the image and data quality by scanning in multiple orthogonal planes and show promise for future studies though they come at the cost of increased imaging time.<sup>33</sup> Finally, one of the main limitations of this study relates to the opioid-exposed patient population and the potential for confounding variables. In the opioid-exposed cohort, 54.5% (6/11) of mothers had reported prenatal exposure to nicotine, other illicit drugs, or both, which can affect brain development. Also, fetal brain development may have been impacted by a range of additional factors such as maternal nutrition, stress, and other environmental factors.

## CONCLUSIONS

This study demonstrates the feasibility of the application of fetal DTI, a highly challenging technique, to quantitatively assess WM integrity in opioid-exposed fetuses. Our multisite data show widespread WM regions with significant DTI abnormalities in the patients, which we hypothesize to be due to prenatal opioid exposure causing impairment during the complex series of neurogenic events (neurogenesis, neuronal migration, synapsis, axonal growth, myelination) in the fetal development and maturation process. Early detection of such abnormalities as well as their progression will provide critical data to inform prenatal counseling, treatment, and intervention strategies with the ultimate aim of optimizing long-term outcomes.

Disclosure forms provided by the authors are available with the full text and PDF of this article at [www.ajnr.org](http://www.ajnr.org).

## REFERENCES

- Ko JY, D'Angelo DV, Haight SC, et al. **Vital signs: prescription opioid pain reliever use during pregnancy: 34 U.S. jurisdictions, 2019.** *MMWR Morb Mortal Wkly Rep* 2020;69:897–903 CrossRef Medline
- Hirai AH, Ko JY, Owens PL, et al. **Neonatal abstinence syndrome and maternal opioid-related diagnoses in the US, 2010-2017.** *JAMA* 2021;325:146–55 CrossRef Medline
- Larson JJ, Graham DL, Singer LT, et al. **Cognitive and behavioral impact on children exposed to opioids during pregnancy.** *Pediatrics* 2019;144:e20190 CrossRef Medline
- Lee SJ, Woodward LJ, Henderson JMT. **Educational achievement at age 9.5 years of children born to mothers maintained on methadone during pregnancy.** *PLoS One* 2019;14:e0223685–20 CrossRef
- Jaekel J, Kim HM, Lee SJ, et al. **Emotional and behavioral trajectories of 2 to 9 years old children born to opioid-dependent mothers.** *Res Child Adolesc Psychopathol* 2021;49:443–57 CrossRef Medline
- Merhar SL, Parikh NA, Braimah A, et al. **White matter injury and structural anomalies in infants with prenatal opioid exposure.** *AJNR Am J Neuroradiol* 2019;40:2161–65 CrossRef Medline
- Merhar SL, Kline JE, Braimah A, et al. **Prenatal opioid exposure is associated with smaller brain volumes in multiple regions.** *Pediatr Res* 2021;90:397–402 CrossRef Medline
- Merhar SL, Jiang W, Parikh NA, et al. **Effects of prenatal opioid exposure on functional networks in infancy.** *Dev Cogn Neurosci* 2021;51:100996 CrossRef Medline
- Radhakrishnan R, Vishnubhotla R. V, Zhao Y, et al. **Global brain functional network connectivity in infants with prenatal opioid exposure.** *Front Pediatr* 2022;10:847037 CrossRef Medline
- Radhakrishnan R, Elsaid NMH, Sadhasivam S, et al. **Resting state functional MRI in infants with prenatal opioid exposure—a pilot study.** *Neuroradiology* 2021;63:585–91 CrossRef Medline
- Radhakrishnan R, Vishnubhotla R. V, Guckien Z, et al. **Thalamocortical functional connectivity in infants with prenatal opioid exposure correlates with severity of neonatal opioid withdrawal syndrome.** *Neuroradiology* 2022;64:1649–59 CrossRef Medline
- Griffiths PD, Bradburn M, Campbell MJ, et al; MERIDIAN collaborative group. **Use of MRI in the diagnosis of fetal brain abnormalities in utero (MERIDIAN): a multicentre, prospective cohort study.** *Lancet* 2017;389:538–46 CrossRef Medline
- Nagaraj UD, Kline-Fath BM, Zhang B, et al. **MRI findings in third-trimester opioid-exposed fetuses with focus on brain measurements: a prospective multicenter case-control study.** *AJR Am J Roentgenol* 2023;220:418–27 CrossRef Medline
- Hornburg KJ, Slosky LM, Cofer G, et al. **Prenatal heroin exposure alters brain morphology and connectivity in adolescent mice.** *NMR Biomed* 2023;36:e4842 CrossRef Medline
- Grecco GG, Shahid SS, Atwood BK, et al. **Alterations of brain microstructures in a mouse model of prenatal opioid exposure detected by diffusion MRI.** *Sci Rep* 2022;12:17085 CrossRef Medline
- Vishnubhotla R. V, Zhao Y, Wen Q, et al. **Brain structural connectome in neonates with prenatal opioid exposure.** *Front Neurosci* 2022;16:952322 CrossRef Medline
- Ebner M, Wang G, Li W, et al. **An automated framework for localization, segmentation and super-resolution reconstruction of fetal brain MRI.** *Neuroimage* 2020;206:116324 CrossRef Medline
- Gholipour A, Rollins CK, Velasco-Annis C, et al. **A normative spatiotemporal MRI atlas of the fetal brain for automatic segmentation and analysis of early brain growth.** *Sci Rep* 2017;7:476 CrossRef Medline
- Mori S, Wakana S, van Zijl PC, et al. *MRI Atlas of Human White Matter.* Elsevier; 2005
- Khan S, Vasung L, Marami B, et al. **Fetal brain growth portrayed by a spatiotemporal diffusion tensor MRI atlas computed from in utero images.** *Neuroimage* 2019;185:593–608 CrossRef Medline
- Fortin JP, Parker D, Tunç B, et al. **Harmonization of multi-site diffusion tensor imaging data.** *Neuroimage* 2017;161:149–70 CrossRef Medline
- Walhovd KB, Watts R, Amlien I, et al. **Neural tract development of infants born to methadone-maintained mothers.** *Pediatr Neurol* 2012;47:1–6 CrossRef Medline
- Monnelly VJ, Anblagan D, Quigley A, et al. **Prenatal methadone exposure is associated with altered neonatal brain development.** *Neuroimage Clin* 2018;18:9–14 CrossRef Medline
- Walhovd KB, Westlye LT, Moe V, et al. **White matter characteristics and cognition in prenatally opiate- and polysubstance-exposed children: a diffusion tensor imaging study.** *AJNR Am J Neuroradiol* 2010;31:894–900 CrossRef Medline
- Peterson BS, Rosen T, Dingman S, et al. **Associations of maternal prenatal drug abuse with measures of newborn brain structure, tissue organization, and metabolite concentrations.** *JAMA Pediatr* 2020;174:831–42 CrossRef Medline

26. Lebel C, Warner T, Colby J, et al. **White matter microstructure abnormalities and executive function in adolescents with prenatal cocaine exposure.** *Psychiatry Res* 2013;213:161–68 CrossRef Medline
27. Song SK, Sun SW, Ju WK, et al. **Diffusion tensor imaging detects and differentiates axon and myelin degeneration in mouse optic nerve after retinal ischemia.** *Neuroimage* 2003;20:1714–22 CrossRef Medline
28. Niogi SN, Mukherjee P. **Diffusion tensor imaging of mild traumatic brain injury.** *J Head Trauma Rehabil* 2010;25:241–55 CrossRef Medline
29. Yen E, Madan N, Tarui T, et al. **Sex-specific inflammatory and white matter effects of prenatal opioid exposure: a pilot study.** *Pediatr Res* 2023;93:604–11 CrossRef Medline
30. Jantzie LL, Maxwell JR, Newville JC, et al. **Prenatal opioid exposure: the next neonatal neuroinflammatory disease.** *Brain Behav Immun* 2020;84:45–58 CrossRef Medline
31. Zanin E, Ranjeva JP, Confort-Gouny S, et al. **White matter maturation of normal human fetal brain: an in vivo diffusion tensor tractography study.** *Brain Behav* 2011;1:95–108 CrossRef Medline
32. Machado-Rivas F, Afacan O, Khan S, et al. **Tractography of the cerebellar peduncles in second- and third-trimester fetuses.** *AJNR Am J Neuroradiol* 2021;42:194–200 CrossRef Medline
33. Machado-Rivas F, Afacan O, Khan S, et al. **Spatiotemporal changes in diffusivity and anisotropy in fetal brain tractography.** *Hum Brain Mapp* 2021;42:5771–84 CrossRef Medline

# Acute and Chronic Kernicterus: MR Imaging Evolution of Globus Pallidus Signal Change during Childhood

J. Gburek-Augustat,<sup>1</sup> I. Sorge,<sup>2</sup> M. Stange,<sup>3</sup> J. Kern,<sup>4</sup> A. Merckenschlager,<sup>5</sup> T. Nägele, and I. Krägeloh-Mann<sup>6</sup>



## ABSTRACT

**BACKGROUND AND PURPOSE:** Despite its rarity in Western countries, kernicterus resulting from severe neonatal hyperbilirubinemia and its associated neurologic consequences still persists. Subtle MR imaging patterns may be overlooked, leading to diagnostic and prognostic uncertainties. The study systematically analyzes MR imaging pattern over time.

**MATERIALS AND METHODS:** A retrospective MR imaging study was conducted in Departments of Pediatric Neurology at the University Children's Hospitals in Leipzig, Germany, or Tübingen, Germany, between 2012 and 2022 in patients who presented beyond the neonatal period suspected of having chronic kernicterus.

**RESULTS:** Eight patients with a total of 15 MR images were identified. The clinical diagnosis of kernicterus was confirmed in all cases on the basis of typical MR imaging findings: Bilateral, diffuse hyperintensity of the globus pallidus was observed in the neonatal period on T1WI (1 MR imaging, at 2 weeks), in infancy on T2WI (4 MR images, at 9–26 months). In children 2 years of age and older, bilateral hyperintensity on T2WI was limited to the borders of the globus pallidus (8 MR images, at 20 months –13 years). Notably, 2 children exhibited normal initial MR imaging findings at 2 months of age. Hence, MR imaging depiction of kernicterus pathology evolves with time, first evident on T1WI, subsequently on T2WI, with a “blind window” during early infancy. The T2WI signal change initially involves the entire globus pallidus and later is limited to the borders. Kernicterus had not been diagnosed in any except 2 patients by previous investigators.

**CONCLUSIONS:** All patients presented with a characteristic clinical history and signs and an evolving MR imaging pattern. Nonetheless, the diagnosis of kernicterus was frequently missed. Abnormalities on later MR images appear to be underrecognized.

**ABBREVIATIONS:** ABE = acute bilirubin encephalopathy; BFMF = Bimanual Fine Motor Function; CP = cerebral palsy; GMFCS = Gross Motor Function Classification System; GP = globus pallidus

In neonates, the physiologic increase of unconjugated bilirubin typically occurs around days 5–7. Bilirubin, being lipophilic, can be freely distributed throughout all tissues. This is not problematic as long as the increase is moderate. However, at high concentrations, deposition occurs in various tissues, especially in the basal ganglia, hippocampus, cerebellum, and cranial nerve nuclei. Failure to initiate appropriate therapy such as phototherapy or

exchange transfusion may result in bilirubin deposition causing damage to vulnerable brain structures (basal ganglia and brainstem nuclei), leading to the clinical manifestations of kernicterus.<sup>1,2</sup> Symptoms of acute bilirubin encephalopathy (ABE) include lethargy, muscular hypotonia, feeding problems, high-pitched crying, retrocollis, fever, apnea, and seizures. Chronic kernicterus refers to the residual damage that occurs following the acute phase. It is a spectrum disease, depending on the severity, duration, and timing of exposure to unconjugated bilirubin.<sup>3</sup> Long-term sequelae commonly observed are dyskinetic cerebral palsy (CP) with varying degrees of severity and hearing disorders up to complete deafness. Also, eye-movement disorders, in particular vertical gaze palsy, are typical. Dental enamel dysplasia may also develop. Historically, kernicterus accounted for approximately 10% of cases of CP, notably the dystonic or athetoid form.<sup>4</sup>

With an improved understanding of the underlying pathomechanism, bilirubin is now monitored in neonates, and prophylactic treatment with phototherapy and, in severe cases, exchange

Received April 9, 2023; accepted after revision June 25.

From the Division of Neuropaediatrics (J.G.-A., A.M.), and Department of Pediatric Radiology (I.S.), University Hospital for Children and Adolescents, University Leipzig, Germany; Department of Pediatrics (M.S.), University Hospital Halle, Halle, Germany; Department of Paediatric Neurology (J.K., I.K.-M.), University Children's Hospital, Tübingen, Germany; and Department of Diagnostic and Interventional Neuroradiology (T.N.), Tübingen University Hospital, Tübingen, Germany.

Please address correspondence to Janina Gburek-Augustat, MD, University Hospital Leipzig, Division of Neuropaediatrics, Hospital for Children and Adolescents, Liebigstr 20a, D- 04104 Leipzig, Germany; e-mail: Janina.Gburek-Augustat@medizin.uni-leipzig.de



Indicates article with online supplemental data.

<http://dx.doi.org/10.3174/ajnr.A7948>

**Table 1: Absolute inclusion and exclusion criteria**

Inclusion Criteria	Exclusion Criteria
Dyskinetic CP	Movement disorder with onset after infancy
Developmental delay since neonatal period	Progressive disorder
Hyperbilirubinemia in neonatal period	Other explanatory causes

**Table 2: Relative inclusion criteria**

Hearing impairment
Vertical gaze palsy
Dental enamel dysplasia

transfusions is established. Phototherapy is recommended when bilirubin levels reach  $\geq 20$  mg/dL after 72 hours of life. If the neonate has an infection, is premature, or has an early and rapid rise in bilirubin, treatment is indicated at lower levels. These interventions have dramatically reduced the incidence of kernicterus. In countries with low infant mortality, the incidence was estimated to be 0.4–2.7 per 100,000 between 1988 and 2005.<sup>5</sup>

However, kernicterus has not disappeared completely. Hemolytic disorders such as Rh or ABO incompatibility or predisposing underlying diseases associated with excessive hyperbilirubinemia in the neonatal period, eg, glucose-6-phosphate dehydrogenase deficiency and Crigler-Najjar syndrome, can lead to kernicterus if not rigorously treated. In addition, critically ill neonates with sepsis and hypoalbuminemia or preterm-born children are at higher risk. Monitoring bilirubin in neonates may be insufficient. In Western countries, this is possibly due to neglect because the disease has lost its terror and the consequences are no longer present. Early hospital discharge, breastfeeding, and negligent neonatal monitoring contribute to an increased risk.<sup>6–10</sup> In developing countries, comprehensive monitoring of neonates may not be widely established, resulting in a higher incidence of untreated hyperbilirubinemia. The availability of therapies and the decline in incidence have led to a reduced awareness of kernicterus and its diagnostic criteria.<sup>6</sup>

In MR imaging, the typical pattern observed in kernicterus is bilateral hyperintensity in the globus pallidus (GP), which varies with time. This characteristic finding is not always prominent and can be easily overlooked. During the acute phase in the neonatal period, the GP demonstrates a bilateral signal increase on T1WI, while in the chronic phases, the signal increase is observed on T2WI.<sup>11</sup> Additionally, there may be a bilateral signal increase in the subthalamic nucleus and volume loss in the hippocampus.<sup>12</sup>

The diagnosis of chronic kernicterus signifies an acquired and nonprogressive encephalopathy and enables counseling regarding future development.

This study aimed to retrospectively analyze MR imaging findings of patients clinically suspected of having chronic kernicterus, with a focus on changes in the GP signal.

## MATERIALS AND METHODS

A retrospective MR imaging study was conducted on patients who presented beyond the neonatal period and were suspected of having chronic kernicterus in the departments of Pediatric Neurology at the University Hospital for Children and Adolescents in Leipzig,

Germany, or Tübingen, Germany, between 2012 and 2022. The primary purpose of their hospital visits was to diagnose developmental and movement disorders.

The study adhered to ethical guidelines and obtained proper consent (AZ 330–13-18112013). It followed the standards of good clinical practice and the Declaration of Helsinki.

The inclusion criteria for patients were as follows (Tables 1 and 2):

- 1) The presence of dyskinetic CP characterized by involuntary, uncontrolled, recurring, occasionally stereotyped movements; fluctuating muscle tone; and persistent primitive reflex patterns
- 2) Developmental delay with an onset in the neonatal period
- 3) A history of hyperbilirubinemia in the neonatal period
- 4) Hearing impairment, vertical gaze paresis, and dental enamel dysplasia were documented but were not mandatory inclusion criteria.

The following criteria were used to exclude patients:

- 1) Movement disorders with onset after infancy
- 2) Progressive disorders such as neurometabolic diseases
- 3) Other explanatory causes such as peripartum asphyxia; congenital brain anomalies like migration, gyration, and hypomyelinating disorders; and genetic diseases
- 4) No history of hyperbilirubinemia in the neonatal period.

MR imaging analyses were performed by 2 authors (T.N. and I.K.-M.). Analysis was initially conducted independently; then, a consensus was reached for the final allocation.

Signal changes in the GP were classified into the following categories (illustrated in Fig 1):

- 1) Pattern I: diffuse signal increase on T1WI
- 2) Pattern IIa: diffuse signal increase on T2WI and/or FLAIR
- 3) Pattern IIb: signal increase on T2WI and/or FLAIR involving only borders.

Additional changes were noted as either present or absent in the following areas: hippocampal structures (including signal change or atrophy defined as enlarged surrounding spaces) and other brain areas as specified.

## RESULTS

A total of 8 patients (followed up for 6–13 years) were included in the study, and a total of 15 MR imaging examinations were performed. All patients had at least 1 MR image, 6 patients had 2, and 1 patient had 3 MR images (Online Supplemental Data).

### Case 1

Patient 1 developed hyperbilirubinemia with a maximum bilirubin level of 30 mg/dL because of glucose-6-phosphate dehydrogenase deficiency and was treated by phototherapy. At 10 years of age, he showed mild dyskinetic CP (Gross Motor Function Classification System [GMFCS I], Bimanual Fine Motor Function [BFMF II], Viking Speech Scale II).

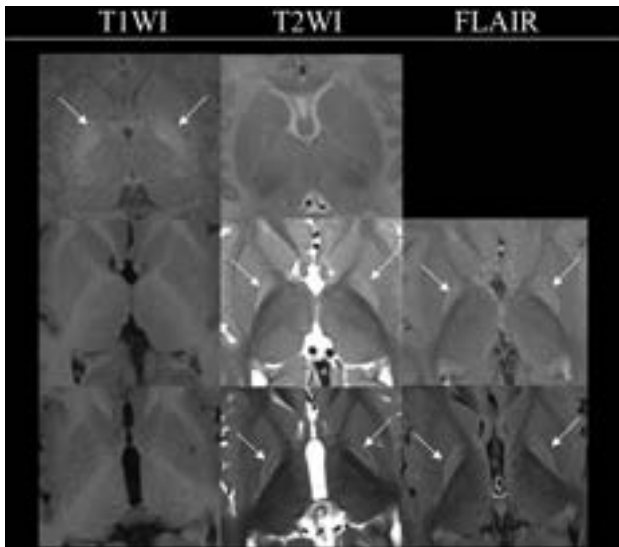


**FIG 1.** Examples illustrating the various patterns observed with respect to bilateral signal change in the GP in kernicterus. The upper row displays pattern I, characterized by a diffuse signal increase on T1WI (arrows), while T2WI shows no abnormalities (sample case one, 2 weeks). The middle row represents pattern IIa, where T1WI appears normal, but there is a diffuse signal increase on T2WI (arrows) and FLAIR (arrows), (sample case three, 11 months of age). The lower row shows pattern IIb, featuring normal T1WI findings and a signal increase on T2WI (arrows) and FLAIR (arrows), limited to the borders (sample case two, 2 years 10 months of age).

#### Case 2

Patient 2 had ABE diagnosed at day 6 after birth. His bilirubin level was 36.4 mg/dL. He underwent phototherapy, exchange transfusion, immunoglobulin infusion, and anticonvulsant therapy with phenobarbital. He developed epilepsy beyond the neonatal period. The clinical examination at 6 years of age revealed dyskinetic CP (GMFCS V, BFMF V, Viking Speech Scale IV), vertical gaze palsy, enamel dysplasia, deafness, and dysphagia.

#### Case 3

The child was born as a twin at 33 + 6 weeks of gestation with a birth weight of 1490 g. On day 2, phototherapy was started; the maximum bilirubin level was 11.7 mg/dL. During the first days, hypoalbuminemia was noticed (2.4 mg/dL). At 7.5 years of age, he had dyskinetic CP (GMFCS V, BFMF V, Viking Speech Scale IV). A severe hearing loss was treated with a cochlear implant.

#### Case 4

A girl born at 34 + 5 weeks of gestational age developed necrotizing enterocolitis and subsequent sepsis postpartum. The bilirubin level increased to 25 mg/dL when phototherapy was started (though phototherapy is recommended in such a situation, prematurity and sepsis, at a bilirubin level of  $\geq 12$  mg/dL). Clinical examination at 13 years of age showed dyskinetic CP (GMFCS V, BFMF V, Viking Speech Scale IV), vertical gaze palsy, and deafness treated with hearing aids.

#### Case 5

The girl was born in Pakistan at 36 weeks of gestation. A few days postpartum, she developed ABE. The bilirubin level was not

measured. At 6 years of age, she had dyskinetic CP (GMFCS IV, BFMF IVa, Viking speech scale IV), vertical gaze palsy, and deafness.

#### Case 6

The patient was born preterm at 35 weeks of gestational age and had severe neonatal sepsis. His bilirubin level increased to 25 mg/dL, so he was treated by exchange transfusion. The clinical examination at 11 years of age revealed mild dyskinetic CP (GMFCS I, BFMF II, Viking Speech Scale II), vertical gaze palsy, and hearing loss treated with a cochlear implant.

#### Case 7

The boy was born in Iran. He had ABE with a hyperbilirubinemia level of 29 mg/dL. Phototherapy and exchange transfusion were performed. Clinical findings at 6 years of age revealed severe dyskinetic CP (GMFCS V, BFMF V, Viking speech scale IV), recurrent dystonic crises, vertical gaze palsy, and dysphagia.

#### Case 8

The boy was born in Afghanistan and developed ABE on the fourth day of life. Clinical examination at age 11.5 years revealed severe dyskinetic CP (GMFCS V, BFMF V, Viking Speech Scale IV), vertical gaze palsy, dental enamel hypoplasia, and deafness. Due to dysphagia, he developed cachexia.

According to the clinical criteria, the diagnosis of kernicterus could be made in all the above-reported patients, but only 2 had been diagnosed by the previous MR imaging investigators (patients 1 and 3). In 2 other patients (patients 4 and 5), abnormalities in the GP were noticed (patient 5 only on the second MR imaging), but these findings were not assigned to kernicterus. In the initial reporting, 10 of 15 MR images had been evaluated with unremarkable findings.

A total of 15 MR images were re-evaluated using the above criteria (Figs 1 and 2). The assessment by the 2 raters did not differ. The MR images had been obtained in different hospitals (even in different countries) on different scanners (usually 1.5T) with different sequences, resulting in varying image quality.

On re-examination, 13 of the 15 MR images showed pathologic findings, characterized by a signal increase in the GP observed on either T1WI or T2WI. The 2 MR images considered to have unremarkable findings were obtained at 2 months of age (patients 2 and 3, the latter at the corrected age of 2 months), but subsequent follow-up at later ages revealed typical signal changes in the GP on T2WI. Thus, on the basis of the clinical criteria and the MR images, kernicterus was confirmed in all 8 patients, including the 6 patients with previously unconfirmed diagnoses based on radiology.

Analysis of the signal abnormalities in the GP across time revealed the following distinct evolution pattern.

Bilateral, diffuse hyperintensity on T1WI was observed in the neonatal period (1 MR image at 2 weeks). Subsequently, bilateral, diffuse hyperintensity of the GP on T2WI (pattern IIa) appeared during infancy (4 MR images at 9, 11, 24, and 26 months of age). In children 2 years of age and older, bilateral hyperintensity on T2WI was observed, specifically involving the

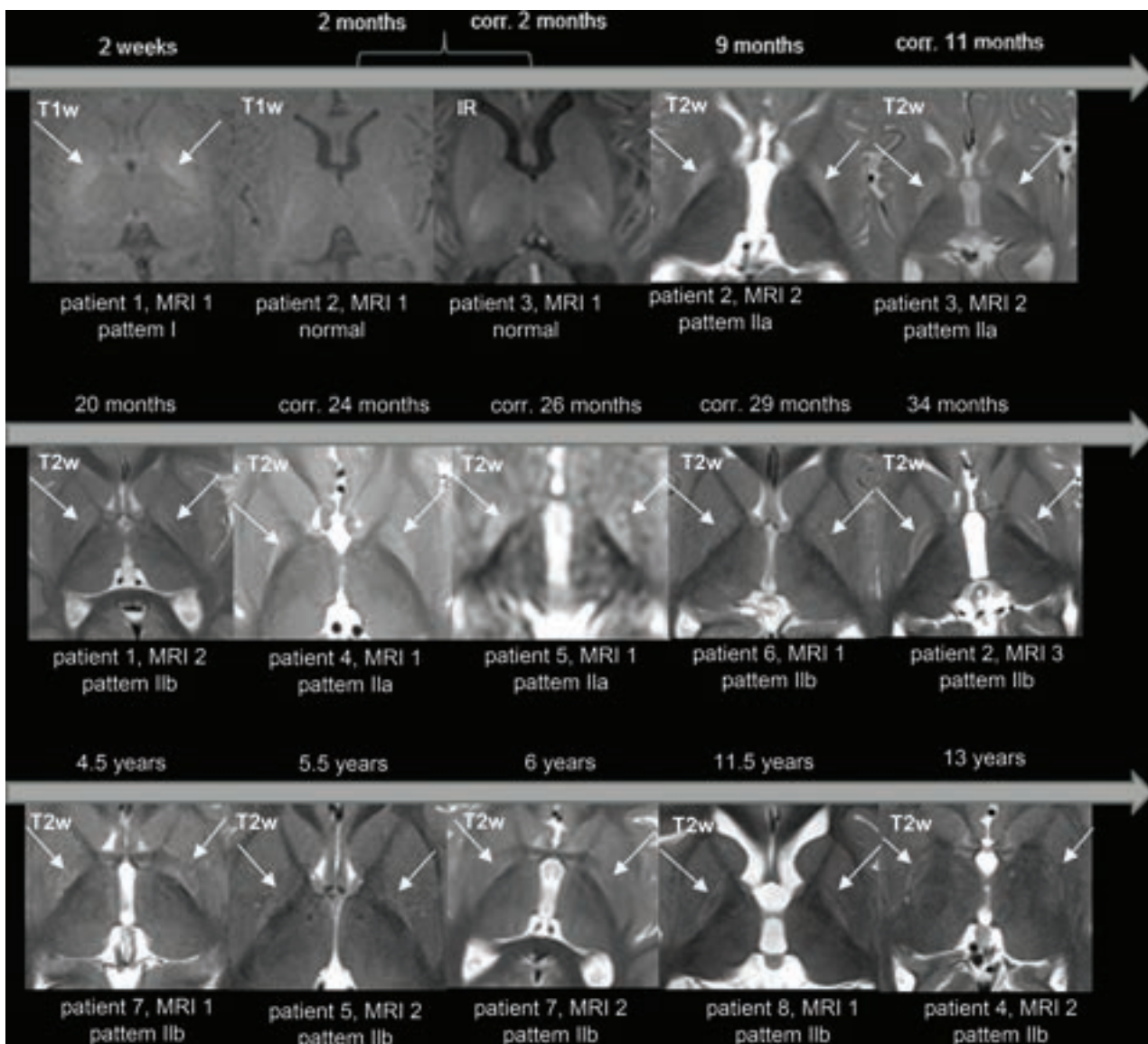


**FIG 2.** The temporal progression of the GP signal changes in 8 patients. A bilateral signal change in the GP is the characteristic sign of kernicterus. In the neonatal period, hyperintensity is observed on T1WI (arrows). However, at approximately 2 months of age, a “blind diagnostic window” is encountered, where neither T1WI nor T2WI/FLAIR show abnormal findings. Subsequently, during infancy, there is signal hyperintensity of the entire GP on T2WI/FLAIR (arrows). After around 2 years, the signal hyperintensity on T2/FLAIR is limited to the borders of the GP (arrows). IR indicates inversion recovery; corr., corrected age related to gestational age.

borders of the GP (pattern IIb) (8 MR images at 20, 29, 34 months of age, 4.5, 5.5, 6, 11.5 and 13 years). Therefore, the pathology associated with kernicterus, as depicted by the MR images, changed with time, initially evident on T1WI and then on T2WI. Furthermore, considering the 2 children initially imaged at 2 months of age with normal MR imaging findings, a “blind window” in early infancy seems to exist. Notably, the signal change on T2WI initially involved the entire GP, and later, after the second year (with some overlap), it primarily affected the borders (Figs 2 and 3).

Two patients exhibited a thinned hippocampus (patients 2 and 8, Fig 4), and these cases represented the most severe manifestations. Thus, it is hypothesized that hippocampal volume loss correlates with the severity of residual damage. No further MR imaging pathologies were observed.

## DISCUSSION

Kernicterus continues to be present in the Western world in neonates with predisposing diseases representing a higher risk. Additionally, the influx of patients from regions with inadequate neonatal care, where kernicterus is more prevalent, has contributed to its persistence.

Our study confirmed that the pathology of kernicterus, as observed through MR images, evolves with time. Previous literature<sup>13-16</sup> has extensively reported different signal characteristics on T1WI and T2WI during the neonatal period. Coskun et al,<sup>14</sup> in 2005, reported increased T1 in the GP as a common and characteristic finding of acute kernicterus. They observed this abnormality in 8 of 13 neonates (gestational ages, 34–40 weeks) between 5 and 25 days after birth. Okumura et al,<sup>17</sup> in 2021, found MR imaging abnormalities in the GP less frequently in preterm infants with bilirubin encephalopathy (scanned between 36 and 41 weeks’

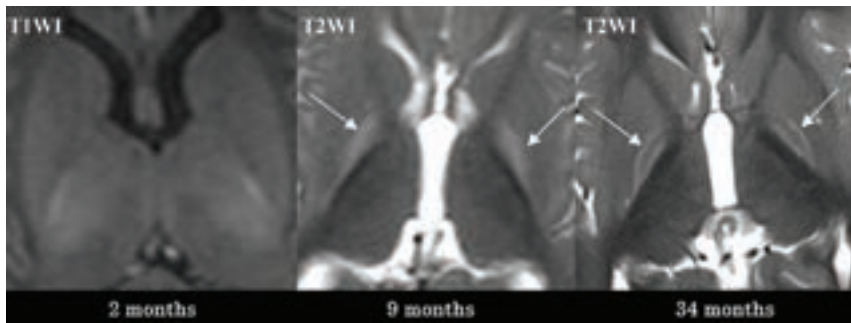


**FIG 3.** Case 2 demonstrates the typical temporal sequence in a single patient (patient 2). The initial MR imaging was performed at approximately 2 months of age, revealing no abnormalities (illustrated on T1WI, left). At 9 months of age (middle), the entire GP exhibited a diffuse signal increase on T2WI (pattern 1a, arrows). At 34 months of age (right), a signal increase on T2WI was observed solely at the borders of the GP (pattern 1b, arrows).

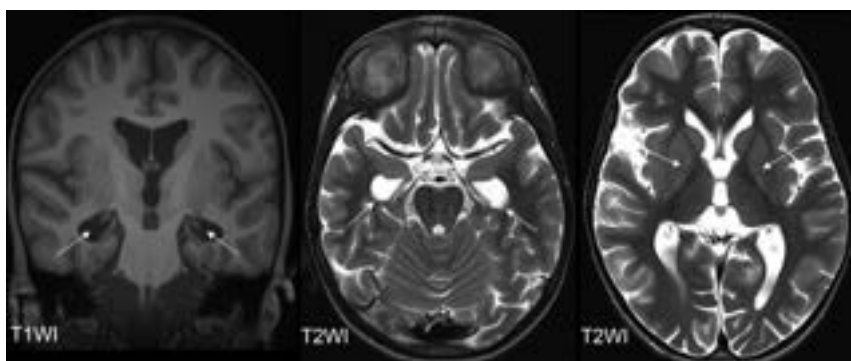


**FIG 4.** Hippocampal volume loss is illustrated in patient 8 at the age of 11.5 years. The coronal T1WI (left) displays the head of the hippocampus only as filiform structures (arrows), resulting in enlarged temporal horns, as also depicted in the axial T2WI (arrows, middle). Both the external and internal spaces are globally enlarged (axial T2WI, right). The right images highlights the bilateral signal changes in the GP (arrows), indicative of pattern 1b.

corrected gestational age) compared with mature infants. They reported that this discrepancy may be attributed to the timing of the MR image acquisition with respect to the less clear onset of bilirubin encephalopathy in preterm infants. Wisnowski et al<sup>11</sup> cautioned about the possibility of false-positive interpretations of high T1 signal in the neonatal period. They mentioned that abnormal T1-signal in the GP and subthalamic nucleus can be confused with “normal” T1 signal related to myelination, particularly with higher field strengths and modern 3D T1-weighted sequences that provide better SNR and increased sensitivity to pathology as well as normal developmental processes like myelination.

Apart from the known changes in the GP, we discovered that these changes progress through 4 phases: In phase 1, occurring during acute kernicterus in the neonatal period, there is a diffuse increase in signal intensity in the GP on T1WI. This is followed by a phase 2 interval in which no abnormalities are apparent on either T1WI or T2WI, creating a blind window that was observed at 2 months of age. Subsequently, in phase 3 during infancy, a characteristic diffuse hyperintensity of the entire GP is evident on T2WI. From approximately 2 years of age, with some overlap, the signal increase becomes evident only at the border of the GP in phase 4.

Yokochi,<sup>18</sup> in 1995, described the posterior medial border of the GP as the most sensitive to bilirubin by MR imaging. This finding could explain why this area exhibits longer-lasting and probably permanent T2 signal changes on MR images, indicating significant damage.

We were able to demonstrate 2 novel aspects, to the best of our knowledge: first, the presence of a potentially blind window after the neonatal period, in which the signal changes are not apparent on either T1WI or T2WI. Second, the development of GP hyperintensity characteristics on T2WI in chronic kernicterus, with the signal changes initially involving the entire GP and later confined to its borders.

A normal MR imaging finding beyond the neonatal period but in the first year of life, should be controlled, especially when the typical clinical signs of kernicterus are present. Furthermore, MR imaging changes in the GP after 2 years of age may be subtle. When kernicterus is suspected clinically, thin slices in the diencephalon are recommended to avoid missing the pathology. Additionally, the mild neuroradiologic findings contrast with the severe movement disorder often observed in patients with chronic kernicterus.

Another significant finding was that the characteristic MR imaging pattern of kernicterus was frequently overlooked by pre-examiners, despite the presence of typical and severe clinical symptoms. In particular, when a neonatal MR image is not available, abnormalities on later MR images appear to be underrecognized.

An earlier diagnosis of kernicterus would have spared our patients the unnecessary diagnostic procedures, such as CSF analysis (patients 5 and 7), muscle biopsy (patient 6), and extensive genetic testing (patients 3, 4, 5, 6, 7). Moreover, MR imaging follow-up, which required sedation for these patients, would have been unnecessary if the diagnosis had been clear. This diagnosis would have alleviated stress for the patients and provided the families with earlier certainty regarding the diagnosis and prognosis of the disease.

A limitation of the study is that patients were identified individually during several years in 2 German university centers; thus, this study has no clear population basis. The emphasis is less on the prevalence of the problem but on the description of signal changes in the GP with time.

The patient group is small, reflecting the rarity of the disease currently. A larger patient group would be beneficial to validate our observations. Furthermore, our study focused on children up to 13 years of age. It would be interesting to investigate the

further MR imaging course in adolescents and young adults with chronic kernicterus to understand whether the signal increase continues to decrease in the GP.

## CONCLUSIONS

Despite the presence of typical MRI patterns, characteristic clinical history, and signs in all patients, the diagnosis of kernicterus was frequently overlooked. Especially, when a neonatal MR image with its typical signal increase on T1WI of the entire GP is not available, abnormalities on later MR images seem to be underrecognized. Furthermore, early infancy MR images may not reveal any pathology on T1WI or T2WI. The typical signal increase of the entire GP on T2WI becomes apparent only toward the end of the first year and beyond. Beyond the second year, the signal increase on T2WI is observed only at the borders of the GP.

Disclosure forms provided by the authors are available with the full text and PDF of this article at [www.ajnr.org](http://www.ajnr.org).

## REFERENCES

1. Dasari VR, Shapiro SM, Yeh HW, et al. **Kernicterus Spectrum Disorders Diagnostic Toolkit: validation using retrospective chart review.** *Pediatr Res* 2022;91:862–66 CrossRef Medline
2. Le Pichon JB, Riordan SM, Watchko J, et al. **The neurological sequelae of neonatal hyperbilirubinemia: definitions, diagnosis and treatment of the Kernicterus Spectrum Disorders (KSDs).** *Curr Pediatr Rev* 2017;13:199–209 CrossRef Medline
3. Shapiro SM. **Definition of the clinical spectrum of kernicterus and bilirubin-induced neurologic dysfunction (BIND).** *J Perinatol* 2005;25:54–59 CrossRef Medline
4. Riordan SM, Shapiro SM. **Review of bilirubin neurotoxicity, I: molecular biology and neuropathology of disease.** *Pediatr Res* 2020;87:327–31 CrossRef Medline
5. Helal NF, Ghany EA, Abuelhamd WA, et al. **Characteristics and outcome of newborn admitted with acute bilirubin encephalopathy to a tertiary neonatal intensive care unit.** *World J Pediatr* 2019;15:42–48 CrossRef Medline
6. Bjerre JV, Ebbesen F. **Incidence of kernicterus in newborn infants in Denmark** [in Danish]. *Ugeskr Laeger* 2006;168:686–91 Medline
7. Ogunlesi TA, Dedek IO, Adekanmbi AF, et al. **The incidence and outcome of bilirubin encephalopathy in Nigeria: a bi-centre study.** *Niger J Med* 2007;16:354–59 Medline
8. Olusanya BO, Ogunlesi TA, Slusher TM. **Why is kernicterus still a major cause of death and disability in low-income and middle-income countries?** *Arch Dis Child* 2014;99:1117–21 CrossRef Medline
9. Olusanya BO, Kaplan M, Hansen TWR. **Neonatal hyperbilirubinaemia: a global perspective.** *Lancet Child Adolesc Health* 2018;2:610–20 CrossRef Medline
10. Alkén J, Håkansson S, Ekéus C, et al. **Rates of extreme neonatal hyperbilirubinemia and kernicterus in children and adherence to national guidelines for screening, diagnosis, and treatment in Sweden.** *JAMA Netw Open* 2019;2:e190858 CrossRef Medline
11. Wisnowski JL, Panigrahy A, Painter MJ, et al. **Magnetic resonance imaging of bilirubin encephalopathy: current limitations and future promise.** *Semin Perinatol* 2014;38:422–28 CrossRef Medline
12. Mendes VC, Costa F, Silva A, et al. **Magnetic resonance imaging of bilateral mesial temporal sclerosis in chronic kernicterus.** *J Pediatr Neurosci* 2009;4:120–21 CrossRef Medline
13. Govaert P, Lequin M, Swarte R, et al. **Changes in globus pallidus with (pre)term kernicterus.** *Pediatrics* 2003;112:1256–63 CrossRef Medline
14. Coskun A, Yikilmaz A, Kumandas S, et al. **Hyperintense globus pallidus on T1-weighted MR imaging in acute kernicterus: is it common or rare?** *Eur Radiol* 2005;15:1263–67 CrossRef Medline
15. Gkoltsiou K, Tzoufi M, Counsell S, et al. **Serial brain MRI and ultrasound findings: relation to gestational age, bilirubin level, neonatal neurologic status and neurodevelopmental outcome in infants at risk of kernicterus.** *Early Hum Dev* 2008;84:829–38 CrossRef Medline
16. Wu M, Shen X, Lai C, et al. **Detecting neonatal acute bilirubin encephalopathy based on T1-weighted MRI images and learning-based approaches.** *BMC Med Imaging* 2021;21:103 CrossRef Medline
17. Okumura A, Kitai Y, Arai H. **Magnetic resonance imaging abnormalities during the neonatal period in preterm infants with bilirubin encephalopathy.** *Pediatr Neonatol* 2021;62:567–68 CrossRef Medline
18. Yokochi K. **Magnetic resonance imaging in children with kernicterus.** *Acta Paediatr* 1995;84:937–39 CrossRef Medline

# Validity of the Bern Score as a Surrogate Marker of Clinical Severity in Patients with Spontaneous Intracranial Hypotension

J.L. Houk, S. Morrison, S. Peskoe, T.J. Amrhein, and P.G. Kranz



## ABSTRACT

**BACKGROUND AND PURPOSE:** The Bern score is a quantitative scale characterizing brain MR imaging changes in spontaneous intracranial hypotension. Higher scores are associated with more abnormalities on brain MR imaging, raising the question of whether the score can serve as a measure of disease severity. However, the relationship between clinical symptom severity and the Bern score has not been evaluated. Our purpose was to assess correlations between Bern scores and clinical headache severity in spontaneous intracranial hypotension.

**MATERIALS AND METHODS:** This study was a single-center, retrospective cohort of patients satisfying the International Classification of Headache Disorders-3 criteria for spontaneous intracranial hypotension. Fifty-seven patients who completed a pretreatment headache severity questionnaire (Headache Impact Test-6) and had pretreatment brain MR imaging evidence of spontaneous intracranial hypotension were included. Pearson correlation coefficients ( $\rho$ ) for the Headache Impact Test-6 and Bern scores were calculated. Receiver operating characteristic curves were used to assess the ability of Bern scores to discriminate among categories of headache severity.

**RESULTS:** We found low correlations between clinical headache severity and Bern scores ( $\rho = 0.139$ ; 95% CI,  $-0.127$ – $0.385$ ). Subgroup analyses examining the timing of brain MR imaging, symptom duration, and prior epidural blood patch showed negligible-to-weak correlations in all subgroups. Receiver operating characteristic analysis found that the Bern score poorly discriminated subjects with greater headache severity from those with lower severity.

**CONCLUSIONS:** Pretreatment Bern scores show a low correlation with headache severity in patients with spontaneous intracranial hypotension. This finding suggests that brain imaging findings as reflected by Bern scores may not reliably reflect clinical severity and should not replace clinical metrics for outcome assessment.

**ABBREVIATIONS:** AUC = area under the curve; EBP = epidural blood patch; HIT-6 = Headache Impact Test-6; ROC = receiver operating characteristic; SIH = spontaneous intracranial hypotension

Spontaneous intracranial hypotension (SIH) is a condition that usually presents with orthostatic headaches and demonstrates

$\geq 1$  typical finding on brain MR imaging in most cases.<sup>1-3</sup> The Bern score is a quantitative scoring system based on these brain MR imaging findings that predicts the probability of extradural CSF on subsequent spinal imaging, with higher scores reflecting greater imaging abnormalities.<sup>4</sup>

Changes of SIH on MR imaging typically reverse following successful treatment.<sup>5,6</sup> Given that Bern scores reflect the degree of abnormality on brain imaging, these scores could be used as a metric of disease severity and potentially as an outcome measure after interventions. To be useful as a severity measure, however, higher Bern scores should be correlated with higher levels of clinical severity because clinical symptom severity (typically headache severity) is the primary factor that motivates patients to seek medical care. The correlation between the severity of brain imaging abnormalities, as measured by the Bern score, and clinical severity has not yet been evaluated, to our knowledge.

Received April 3, 2023; accepted after revision July 6.

From the Departments of Radiology (J.L.H., T.J.A., P.G.K.), and Biostatistics and Bioinformatics (S.M., S.P.), Duke University School of Medicine, Durham, North Carolina.

This work is supported by the Biostatistics, Epidemiology, Research Design Methods Core funded through grant award No. UL1TR002553 from the National Center for Advancing Translational Sciences, a component of the National Institutes of Health.

The content is solely the responsibility of the authors and does not necessarily represent the official views of the National Institutes of Health.

Please address correspondence Peter G. Kranz, MD, Department of Radiology, Box 3808, Duke University Medical Center, Durham, NC 27710; e-mail: peter.kranz@duke.edu; @jhoukMD; @PeterGKranz; @TimAmrheinMD

Indicates open access to non-subscribers at www.ajnr.org

Indicates article with online supplemental data.

<http://dx.doi.org/10.3174/ajnr.A7962>

The purpose of this investigation was to determine the degree of correlation between Bern scores and headache severity in SIH. Specifically, we sought to determine whether a correlation exists between pretreatment Bern scores and headache severity as measured by a validated headache severity questionnaire. Secondly, we assessed the ability of the Bern score to discriminate patients with SIH whose headaches caused greater impact from those patients who were less clinically impacted.

## MATERIALS AND METHODS

### Subjects

This is a single-center, retrospective cohort of consecutive adult (18 years of age or older) patients who underwent a work-up for SIH at our institution between April 2016 and February 2018. As part of standard clinical care, patients routinely completed a questionnaire assessing clinical headache severity (the Headache Impact Test [HIT-6]) at presentation.<sup>7</sup> This study was approved by our institutional review board and is compliant with the Health Insurance Portability and Accountability Act.

We included patients with pretreatment brain MR imaging showing signs of SIH, defined as the presence of any one of the following: diffuse pachymeningeal enhancement, brain sagging, or venous distension. Subjects were excluded if available pretreatment brain MR imaging was >6 months from the date that the HIT-6 questionnaire was administered or if HIT-6 data were missing. Subjects were also excluded if the brain MR imaging was performed without IV contrast, because these studies lacked sufficient data to calculate an accurate Bern score.

### Evaluation of Headache Severity

All subjects completed a headache severity questionnaire before their visit to our institution. The 6-item HIT-6 is a validated instrument used to assess adverse headache impact and is used widely in clinical research and practice.<sup>8</sup> HIT-6 scores range from 36 to 78, with a larger score indicating worse impact of headaches, stratified into 4 categories: little or no impact ( $\leq 49$ ), some impact (50–55), substantial impact (56–59), and severe impact (60–78).<sup>8</sup>

### Bern Score Calculation

Bern scores were calculated using established methodology previously described in the literature.<sup>4</sup> A neuroradiology fellow with prior research experience in assessing brain MR imaging changes of SIH completed a supervised training set of cases constituting approximately 20% of the study population, to establish concordance with scores provided by a board-certified neuroradiologist with 14 years of experience in treating SIH. Bern scores for each subject were then calculated by the fellow, who was blinded to patient HIT-6 scores.

### Statistical Analysis

Demographics, HIT-6 scores, and Bern scores were reported using the mean (SD) for continuous data or counts and percentages for categorical data for the overall cohort and the subgroups on the basis of the timing of brain MR images, symptom duration, and a prior epidural blood patch (EBP). The Pearson correlation coefficient ( $\rho$ ) and 95% CIs using the Fisher Z-transform were calculated to assess correlations between the HIT-6 and Bern scores for the overall cohort and the subgroups.

### Subgroup Analyses

We conducted subgroup analyses to determine whether correlations were affected by 3 variables: the timing of brain MR imaging, symptom duration, and a history of a prior EBP. To assess the impact of the length of time since brain MR imaging on the correlation between Bern scores and HIT-6 scores, we calculated correlation coefficients for the subgroups of patients whose MR imaging was obtained either 0–3 months or 3–6 months before HIT-6 assessment. To assess the impact of symptom duration, we calculated correlation coefficients between Bern scores and HIT-6 scores for the subgroups of patients whose symptoms started either <3 months or >3 months before brain MR imaging. Finally, correlation coefficients were calculated for the subgroups of patients who had or did not have an EBP performed in the interval between brain MR imaging and HIT-6 administration.

### Receiver Operating Characteristic Analysis

To determine the ability of the Bern score to discriminate between subjects falling into the most severe headache stratum from those in less severe strata, we conducted a receiver operating characteristic (ROC) analysis. We grouped the HIT-6 scores into categories of severe ( $\geq 60$ ) and not severe ( $< 60$ ) and constructed an ROC curve for the overall cohort to assess the ability of the Bern score to discriminate between these 2 groups. An ROC curve was also generated for the subgroup of subjects who completed the HIT-6 questionnaire within 0–3 months of brain MR imaging. There were insufficient data to generate an ROC curve for the subgroup of patients with brain MR images obtained 3–6 months before completing the HIT-6 questionnaire because all subjects were in the severe category. The area under the curve (AUC) and the 95% CI using a normal approximation were reported for each ROC curve.<sup>9</sup>

## RESULTS

A total of 105 subjects with positive findings on pretreatment brain MR imaging were initially included. Forty-two patients were excluded because the MR imaging with positive findings was obtained >6 months from the HIT-6 score evaluation, and 5 patients were excluded because the initial MR imaging of the brain was performed without contrast administration, therefore providing an incomplete Bern score calculation. One patient was excluded due to an incomplete HIT-6 questionnaire.

The final study population thus consisted of 57 subjects, of whom 35 (61.4%) were women. The mean age was 53.6 (SD, 10.6) years (range, 30–73 years). CSF leaks were found to be caused by CSF-venous fistulas in 7 cases (12.3%), ventral dural tears in 13 cases (22.8%), lateral dural tears (ie, nerve root sleeve diverticula) in 9 cases (15.8%), and undetermined etiology with no visible epidural fluid in 28 cases (49.1%). Eighteen (31.6%) subjects had received a blood patch between brain MR imaging and HIT-6 administration.

The distribution of HIT-6 and Bern scores for the overall cohort and subgroups is listed in the Online Supplemental Data. Most subjects had reported the headache impact falling into the most severe category ( $n = 50$ , 87.7%), with only 1 (1.8%) subject's score reflecting "some impact," with no subjects falling into the lowest category of "little to no impact." Regarding Bern scores,

most subjects ( $n=44$ , 77.2%) fell into the high-probability category (ie, Bern score  $\geq 5$ ), with few subjects ( $n=2$ , 3.5%) in the low-probability category (ie, Bern score  $\leq 2$ ). Because the presence of at least 1 sign of SIH on brain MR imaging was an inclusion criterion for this study, no subjects had a Bern score of 0.

In the overall cohort, the correlation between paired HIT-6 and Bern scores was negligible ( $\rho = 0.139$ ; 95% CI,  $-0.127$ – $0.385$ ) (Fig 1).

### Subgroup Analysis Results

The correlations were negligible for both subgroups on the basis of the length of time between brain MR imaging and HIT-6 administration (Fig 2), with slightly lower correlation values in the group with brain MR imaging obtained 3–6 months before HIT-6 score collection ( $\rho = 0.070$ ; 95% CI,  $-0.459$ – $0.562$ ) compared with the group with brain MR imaging obtained 0–

3 months before HIT-6 administration ( $\rho = 0.162$ ; 95% CI,  $-0.150$ – $0.444$ ).

Similarly, for subgroups based on the time from symptom onset to brain MR imaging (Fig 3), there was negligible correlation in the subgroup whose symptoms started  $>3$  months before brain MR imaging ( $\rho = 0.078$ ; 95% CI,  $-0.218$ – $0.360$ ). A slightly stronger but still overall weak correlation was seen in the subgroup whose symptom onset was 0–3 months before brain MR imaging ( $\rho = 0.343$ ; 95% CI,  $-0.323$ – $0.782$ ).

For subgroups based on whether subjects had received an EBP in the interval between brain MR imaging and HIT-6 administration (Fig 4), there was negligible correlation for those who had received an EBP ( $\rho = -0.155$ ; 95% CI,  $-0.580$ – $0.337$ ) and a weak correlation for those who had not received an EBP ( $\rho = 0.313$ ; 95% CI,  $-0.002$ – $0.572$ ).

The Bern score performed poorly at discriminating subjects who fell into the headache severity categories of severe versus not severe in the overall cohort, as well as in the subgroup of subjects whose brain MR imaging was obtained 0–3 months before completing the HIT-6 score (AUC = 0.606; 95% CI, 0.347–0.864, and AUC = 0.635; 95% CI, 0.385–0.884, respectively) (Fig 5). Wide 95% CIs for the AUC values reflect the relatively small number of patients whose headaches did not fall into the severe subgroup.

### DISCUSSION

Our investigation found a low correlation between clinical headache severity, as measured by HIT-6, and Bern scores. We also found that Bern scores showed limited ability to distinguish patients with the most severe headaches from those with lower headache severity. These findings suggest that

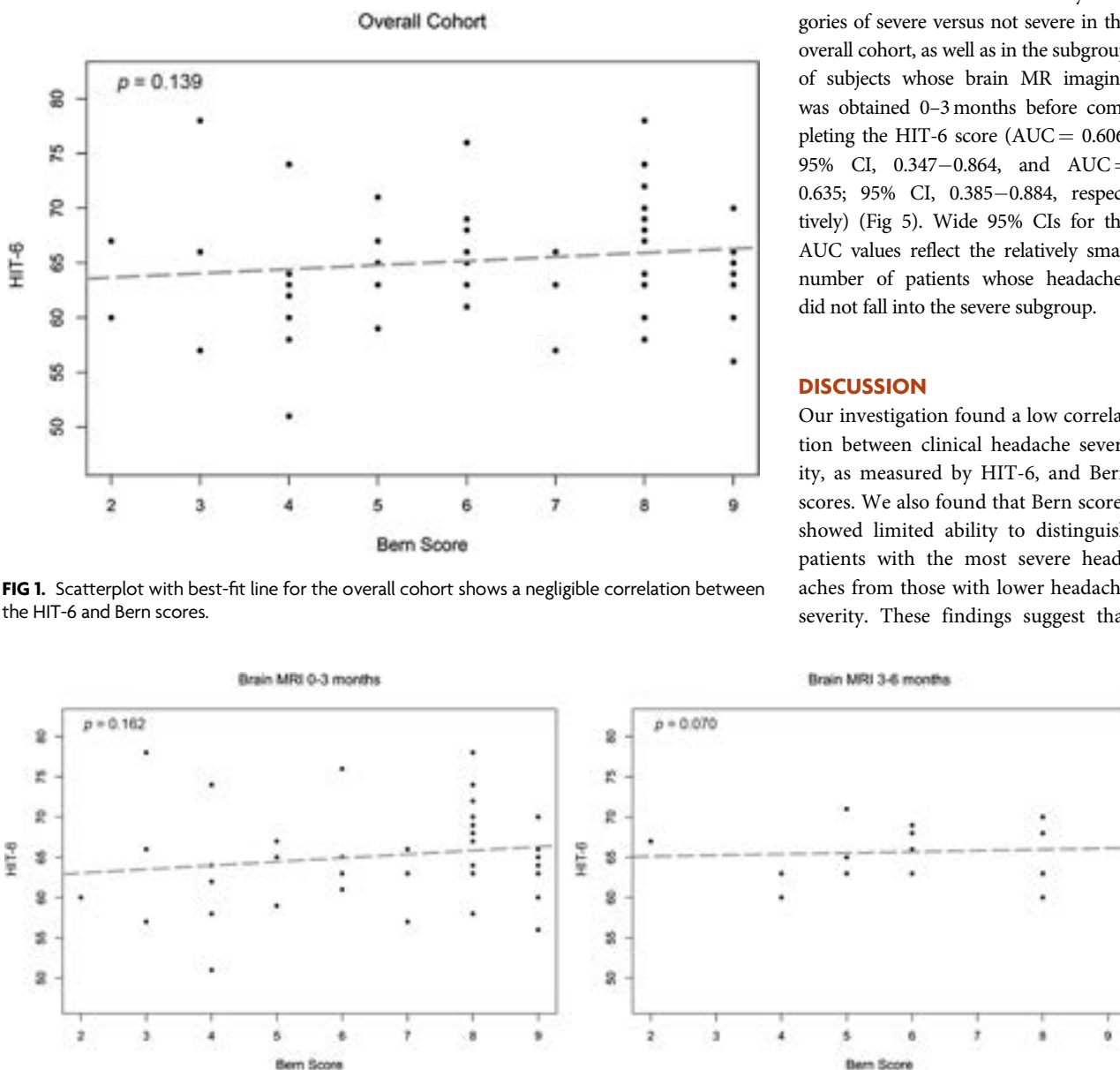


**FIG 1.** Scatterplot with best-fit line for the overall cohort shows a negligible correlation between the HIT-6 and Bern scores.

**FIG 2.** Subgroup analysis of subjects based on the time interval between brain MR imaging and HIT-6 administration. Scatterplots with best-fit lines show negligible correlations between the Bern score and the HIT-6 score in both the 0- to 3-month and 3- to 6-month subgroups.

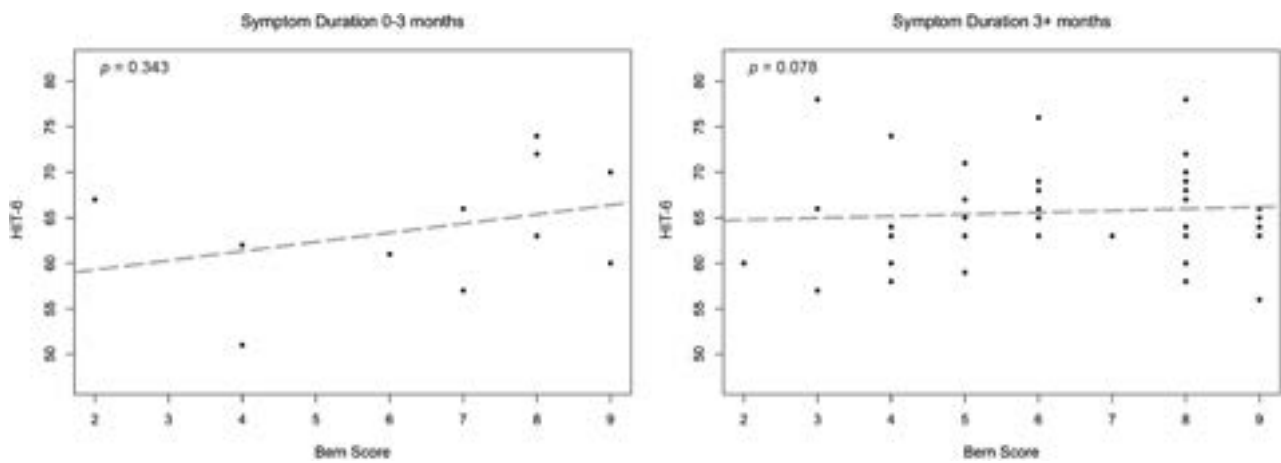


**FIG 3.** Subgroup analysis of subjects based on symptom duration before brain MR imaging. Scatterplots with best-fit lines show weak correlation between Bern scores and HIT-6 scores for subjects with symptoms of 0- to 3-month duration and negligible correlation for subjects with symptoms of >3 months' duration.

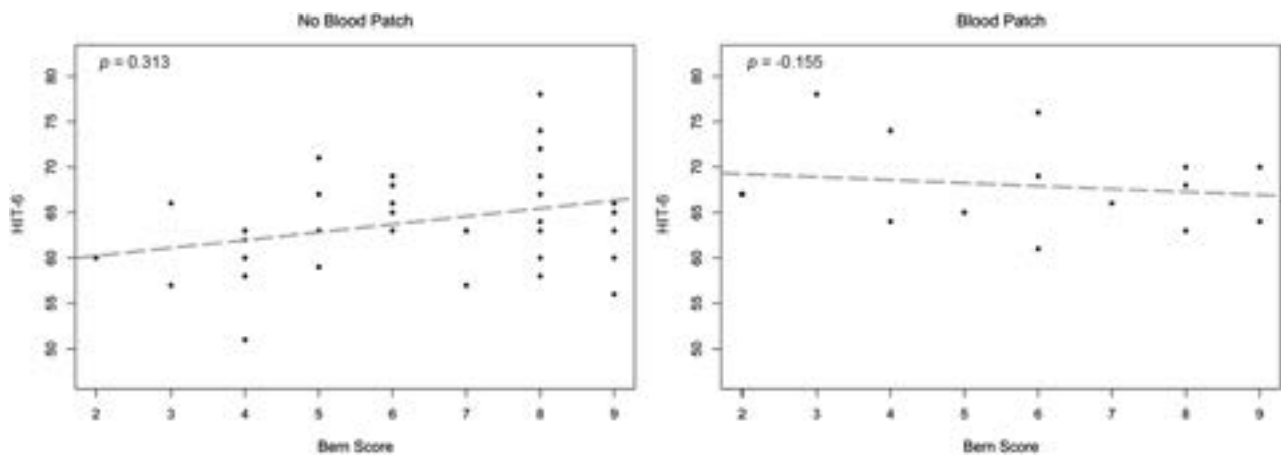


**FIG 4.** Subgroup analysis of subjects who received or did not receive an EBP in the interval between brain MR imaging and HIT-6 administration. Scatterplots with best-fit lines show negligible correlation between HIT-6 and Bern scores in subjects who received an EBP and weak correlation in subjects who did not receive an EBP.

brain imaging manifestations of SIH are poor predictors of clinical headache severity; thus, imaging findings in isolation may have limited utility as primary outcome measures when assessing treatment response.

Correlations between the Bern score and HIT-6 scores were slightly higher, but still weak, among those patients whose symptom onset was <3 months before brain MR imaging compared with those with a longer symptom duration. This result likely reflects brain imaging findings tending to become less pronounced with time,<sup>10</sup> tending to weaken correlations between imaging and clinical symptomatology. We also found that subjects who had not undergone an EBP showed slightly higher correlation compared with those who had not undergone an EBP, likely reflecting partial treatment effect as a result of this treatment. Still, even among these subgroups in which correlations were slightly stronger, the magnitude of the correlations between HIT-6 and the Bern score was still weak.

The Bern score was developed as a tool for predicting which patients with SIH would have a visible epidural fluid leak on

either conventional dynamic myelography or CT myelography.<sup>4</sup> Although the initial derivation of the score did not include patients with CSF-venous fistulas, a subsequent investigation of patients with SIH with no epidural fluid found that the Bern score also predicted which patients would have a visible CSF-venous fistula on a lateral decubitus digital subtraction myelogram.<sup>11</sup>

Because the Bern score reflects brain imaging abnormalities and those abnormalities can reverse after treatment, it is tempting to consider that improvement in this score might serve as an indicator of successful treatment. An objective score based on brain imaging such as the Bern score would be especially attractive in light of the fact that rebound intracranial hypertension often occurs after successful closure of CSF leaks and can produce headaches that confound a clear posttreatment assessment of headache severity.<sup>12,13</sup> To be useful, however, the score would need to strongly correlate with clinical symptomatology, because it is clinical symptoms that impact patient quality of life and thus drive treatment. Unfortunately, we found low correlations between Bern scores and headache severity, suggesting that while

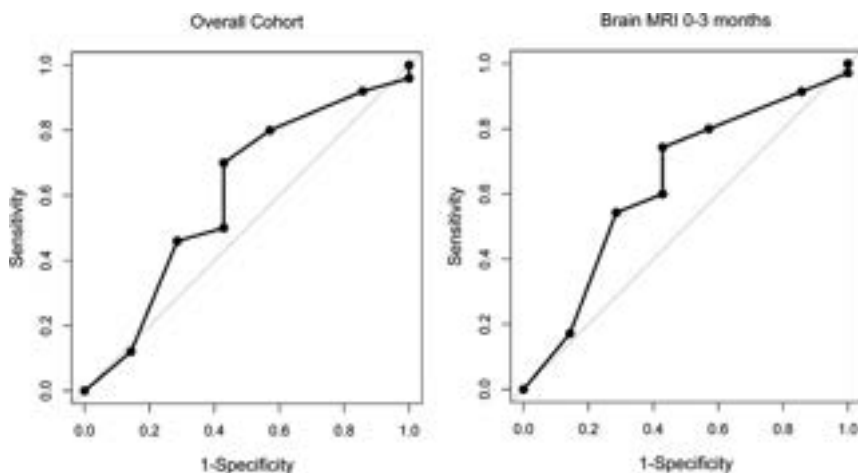


**FIG 5.** ROC curves depicting the ability of the Bern score to discriminate severe from not severe HIT-6 groups in both the overall cohort (AUC = 0.606; 95% CI, 0.347–0.864) and subgroup of subjects with brain MR imaging 0–3 months from completion of the HIT-6 (AUC = 0.635; 95% CI, 0.385–0.884). Bern scores performed poorly in both groups in discriminating clinical headache severity.

the Bern score clearly reflects physiologic alterations underlying SIH, more severe scores do not necessarily imply a more severe clinical manifestation of disease.

Limitations of this study include its retrospective nature and the single-institution design; our patient cohort consists of patients seeking care at a quaternary care center, which may impact generalizability and introduce spectrum bias. Second, readers of the brain MR imaging were not blinded to the diagnosis of SIH, which could have potentially biased Bern score assignments, though they were blinded to the HIT-6 score. Although all patients in this cohort met the criteria for SIH, we cannot guarantee that coexisting headache syndromes were not present. Additionally, the HIT-6 has not yet been validated specifically in SIH; however, it remains a widely validated scale to assess the impact of headache severity on the quality of life in other headache types, including episodic and chronic migraine, and has been used in clinical trials to assess disability due to headache.<sup>8,14</sup> Moreover, from a practical perspective, there are no headache severity scores that have been specifically validated in SIH that could serve as alternatives.

Future effort to develop validated clinical outcome measures for SIH that account for the diversity of clinical presentations and posttreatment rebound intracranial hypertension is still very much needed, particularly because novel interventional techniques are developed for treatment of various leak subtypes. While this investigation suggests that assessment of brain imaging alone is unlikely to supplant clinical assessment as a surrogate marker of outcomes, the Bern score remains a valuable tool for standardizing assessment of brain imaging features and has been shown to be predictive of the diagnostic yield of spine imaging in multiple investigations. It will likely continue to be useful as part of the pre- and posttreatment assessment of patients with SIH.

## CONCLUSIONS

Pretreatment Bern scores show a low correlation with clinical headache severity as measured by the HIT-6 in patients with SIH.

This finding suggests that Bern scores do not reliably reflect headache severity and should not replace clinical outcome measures when assessing the effectiveness of SIH treatment.

Disclosure forms provided by the authors are available with the full text and PDF of this article at [www.ajnr.org](http://www.ajnr.org).

## REFERENCES

- Schievink WI. Spontaneous intracranial hypotension. *N Engl J Med* 2021;385:2173–78 CrossRef Medline
- Kranz PG, Gray L, Malinzak MD, et al. CSF-venous fistulas: anatomy and diagnostic imaging. *AJR Am J Roentgenol* 2021;217:1418–29 CrossRef Medline
- Kranz PG, Gray L, Malinzak MD, et al. Spontaneous intracranial hypotension: pathogenesis, diagnosis, and treatment. *Neuroimaging Clin N Am* 2019;29:581–94 CrossRef Medline
- Dobrocky T, Grunder L, Breiding PS, et al. Assessing spinal cerebrospinal fluid leaks in spontaneous intracranial hypotension with a scoring system based on brain magnetic resonance imaging findings. *JAMA Neurol* 2019;76:580–87 CrossRef Medline
- Dobrocky T, Hani L, Rohner R, et al. Brain spontaneous intracranial hypotension score for treatment monitoring after surgical closure of the underlying spinal dural leak. *Clin Neuroradiol* 2022;32:231–38 CrossRef Medline
- Brinjikji W, Garza I, Whealy M, et al. Clinical and imaging outcomes of cerebrospinal fluid-venous fistula embolization. *J Neurointerv Surg* 2022;14:953–56 CrossRef Medline
- Zhang Y, Kong Q, Chen J, et al. International Classification of Headache Disorders 3rd edition beta-based field testing of vestibular migraine in China: demographic, clinical characteristics, audiometric findings and diagnosis statuses. *Cephalalgia* 2016;36:240–48 CrossRef Medline
- Kosinski M, Bayliss MS, Bjorner JB, et al. A six-item short-form survey for measuring headache impact: the HIT-6. *Qual Life Res* 2003;12:963–74 CrossRef Medline
- DeLong ER, DeLong DM, Clarke-Pearson DL. Comparing the areas under two or more correlated receiver operating characteristic curves: a nonparametric approach. *Biometrics* 1988;44:837–45 Medline
- Kranz PG, Amrhein TJ, Choudhury KR, et al. Time-dependent changes in dural enhancement associated with spontaneous intracranial hypotension. *AJR Am J Roentgenol* 2016;207:1283–87 CrossRef Medline
- Kim DK, Carr CM, Benson JC, et al. Diagnostic yield of lateral decubitus digital subtraction myelogram stratified by brain MRI findings. *Neurology* 2021;96:e1312–18 CrossRef Medline
- Kranz PG, Amrhein TJ, Gray L. Rebound intracranial hypertension: a complication of epidural blood patching for intracranial hypotension. *AJNR Am J Neuroradiol* 2014;35:1237–40 CrossRef Medline
- Wang TY, Karikari IO, Amrhein TJ, et al. Clinical outcomes following surgical ligation of cerebrospinal fluid-venous fistula in patients with spontaneous intracranial hypotension: a prospective case series. *Oper Neurosurg (Hagerstown)* 2020;18:239–45 CrossRef Medline
- Yang M, Rendas-Baum R, Varon SF, et al. Validation of the Headache Impact Test (HIT-6) across episodic and chronic migraine. *Cephalalgia* 2011;31:357–67 CrossRef Medline

# Contribution of the MP2RAGE 7T Sequence in MS Lesions of the Cervical Spinal Cord

B. Testud,<sup>1</sup> N. Fabiani,<sup>2</sup> S. Demortière,<sup>3</sup> S. Mchinda,<sup>4</sup> N.L. Medina,<sup>5</sup> J. Pelletier,<sup>6</sup> M. Guye,<sup>7</sup> B. Audoin,<sup>8</sup> J.P. Stellmann, and V. Callot<sup>9</sup>

## ABSTRACT

**BACKGROUND AND PURPOSE:** The detection of spinal cord lesions in patients with MS is challenging. Recently, the 3D MP2RAGE sequence demonstrated its usefulness at 3T. Benefiting from the high spatial resolution provided by ultra-high-field MR imaging systems, we aimed to evaluate the contribution of the 3D MP2RAGE sequence acquired at 7T for the detection of MS lesions in the cervical spine.

**MATERIALS AND METHODS:** Seventeen patients with MS participated in this study. They were examined at both 3T and 7T. The MR imaging examination included a Magnetic Imaging in MS (MAGNIMS) protocol with an axial T2\*-WI gradient recalled-echo sequence ("optimized MAGNIMS protocol") and a 0.9-mm isotropic 3D MP2RAGE sequence at 3T, as well as a 0.7-mm isotropic and 0.3-mm in-plane-resolution anisotropic 3D MP2RAGE sequences at 7T. Each data set was read by a consensus of radiologists, neurologists, and neuroscientists. The number of lesions and their topography, as well as the visibility of the lesions from one set to another, were carefully analyzed.

**RESULTS:** A total of 55 lesions were detected. The absolute number of visible lesions differed among the 4 sequences (linear mixed effect ANOVA,  $P = .020$ ). The highest detection was observed for the two 7T sequences with 51 lesions each (92.7% of the total). The optimized 3T MAGNIMS protocol and the 3T MP2RAGE isotropic sequence detected 41 (74.5%) and 35 lesions (63.6%), respectively.

**CONCLUSIONS:** The 7T MP2RAGE sequences detected more lesions than the 3T sets. Isotropic and anisotropic acquisitions performed comparably. Ultra-high-resolution sequences obtained at 7T improve the identification and delineation of lesions of the cervical spinal cord in MS.

**ABBREVIATIONS:** GRE = gradient recalled-echo; LME = linear mixed effect; MAGNIMS = Magnetic Resonance Imaging in MS; UNI = uniform

MS is an immune-mediated disease that is responsible for the formation of demyelinating lesions of the CNS, in which spinal cord involvement is very common (80%–90%<sup>1</sup> of diagnosed patients) and responsible for a large portion of the

disability.<sup>2,3</sup> Lesion assessment within the spinal cord, which is 1 of the 4 locations to confirm temporal and spatial dissemination,<sup>4</sup> is thus crucial for the diagnosis of MS and for eliminating various differential diagnoses.

The Magnetic Resonance Imaging in MS (MAGNIMS) guidelines<sup>5</sup> recommend the study of the entire spinal cord using at least 2 MR images (eg, sagittal T2WI, proton density-weighted or STIR sequences, and/or T1WI postgadolinium) to increase the confidence in lesion detection. Axial T2WI or T2\*-WI sequences are also proposed to corroborate, characterize, or confirm the presence of visible lesions. Indeed, previous studies demonstrated their relevant value for both improved lesion detection and confidence in the interpretation.<sup>6–8</sup>

In practice, lesion detection in the spinal cord of patients with MS is difficult and challenging, even using 3T MR images. These difficulties are related to physiological noise such as breathing or CSF flow<sup>9</sup> and to the relatively low spatial resolution of sequences acquired at lower field strengths such as 1.5 and 3T, resulting in

Received April 17, 2023; accepted after revision July 6.

From the Center for Magnetic Resonance in Biology and Medicine (B.T., N.F., S.D., S.M., N.L.M., J.P., M.G., B.A., J.P.S., V.C.), Aix-Marseille University, Centre national de la recherche scientifique, Marseille, France; Assistance Publique-Hopitaux de Marseille (B.T., N.F., S.D., S.M., N.L.M., J.P., M.G., B.A., J.P.S., V.C.), Hôpital Universitaire Timone, CEMEREM, Marseille, France; and Department of Neurology (S.D., J.P., B.A.), Assistance Publique-Hopitaux de Marseille, Hôpital Universitaire Timone, Marseille, France.

This work was supported by the Fondation pour l'Aide à la recherche sur la Sclérose en Plaques and the Centre National de la Recherche Scientifique. It was performed within a laboratory member of the France Life Imaging network (grant ANR-II-INBS-0006), on the platform 7T-AMI, a French "investissements d'avenir" program (grant ANR-II-EQPX-0001).

Please address correspondence to Benoit Testud, MD, Centre d'exploration métabolique par résonance magnétique, APHM La Timone, 264 Saint-Pierre St, 13385 Marseille cedex, France; e-mail: Benoit.testud@ap-hm.fr

<http://dx.doi.org/10.3174/ajnr.A7964>

**Table 1: Main sequence parameters**

Magnetic Field Sequence	3T				7T	
	T2*-WI	T2WI	STIR-WI	MP2RAGE	MP2RAGE Isotropic	MP2RAGE Anisotropic
Dimension/orientation	2D Axial	2D Sagittal	2D Sagittal	3D Sagittal	3D Coronal	3D Axial
TR (sec)	0.5	4	3.2	4	5	5
TE (ms)	27	113	53	2.48	2.15	3.05
FOV (mm)	180	280	320	300	260	256
Resolution (mm <sup>3</sup> )	0.5 × 0.5 × 5	1.1 × 0.9 × 2	0.9 × 0.7 × 3	0.9 × 0.9 × 0.9	0.7 × 0.7 × 0.7	0.3 × 0.3 × 4
Slices	9 Per slab, 2 Slabs <sup>a</sup>			176	192	64 Slices per slab, 1 or 2 Slabs <sup>a,b</sup>
Acq. time (min)	5.26	1.54	2.18	7.18	8.47	6.02/Slab

**Note:**—Acq. indicates acquisition.

<sup>a</sup>Placed perpendicular to the cord.

<sup>b</sup>Depending on cord curvature.

partial volume effects. Due to the increase in both SNR and the contrast-to-noise ratio, ultra-high-field MR imaging at 7T of the cervical spinal cord now allows a higher spatial resolution and more defined anatomic details,<sup>10,11</sup> which can help detect and delineate cervical spinal MS lesions compared with the 3T evaluation.<sup>11,12</sup> 7T also reveals information about lesion distribution in the spinal cord.<sup>13</sup> In the meantime, Demortière et al<sup>14</sup> illustrated the value of the 3D MP2RAGE<sup>15</sup> sequence at 3T, which allowed the detection of a greater number of MS lesions than sequences recommended by the MAGNIMS consensus. The MP2RAGE sequence has been used broadly in the brain<sup>16,17</sup> and was more recently optimized for the cervical spinal cord at both 3T and 7T.<sup>18,19</sup>

In line with these results, our goal was to determine the potential added value of the 7T 3D MP2RAGE sequence over a 3T MR imaging evaluation for detecting cervical spinal cord lesions in patients with MS.

## MATERIALS AND METHODS

### Population

We analyzed data collected from a prospective study focusing on the 3T and 7T multimodal assessment of the spinal cord in MS that took place from December 2017 to September 2019. The study was approved by the local Aix-Marseille University ethics committee, and written informed consent was collected from each participant before the MR imaging examinations. Inclusion criteria were a diagnosis of MS according to the revised McDonald 2017 criteria,<sup>4</sup> patients older than 18 years of age, clinical symptoms suggesting spinal cord involvement, and an MR imaging examination performed at least 3 months after steroid infusion. Patients with uncertain diagnosis, in relapse, or with a standard contraindication to an MR imaging examination such as incompatible implanted equipment, claustrophobia, agitation, and intrabody metal fragments were excluded.

### Image Acquisition

All MR imaging examinations were performed on the same day using 3T (Verio; Siemens) and 7T (Magnetom; Siemens) MR imaging systems. MR imaging at 3T was performed using the body coil for transmission and standard 12-channel head, 4-channel neck, and 24-channel spine matrix array coils for reception. MR imaging at 7T was performed using a customized 8Tx/8Rx

transceiver coil array (RAPID Biomedical), used in the compact polarimetric mode. The 7T examination was performed in the morning, and the 3T examination, in the afternoon. The 3T MR imaging protocol included the sequences recommended by the MAGNIMS consensus,<sup>20</sup> ie, sagittal 2D T2 TSE-WI and STIR-WI, as well as an axial 2D T2\*-WI multiecho gradient recalled-echo (GRE) sequence, hence forming an “optimized MAGNIMS” set. The 3T protocol also included 1 sagittal 3D MP2RAGE sequence with isotropic resolution (0.9 mm<sup>3</sup>), which covered both the brain and cervical spinal cord<sup>18</sup> and provided 2 contrasted images (TI1, TI2) from which a uniform (UNI) image and a T1 map were derived.

At 7T, the MR imaging protocol included an axial 3D MP2RAGE sequence with a spatial resolution of 0.3 × 0.3 × 4 mm<sup>3</sup> and a coronal 3D MP2RAGE sequence with an isotropic spatial resolution of 0.7 mm<sup>3</sup>. A fast T2 TSE sequence was also performed to locate the vertebral level on the 3D MP2RAGE anisotropic sequence.

The main sequence parameters are summarized in Table 1.

### Lesion Detection and Scoring

Lesion detection was performed by a consensus of a senior neuro-radiologist (B.T.), a senior neurologist (S.D.), a neuroradiology resident (N.F.), and 3 neuroscientists specialized in spinal cord MR imaging and MS (S.M., N.L.M., and V.C.), all blinded to clinical data, using the Horos Viewer (<https://horosproject.org>).

Each set (Optimized MAGNIMS, 3T MP2RAGE, 7T MP2RAGE with isotropic resolution, and 7T MP2RAGE with anisotropic resolution) was viewed successively and individually by the reading group with a 3-week delay between each session, and the viewing order of the subjects was randomly generated for each set to avoid memory bias. The 3T sequences were observed before the 7T sequences to avoid potential learning biases on 3T images due to more informative 7T images. Finally, once all imaging sets had been observed, the 4 imaging sets were displayed simultaneously to obtain a lesion concordance among imaging sets. The UNI image or the T1 map of the 3D MP2RAGE sequences or both were used for interpretation. Lesions visible on at least 2 consecutive slices and whose radiologic characteristics were in favor of MS lesions were retained for the lesion count. For each lesion, the vertebral level (from C1 to C7), the location in the transverse section plane (anterior,

lateral, posterior), and the involvement of the white and/or gray matter were recorded. Lesions in front of the intervertebral disc were considered to belong to the overlying level.

### Statistics

We performed descriptive statistics on the cohort and compared the total number of lesions visualized per sequence. We compared the absolute number of visible lesions over all sequences by computing the ANOVA of a linear mixed effect (LME) model, accounting for recurrent measurements in patients. We also computed the Dice score for pair-wise comparisons as an indicator of

the similarity. The LME approach was also applied to explore differences among spinal cord levels. *P* values below .05 were considered significant. All statistical analyses were performed using R statistical and computing software (<http://www.r-project.org>).

### RESULTS

#### Population

Of the 19 patients, 2 were excluded because the spinal cord presented with inseparable lesions (diffuse aspect). Consequently, 17 patients participated in the study (12 women/5 men; mean age, 30.2 [SD, 9.9] years; range, 20–41 years), all with a relapsing-remitting form of the disease. The study population presented with a mild disability, with a median Expanded Disability Status Scale score of 1.5 (mean, 0.9 [SD, 1]; range, 0–3) and a short disease duration, with a median of 17 months (mean, 40.8 [SD, 7.3] months; range, 6–189 months). Six patients in the study had no therapy. Detailed demographic data, clinical characteristics, and lesion counts, reported as the maximum number of lesions visualized in each patient, are summarized in Table 2. The 7T isotropic resolution 3D MP2RAGE sequence was missing for 3/17 patients.

#### Lesion Characteristics

Four patients presented with no lesions. Among the 14 patients who had 4 complete sets of images, 55 lesions were identified in total, 31 located in the posterior part of the spinal cord (56.4%), 17 lateral (30.9%), 6 anterior (10.9%), and 1 central. Twenty-eight lesions (50.9%) affected the white matter only; the remaining affected both the white and gray matter. Figure 1 shows the proportion of lesions detected by each sequence on the spinal cord globally and for each level, considering only the patients who had all 4 imaging sets. The absolute number of visible lesions differed among the 4 sequences (LME ANOVA, *P* = .020). The highest

**Table 2: Demographic and clinical characteristics**

Patients	Age (yr)	Sex	Disease Course	Disease Duration (mo)	EDSS	Lesion Count
P1	40	M	RR	95	2	7
P2 <sup>a</sup>	20	F	RR	58	2.5	3
P3	30	F	RR	87	1.5	6
P4	27	F	RR	17	3	6
P5	23	F	RR	47	0	5
P6	31	F	RR	6	0	0
P7	35	F	RR	33	1	3
P8	28	F	RR	6	0	3
P9	38	F	RR	7	1	0
P10	33	M	RR	17	0	3
P11	31	F	RR	189	0	12
P12	41	F	RR	45	1	7
P13	26	M	RR	12	0	3
P14	20	M	RR	44	0	0
P15	30	F	RR	10	1	0
P16 <sup>a</sup>	35	M	RR	11	2	12
P17 <sup>a</sup>	26	F	RR	10	1	8

**Note:**—RR indicates relapsing-remitting; F, female; M, male; EDSS, Expanded Disability Status Scale.

<sup>a</sup>The patients who could not have the examination with the 7T isotropic MP2RAGE sequence.

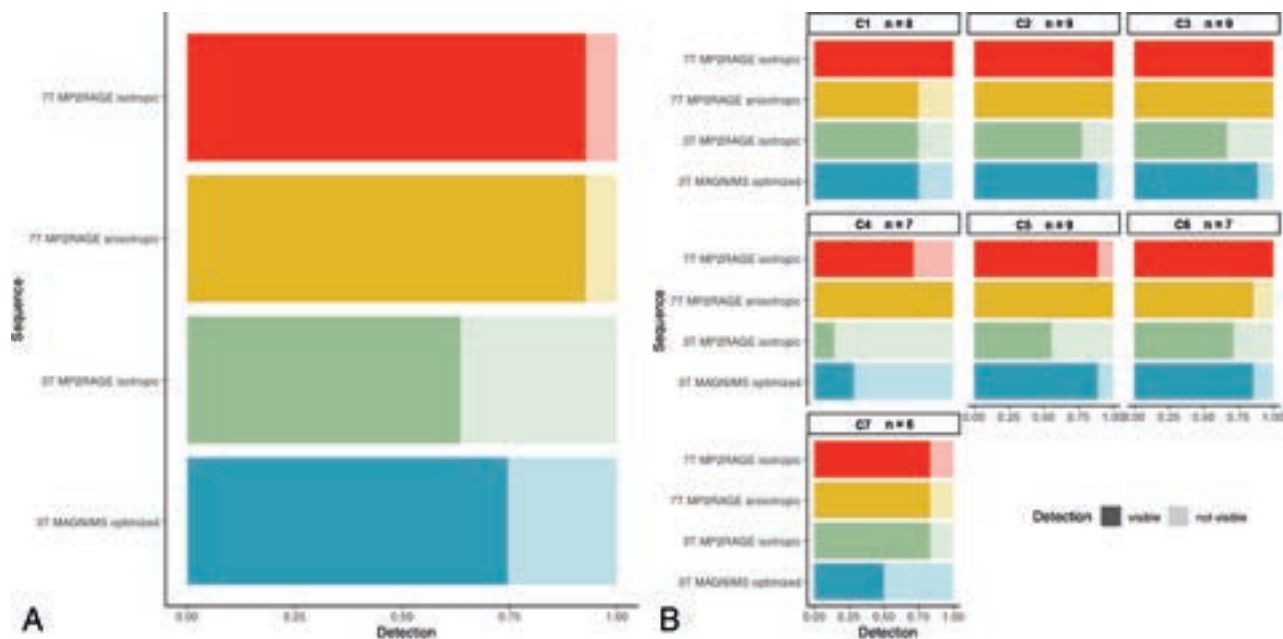


**FIG 1.** Proportion of lesion detection by sequence (A) and by sequence per vertebral level (B) for the patients having the 4 imaging sets (14 patients). The number of lesions (*n*) is detected for each cervical level.

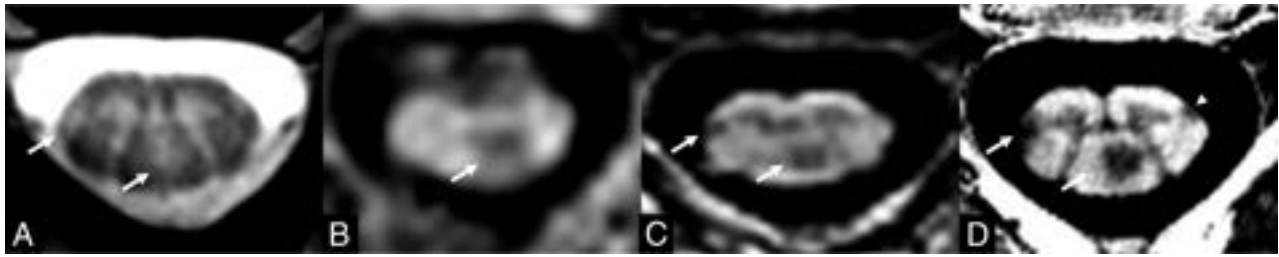


**FIG 2.** Axial presentation at the C4 level for patient P11. Images were acquired with the T2\*-WI GRE (A), 3T UNI MP2RAGE (B), 7T isotropic UNI MP2RAGE (C), and 7T anisotropic UNI MP2RAGE (D) sequences. The posterior lesion was visible on each image, the right lateral lesion was not visible on the 3T UNI MP2RAGE sequence (B), and the left lateral lesion (white arrowhead) was only detected with the 7T anisotropic UNI MP2RAGE sequence (D).

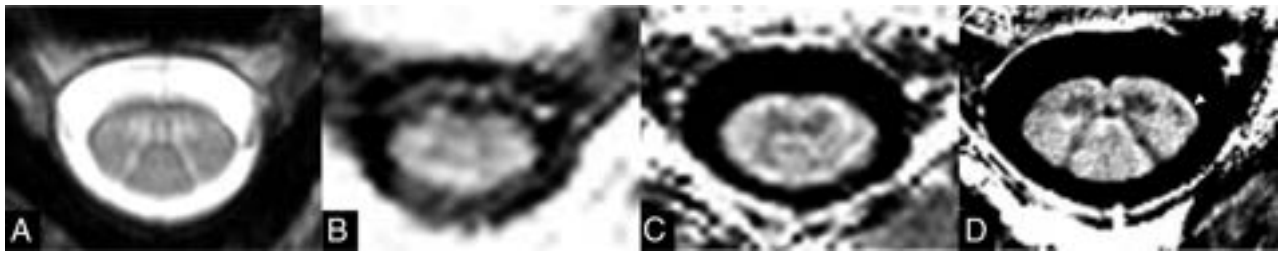


**FIG 3.** A patient P13 presenting with a C4 left lateral lesion (arrowhead). The lesion was not detected on axial T2\*-WI GRE image (A), the 3T UNI MP2RAGE (B), nor the 7T isotropic UNI MP2RAGE (C). It was only detected using the 7T anisotropic UNI MP2RAGE (D).

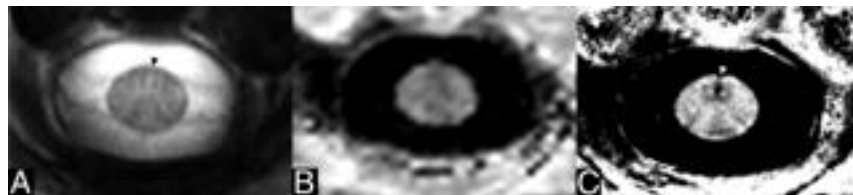


**FIG 4.** Patient P17 presented with a small lesion (arrowhead) in contact with the anterior fissure of the spinal cord at the C1–C2 level. The lesion was seen on a T2\*-WI GRE (A) image, not seen on 3T UNI MP2RAGE (B), and easily seen on 7T anisotropic UNI MP2RAGE (C) image.

that was too low: Three lesions were not detected on the 7T MP2RAGE isotropic sequence but were visible on the 7T MP2RAGE anisotropic sequence and 2 lesions that had a very small diameter in the sagittal and coronal planes were not seen on the 7T MP2RAGE anisotropic sequence due to section thickness partial volume effects but were visible on the 7T MP2RAGE isotropic sequence.

detection was observed for the two 7T sequences with 51 lesions each (LME ANOVA,  $P = 1$ , Dice = 0.92). Detection at 7T was higher on average (the whole cervical cord considered) than at 3T (LME ANOVA 3T versus 7T,  $P = .003$ , Dice = 0.59). Figures 2–5 show examples of lesions that were only visible at 7T. For the 3T MP2RAGE isotropic sequence, 35 lesions were detected (Dice = 0.57), which were not significantly less than the optimized MAGNIMS protocol with 41 lesions (Dice = 0.61; LME ANOVA,  $P = .239$ ). The spatial distribution of lesions showed the highest absolute numbers at the C2, C3, and C5 levels.

Concerning patients who could not have the examination with the 7T isotropic MP2RAGE sequence, the highest lesion detection was with the 7T anisotropic sequence with 23 lesions. 3T MP2RAGE and optimized MAGNIMS performed similarly with 15 lesions detected each.

Among all patients in the cohort, 8/78 lesions (10%) were not detected at 7T, 4 with the 7T MP2RAGE anisotropic and 4 with the 7T MP2RAGE isotropic sequences. For 3 lesions, this issue was related to artifacts that interfered with the lesion detection. For the 5 remaining lesions, this was related to having a spatial resolution

## DISCUSSION

This study showed promising results on the contribution of ultra-high-field (7T) 3D MP2RAGE sequences to cervical spinal cord involvement in MS. In addition, it provides several useful comments for clinical research practice.

In line with the literature,<sup>11</sup> the expected increase in the contrast-to-noise ratio and SNR at ultra-high field<sup>10</sup> and the high resolution allowed detection of a greater number of lesions than at 3T. The study additionally provides an objective 3T/7T comparison using the MP2RAGE sequence, compared with Dula et al,<sup>11</sup> who compared slightly different contrasts (7T T2\*-WI fast-field echo versus 3T T2WI FSE axial sequences). The readers experienced an improved viewing even in the case of numerous and coalescing lesions at 7T compared with 3T. 7T 3D-MP2RAGE allows better lesion delineation, leading to a more accurate and reliable counting compared with 3T imaging sets. The readers were able, on several occasions, to easily confirm the presence of hardly visible lesions or lesions referred to as nonspecific signal anomalies on 3T images, even an inexperienced reader. Among the patients who had the two 7T MP2RAGE sequences, we did

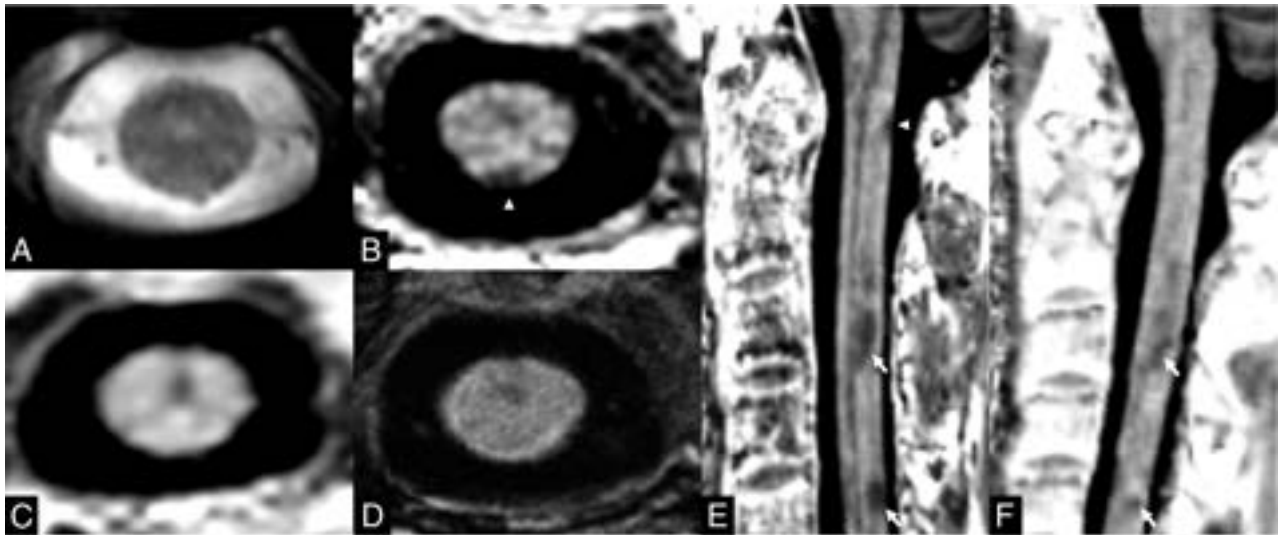


**FIG 5.** Patient P3 presented with a small posterior lesion (*white arrowhead*) at the C1 level that was not seen on axial T2\*-WI GRE (A) image nor with 3T UNI MP2RAGE (B). At 7T, the lesion was seen on the axial plane of the isotropic UNI MP2RAGE sequence (C), but it was not seen on the anisotropic 7T UNI MP2RAGE image (D). The sagittal plane (E) of the 7T isotropic UNI MP2RAGE sequence shows that this lesion (*white arrowhead*) has a small height. This lesion is not seen on the sagittal 3T UNI MP2RAGE (F). Additional lesions (*white arrows*) can be seen at the C3 and C5 levels on both sagittal planes (E and F).

not observe any difference in terms of detection. All visible lesions at 3T were identified on 1 of the two 7T sets, and only 8 lesions visible at 3T were not seen on 1 of the two 7T sets in the entire cohort. Not detecting lesions at 7T was due to artifacts or very small lesions in the z-axis (respect to transverse) plane, which penalized the 7T MP2RAGE anisotropic (respect to 7T MP2RAGE isotropic) sequence. The 7T 3D MP2RAGE sequence with isotropic resolution, which had a long acquisition time, was acquired last in our protocol, potentially making it more vulnerable to motion artifacts.

Considering the 3T data sets, Demortière et al<sup>14</sup> previously reported improved lesion detection using the 3T MP2RAGE sequence compared with the conventional MAGNIMS set. In our protocol, an “optimized” MAGNIMS set including an axial 2D T2\*-WI GRE sequence, providing high in-plane axial resolution (0.5 mm) with high white matter/gray matter/lesion contrast, was used instead. Despite being considered as optional according to the latest guidelines,<sup>5</sup> the T2\*-WI GRE sequence, nonetheless, allowed the detection of many lesions not visible otherwise, thus explaining the relative success of our optimized MAGNIMS compared with the 3T MP2RAGE. The relatively poor performance of 3T sequences at the C4 level may be attributed to the acquisition of the T2\*-WI sequence in 2 slabs, where C4 constitutes the junction between the slabs. This acquisition may have interfered with the viewing. No specific reason was identified for the 3T MP2RAGE sequence, and this issue should be further investigated in a larger cohort. An objective comparison among 2D T2\*-WI GRE, MP2RAGE, and the conventional MAGNIMS set at 3T was beyond the scope of the present study. However, such a comparison may be of interest in the future because the 3D MP2RAGE sequence offers a shorter acquisition time than the optimized MAGNIMS, as well as simultaneous coverage of both the brain and cervical cord<sup>18</sup> with an isotropic resolution. It would thus be particularly relevant for MS and

may be a good alternative to the MAGNIMS set in clinical practice.

Regarding the lesion location, lesions were more frequent in the upper cervical cord (C2–C3), and lesions in the posterior and lateral cords were the most numerous, in agreement with the literature.<sup>21,22</sup>

No specific radiologic pattern was better detected at 7T than at 3T. However, the gain in contrast and resolution allowed the detection of small lesions in locations that were not easily accessible at 3T, such as the anterior cord or on the outer edge of the cord in contact with the CSF. In addition, readers experienced a learning effect of imaging at 7T, ie, some lesions not reported at 3T could subsequently be retained after the 7T reading. Lefevre et al<sup>23</sup> could establish the existence of subpial white matter lesions using an animal experimental autoimmune encephalomyelitis model of the spinal cord, which has not been reported so far in the human spinal cord. These lesions were revealed by ex vivo ultra-high-resolution 7T MR imaging (3D T2\*-WI with an in-plane resolution of 70  $\mu\text{m}$  and a section thickness of 200  $\mu\text{m}$ ) and, thus, were unrevealable by our study.

In this study, we chose to focus on the MP2RAGE sequence, which was shown to be more robust. While the T2\*-WI of the spinal cord at 7T is a high-reward sequence with high resolution and a high contrast for lesion detection,<sup>11,13,23</sup> it is also a high-risk sequence, which is sensitive to inhomogeneities of the magnetic field and to motion artifacts.<sup>24</sup>

Our study has several limitations. It is a retrospective study with a small sample size. Although our lesion features are comparable with those in the literature and provide a representative sample of spinal cord injury in MS, a further study with a larger sample size is needed to confirm our results.

The learning effect on readers may also be a potential bias in this work, which may have led to an improvement in the performance of the readers. Nonetheless, we assume that this was

minimized by interpreting the images in different sessions with a minimum interval of 3 weeks and presenting the patients in a random order.

For each patient, the 7T MR imaging examination was performed first, and this choice may have benefited the 7T evaluation by having less risk of motion artifacts than the 3T evaluation performed later. However, patients had a long break between the 2 examinations, which limited this bias. Last, our reading process did not allow reporting of individual confidence, nor did we perform a concordance among readers, possibly limiting the relevance of our results. Nevertheless, it allowed establishing a level-by-level lesion concordance among imaging sets.

From a practical point of view, 7T sequences detected more lesions than 3T sequences. However, this added value in lesion detection must be balanced with a potentially longer acquisition time. While the 3T MP2RAGE sequence seems to be an interesting alternative to the MAGNIMS set with a T2\* axial sequence, given the equivalent acquisition time, similar lesion detection, and the possibility of covering the brain (included in the FOV), the 7T sequences are more oriented toward more precise indications. For example, the use of the 7T MP2RAGE sequence with ultra-high resolution in the axial plane could contribute beyond MS in the fine characterization of cervical myelitis or to better appreciate possible doubtful lesions.

## CONCLUSIONS

Due to increased spatial resolution, 7T 3D MP2RAGE sequences allowed improved identification and delineation of lesions compared with 3T. It would be interesting to study longitudinally the potential impact of the 7T MP2RAGE sequences on the management of patients with MS. The clinical research perspectives of 7T MR imaging now require technical advances to image the thoracic and lumbar spinal cord and to reduce the acquisition time in implementing a “compressed-sensing” version of the method<sup>25</sup> for the cord. While we are waiting for the full development and greater availability of 7T systems, it would also be interesting to investigate further the potential of the 3T 3D MP2RAGE protocol dedicated to both the brain and cervical spinal cord as an alternative to the conventional MAGNIMS protocol.

## ACKNOWLEDGMENTS

The authors thank V. Gimenez, L. Pini, C. Costes, P. Durozard, A. Rico, A. Maarouf, and M.P. Ranjeva for study logistics, as well as Tobias Kober from Siemens for MR image support.

Disclosure forms provided by the authors are available with the full text and PDF of this article at [www.ajnr.org](http://www.ajnr.org).

## REFERENCES

1. Bot JC, Blezer EA, Kamphorst W, et al. **The spinal cord in multiple sclerosis: relationship of high-spatial-resolution quantitative MR imaging findings to histopathologic results.** *Radiology* 2004;233:531–40 CrossRef Medline
2. Gass A, Rocca MA, Agosta F, et al; MAGNIMS Study Group. **MRI monitoring of pathological changes in the spinal cord in patients with multiple sclerosis.** *Lancet Neurol* 2015;14:443–54 CrossRef Medline
3. Brownlee WJ, Altmann DR, Prados F, et al. **Early imaging predictors of long-term outcomes in relapse-onset multiple sclerosis.** *Brain* 2019;142:2276–87 CrossRef Medline
4. Thompson AJ, Banwell BL, Barkhof F, et al. **Diagnosis of multiple sclerosis: 2017 revisions of the McDonald criteria.** *Lancet Neurol* 2018;17:162–73 CrossRef Medline
5. Wattjes MP, Ciccarelli O, Reich DS, et al; North American Imaging in Multiple Sclerosis Cooperative MRI guidelines working group. **2021 MAGNIMS–CMSC–NAIMS consensus recommendations on the use of MRI in patients with multiple sclerosis.** *Lancet Neurol* 2021;20:653–70 CrossRef Medline
6. Weier K, Mazraeh J, Naegelin Y, et al. **Biplanar MRI for the assessment of the spinal cord in multiple sclerosis.** *Mult Scler* 2012;18:1560–69 CrossRef Medline
7. Galler S, Stellmann JP, Young KL, et al. **Improved lesion detection by using axial T2-weighted MRI with full spinal cord coverage in multiple sclerosis.** *AJNR Am J Neuroradiol* 2016;37:963–69 CrossRef Medline
8. Bergers E, Bot JC, De Groot CJ, et al. **Axonal damage in the spinal cord of MS patients occurs largely independent of T2 MRI lesions.** *Neurology* 2002;59:1766–71 CrossRef Medline
9. Stroman PW, Wheeler-Kingshott C, Bacon M, et al. **The current state-of-the-art of spinal cord imaging: methods.** *Neuroimage* 2014;84:1070–81 CrossRef Medline
10. Barry RL, Vannesjo SJ, By S, et al. **Spinal cord MRI at 7T.** *Neuroimage* 2018;168:437–51 CrossRef Medline
11. Dula AN, Pawate S, Dortch RD, et al. **Magnetic resonance imaging of the cervical spinal cord in multiple sclerosis at 7T.** *Mult Scler* 2016;22:320–28 CrossRef Medline
12. Kreiter DJ, van den Hurk J, Wiggins CJ, et al. **Ultra-high field spinal cord MRI in multiple sclerosis: where are we standing? A literature review.** *Mult Scler Relat Disord* 2022;57:103436 CrossRef Medline
13. Ouellette R, Treaba CA, Granberg T, et al. **7 T imaging reveals a gradient in spinal cord lesion distribution in multiple sclerosis.** *Brain* 2020;143:2973–87 CrossRef Medline
14. Demortière S, Lehmann P, Pelletier J, et al. **Improved cervical cord lesion detection with 3D-MP2RAGE sequence in patients with multiple sclerosis.** *AJNR Am J Neuroradiol* 2020;41:1131–34 CrossRef Medline
15. Marques JP, Kober T, Krueger G, et al. **MP2RAGE, a self bias-field corrected sequence for improved segmentation and** *Neuroimage* 2010;49:1271–81 CrossRef Medline
16. Okubo G, Okada T, Yamamoto A, et al. **MP2RAGE for deep gray matter measurement of the brain: a comparative study with MPRAGE—MP2RAGE for deep gray matter measurement.** *J Magn Reson Imaging* 2016;43:55–62 CrossRef Medline
17. Marques JP, Gruetter R. **New developments and applications of the MP2RAGE sequence: focusing the contrast and high spatial resolution R1 mapping.** *PLoS One* 2013;8:e69294 CrossRef Medline
18. Forodighasemabadi A, Rasoanandrianina H, El Mendili MM, et al. **An optimized MP2RAGE sequence for studying both brain and cervical spinal cord in a single acquisition at 3T.** *Magn Reson Imaging* 2021;84:18–26 CrossRef Medline
19. Massire A, Taso M, Besson P, et al. **High-resolution multi-parametric quantitative magnetic resonance imaging of the human cervical spinal cord at 7T.** *Neuroimage* 2016;143:58–69 CrossRef Medline
20. Filippi M, Rocca MA, Ciccarelli O, et al; MAGNIMS Study Group. **MRI criteria for the diagnosis of multiple sclerosis: MAGNIMS consensus guidelines.** *Lancet Neurol* 2016;15:292–303 CrossRef Medline
21. Eden D, Gros C, Badji A, et al. **Spatial distribution of multiple sclerosis lesions in the cervical spinal cord.** *Brain* 2019;142:633–46 CrossRef Medline
22. Kearney H, Miller DH, Ciccarelli O. **Spinal cord MRI in multiple sclerosis: diagnostic, prognostic and clinical value.** *Nat Rev Neurol* 2015;11:327–38 CrossRef Medline

23. Lefeuvre JA, Guy JR, Luciano NJ, et al. **The spectrum of spinal cord lesions in a primate model of multiple sclerosis.** *Mult Scler* 2020;26:284–93 CrossRef Medline
24. Frebourg G, Massire A, Pini L, et al. **The good, the bad and the ugly: a retrospective study of human cervical spinal cord image quality at 7T.** In: *Proceedings of the Annual Meeting and Exhibition of the International Society for Magnetic Resonance in Medicine*, May 15–20, 2021; Virtual
25. Mussard E, Hilbert T, Forman C, et al. **Accelerated MP2RAGE imaging using Cartesian phyllotaxis readout and compressed sensing reconstruction.** *Magn Reson Med* 2020;84:1881–94 CrossRef Medline

## Regarding “Automated Segmentation of Intracranial Thrombus on NCCT and CTA in Patients with Acute Ischemic Stroke Using a Coarse-to-Fine Deep Learning Model”

We read the article by Zhu et al<sup>1</sup> with interest. The authors provided a new method to automatically segment intracranial thrombus on NCCT and CTA in patients with acute ischemic stroke (AIS) using a deep learning (DL) model. The authors should be congratulated for reaching optimal results such as predicting the thrombi length and volume, which were correlated with the manual segmentation ( $r = 0.88$  and  $0.87$ , respectively;  $P < .001$ ) in the internal cohort with similar results in the external cohort length ( $r = 0.73$ ) and volume ( $r = 0.80$ ) with a sensitivity of 94.12% and a specificity of 97.96% in differentiating large-vessel occlusion (LVO) from no LVO (including medium vessel occlusion and no occlusion). Their study gives a new indication of the development of a quantitative automated method for thrombus segmentation.

However, some limitations and concerns should be considered when interpreting the results.

First, the limitations of automatic thrombus segmentation on CT models, including partial volumes, artifacts, and calcifications, were mentioned in the text. To eliminate partial volumes and artifacts from the analysis, the authors excluded patients whose images had thick sections ( $>2.5$  mm), irremediable coregistration errors, severe motion artifacts, and beam-hardening artifacts. In our opinion, as also partly described in the text, these represent selection bias. In addition, regarding calcifications, which, in our opinion, represent the most important problem in the evaluation of vessel patency (mural or dural calcification versus thrombus), nothing was said or proposed.

Moreover, it is not clear whether in the internal validation cohort or external validation group, patients with acute hemorrhagic pathologies were included. In a previous study by Schmitt et al,<sup>2</sup> instances of false-positives and false-negatives that a DL model might include in the detection of hemorrhagic stroke were described. In particular, the DL model could not depict and differentiate an SAH in the cisterns by means of a vessel clot (hyperdensity linear thrombus), which could be concurrent in the clinical scenario of suspected AIS. Another example could be basilar artery hyperdensity due to an aneurysm that could be mistaken for

thrombus occluding the posterior circulation. It would be interesting to learn whether these patients were included, and, if not, how the authors would plan to address this previously described limitation of the DL model. Likewise, patients with postoperative and postischemic defects, tumors, hyperattenuated media sign, cavernomas, malformations, or arteriovenous fistulas were not included in the evaluations. All these conditions represent incorrectly flagged findings and missed findings as described by Seyam et al.<sup>3</sup>

Although we applaud the authors for the manual thrombus segmentation and DL model training methodologies, we believe that the findings were considerably impacted by the authors' strict patient selection. The 100% specificity value, which should not, in our opinion, be included in medical research literature, would therefore be justified.

In this regard, it is yet unclear whether this model can be incorporated into current daily hospital routine.

Disclosure forms provided by the authors are available with the full text and PDF of this article at [www.ajnr.org](http://www.ajnr.org).

### REFERENCES

1. Zhu K, Bala F, Zhang J, et al. **Automated segmentation of intracranial thrombus on NCCT and CTA in patients with acute ischemic stroke using a coarse-to-fine deep learning model.** *AJNR Am J Neuroradiol* 2023;44:641–48 CrossRef Medline
2. Schmitt N, Mokli Y, Weyland CS, et al. **Automated detection and segmentation of intracranial hemorrhage suspect hyperdensities in non-contrast-enhanced CT scans of acute stroke patients.** *Eur Radiology* 2022;32:2246–54 CrossRef Medline
3. Seyam M, Weikert T, Sauter A, et al. **Utilization of artificial intelligence-based intracranial hemorrhage detection on emergent non-contrast CT images in clinical workflow.** *Radiol Artif Intell* 2022;4:e210168 CrossRef Medline

● M. Tortora

Department of Advanced Biomedical Sciences  
University of Naples “Federico II”  
Naples, Italy

● F. Pacchiano

Radiology School, Department of Precision Medicine  
University of Campania “L. Vanvitelli”  
Caserta, Italy